CAAP Final Report

Date of Report: 12/24/2023

Prepared for: *U.S. DOT Pipeline and Hazardous Materials Safety Administration*

Contract Number: *693JK31950008CAAP*

Project Title: *Distributed Fiber Optic Sensor Network for Real-time Monitoring of Pipeline Interactive Anomalies*

Prepared by: *Yi Bao and Ying Huang*

Contact Information: yi.bao@stevens.edu (Yi Bao), ying.huang@ndsu.edu (Ying Huang)

Executive Summary

The transportation pipeline network is the vital infrastructure supplying essential energy products, ensuring the uninterrupted functioning of homes and businesses across the United States. Although numerous safety measures have contributed to maintaining a low pipeline failure rate, unfortunate incidents continue to occur, resulting in fatalities, injuries, and substantial financial losses. Recent investigations conducted by the National Transportation Safety Board (NTSB) have shed light on the significant role played by interactive anomalies in these pipeline incidents.

The goal of this project is to develop an advanced distributed fiber optic sensor network capable of detecting, locating, and quantifying interactive anomalies for pipelines. The primary research objectives encompass: (1) Development and calibration of fiber optic sensor network: Creating, calibrating, and validating a distributed fiber optic sensor network for various pipeline anomalies, while also assessing their interactions. (2) Real-time data processing: Designing and validating data processing programs for analyzing sensor data in real time. (3) Workforce development: Offering training opportunities to graduate and undergraduate students for the pipeline industry.

To achieve these objectives, this project has used a comprehensive research approach, including theoretical analysis, laboratory testing, and advanced computational techniques such as machine learning, metaheuristic optimization, and finite element analysis. The laboratory testing phase has been divided into two key stages: (1) Individual anomalies investigation: This phase explored the effects of individual anomalies (crack, dent, excavation-induced impact, and corrosion) on the measurements obtained from distributed sensors. (2) Interactive anomalies investigation: Building upon the understanding of sensing abilities, interactive anomalies involving various combinations of individual anomalies were investigated, including deformations and cracks, dent and corrosion, deformations and dents, impact and corrosion, and deformations, dents, cracks, and corrosion.

The research efforts have culminated in the development of a distributed fiber optic sensor network that seamlessly integrates multifunctional distributed and point fiber optic sensors. This network provides continuous measurements along the length of pipelines and has been deployed on various pipelines. The performance of the distributed fiber optic sensor network has undergone rigorous evaluation through extensive experiments conducted under diverse testing conditions.

The results have demonstrated the remarkable capabilities of the distributed fiber optic sensor network, including: (1) Real-time 3D strain field measurement: The network can measure arbitrary strain fields in real time. The strain fields are invaluable for assessing the mechanical condition of pipelines and guiding their operation. (2) Crack detection and visualization: The system can detect, locate, quantify, and visualize cracks in pipelines. A theoretical model was developed to support the measurements. (3) Dent and buckling detection: The network is able to detect, locate, quantify, and visualize dents and buckling in pipelines, supported by theoretical models for both global and local deformations. (4) Corrosion detection and warning: It can detect, localize, quantify, visualize, and issue warnings related to pipeline corrosion. A theoretical model for corroded pipelines has been developed. (5) Interactive anomaly detection: The network can detect and discriminate interactive anomalies, a crucial capability given that different anomaly types can exacerbate each other and accelerate pipeline degradation when occurring in the same positions. In summary, the distributed fiber optic sensor network represents a promising solution for monitoring interactive anomalies, with the goal of enhancing pipeline safety, improving management and maintenance practices, extending service life, and enhancing transport efficiency in the pipeline industry.

Table of Contents

List of Figures

List of Tables

List of Acronyms

AC	alternating current
AE	acoustic emission
AI	artificial intelligence
BOTDA	Brillouin optical time domain analysis
BOTDR	Brillouin optical time domain reflectometry
CCTV	closed-circuit television
CDO	colliding bodies optimization
CFRP	carbon-fiber-reinforced polymer
CIL	cohesive interface law
CR	corrosion rate
CSP	cross-stage partial
DC	direct current
DFOS	distributed fiber optic sensor
EMAT	electromagnetic acoustic transducer
EMI	electromagnetic interference
FBG	fiber Bragg grating
FC	fully-connected
FFT	fast Fourier transform
FN	number of missed objects
FP	number of wrongly detected objects
GA	genetic algorithm
GPIR	ground penetrating imaging radar
GPR	ground penetrating radar
GWT	guided wave testing
ILI	in-line inspection
IM	integrity management
IOU	intersection over union
LEC	Lorentz force eddy current
LVDT	Linear Variable Differential Transformer
MAE	maximum absolute error
mAP	mean average precision
MCP	mechanical contact probe
MEC	magnetic eddy current
MFL	magnetic flux leakage
NACE	National Association of Corrosion Engineers
NDE	nondestructive evaluation
NS	number of search agents
NTSB	National Transportation Safety Board
OFDR	Optical Frequency Domain Reflectometry
PC	crossover probability
PEC	pulsed eddy current
PSO	particle swarm optimization
PVC	polyvinyl chloride

PPP-BOTDA	Pulse-pre-pump Brillouin optical time domain analysis
R^2	coefficient of determination
RBF	radial basis function
RFEC	remote field eddy current
RMSE	root mean square error
ROW	right-of-way
SGD	stochastic gradient descent
SSD	single shot multibox detector
SSE	sum of squares due to error
STFT	short time Fourier transform
SVM	support vector machine
TN	number of successfully detected non-objects
TP	number of successfully detected objects
XGBoost	extreme gradient boosting
YOLO	You Only Look Once

1. Introduction

1.1. Background

“More than 2.6 million miles of transportation pipelines deliver the energy products the American public needs to keep its homes and businesses running” – USDOT PHMSA [1]. From 2003 to 2022, despite the best effort made to improve the safety of pipelines, over 12,781 incidents occurred, resulting in substantial property damage and significant injuries [2]. Figure 1.1.1 shows the number of fatalities and injuries, and the costs of the incidents [2]. Besides, significant annual investment is made for inspection and maintenance of pipelines. According to a survey performed by the National Association of Corrosion Engineers (NACE) International in 2002, the average, annual, corrosion-related costs for U.S. pipeline operators to monitor, replace, and maintain assets is over $12 billion. Therefore, pipeline integrity and its impact on the economy and prosperity of the U.S. cannot be treated light in any measure.

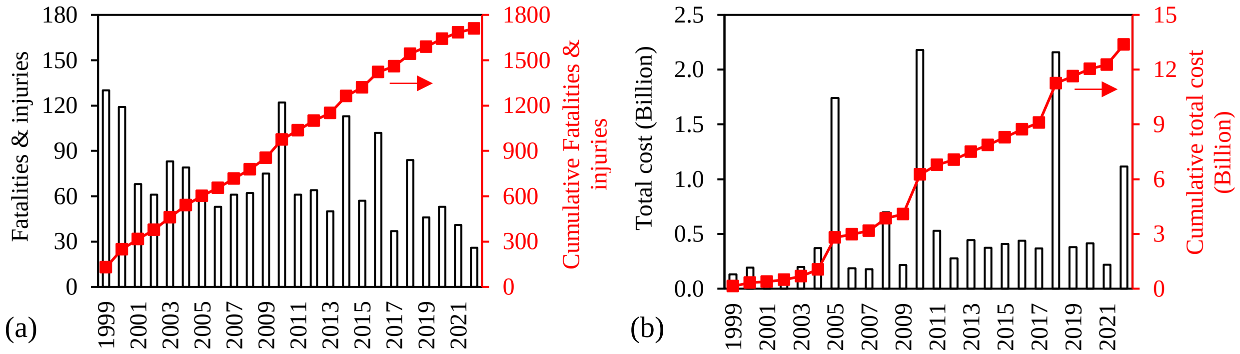

Figure 1.1.1. Pipeline incidents in 1999-2022: (a) number of fatalities and injuries, and (b) costs.

The incidents were mainly caused by corrosion, excavation damage, natural force damage, other outside force damage, material/weld failure, equipment failure, and incorrect operation [3]. Typical anomalies in pipelines include cracks, deformation (e.g., dent, gouge, ovality, buckle, roof topping, ripple/wrinkle), and corrosion [4]. Extensive research on each type of anomaly has been conducted individually, including the causes, detection methods, potential effects on pipeline performance, repair and maintenance methods [5-7]. Specifications have been issued to guide the maintenance of pipelines [4]. Although these efforts improved the safety and management of pipelines, the number of incidents retained about 600-700 per year in 2003-2022 [2]. During 2011-2015, the National Transportation Safety Board (NTSB) investigated three major gas transmission pipeline incidents. Based on the investigation, NTSB reported “the inadequate evaluation of interactive threats is a frequently cited shortcoming of integrity management (IM) programs, which may lead to underestimating the true magnitude of risks to a pipeline” [8], and suggested “update guidance for gas transmission pipeline operators and inspectors on the evaluation of interactive threats” [8]. Currently, knowledge on interactive anomalies remains lacking, and the knowledge gap limits the capability of improving the safety and management of pipelines. There is an urgent need for effective detection and evaluation techniques for interactive anomalies.

1.2. Existing solutions and challenges

There are four primary types of pipeline integrity assessment methods allowed by the IM regulations [9]: (1) in-line inspection (ILI) using “smart pigs”, (2) pressure testing, (3) direct assessment, and (4) other technologies such as novel sensors. Typically, pressure testing is destructive; direct assessment involves multiple steps and only examines a small sub-segment of pipeline [8]. The ILI technologies and sensors installed on pipeline are two promising categories of nondestructive evaluation (NDE) methods for pipeline. As presented in Table 1.1.1, each method has its strengths and limitations in inspecting pipeline integrity. The limitations have potential to cause severe consequences in the presence of interactive anomalies.

Table 1.1.1. Two categories of NDE methods for pipeline integrity

Category	Advantage	Disadvantage
ILI	Spatially distributed information.	(1) Delayed information. (2) Insufficient reliability.
Sensors installed on pipelines	(1) Real-time condition assessment. (2) High reliability.	Spatially discrete information.

To date, ILI technologies have been widely applied for detecting and sizing pipeline anomalies, with the use of "smart pigs" that are instrumented with NDE tools and travel along the pipeline for inspection, as depicted in Figure 1.1.2 [10]. The NDE technologies that have been incorporated in smart pigs included but not limited to: (i) magnetic flux tools for metal loss [11], (ii) ultrasonic tools for cracks, wall thickness, and metal loss [12], and (iii) tools for deformation, such as dent and gouge [13]. Typically, a smart pig incorporates multiple sensors for transmitting, receiving, and recording NDE signals. Then, the data are processed and interpreted by trained professionals using sophisticated programs. In this way, anomalies are mapped over the entire pipeline, and delivered to decision makers for the management (e.g., maintenance, repair, or replacement) of the pipeline finally. Recently, multiple NDE tools have been employed in a single smart pig to assess multiple types of anomalies simultaneously. The incorporation of multiple NDE tools has the potential to improve the effectiveness in detecting and sizing anomalies, and has implications in promoting the detection, characterization, and understanding of interactive anomalies in pipelines.

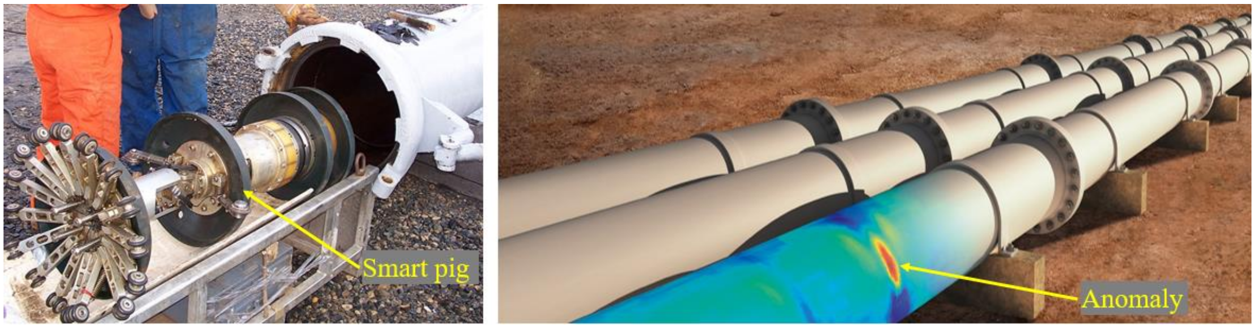

Figure 1.1.2. A smart pig travels along a pipeline and detects anomalies in the pipeline with use of the NDE tools incorporated in the smart pig.

The development and applications of the ILI technologies facilitate the pipeline inspection and management, and improved the safety and economic aspects. However, the ILI tools have their limitations. First, the inspection of anomalies using ILI is only performed as needed or scheduled maintenance, not in real time. The time delay between each inspection trail has potential to hinder timely actions to avoid accidents. Second, the reliability of smart pigs has been questioned [14]. In 2013, ExxonMobil's Mayflower oil spill caused serious damages due to pipeline rupture, which resulted from seam hook cracks that were not detected by smart pigs in advance. The failure to detect the anomaly was likely due to the technical limitations of the NDE tools, which have a dilemma of the detection efficiency and accuracy. Since the smart pigs move along the pipeline for inspection, the measurement rate (efficiency) needs to be high, potentially compromising the accuracy. Considering environmental effects, such as noises or electromagnetic interference (EMI), the measurement accuracy is further compromised. The presence of interactive anomalies likely further increases the challenge in detecting different types of anomalies, because one type of anomaly may affect the detection of other types of anomalies or even disable the smart pig. For instance, significant geometry change such as dent may stop the smart pig in a pipeline.

Meanwhile, various sensors have been developed and applied on pipelines for nondestructive inspection. For example, acoustic sensors have been installed on the exterior wall of pipelines to detect and size anomalies such as cracks [15]. The acoustic sensors continuously monitor cracking in the pipelines in real time. While the acoustic sensing techniques are effective in detecting cracks, removing the pipeline coating for installing the acoustic sensors potentially triggers additional corrosion. Besides, in order to inspect pipeline network in a large area or long distance, numerous sensors must be deployed at different locations along the pipeline. The large number of sensors increase the sensor cost and lead to challenges for data acquisition and processing.

Alternatively, fiber optic sensors were proposed for real-time condition monitoring. Fiber optic sensors are made using optical fibers measuring 125 μm in diameter. In general, fiber optic sensors are immune to EMI, lightweight, small in size, and have high chemical and thermal stability. The sensor installation is straightforward and does not require removing pipeline coating. Fiber optic sensors are gaining increasing interests in condition assessment of engineering structures [16-18]. Most fiber optic sensors used are point sensors, which measure temperature and strain at a local spot [19]. Fiber optic sensors have been developed to detect corrosion [20-22] by coating nano silver film and Fe-C layer on the fiber optic sensor surface as shown in Figure 1.1.3 for the design and fabrication process of the sensors [23].

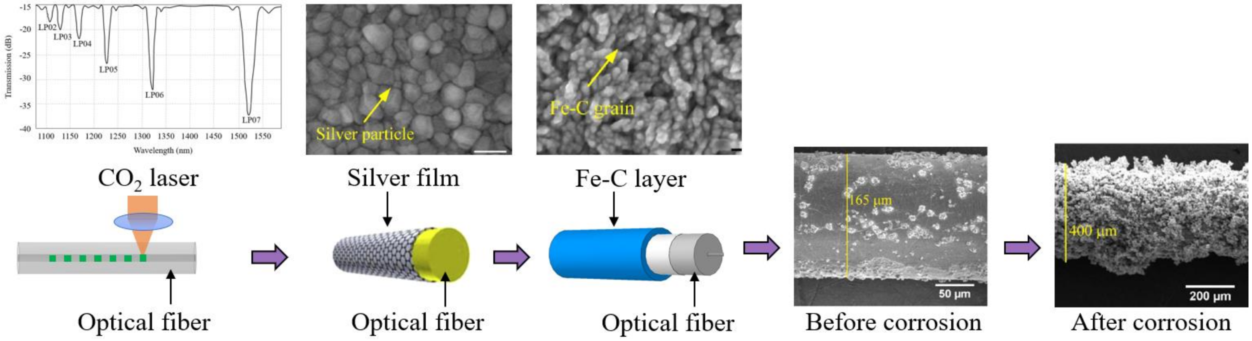

Figure 1.1.3. Optical fiber functionalized by depositing functional materials on the surface of the optical fiber for measuring steel corrosion.

The point fiber optic sensors are simultaneously sensitive to multiple variables such as strains, temperature, corrosion, cracks, etc. To distinguish the multiple variables, a typical solution is to deploy multiple co-located sensors at the monitored site, with one of the sensors only subjected to temperature change for temperature compensation, one subjected to temperature and strain changes, and one subjected to temperature change and corrosion. Thus, the point fiber optic sensors have potential to measure multiple parameters, although it may be costly to install enough sensors for a large monitoring area or long distance. Searching for monitoring technique in a large area, there is a need for a cost-effective real-time inspection solution that can efficiently monitor interactive anomalies along the entire length of the pipeline.

1.3. Objectives

This research aims to develop a **distributed fiber optic sensor (DFOS) network** for real-time monitoring of the initiation and development of anomalies and their interactions in pipelines. The development of the DFOS network is a part of the systematic research on **bio-inspired intelligent pipelines**, as shown in Figure 1.1.4. Inspired by the biological systems that have sensory nerves, we are developing smart pipelines with DFOS networks which provide detailed measurements of temperatures and strains along the length of the pipelines. The role of the DFOS network is like the role of sensory nerves of biological systems.

In addition to the DFOS network used for measurement and data collection, another essential component of the intelligent pipeline system is a **machine learning-based AI model** which is developed for analyzing and interpreting the DFOS sensor data automatically, without human intervention. The AI model is necessary because the DFOS network generates a large amount of sensor data. It is unrealistic to manually analyze and interpret the large amount of sensor data by humans. With the AI model, it is envisioned that the intelligent pipeline system will achieve the ability to monitor its condition **in real time** because the AI model has high time efficiency in data analysis and interpretation. Furthermore, the DFOS network and the AI model provide data for establishing **digital twins** for the physical pipelines, and the digital twins will be live digital twins or updatable digital twins because the digital twins will be updated according to the data provided by the DFOS network and the AI model.

This project primarily focuses on the development of the DFOS network based on laboratory experiments, aimed at testing the feasibility of using the DFOS network to achieve the envisioned capabilities of intelligent pipeline systems. This report also includes preliminary research on the development of the AI model to prove the feasibility of AI-powered sensor data interpretation.

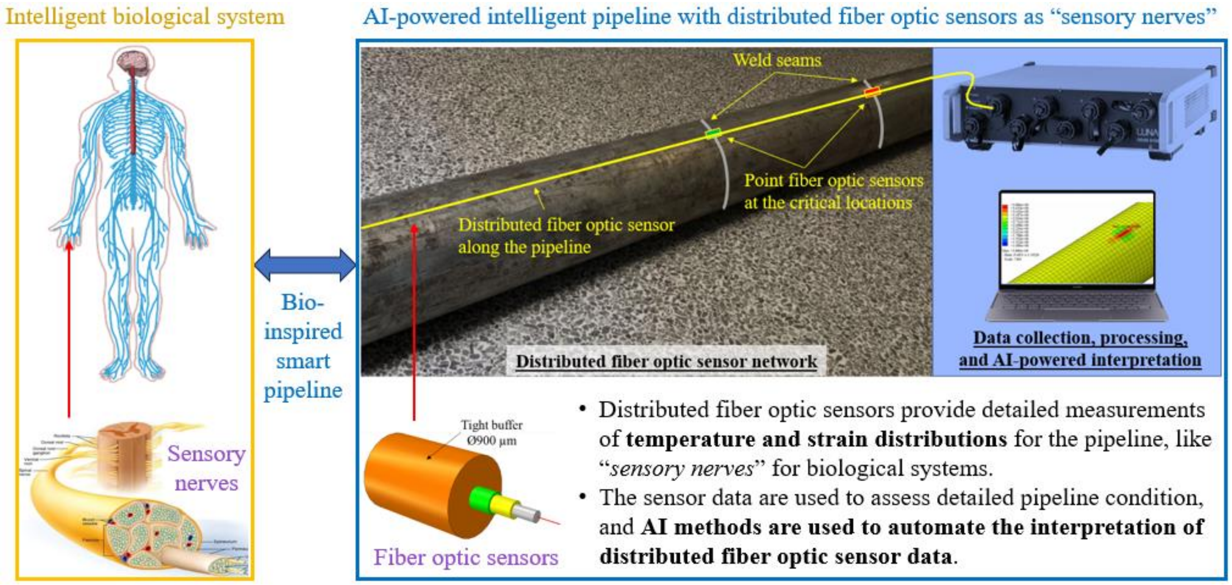

- Distributed fiber optic sensors provide detailed measurements of **temperature and strain distributions** for the pipeline, like "*sensory nerves*" for biological systems.
- The sensor data are used to assess detailed pipeline condition, and **AI methods are used to automate the interpretation of distributed fiber optic sensor data**.

Figure 1.1.4. Concept of the DFOS network for monitoring interactive anomalies in pipelines.

The concept of the DFOS network for real-time anomaly monitoring is shown in Figure 1.1.4. The proposed DFOS network will seamlessly integrate multifunctional distributed and point fiber optic sensors and provide fully distributed measurements of temperatures and strains along the fiber optic cable for the detection, localization, characterization, and quantification of interactive anomalies in pipelines. A telecommunication-grade single-mode fiber optic cable is utilized as a distributed sensor that provides spatially distributed measurement along the fiber, and point fiber optic sensors (i.e., FBG sensors) are integrated at critical locations for improving measurement accuracy and reliability. The fiber optic cable can be installed along the entire pipeline or at the selected pipeline segments as a continuous sensor. Both the distributed and point fiber optic sensors measure multiple pipeline anomalies and their interactions that are associated with the integrity of the pipeline.

The various anomalies inform the desired measurands of the proposed DFOS network, as shown in Figure 1.1.5. This project focused on four types of representative threats or anomalies, which are excavation, cracking, deformation, corrosion, and their interactions, to exemplify the functions of the sensor network. Excavation generates impacts or vibrations to the optical fiber. Cracking changes temperature and strain in the optical fiber. Dent was considered as an example type of deformation, which induces local deformations in the optical fiber. Corrosion was detected using fiber optic strain sensors or by measuring the strain change in the optical fiber.

The overarching **goal** of this research is to develop a multifunctional DFOS network for real-time detection and characterization of interactive anomalies in pipelines. To reach this goal, the following main objectives will be achieved:

(1) To develop and demonstrate an innovative multifunctional DFOS network for accurate detection, localization, characterization, and quantification of various anomalies along pipelines, and their interactions in between different anomalies.
(2) To develop data processing and analysis programs for sensor data analysis to identify interactions between different anomalies and improve decision making for effective and efficient management of pipelines.
(3) To train graduate and undergraduate students through conducting cutting-edge research on pipeline anomaly detection to prepare them for future careers in related industry.

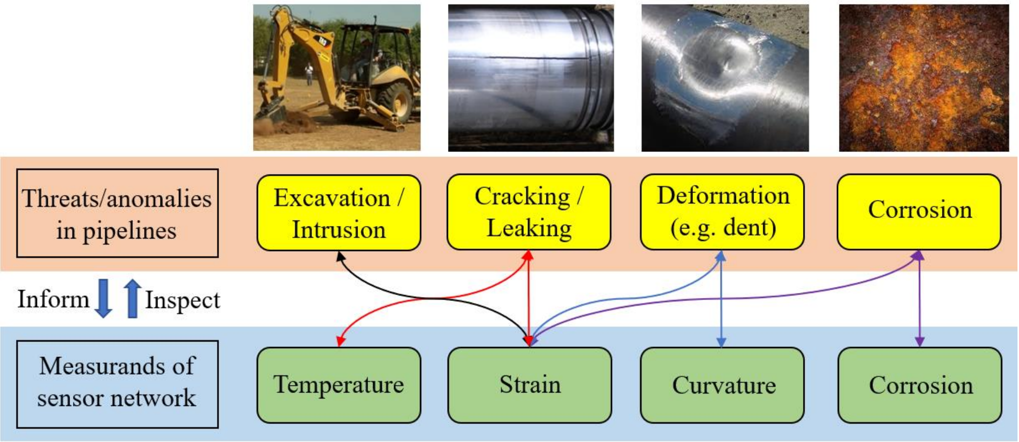

Figure 1.1.5. Pipelines with multiple threats/anomalies, revealing the desired functions of DFOS networks.

2. Theoretical and Experimental Research

In this research, laboratory experiments were designed to achieve the research objectives in two main phases:

- Phase I: Considering the complexity of interactive anomalies, individual anomalies were first investigated to establish basic understandings of the effects of individual anomalies on the measurements from DFOS networks and to develop the capabilities of monitoring individual anomalies. The anomalies investigated in this phase include the strain fields, cracks, dents, excavation induced impacts, and corrosion.
- Phase II: Based on the sensing capabilities gained through Phase I, Phase II focused on the interactive anomalies with different combinations of individual anomalies.

The following 12 experimental research has been designed and conducted in this project. The results from the first five experiments have generated peer-reviewed journal papers, and the results from the last five experiments have been utilized to generate journal papers that are either under review or in preparation for journal and conference papers.

- Experiment 1: Measurement of arbitrary strain fields [24-26]
- Experiment 2: Detection, localization, and quantification of cracks [27]
- Experiment 3: Interfacial mechanics of distributed sensors undergoing debonding [28]
- Experiment 4: Detection, localization, quantification, and visualization of buckling/dent [29]
- Experiment 5: Detection, localization, quantification, and visualization of corrosion [30]
- Experiment 6: Investigation of different types of fiber optic cables and installation methods
- Experiment 7: Detection of excavation induced impacts on pipelines
- Experiment 8: Measurement of interactive deformations and cracks
- Experiment 9: Measurement of interactive dent and corrosion
- Experiment 10: Measurement of interactive deformations and dent
- Experiment 11: Measurement of interactive impact loads and corrosion
- Experiment 12: Measurement of interactive deformations, dent, crack, and corrosion

In addition to the above experimental research, finite element analysis and theoretical studies have been conducted. In addition, machine learning-based AI models have been developed for automatic analysis and interpretation of DFOS data, thereby proving the concept and feasibility of the vision for intelligent pipeline system shown in Figure 1.1.4. The conducted research has been elaborated in the following sections.

2.1. Optical fibers and sensing principle

2.1.1. Optical fibers

This study investigates four types of telecommunication-grade single-mode fiber optic cables (Corning SMF 28e+®) as DFOS, including three types of fiber optic cables as distributed strain sensors and one type of fiber optic cable as distributed temperature sensors. The three types of fiber optic cables as distributed strain sensors include a bare fiber and two coated fibers, as shown in Figure 2.1.1.

The bare fiber had a fused silica core (diameter: 8.2 µm), a fused silica cladding (outer diameter: 125 µm), an inner coating (outer diameter: 190 µm), an outer coating (outer diameter: 242 µm), as shown in Figure 2.1.1(a). The inner coating is a soft acrylic layer which protects the glass fiber from mechanical impact. Another important function of the inner coating is to facilitate operations such as stripping off the coatings without damaging the fused silica fiber. The outer coating is a stiff acrylic layer which is utilized to protect the glass fiber from abrasion and environmental exposure. Both coatings are composed of complex mixtures of raw materials, such as monomers, oligomers, photoinitiators, and additives. To enhance the mechanical strength, two coated fibers are packaged with tight polyvinyl chloride buffers with diameters of 650 µm and 900 µm, respectively, as shown in Figure 2.1.1(b) and Figure 2.1.1(c).

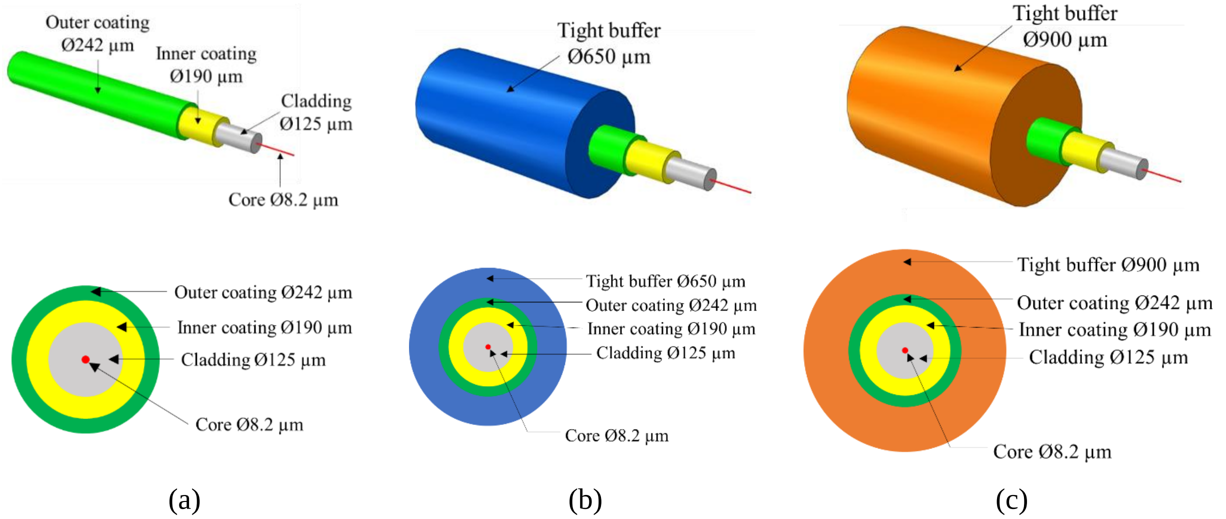

Figure 2.1.1. Cross section of the fiber coated with tight buffer: (a) 242-µm-diameter bare fiber; (b) 650-µm-diameter coated fiber; and (c) 900-µm-diameter coated fiber.

The sensing part is the fiber core. Light waves propagate along the fiber optic cable via total internal reflection at the core-cladding interface, as shown in Figure 2.1.2. In the manufacturing of optical fiber, the inner and outer coatings are applied sequentially in a liquid form as the glass fiber is drawn and are sequentially cured by exposure to ultraviolet light sources. Table 2.1.1 shows the dimensions and the elastic moduli of the different components of the fiber optic cables.

Table 2.1.1. Main properties of the fiber optic cables

Components		Material	Outer diameter	Elastic modulus	Poisson’s ratio
Fiber core	Core	Fused silica	8.2 μm	70.2 GPa	0.26
	Cladding	Fused silica	125 μm	70.2 GPa	0.26
Coating	Inner coating	Acrylate	190 μm	0.6 MPa	0.48
	Outer coating	Acrylate	242 μm	2550 MPa	0.42

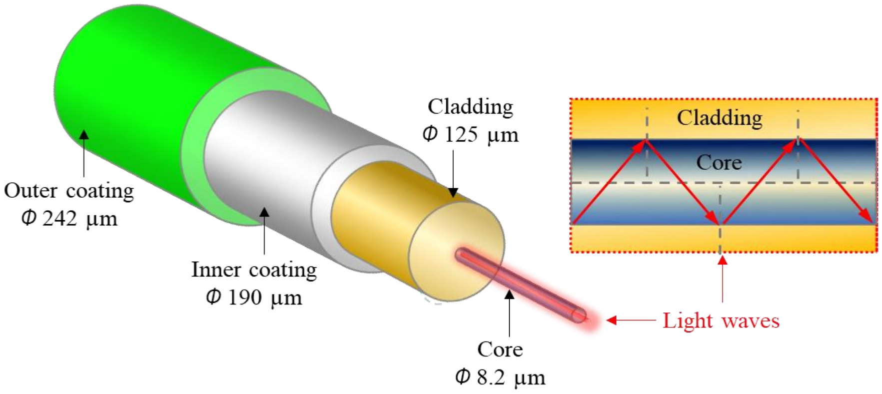

Figure 2.1.2. Structures of a single-mode optical fiber and propagation of light waves along the fiber.

The fiber optic cable used for temperature measurement is shown in Figure 2.1.3. A fiber optic cable for strain measurement is shown in Figure 2.1.3(a), and a fiber optic cable for temperature measurement is shown in Figure 2.1.3(b). The fiber optic cable for temperature measurement was composed of a fiber optic strain cable, a layer of aramid yarn, and a cable jacket. The aramid yarn is made from Kevlar®, which is crimped to the cable jacket after assembly. Therefore, the stresses applied to the fiber optic cable are mainly carried by the aramid yarn instead of the glass fiber. In this way, the fiber optic cable is not sensitive to mechanical strain but sensitive to the temperature effect. Finally, an outer jacket (typically a soft plastic material measuring in about 3 mm in diameter) is applied outside the yarn and the buffered fiber for mechanical protection. Previous research revealed that the fiber optic cables successfully survived fiber installation and concrete casting processes.

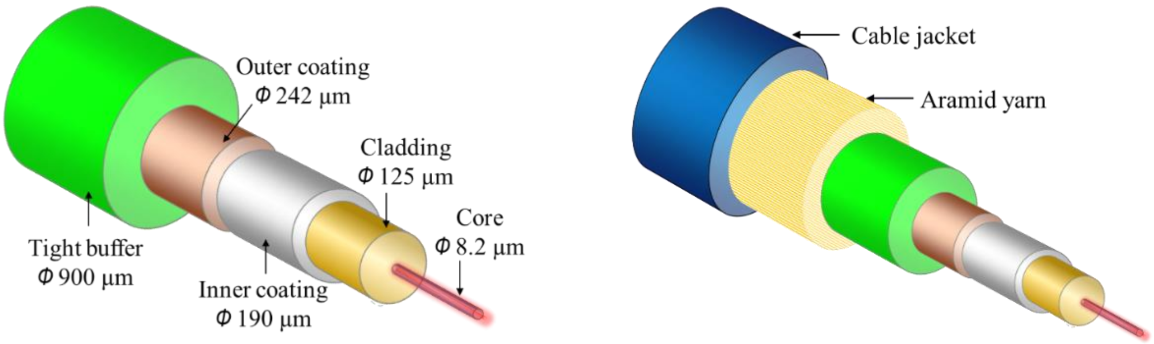

(a) (b)

Figure 2.1.3. Cross section of single mode optical fibers for: (a) distributed fiber optic strain sensors; and (b) distributed fiber optic temperature sensors.

2.1.2. *Sensing principle*

The sensing principle of DFOS for measuring strain and temperature changes is based on light scatterings. Rayleigh scattering in a fiber optic cable is an elastic scattering phenomenon that occurs when transmitted light interacts with the irregular microstructure of the fused silica. The occurrence of irregularities can be attributed to the fabrication process of fiber optic cables. The irregularities have sizes comparable with the wavelength of light waves, leading to changes in the refractive index and the density of fiber core. This project mainly utilized an Optical Frequency Domain Reflectometry (OFDR) technique [31], which measures temperature and strain changes based on Rayleigh scattering in two different states: the reference state and the perturbed state. In each state, a light wave is beamed into the optical fiber, generating Rayleigh scattering. The backscattered signal is measured from the optical fiber along the fiber length. At each point of the fiber, the amplitude of the backscattered signal is plotted against the wavelength of the light. The amplitude versus wavelength data are converted into intensity versus frequency via Fast Fourier Transform (FFT). Cross-correlation operation is performed for the reference and the perturbed states, and a frequency shift can be identified, as shown in Figure 2.1.4. The distance is determined by the travelling time of the backscattered signals.

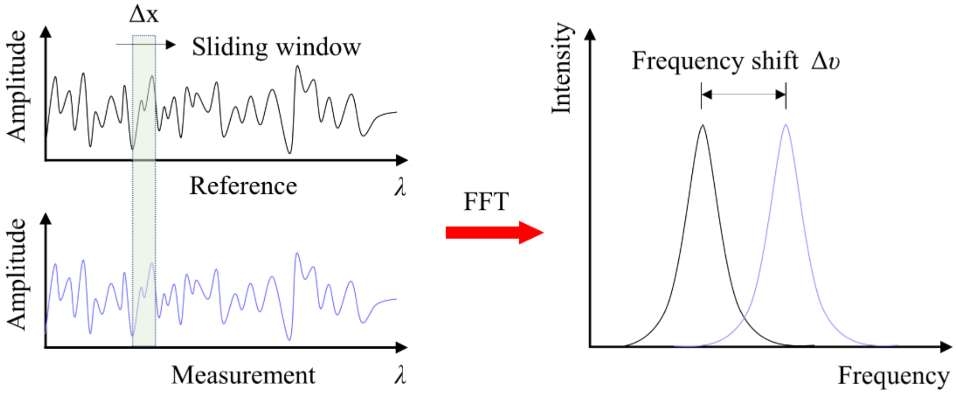

Figure 2.1.4. Sensing principle of optical frequency domain reflectometry for measuring strain change.

The frequency shift is associated with strain and temperature changes:

$$\frac{\Delta\lambda}{\lambda} = \frac{\Delta\upsilon}{\upsilon} = K_T T + K_\varepsilon \varepsilon \tag{2.1.1}$$

where λ and υ are the mean optical wavelength and frequency, respectively; and K_T and K_ε are the temperature and strain sensitivity coefficients.

At a constant temperature, the spectral shift can be converted into strain along the fiber optical cable with a calibrated strain sensitivity coefficient. When the temperature changes, a fiber optic cable free of strain change can be used for temperature compensation.

In this project, an OFDR data acquisition system (model: Luna ODiSi 6) was used to perform measurements. The measurement accuracy specified by the manufacturer was ±5 με for strain and ±2.2 ºC for temperature. The range of spatial resolution was 0.65 mm to 5.2 mm. The maximum length of fiber optic cable sensor supported by the OFDR system was longer than 200 m in length for each channel with extended range remote modules.

Although OFDR is adopted in this study, it is noted that there are other types of distributed fiber optic sensing technologies, such as Brillouin optical time domain analysis (BOTDA) and Brillouin optical time domain reflectometry (BOTDR). In general, there is a trade-off between the measurement distance and spatial resolution. With OFDR, the spatial resolution can be finer than 1 mm, but the measurement distance is typically shorter than 1 km. With BOTDA and BOTDR based on Brillouin scattering, the measurement distance can be longer than 100 km, but the spatial resolution is at the scale of meter or half-meter. Based on BOTDA, a PPP-BOTDA technology achieved a spatial resolution as fine as 2 cm [32]. In real practice, if the length of the pipeline segment that needs to be monitored is longer than the measurement distance of the DFOS, multiple segments of distributed sensors can be used. If the data acquisition system has multiple channels, one system can be placed in the middle of two adjacent pipeline segments to duplicate the distance.

2.1.3. Calibration of sensitivity coefficients

The strain sensitivity coefficient was calibrated in uniaxial tensile tests using a load frame at room temperature (25 °C). The tests were conducted under a displacement rate of 1 mm/min. The applied load and extension were measured by the transducer and the extensometer of the load frame, respectively. The frequency shift due to strain change was measured using the OFDR data acquisition system. The coefficient of determination for the linear regression is close to 1.0, indicating a good correlation. The slope represents the strain sensitivity coefficient (K_{ε}) of the optical fiber, which was determined to be -0.15 MHz/με. Similarly, the temperature sensitivity coefficient (K_T) was calibrated and determined to be -1.46 MHz/ºC.

2.2. Measurement of arbitrary strain fields

2.2.1. Strain transfer effect

Fiber optic sensors are usually packaged with protective coatings to enhance the mechanical strength and workability. The sensors are either embedded in or attached to host materials for measurement. The strain changes sensed by fiber optic sensors can be different from (and usually smaller than) the strain changes in the host matrix because of the coating. This is known as the strain transfer effect.

Strain transfer effect has been extensively studied for point fiber optic sensors in literature [33-44]. For example, a theoretical study was conducted on the strain transfer of a coated fiber optic sensor embedded in a composite matrix based on the mechanics of elasticity [35]. The study assumed the host matrix to be infinite and subjected to a far-field longitudinal shear load parallel to both the optical and the structural fibers, and derived closed-form solutions for the strain transfer ratio based on the assumptions. It was found that the strain transfer was related to the coating thickness and the elastic moduli of the coating and host material [34]. The shear-lag theory was used to develop a mechanical model to describe the strain transfer behavior of a coated optical fiber embedded in a host matrix [33], and the model was validated using a white light Michelson interferometric sensor [36]. Subsequently, an expression of the axial strain distribution was derived for an embedded fiber optic sensor packaged with elastic coating material under an arbitrary strain field [38], and a theoretical strain transfer model was proposed to consider an ideal elastoplastic coating [39]. The strain transfer ratio was studied when the coating material worked at different stages (elastic, elastoplastic, plastic, and post-plastic) [41]. Based on the above advances, strain transfer behaviors have been considered for fiber Bragg grating (FBG) sensors under axial stresses [43] and non-axial stresses [42]. Furthermore, research was extended to multi-layer composite materials under a non-uniform strain field, and the FBG's reflection spectrum was observed to be broadened or even split into multiple peaks, which was different from a single sharp peak found in a uniform strain field [40]. Overall, the strain transfer ratio was about 0.90 to 0.96 and associated with the sensor's orientation [44]. In addition, it was found that the presence of packaged point sensors could affect the strain distribution in the host material [37].

The above review indicates that the previous studies focused on the strain transfer effect in point sensors, such as FBG and interferometer sensors. Due to the limited sensing length, most often, a point sensor can be considered working in uniform strain fields. In addition, the previous formulae for point sensors were validated in an average sense. The average strain transfer over the whole sensor length was derived and correlated to the strain measurements [36, 42]. However, this is not satisfied in DFOS, which are often used to measure non-uniform strain distributions [45, 46]. To date, the understanding of strain transfer in DFOS is still lacking. There is no effective method to quantify the strain transfer effect in the case of DFOS. It is still a challenge to assess and improve the accuracy of strain measurement using DFOS.

2.2.2. Forward strain transfer analysis

The governing equation was derived to analyze the strain transfer effect of DFOS embedded in a host structure. The governing equation was solved under different strain field conditions. An arbitrary infinitesimal segment of a fiber optic cable with a dual-layer coating embedded in host matrix is shown in Figure 2.2.1.

Typical types of host matrix include cementitious matrix (e.g., mortar or paste) and polymetric matrix (e.g., epoxy). The following assumptions are employed for the sake of simplicity: (1) All materials work linearly elastically. (2) All interfaces are well bonded. (3) Only stresses that are parallel to the optical fiber are considered. (4) The impact of the optical fiber's presence on the host matrix's strain field is neglected. Due to symmetry, only half the structure is shown.

The shear stresses in the inner and outer coatings are represented by $\tau_i(x, r)$ and $\tau_o(x, r)$, respectively. The shear stress between the host matrix and the outer coating is represented by $\tau_o(x, r_o)$. The shear stress between the outer and inner coatings is represented by $\tau_i(x, r_i)$. The shear stress at the interface between the inner coating and the fiber core is represented by $\tau_f(x)$. The normal stresses in the fiber core, the outer coating, the inner coating, and the vicinity of host matrix are represented by $\sigma_f(x)$, $\sigma_o(x)$, $\sigma_i(x)$, and $\sigma_h(x)$, respectively. The deformations of the optical fiber, inner coating, outer coating, and the host matrix are represented by δ_f, δ_o, δ_i, and δ_h, respectively, at x with a segment of dx length. The shear strains in inner and outer coatings are represented by

γ_i and γ_o, respectively. For each segment, no deformation is shown on the left side. The deformations represent the total deformation of both sides.

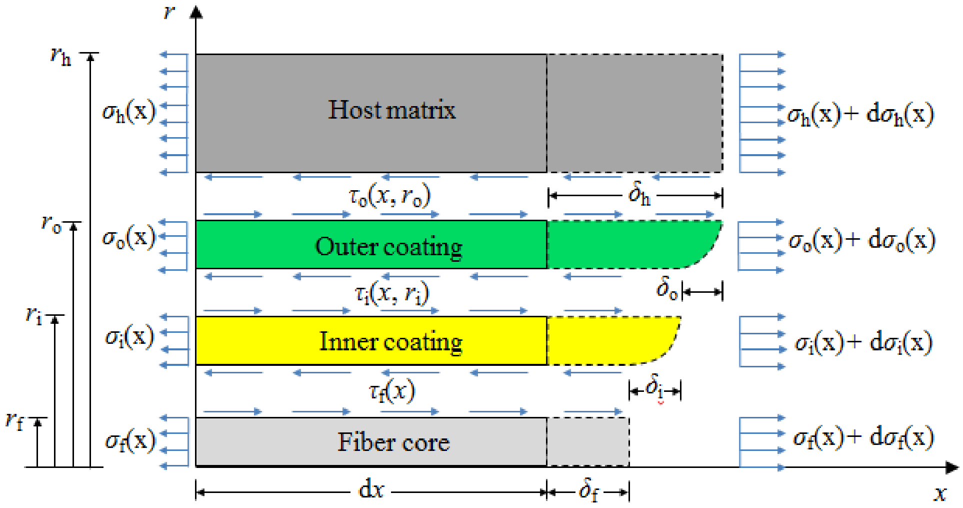

Figure 2.2.1. Stress analysis of an optical fiber packaged with multi-layer coatings embedded in concrete.

Equations of equilibrium in the *x*-direction are:

$$(\pi r_f^2)\,d\,\sigma_f(x) + (2\pi r_f)\tau_f(x)\,d\,x = 0 \tag{2.2.1}$$

$$(\pi r^2 - \pi r_f^2)\,d\,\sigma_i\,(x) + (2\pi r_f)\tau_i(x,r)\,d\,x = (2\pi r_f)\tau_f(x)\,d\,x,\ r_f \le r \le r_i \tag{2.2.2}$$

$$(\pi r^2 - \pi r_i^2)\,d\,\sigma_o\,(x) + (2\pi r)\tau_o(x,r)\,d\,x = (2\pi r_i)\tau_i(x,r_i)\,d\,x,\ r_i \le r \le r_o \tag{2.2.3}$$

Considering that no force is directly applied on the coatings at *x* = 0, integrating from 0 to *x*, Eqs. (2.2.2) and (2.2.3) can be rewritten as:

$$(\frac{r^2-r_f^2}{2x})\sigma_i(x) + r\tau_i(x,r) = r_f\tau_f(x),\ r_f \le r \le r_i \tag{2.2.4}$$

$$(\frac{r^2-r_f^2}{2x})\sigma_o(x) + r\tau_o(x,r) = r_i\tau_i(x,r_i),\ r_i \le r \le r_o \tag{2.2.5}$$

Since the diameter of the optical fiber is small compared with its length, the first terms in Eqs. (2.2.4) and (2.2.5) vanish, except for the vicinity at the two ends of the optical fiber [46]. Then, Eqs. (2.2.4) and (2.2.5) can be rewritten as:

$$r\tau_i(x,r) = r_f\tau_f(x),\ r_f \le r \le r_i \tag{2.2.6}$$

$$r\tau_o(x,r) = r_i\tau_i(x,r_i) = r_f\tau_f(x),\ r_i \le r \le r_o \tag{2.2.7}$$

According to the assumption (1), the optical fiber's longitudinal strain can be expressed as:

$$\sigma_f(x) = E_f\varepsilon_f(x) \tag{2.2.8}$$

Thus, Eq. (2.2.1) can be rewritten as:

$$\tau_f(x) = -\frac{E_f\,r_f}{2}\frac{d\,\varepsilon_f(x)}{d\,x} \tag{2.2.9}$$

Plug Eq. (2.2.9) into Eq. (2.2.6) and Eq. (2.2.7), respectively:

$$\tau_{\mathrm{i}}(x,r) = -\frac{E_{\mathrm{f}}\, r_{\mathrm{f}}^2}{2r}\frac{d\,\varepsilon_{\mathrm{f}}(x)}{d\,x},\ r_{\mathrm{f}} \le r \le r_{\mathrm{i}} \tag{2.2.10}$$

$$\tau_o(x,r) = -\frac{E_{\mathrm{f}}\, r_{\mathrm{f}}^2}{2r}\frac{d\,\varepsilon_{\mathrm{f}}(x)}{d\,x},\ r_{\mathrm{i}} \le r \le r_{\mathrm{o}} \tag{2.2.11}$$

According to the assumption (2), the deformations in Figure 2.2.1 satisfy:

$$\delta_{\mathrm{h}} = \delta_{\mathrm{f}} + \delta_{\mathrm{i}} + \delta_{\mathrm{o}} \tag{2.2.12}$$

The longitudinal deformations of the host matrix and the glass fiber can be expressed as:

$$\delta_{\mathrm{h}} = \varepsilon_{\mathrm{h}}(x)\,\mathrm{d}\,x,\ \delta_{\mathrm{f}} = \varepsilon_{\mathrm{f}}(x)\,\mathrm{d}\,x \tag{2.2.13}$$

The strain transfer from the host matrix to the optical fiber core depends on the shear strain in the interlayer which is due to the relative deformation between the host matrix and fiber core. Therefore, for the inner and outer coatings:

$$\delta_{\mathrm{i}} = \int_{r_{\mathrm{f}}}^{r_{\mathrm{i}}} \mathrm{d}\,\gamma_{\mathrm{i}}\,(x,r)\,\mathrm{d}\,r = \frac{1}{G_{\mathrm{i}}}\int_{r_{\mathrm{f}}}^{r_{\mathrm{i}}} \mathrm{d}\,\tau_{\mathrm{i}}\,(x,r)\,\mathrm{d}\,r \tag{2.2.14}$$

$$\delta_{\mathrm{o}} = \int_{r_{\mathrm{i}}}^{r_{\mathrm{o}}} \mathrm{d}\,\gamma_{\mathrm{o}}\,(x,r)\,\mathrm{d}\,r = \frac{1}{G_{\mathrm{o}}}\int_{r_{\mathrm{i}}}^{r_{\mathrm{o}}} \mathrm{d}\,\tau_{\mathrm{o}}\,(x,r)\,\mathrm{d}\,r \tag{2.2.15}$$

where, $\gamma_{\mathrm{i}} = \tau_{\mathrm{i}} / G_{\mathrm{i}}$, and $\gamma_{\mathrm{o}} = \tau_{\mathrm{o}} / G_{\mathrm{o}}$.

Plugging Eq. (2.2.13), Eq. (2.2.14) and Eq. (2.2.15) into Eq. (2.2.12):

$$\varepsilon_{\mathrm{h}}(x)\mathrm{d}x = \varepsilon_{\mathrm{f}}(x)\,\mathrm{d}\,x + \frac{1}{G_{\mathrm{i}}}\int_{r_{\mathrm{f}}}^{r_{\mathrm{i}}} \mathrm{d}\,\tau_{\mathrm{i}}\,(x,r)\,\mathrm{d}\,r + \frac{1}{G_{\mathrm{o}}}\int_{r_{\mathrm{i}}}^{r_{\mathrm{o}}} \mathrm{d}\,\tau_{\mathrm{o}}\,(x,r)\,\mathrm{d}\,r \tag{2.2.16}$$

Plugging Eq. (2.2.10) and Eq. (2.2.11) into Eq. (2.2.16), and rearranging the nonzero term d*x*, Eq. (2.2.16) can be rewritten as:

$$\varepsilon_{\mathrm{h}}(x) = \varepsilon_{\mathrm{f}}(x) - \frac{E_{\mathrm{f}}\, r_{\mathrm{f}}^2}{2}\left[\frac{\mathrm{In}(r_{\mathrm{i}}/r_f)}{G_{\mathrm{i}}} + \frac{\mathrm{In}(r_{\mathrm{o}}/r_{\mathrm{i}})}{G_{\mathrm{o}}}\right]\frac{d^2\varepsilon_{\mathrm{f}}(x)}{\mathrm{d}x^2} \tag{2.2.17}$$

By introducing a positive coefficient *k*, Eq. (2.2.17) can be rewritten as [47]:

$$\varepsilon_{\mathrm{f}}''(x) - k^2\varepsilon_{\mathrm{f}}(x) + k^2\varepsilon_{\mathrm{h}}(x) = 0 \tag{2.2.18a}$$

$$k^2 = \frac{2}{E_{\mathrm{f}}\, r_{\mathrm{f}}^2\left[\frac{\mathrm{In}(r_{\mathrm{i}}/r_f)}{G_{\mathrm{i}}} + \frac{\mathrm{In}(r_{\mathrm{o}}/r_{\mathrm{i}})}{G_{\mathrm{o}}}\right]} \tag{2.2.18b}$$

For the optical fiber packaged with a dual-layer coating (Figure 2.1.1), *k* can be determined 55 m^{-1}, according to the optical fiber's dimensions and material properties.

The strain transfer in optical fibers with multi-layer coatings can be analyzed following the same process. As a matter of fact, Eq. (2.2.18b) can be extended to a generalized form for optical fibers with multi-layer coatings, as long as k^2 is modified as:

$$k^2 = \frac{2}{E_{\mathrm{f}}\, r_{\mathrm{f}}^2[\frac{\mathrm{In}(r_1/r_f)}{G_1} + \frac{\mathrm{In}(r_2/r_1)}{G_2} + \cdots + \frac{\mathrm{In}(r_{\mathrm{n}}/r_{\mathrm{n-1}})}{G_{\mathrm{n}}}]} \tag{2.2.18c}$$

where n represents the number of coating layers.

The solution of Eq. (2.2.18) can be expressed as [48]:

$$\varepsilon_\mathrm{f}(x) = C_1 \cosh(kx) + C_2 \sinh(kx) + \varepsilon^\mathrm{p}(x) \tag{2.2.19}$$

where the first two terms represent the general solution; the third term $\varepsilon^\mathrm{p}(x)$ is the particular solution associated with $\varepsilon_\mathrm{h}(x)$, which denotes the strain distribution in the host matrix along the optical fiber. The integration constants, C_1 and C_2, are determined by the boundary conditions.

In general, the form of $\varepsilon_\mathrm{h}(x)$ can be different in various problems. Thus, the particular solution $\varepsilon^\mathrm{p}(x)$ can be different, correspondingly. For an arbitrary condition, $\varepsilon_\mathrm{h}(x)$ can be expressed using a Fourier series. However, for a large amount of engineering problems, $\varepsilon_\mathrm{h}(x)$ can be segmentally expressed as or approximated by a series of polynomials, as shown in Eq. (2.2.20).

$$\varepsilon_\mathrm{h}(x) = \sum_{i=0}^{m} a_i x^i \tag{2.2.20}$$

where m represents the order, and a_i (i=0, 1, 2, … , m) represent the coefficients.

$\varepsilon^\mathrm{p}(x)$ can be determined as a polynomial of the same order in each segment where $\varepsilon_\mathrm{h}(x)$ is continuous and differentiable regarding to x [48]. Therefore, $\varepsilon^\mathrm{p}(x)$ and $\varepsilon_\mathrm{f}(x)$ can be written as:

$$\varepsilon^\mathrm{p}(x) = \sum_{i=0}^{m} b_i x^i \tag{2.2.21a}$$

$$\varepsilon_\mathrm{f}(x) = C_1 \cosh(kx) + C_2 \sinh(kx) + \sum_{i=0}^{m} b_i x^i \tag{2.2.21b}$$

where b_i (i = 0, 1, 2, … , m) are the coefficients. The relationship between a_i and b_i are as follows.

When $m < 2$,

$$a_i = b_i \tag{2.2.22}$$

When $m \geq 2$,

$$a_i = \begin{cases} b_i & , \quad i = m-1, m \\ b_i - (i+2)(i+1) b_{i+2}/k^2 & , \quad i \leq m-2 \end{cases} \tag{2.2.23}$$

The strain transfer ratio is defined:

$$\alpha(x) = \varepsilon_\mathrm{f}(x)/\varepsilon_\mathrm{h}(x) \tag{2.2.24}$$

2.2.2.1. Uniform strain fields

An optical fiber is attached along a pipe subjected to a uniform cross section, as shown in Figure 2.2.2. The normal strain in the pipe is expressed as: $\varepsilon_\mathrm{h}(x) = \varepsilon_0$.

The normal strain in the optical fiber can be determined from Eq. (2.2.21b) as:

$$\varepsilon_\mathrm{f}(x) = C_1 \cosh(kx) + C_2 \sinh(kx) + \varepsilon_0 \tag{2.2.25}$$

Then, the shear stress in the optical fiber is determined from Eq. (2.2.10), as shown in:

$$\tau_\mathrm{f}(x) = -0.5\, E_\mathrm{f} r_\mathrm{f} [kC_1 \sinh(kx) + kC_2 \cosh(kx)] \tag{2.2.26}$$

The boundary conditions are:

$$\varepsilon_{\mathrm{f}}(x=0)=0 \tag{2.2.27a}$$

$$\varepsilon_{\mathrm{f}}(x=L)=0 \tag{2.2.27b}$$

Plugging Eq. (2.2.27) into Eq. (2.2.25) and Eq. (2.2.26), coefficients C_1 and C_2 are determined:

$$C_1=-\varepsilon_0,\, C_2=\varepsilon_0 \tanh(kL/2)$$

In this case, another boundary can be used to replace Eq. (2.2.27a) or Eq. (2.2.27b):

$$\tau_{\mathrm{f}}(x=L/2)=0 \tag{2.2.27c}$$

With Eq. (2.2.27c), the same results of the coefficients C_1 and C_2 can be obtained.

Therefore, the normal strain and shear stress are:

$$\varepsilon_{\mathrm{f}}(x)=\varepsilon_0[1-\cosh(kx)+\tanh(kL/2)\sinh(kx)] \tag{2.2.28}$$

$$\tau_{\mathrm{f}}(x)=-0.5E_{\mathrm{f}}r_{\mathrm{f}}k\varepsilon_0[\tanh(\mathrm{kL}/2)\cosh(kx)-\sinh(kx)] \tag{2.2.29}$$

The strain transfer ratio is:

$$\alpha(x)=1-\cosh(kx)+\tanh(kL/2)\sinh(kx) \tag{2.2.30}$$

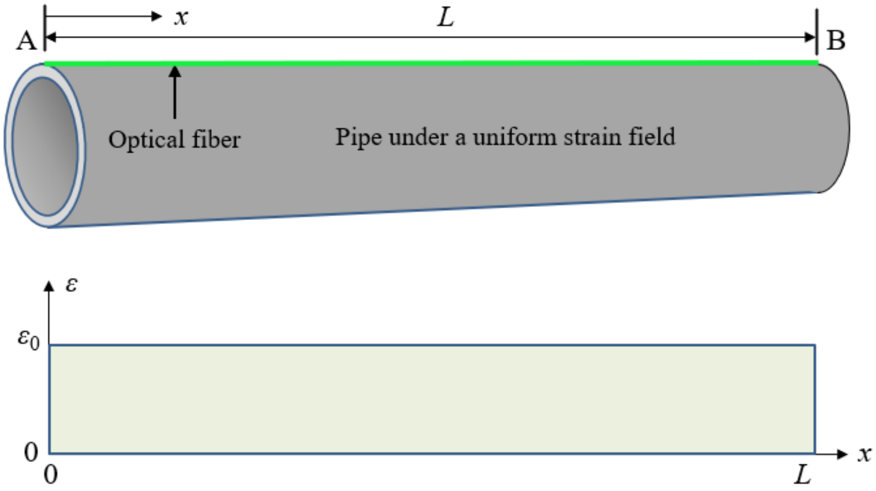

Figure 2.2.2. Optical fiber attached to the exterior surface of a pipe subjected to a uniform strain field.

The strain transfer ratio can be plotted against x ($0 \leq x \leq L/2$ for the left half), as shown in Figure 2.2.3(a). The right half ($L/2 < x \leq L$) is symmetrical to the left half. At each end of the optical fiber, there is a development length where the measured strain is smaller than the real strain due to the strain transfer effect.

The strain is gradually developed within that length, and the strain transfer ratio will be approximately 1.0 beyond that length. The development length is dependent on k that is related to the material and geometry of the optical fiber and independent of the applied strain ε_0. For the optical fiber with a dual-layer coating in this study, 95% of the strain could be developed in 55 mm, and 99% of strain could be developed in 84 mm. Eq. (2.2.30) can be used to correct the measured strains within the development length. As indicated in Eq. (2.2.30), the strain transfer ratio is dependent on L. With $k = 55\ \mathrm{m}^{-1}$, $\tanh(kL/2)$ increases to 0.95 at $L = 66$ mm, as shown in Figure 2.2.3(b). When the specimen length is longer than 100 mm, the influence of specimen length will be negligible. Therefore, no significant difference can be observed between the three curves in Figure 2.2.3(a).

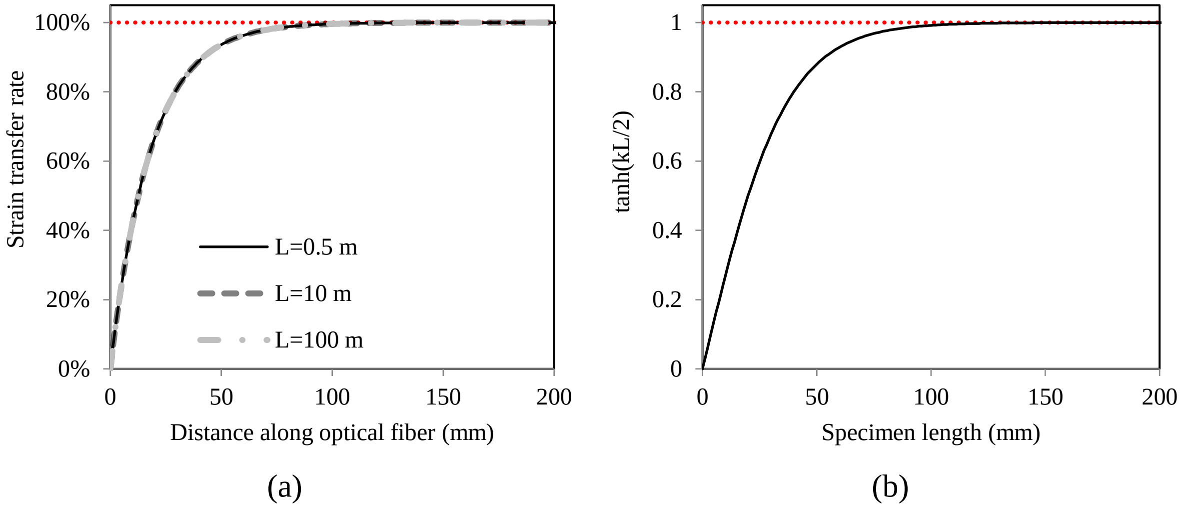

(a) (b)

Figure 2.2.3. Strain transfer ratio in uniform strain field: (a) strain transfer ratio versus distance; and (b) tanh(kL/2) versus specimen length.

2.2.2.2. Non-uniform strain fields

A DFOS can be subjected to a complex strain field, because of the long sensor length. In general, it might be difficult to use a single polynomial to describe the strain field, as illustrated in Figure 2.2.4. Regarding an arbitrary strain field, the field can be divided into multiple segments along the length of the DFOS. Within each segment, the strain field can be described using a single or combination of polynomials.

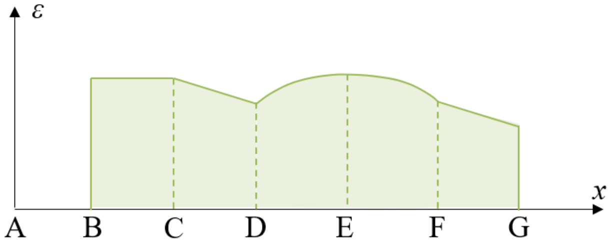

Figure 2.2.4. Arbitrary strain field of the host matrix. The strain field is divided into multiple segments along the length of the DFOS.

Therefore, a general procedure for solving a non-uniform strain field is proposed: (1) Step 1: Judge whether the strain field needs to be divided into multiple segments, and determine the polynomial expression of the strain field. (2) Step 2: Determine the boundary conditions. If there are multiple segments, the boundary conditions of each segment should be determined. (3) Solve the strain distribution in the DFOS. After the strain transfer within each segment is solved, the strain distribution along the entire fiber length can be obtained by combining all the segments.

A representative non-uniform strain field is investigated, as shown in Figure 2.2.5. In the length (L) of the pipe between points A and B, the normal strain linearly increases from ε_1 to ε_2. Regarding pipes subjected to more complicated non-uniform strain fields, the pipe can be divided into multiple segments. When the length of the segments is small, each segment can be considered subjected to the representative strain field.

To describe the relationship between ε_1 and ε_2, a factor λ is introduced:

$$\varepsilon_2 = \gamma\varepsilon_1 \tag{2.2.31}$$

The normal strain in the pipe can be expressed as:

$$\varepsilon_\mathrm{h}(x) = \varepsilon_1 + \frac{(\varepsilon_2-\varepsilon_1)x}{L} = \varepsilon_1[1 + \frac{(\gamma-1)x}{L}] \tag{2.2.32}$$

Therefore, the normal strain and shear stress of the optical fiber are:

$$\varepsilon_\mathrm{f}(x) = C_1\cosh(kx) + C_2\sinh(kx) + \varepsilon_1[1 + \frac{(\gamma-1)x}{L}] \tag{2.2.33}$$

where C_1 and C_2 are the integration constants, which are determined by the boundary conditions.

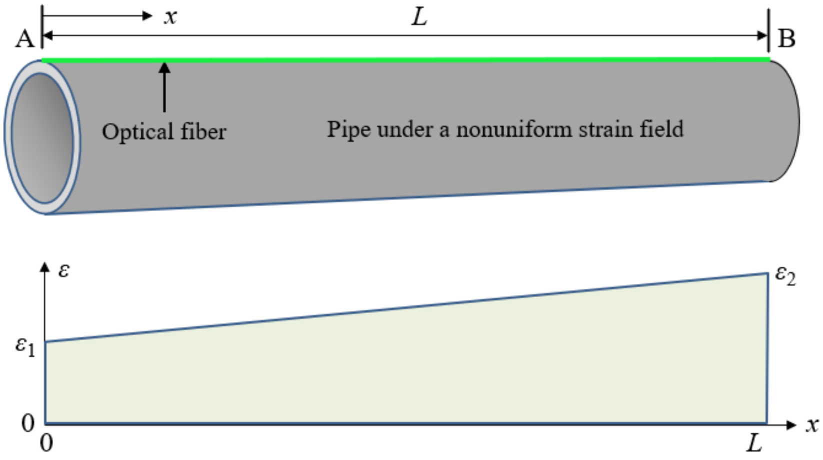

Figure 2.2.5. Optical fiber attached to the exterior surface of a pipe subjected to a linear strain field.

The boundary conditions are:

$$\varepsilon_\mathrm{f}(x=0) = 0 \tag{2.2.34a}$$

$$\varepsilon_\mathrm{f}(x=L) = 0 \tag{2.2.34b}$$

The integration constants can be determined:

$$C_1 = -\varepsilon_1 \tag{2.2.35a}$$

$$C_2 = \gamma\varepsilon_1\tanh(kL/2) \tag{2.2.35a}$$

The strain transfer ratio can be determined:

$$\alpha(x) = 1 - \frac{\gamma\tanh\left(\frac{kL}{2}\right)\sinh(kx) - \cosh(kx)}{1+\frac{(\gamma-1)x}{L}} \tag{2.2.36}$$

The strain in the DFOS can be plotted against x/L, as shown in Figure 2.2.6(a). The strain in the DFOS is lower than the strain in the host matrix within the development lengths at the two ends of the DFOS. Beyond the development length, the strain in the middle length of the DFOS is the same as the strain in the host matrix. The strain transfer ratio along the DFOS is plotted in Figure 2.2.6(b).

Based on the above analysis on a single segment with non-uniform strain distribution, further analysis is performed for multiple segments with different non-uniform strain distributions, as depicted in Figure 2.2.7. The entire length of the pipe is divided into two segments, and the strain distribution is linear along the length of each segment.

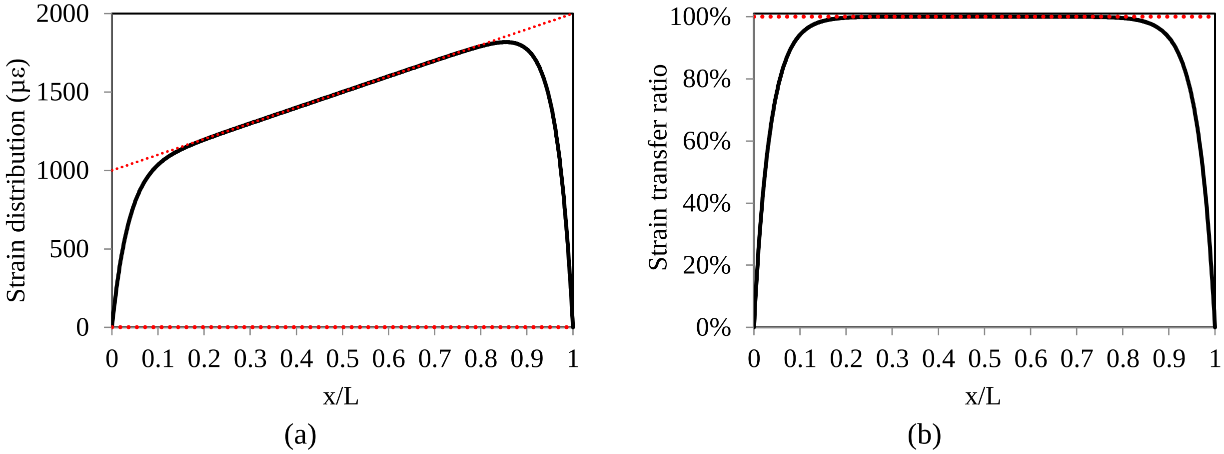

(a) (b)

Figure 2.2.6. Strain transfer analysis results: (a) strain distribution in the DFOS; and (b) strain transfer ratio along the DFOS.

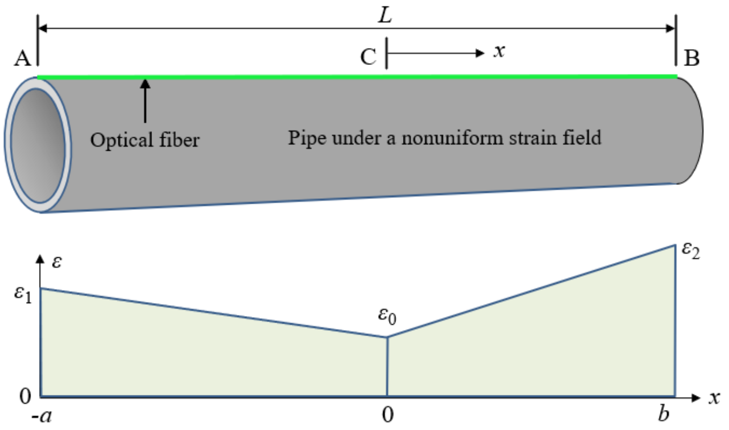

Figure 2.2.7. Depiction of a pipe subjected to a non-uniform strain field.

According to the strain distribution, the pipe is divided into two segments, designated as A-C and C-B, respectively. Within each segment, the strain linearly changes from one end to the other end of the segment. The lengths of the two segments are a and b, respectively, and the total length is denoted as L ($L = a + b$). Within segment A-C, the strain changes from ε_1 to ε_0. Within segment C-B, the strain changes from ε_0 to ε_2. To describe the relationship between ε_0, ε_1 and ε_2, two factors (λ_1 and λ_2) are introduced:

$$\varepsilon_1 = \gamma_1 \varepsilon_0 \tag{2.2.37a}$$

$$\varepsilon_2 = \gamma_2 \varepsilon_0 \tag{2.2.37b}$$

The normal strain in the pipe can be expressed as:

$$\varepsilon_{\mathrm{h}}(x) = \begin{cases} \varepsilon_0[1 - \frac{(\gamma_1 - 1)x}{a}] & x < 0 \\ \varepsilon_0[1 + \frac{(\gamma_2 - 1)x}{b}] & , x \geq 0 \end{cases} \tag{2.2.38}$$

Therefore, the normal strain of the optical fiber is expressed as:

$$\varepsilon_{\mathrm{f}}(x) = \begin{cases} C_1 \cosh(kx) + C_2 \sinh(kx) + \varepsilon_0[1 - \frac{(\gamma_1 - 1)x}{a}] & x < 0 \\ C_3 \cosh(kx) + C_4 \sinh(kx) + \varepsilon_0[1 + \frac{(\gamma_2 - 1)x}{b}] & , x \geq 0 \end{cases} \tag{2.2.39}$$

where C_1 and C_2 are the integration constants, which are determined by the boundary conditions.

The boundary conditions are:

$$\varepsilon_{\mathrm{f}}(x = -a) = 0 \tag{2.2.40a}$$

$$\varepsilon_{\mathrm{f}}(x = 0^-) = \varepsilon_{\mathrm{f}}(x = 0^+) \tag{2.2.40b}$$

$$\tau_{\mathrm{f}}(x = 0^-) = \tau_{\mathrm{f}}(x = 0^+) \tag{2.2.40c}$$

$$\varepsilon_{\mathrm{f}}(x = b) = 0 \tag{2.2.40d}$$

The integration constants can be determined:

$$C_1 = C_3 \tag{2.2.41a}$$

$$C_2 = C_4 + \varepsilon_0\left(\frac{\gamma_1 - 1}{ka} + \frac{\gamma_2 - 1}{kb}\right) \tag{2.2.41b}$$

$$C_3 = -\frac{C_4 \sinh(kb) + \gamma_2 \varepsilon_0}{\cosh(kb)} \tag{2.2.41c}$$

$$C_4 = \varepsilon_0 \frac{\gamma_1 \cosh(kb) - \gamma_2 \cosh(ka) - \left(\frac{\gamma_1 - 1}{ka} + \frac{\gamma_2 - 1}{kb}\right) \sinh(ka) \cosh(kb)}{\sinh(ka + kb)} \tag{2.2.41d}$$

The strain distribution in the DFOS can be obtained by plugging Eq. (2.2.41) into Eq. (2.2.39). The strain in the DFOS can be plotted against *x*/*L*, as shown in Figure 2.2.8(a). The strain in the DFOS is lower than the strain in the host matrix within the development lengths at the two ends of segment. Beyond the development length, the strain in the middle length of segment is the same as the strain in the host matrix. The strain transfer ratio along the length of the DFOS is plotted in Figure 2.2.8(b). Here, a = b = 0.5 m; $\gamma_1 = 1.5$, and $\gamma_2 = 2$.

The strain transfer ratio at *x* = 0 can be determined:

$$\alpha(x = 0) = \frac{\varepsilon_{\mathrm{f}}(x=0)}{\varepsilon_{\mathrm{h}}(x=0)} = 1 - \frac{\gamma_1/\cosh(ka) - \gamma_2/\cosh(kb) - \left(\frac{\gamma_1 - 1}{ka} + \frac{\gamma_2 - 1}{kb}\right)\tanh(ka)}{\tanh(ka)/\tanh(kb) + 1} - \frac{\gamma_2}{\cosh(kb)} \tag{2.2.42}$$

When *a* and *b* reach 0.096 m, the values of cosh(*ka*) and cosh(*kb*) reach 100; and the values of tanh(*ka*) and tanh(*kb*) are more than 0.9999. Thus, the strain transfer ratio at *x* = 0 is rewritten as:

$$\alpha(x=0) \approx 1 - \frac{0-0-\left(\frac{\gamma_1-1}{ka}+\frac{\gamma_2-1}{kb}\right)}{1+1} - 0 = 1 + \frac{\gamma_1-1}{2ka} + \frac{\gamma_2-1}{2kb} \tag{2.2.43}$$

When $a = b = L/2$, the strain transfer ratio at $x = 0$ can be rewritten as:

$$\alpha(x=0) \approx 1 + \frac{\gamma_1+\gamma_2-2}{kL} \tag{2.2.44}$$

The strain transfer ratio at $x = 0$ (Figure 2.2.8) is plotted in Figure 2.2.9. Given $k = 55\ m^{-1}$ and $L = 1.0$ m, the strain transfer ratio at the interface between the two segments (A-C and C-B) follow a linear relationship with ($\gamma_1 + \gamma_2$). “Accurate” and “Approximate” are obtained using Eq. (2.2.42) and Eq. (2.2.44), respectively.

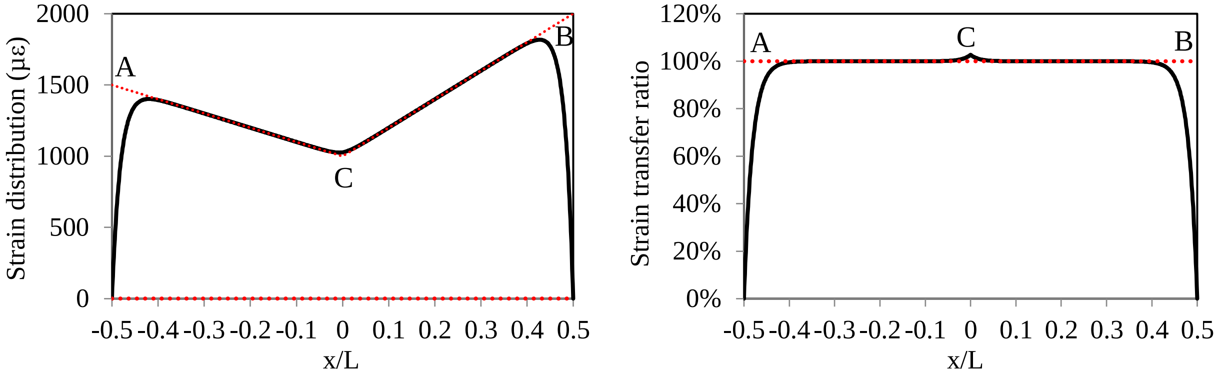

(a) (b)

Figure 2.2.8. Strain transfer analysis results: (a) strain distribution in the DFOS; and (b) strain transfer ratio along the sensor length.

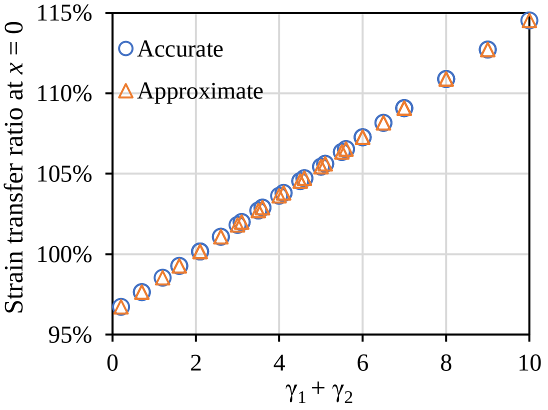

Figure 2.2.9. Results of the strain transfer ratio at x = 0.

A brief summary of the above analysis can be made: For a non-uniform strain field, in addition to the development length at the two ends of the DFOS, the strain transfer at the interface between two adjacent segments should be considered. When the segment length is no less than 0.1 m, if ($\gamma_1 + \gamma_2$) < 5, then, the effect of the strain transfer effect is less than 5%.

2.2.2.3. Validation

The analytical formulae of strain transfer ratio are derived for uniform and representative non-uniform strain fields, and investigated through experimentation using strain distributions measured from DFOS based on OFDR. To validate the derived formulae and analysis in the above analytical study, experiments have been performed in two loading scenarios: (1) uniaxial tensile test, and (2) three-point bending test. The two tests respectively correspond to uniform strain field and non-uniform strain field with a non-differentiable point.

It is noted that aluminum plate specimens have been utilized in the validation testing, rather than using steel pipes, because aluminum plate specimens were available in the laboratory and easier to handle for reliable tests. The availability of the tests using pipe specimens was affected by COVID-19. To avoid delaying the progress, we adopted plates for validating the theoretical studies. The use of plate specimens does not affect the results of validation tests because the theoretical analysis does not rely on the specific material (e.g., API 5L grade steel, or aluminum) and the specific geometry (e.g., pipe, or plate). The tests are used to valid mechanical analysis and derived equations. Based on these considerations, the following validation tests were performed:

An aluminum plate instrumented with a DFOS was tested using a low-capacity load frame (load capacity: 10 kN). A uniaxial tensile testing of an aluminum plate instrumented with a DFOS, as shown in Figure 2.2.10(a).

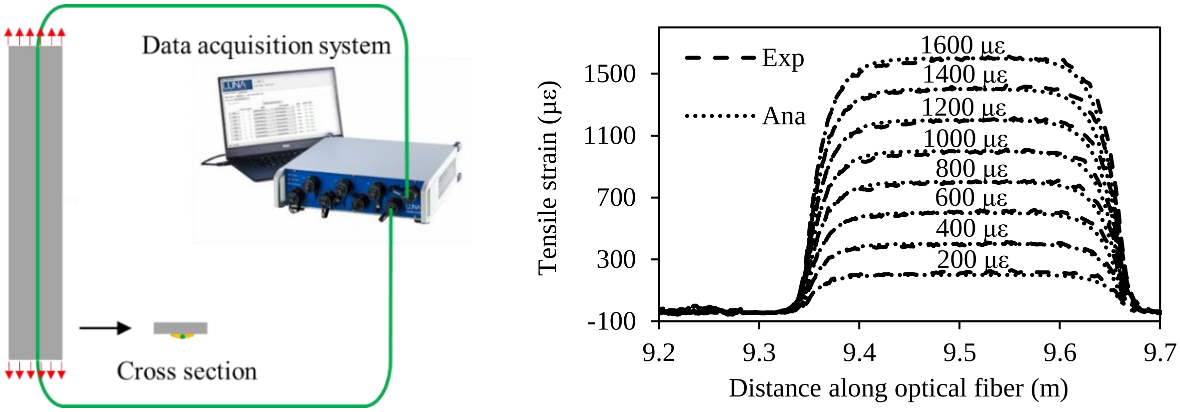

(a) (b)

Figure 2.2.10. Uniaxial tensile test: (a) experimental setup, and (b) strain distribution results.

The aluminum plate measured 300 mm in length, 30 mm in width, and 3 mm in thickness. A DFOS was attached to the surface of plate using a two-part epoxy. The fiber was connected to the distributed sensing system using the same optical fiber. The low-capacity load frame was used to apply tensile forces to the specimen. Before the tensile test, a 4-N preload was applied to allow the load frame and specimen to set. Then, the specimen was stretched to achieve 1600 με with a step size of 200 με. A clip-on strain gauge was calibrated using a caliber and used to measure the strain of the aluminum plate. The strain distribution along the optical fiber was measured at each step of loading. Figure 2.2.10(b) shows the measured strain distributions from the DFOS at different loading levels, and compares the measurement result with the analytical strain distributions. Overall, the experimental results are in good agreement with the analytical results.

The same aluminum plate was tested under a three-point bending using the same load frame, as depicted in Figure 2.2.11(a). The span length was 250 mm. A 4-N preload was applied to allow the load frame and beam to set. The mid-span deflection and settlements were measured using a displacement sensor attached to the mid-span of the specimen. The mid-span deflection was changed from 0 to 1.5 mm with a step size of 0.5 mm. The strain distribution along the optical fiber was measured at each step. Figure 2.2.11(b) compares the measured strain distributions with the analytical strain distributions. Overall, the experimental results were in good agreement with the analytical results, and thus, validated the derived formulae of strain transfer for the non-uniform strain field with a non-differentiable point.

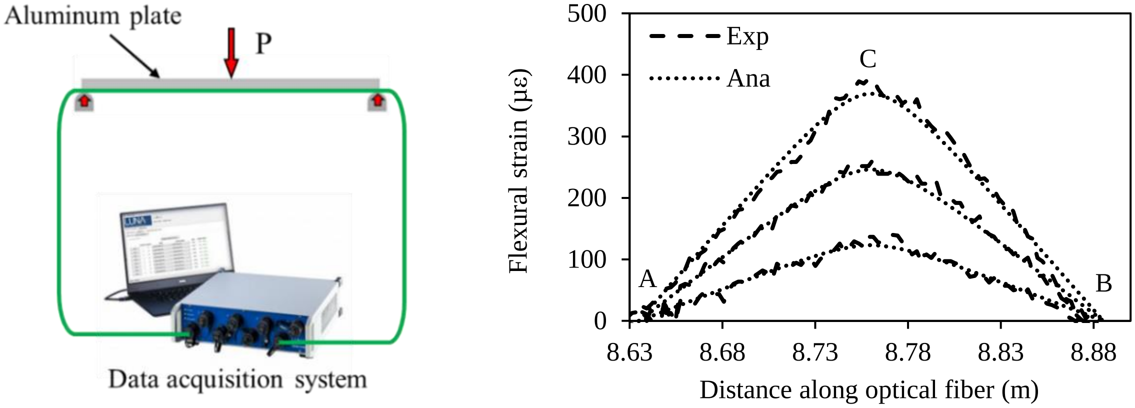

(a) (b)

Figure 2.2.11. Bending test: (a) experimental setup, and (b) strain distribution results. The experimental and analytical results are represented by "Exp" and "Ana", respectively.

2.2.2.4 Summary

Based on the research presented in section 2.2.2, the following conclusions can be drawn:

(1) The strain distributions sensed by packaged distributed fiber optic sensors attached to the surface of a pipe are subjected to strain transfer effects which can significantly influence the strain distribution patterns and values. It is essential to perform strain transfer analysis to properly interpret the distributed sensor data for pipeline monitoring.

(2) The presented strain transfer analysis approach is effective in quantitatively evaluating the strain transfer behaviors of packaged distributed fiber optic sensors. The derived formulae can be used to determine the strain distributions in packaged distributed fiber optic sensors attached to pipelines under various strain field conditions, thereby offering an theoretical basis for using distributed fiber optic sensors.

2.2.3. Inverse strain transfer analysis

The forward analysis in Section 2.2.2 explains the strain transfer effect in distributed fiber optic sensors. However, the forward strain transfer analysis is inapplicable in practice. In most practical problems, a DFOS is used to measure strain distributions in host matrix. In other words, the strain distribution in optical fiber is measured, while the strain distribution in host matrix is unknown. Thus, the task is to convert strain distribution in optical fiber into strain distribution in host matrix. This is an inverse problem opposite to the forward analysis, as shown in Figure 2.2.12 [25].

This section presents an innovative inverse analysis method that is used to convert the strain distribution in optical fiber into strain distribution in host matrix for the first time. The inverse analysis is performed through an optimization process. This study investigates three different metaheuristic optimization algorithms, which are the colliding bodies optimization (CDO), genetic algorithm (GA), and particle swarm optimization (PSO). Based on the proposed methods, case studies were conducted to test the performance of the proposed method under known and unknown strain conditions. In forward problems, with the type and magnitude of the strain in host matrix, a strain transfer analysis can be performed to calculate the strain distribution in optical fiber.

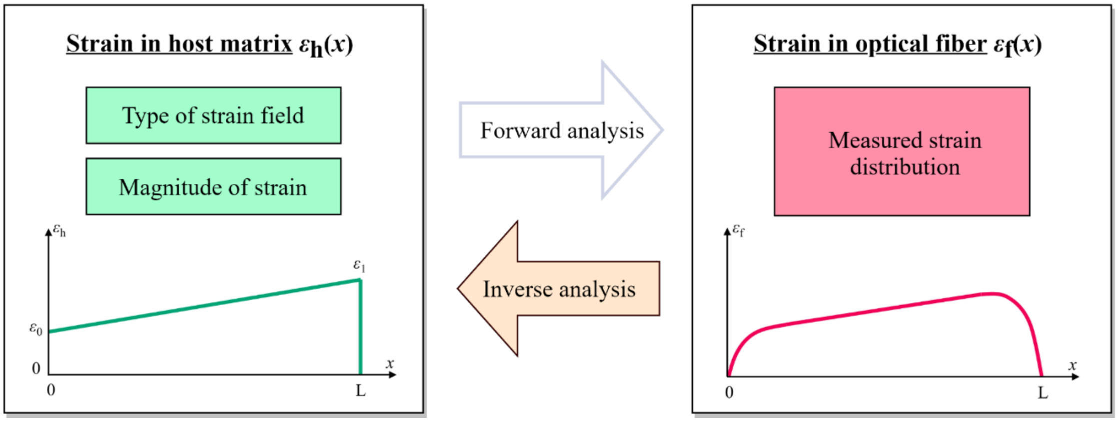

Figure 2.2.12. Comparison of forward and inverse problems of strain transfer analysis for DFOS.

In this study, the strains sensed by DFOS are used to determine the strain distributions in host matrix in two different scenarios:

(1) Scenario 1: When the type of strain field in host matrix is known, only the magnitude of strain needs to be determined. For example, if the strain in host matrix is uniform, the only unknown is the magnitude of uniform strain. When the magnitude of strain distribution in host matrix is assumed, the strain distribution in DFOS can be predicted via the forward analysis method in reference. Since the strain distribution in DFOS is measured, the discrepancy between the predicted and measured strains in DFOS can be used to define the objective function for an optimization analysis that can determine the optimal magnitude of strain to minimize the discrepancy.

(2) Scenario 2: When the type of strain field in host matrix is unknown, both the type and magnitude of strain need to be determined. For example, if the loads applied to a beam are unknown, both the type and magnitude of strain distribution are the unknowns. An innovative method is presented to provide a general method for the formulation of strain distribution based on the principle of superposition.

Figure 2.2.13 shows the flowchart of the proposed method. There are four main steps: (1) Step 1: An inverse problem is formulated. When the type of strain field of host matrix is known, the formulae of strain distribution are used to formulate the strain distribution in optical fiber. When the type of strain field of host matrix is unknown, an innovative method is presented to formulate the strains. (2) Step 2: The discrepancy between the measured and calculated strains in optical fiber is used to define the objective function for optimization. (3) Step 3: Optimization is performed to minimize the discrepancy between measured and calculated strain distributions in optical fiber by varying the strain field in host matrix. (4) Step 4: The results of optimization are used to determine the strain distributed in host matrix.

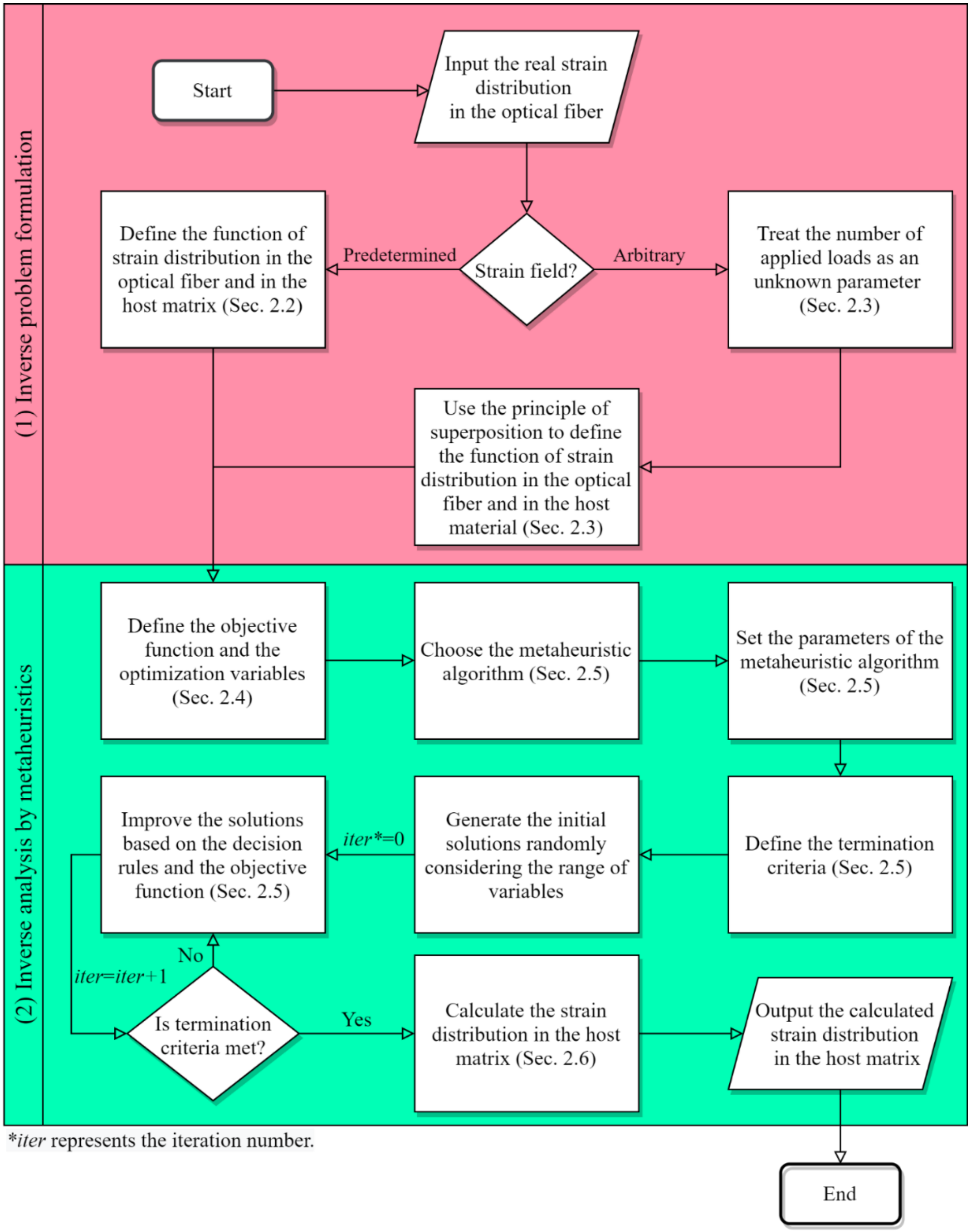

**iter* represents the iteration number.

Figure 2.2.13. Flowchart of the proposed methodology for the inverse analysis of strain distributions.

2.2.3.1. *Scenario 1: Known types of strain field in host matrix*

When the types of strain field in host matrix are known, the strain distribution in the matrix can be formulated using boundary conditions and used to formulate the strain distribution in the DFOS through a forward analysis. Then, the formulation of the strain distribution in the DFOS can be used to formulate the inverse problem that can be solved through an optimization process.

Four representative types of nonuniform strain field in host matrix were considered in prior research, which are (1) continuous linear strain fields, (2) continuous nonlinear strain fields, (3) continuous bi-linear strain fields, and (4) discontinuous strain fields, as shown in Figure 2.2.14. The governing equations and boundary conditions of the four cases are elaborated in Section 2.1.2.

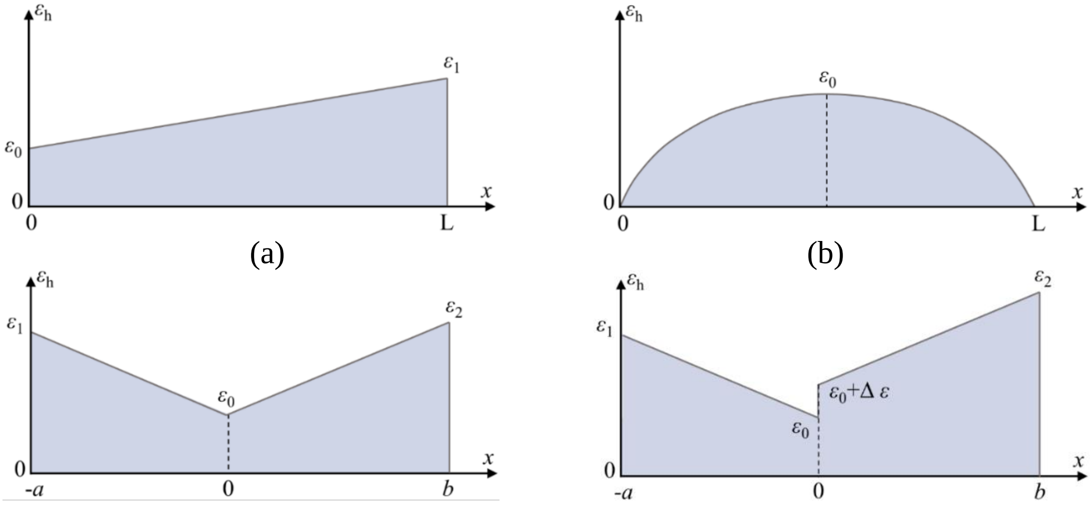

(a) (b)

(c) (d)

Figure 2.2.14. Representative non-uniform strain fields: (a) continuous linear, (b) continuous nonlinear, (c) continuous bi-linear, and (d) discontinuous strain fields.

2.2.3.2. *Scenario 2: Unknown type of strain field in host matrix*

In general, the type of strain field in host matrix is unknown. A general method is presented to solve problems when the strain field in host matrix is unknown. For an arbitrary strain field, the formula of strain distribution in the host matrix caused by an individual load can be derived using the boundary conditions. Then, a forward analysis is applied to formulate the strain distribution in the DFOS caused by the individual load. Next, according to the principle of superposition, the strain distributions in the in the optical fiber caused by several loads can be formulated as the sum of the strain distributions in the optical fiber caused by each of the load, as shown in Figure 2.2.15(a). Similarly, the summation of strain distributions in the host matrix caused by each of the loads equals to the strain distribution in the host matrix, as shown in Figure 2.2.15(b). The number, location, and the magnitude of loads are treated as the unknown parameters of the inverse problem.

The strain in the host matrix can be expressed as:

$$\varepsilon_{\mathrm{h}}(x) = \sum_{i=1}^{N} \varepsilon_{\mathrm{h},i}(x) \tag{2.2.46}$$

where $\varepsilon_{\mathrm{h,i}}(x)$ represents the strains in the host matrix caused by the i-th load; and N is the number of applied loads. Similarly, the strain in the optical fiber can be expressed as:

$$\varepsilon_{\mathrm{f}}(x)=\sum_{i=1}^{N}\varepsilon_{\mathrm{f},i}(x) \tag{2.2.47}$$

where $\varepsilon_{\mathrm{f,i}}(x)$ represents the strain in the fiber caused by the i-th load which is expressed as:

$$\varepsilon_{\mathrm{f,i}}(x)=C_{1,i}\cosh(kx)+C_{2,i}\sinh(kx)+\varepsilon_{\mathrm{h,i}}(x) \tag{2.2.48}$$

where $C_{1,i}$ and $C_{2,i}$ are the integration constants corresponds to the i-th applied load.

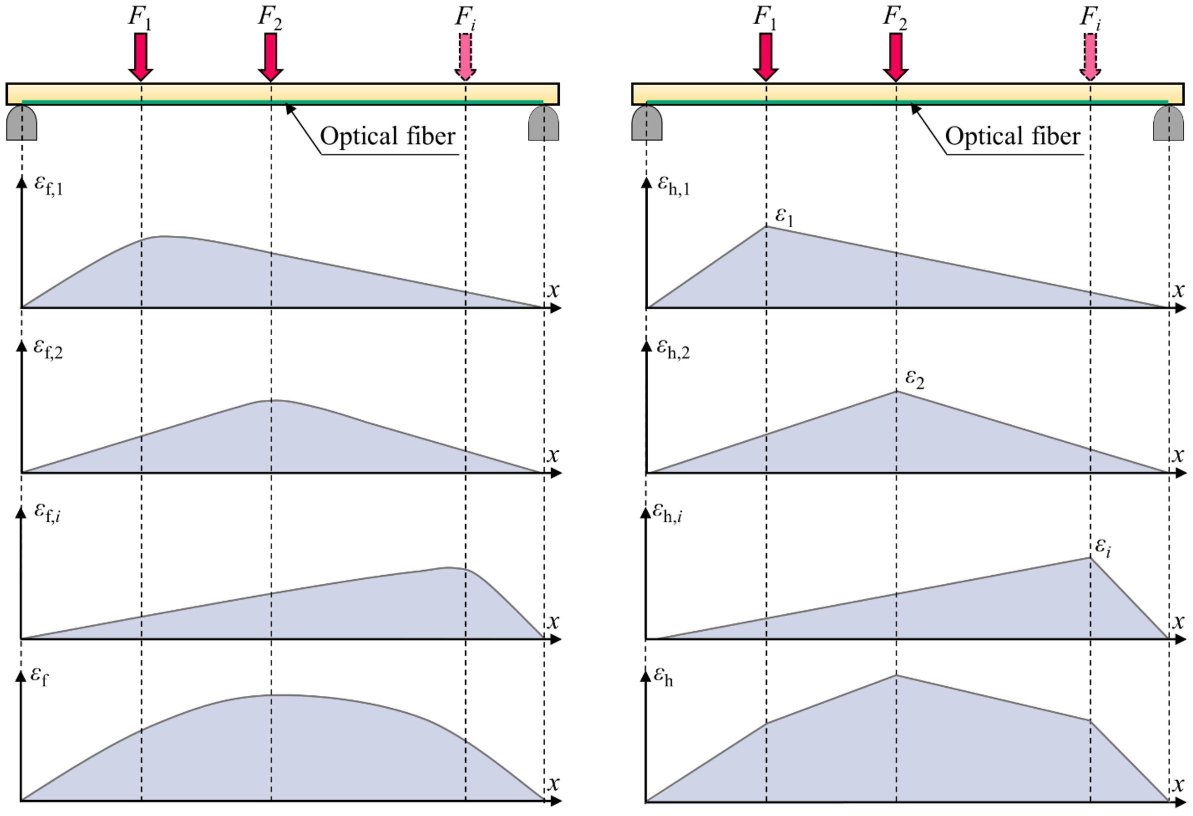

(a) (b)

Figure 2.2.15. Principle of the superposition of the strain fields caused by multiple loads.

According to Eq. (2.2.47), Eq. (2.2.48) can be rewritten as:

$$\varepsilon_{\mathrm{f}}(x)=\left(\sum_{i=1}^{N}C_{1,i}\right)\cosh(kx)+\left(\sum_{i=1}^{N}C_{2,i}\right)\sinh(kx)+\sum_{i=1}^{N}\varepsilon_{\mathrm{h},i}(x) \tag{2.2.49}$$

2.2.3.3. Optimization for inverse analysis

The inverse problem for calculating the strain distribution in the host matrix can be solved through optimization. The objective of the optimization is to minimize the objective function:

$$f(\phi) = MPE(\phi) = \frac{1}{n}\sum_{i=1}^{n}\left|\frac{\varepsilon_{\mathrm{f}}(x_i, \emptyset) - \varepsilon_f^{\wedge}(x_i)}{\varepsilon_f^{\wedge}(x_i)}\right| \tag{2.2.50}$$

where $f(\phi)$ is the objective function; $MPE(\phi)$ is the mean percentage error; $\varepsilon_f^{\wedge}(x_i)$ is the strain measured from a DFOS; $\varepsilon_{\mathrm{f}}(x_i, \emptyset)$ is the calculated strain in the DFOS based on the forward strain transfer analysis; n is the number of measured strains; ϕ is the decision vector consisting N number of optimization variables; and Ω is the search space.

When the type of strain distribution in host matrix is known, the decision vector that contains the optimization variables can be expressed as:

$$\phi = [\varepsilon_1, \varepsilon_2, \ldots, \varepsilon_\alpha, a_1, a_2, \ldots, a_\beta]^T \tag{2.2.51}$$

where ε_i is the i-th strain to be determined; a_j is the j-th length of segment to be determined; α and β are the number of unknown strains and the length of segments, respectively; therefore, the number of variables N is equal to $(\alpha + \beta)$. A candidate solution is feasible, i.e., $\phi \in \Omega$, if the variable bounds are satisfied:

$$-S \le \varepsilon_i \le S \qquad i = 1, 2, \ldots, \alpha \tag{2.2.52}$$

$$0 < a_j < L \qquad j = 1, 2, \ldots, \beta \tag{2.2.53}$$

where S is the absolute maximum value of the strain measurement range of the DFOS, which is set to 7500 με in this study; L is the length of the optical fiber.

When the type of strain distribution in host matrix is unknown, the decision vector is modified:

$$\phi = [\varepsilon_1, \varepsilon_2, \ldots, \varepsilon_\alpha, a_1, a_2, \ldots, a_\beta, NL_1, NL_2, \ldots, NL_\gamma]^T \tag{2.2.54}$$

where NL_i is the number of type-i loads; ɣ is the number of considered load types, which is equal to 1 when the concentrated forces are the only kind of applied loads; α and β are determined based on the maximum number of applied loads for each type of load. The number of variables is equal to $N = \alpha + \beta + \gamma$.

A solution is within the design space when Eq. (2.2.53) and Eq. (2.2.55) are satisfied:

$$0 \le NL_k \le MNL_k \qquad k = 1, 2, \ldots, \gamma \tag{2.2.55}$$

where MNL_k is the maximum number of type-k load, which is set before the optimization process.

2.2.3.4. Metaheuristic optimization algorithms

Three nature-inspired population-based metaheuristic algorithms were considered, which are (1) colliding bodies optimization, (2) genetic algorithm, and (3) particle swarm optimization.

2.2.3.4.1. Colliding bodies optimization

The colliding bodies optimization is inspired by the law of conservation of momentum which states that the total momentum is constant when two bodies collide elastically. A set of objects with different masses are the search agents which move towards the search space and collide with each other. The three steps of the algorithm are as follows:

(1) The objects are sorted based on the mass contribution, which is formulated as:

$$m_i = \frac{1/f(\phi_i)}{1/\sum_{i=1}^{NS} f(\phi_i)} \tag{2.2.56}$$

where $f(\phi_i)$ is the objective function value of the i-th object; ϕ_i is the i-th object; NS is the number of search agents (objects).

(2) The objects are organized into two groups, called stationary and moving groups, and the objects are split into pairs, as shown in Figure 2.2.16.

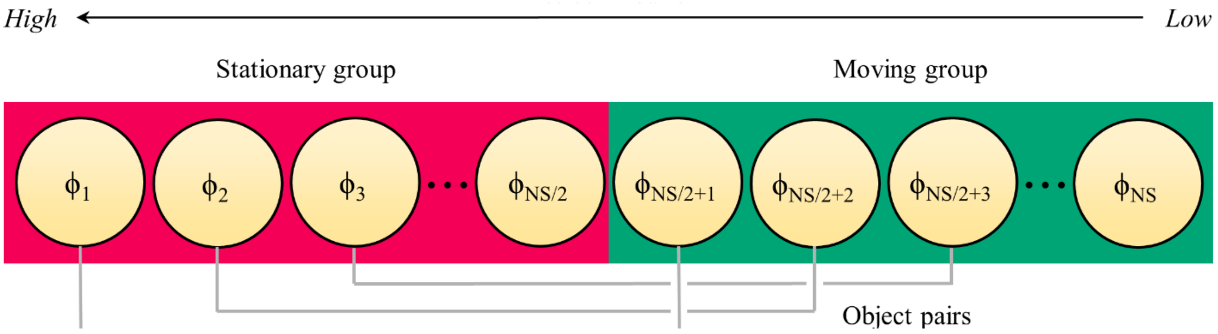

Figure 2.2.16. Arranging the objects into stationary and moving groups and pairing the objects.

(3) A collision occurs between the paired moving and stationary objects. The velocity of moving objects after collision is determined by:

$$v_i' = \frac{\left(m_i - E m_{(i-\frac{NS}{2})}\right) v_i}{m_i + m_{(i-\frac{NS}{2})}} \qquad i = {}^{NS}/_{2} + 1, \ldots, NS \tag{2.2.57}$$

where m_i is the mass contribution of the i-th object; and E is the coefficient of restitution:

$$E = 1 - \frac{iter}{itermax} \tag{2.2.58}$$

where $iter$ and $itermax$ are the number of current iteration and the maximum number of iterations; v_i is the velocity of i-th stationary object before collision which is equal to zero:

$$v_i = 0 \qquad i = 1, \ldots, {}^{NS}/_{2} \tag{2.2.59}$$

The velocity of stationary objects after the collision is formulated as:

$$v_i' = \frac{\left(m_{i+{}^{NS}/_{2}} + E m_{i+{}^{NS}/_{2}}\right) v_{i+{}^{NS}/_{2}}}{m_i + m_{i+{}^{NS}/_{2}}} \qquad i = 1, \ldots, {}^{NS}/_{2} \tag{2.2.60}$$

where $v_{i+{}^{NS}/_{2}}$ is the velocity of moving objects before the collision, which can be calculated as:

$$v_i = \phi_i - \phi_{(i-\frac{NS}{2})} \qquad i = {}^{NS}/_{2} + 1, \ldots, NS \tag{2.2.61}$$

where ϕ_i is the position of the i-th object. The new position of the moving and stationary objects can be calculated as:

$$\phi_i' = \phi_i + rand \cdot v_i' \tag{2.2.62}$$

where ϕ_i' and ϕ_i are the new and current positions of the i-th object; $rand$ is a random vector in the range [0, 1] and has the same size with v_i'; the symbol "·" is element-by-element multiplication.

2.2.3.4.2. Genetic algorithm

Genetic algorithm is an algorithm inspired by Charles Darwin's theory of natural evolution: The individuals that can adapt to changes are able to survive and reproduce. Individuals are the search agents while the chromosomes of individuals are the candidate solutions. Each component of the chromosomes is a gene. The three steps of the algorithm are as follows:

(1) The more suitable chromosomes, i.e., the highest quality solutions, are chosen and allowed to survive. The survival probability of each chromosome is expressed as:

$$P_i = \frac{f(\phi_i)}{\sum_{i=1}^{NS} f(\phi_i)} \tag{2.2.63}$$

(2) The individuals selected in the first step mate with each other with a crossover probability PC. Offspring with new gene assortments are created as shown in Figure 2.2.17(a). PC is 90%.

(3) Mutation occurs with the probability of PM to preserve the diversity from the previous population of individuals to the next one, as shown in Figure 2.2.17(b). PM is set to 10%.

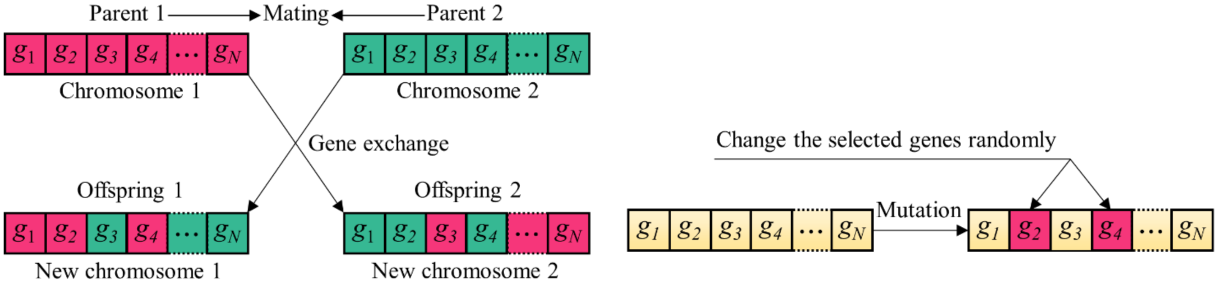

(a) (b)

Figure 2.2.17. Genetic algorithm for the optimization tasks: (a) gene exchange, and (b) mutation.

2.2.3.4.3. Particle swarm optimization

Particle swarm optimization algorithm is inspired by the swarm intelligence of bird flock. The algorithm has two steps:

(1) The velocity of particles (search agents) is calculated using:

$$V_i' = \omega V_i + c_1 r_1 (pbest_i - \phi_i) + c_2 r_2 (gbest_i - \phi_i) \tag{2.2.64}$$

where V_i' and V_i are the new and previous velocity of the i-th particle; ω is the inertia weight constant which is expressed as:

$$\omega = \frac{(itermax - iter)}{(itermax - 1)} (\omega_{max} - \omega_{min}) + \omega_{min} \tag{2.2.65}$$

where ω_{max} and ω_{min} are the maximum and minimum inertia weight, which are set to 0.9 and 0.4; c_1 and c_2 are the acceleration coefficients which are set to 2; r_1 and r_2 are random numbers in the range of [0, 1].

(2) The particles move across the search space based on the following expression:

$$\phi_i' = \phi_i + V_i' \tag{2.2.66}$$

A schematic of the movement mechanism of particles is shown in Figure 2.2.18.

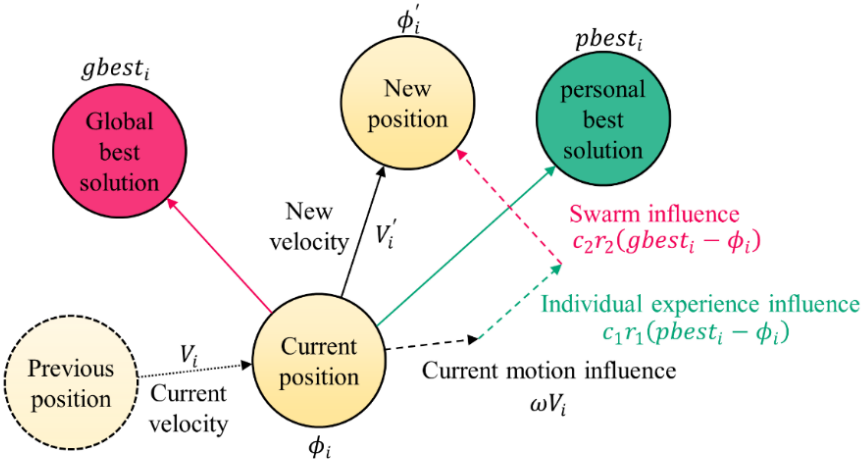

Figure 2.2.18. Schematic illustration of the movement mechanism of the particle swarm optimization.

2.2.3.5. Case studies for scenario 1

This section presents four representative case studies to demonstrate the proposed method in problems of Scenario 1 when the type of strain field in host matrix is known: (1) Case 1: uniform strain field; (2) Case 2: continuous linear strain field; (3) Case 3: continuous bi-linear strain field; and (4) Case 4: discontinuous strain field.

To solve the inverse problems, each of the three metaheuristic optimization algorithms is executed for 50 independent runs for statistical analysis. The termination criterion of the optimization algorithms is defined by the number of evaluations of objective function, which is 10 NS^2 where NS is the number of search agents.

2.2.3.5.1. Case 1: Uniform strain field

A DFOS is applied to measure the strain distribution in a host matrix that is subjected to a uniform strain field with a strain magnitude of 1000 με. According to reference, it is known that a nonuniform strain distribution can be measured from the DFOS. In this study, the measured strain distribution is used to determine the real strain distribution in host matrix through the proposed inverse analysis method.

For each of the metaheuristic algorithms, the number of search agents is set to 10. Figure 2.2.19 shows the convergence curves of the different algorithms. Table 2.2.1 lists the results. Overall, the particle swarm optimization has demonstrated the best performance, because it achieves the smallest values of “Average error”, “Maximum error”, and “Standard deviation”, which indicate the highest effectiveness, precision, and stability, respectively. The average execution time of the particle swarm algorithm is slightly higher than the other algorithms, indicating that the computational efficiency of the particle swarm algorithm is a little lower.

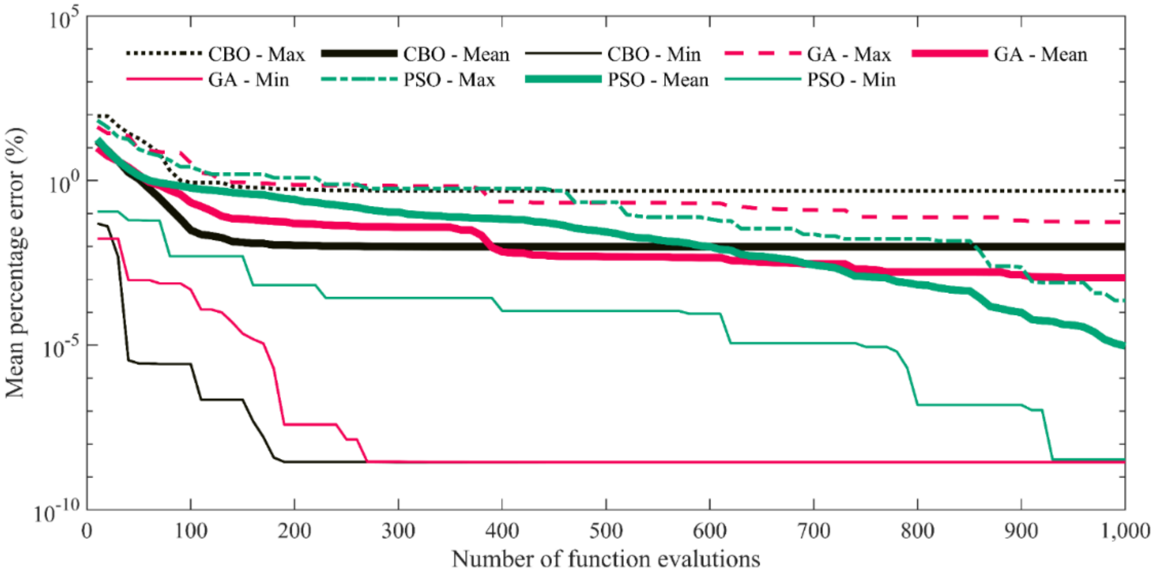

Figure 2.2.19. Convergence of the metaheuristic algorithms on case study 1. CBO, GA, and PSO represent colliding bodies optimization, genetic algorithm, and the particle swarm optimization.

Table 2.2.1. Computational results of the metaheuristics in solving case study 1

Optimization algorithm	Minimum error (%)	Average error (%)	Maximum error (%)	Standard deviation (%)	Average execution time (s)
Colliding bodies optimization	2.80E-09	0.011	0.49	0.071	0.023
Genetic algorithm	2.81E-09	0.001	0.047	0.015	0.031
Particle swarm optimization	3.38E-09	0.000	0.000	0.000	0.038

Figure 2.2.20 shows the results of the particle swarm optimization. Figure 2.2.20(a) plots the strain distributions in DFOS (ε_f), the real strain distribution in host matrix (ε_{hr}), and the calculated strain distribution in host matrix (ε_{hc}). The calculated strain distribution corresponds to the optimization result with the lowest objective function. It is seen that the calculated and real strain distributions in the host matrix are in good agreement. Figure 2.2.20(b) plots the relative error normalized as the percentage of the strain value, including the average error, upper and lower bounds of the error, and the 95% confidence interval of errors for the calculated strains in host matrix. The maximum relative error is less than 0.0001%.

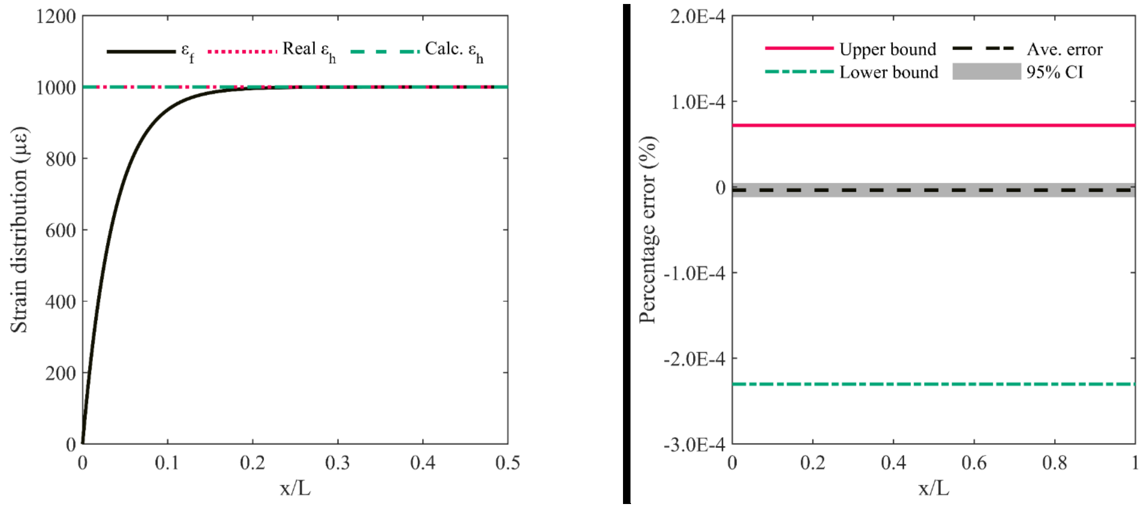

(a) (b)

Figure 2.2.20. Inverse analysis results of Case 1: (a) strain distributions; and (b) relative error along the DFOS. CI represents the confidence interval.

2.2.3.5.2. Case 2: Continuous linear strain field

A DFOS is applied to measure the strain distribution in a host matrix that is subjected to a linear strain field with a strain magnitude increasing from 1000 με to 2000 με. Again, the measured strain distribution is used to determine the real strain distribution in host matrix through the proposed inverse analysis method. For each of the metaheuristic algorithms, the number of search agents is set to 30. Figure 2.2.21 shows the convergence curves of the algorithms.

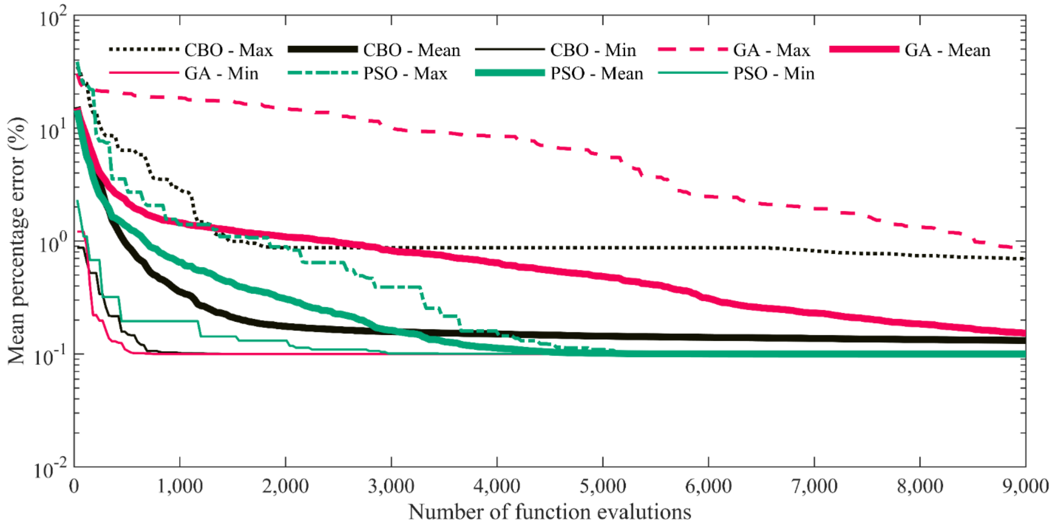

Figure 2.2.21. Convergence of the metaheuristic algorithms on case study 2. CBO, GA, and PSO represent colliding bodies optimization, genetic algorithm, and the particle swarm optimization.

Table 2.2.2 lists the results. Overall, the particle swarm optimization has demonstrated the best performance, because it achieves the smallest values of "Average error", "Maximum error", and "Standard deviation", which indicate the highest effectiveness, precision, and stability, respectively. The average execution time of the particle swarm algorithm is slightly higher than the other algorithms, indicating that the computational efficiency of the particle swarm algorithm is a little lower.

Table 2.2.2. Computational results of the metaheuristics in solving case study 2

Optimization algorithm	Minimum error (%)	Average error (%)	Maximum error (%)	Standard deviation (%)	Average execution time (s)
Colliding bodies optimization	0.10	0.13	0.70	0.10	0.09
Genetic algorithm	0.10	0.15	0.86	0.14	0.10
Particle swarm optimization	0.10	0.10	0.10	0.00	0.12

Figure 2.2.22 shows the results of the particle swarm optimization. Figure 2.2.22(a) plots the strain distributions in DFOS (ε_f), the real strain distribution in host matrix (ε_{hr}), and the calculated strain distribution in host matrix (ε_{hc}). The calculated strain distribution corresponds to the optimization result with the lowest objective function. It is seen that the calculated and real strain distributions in the host matrix are in good agreement. Figure 2.2.22(b) plots the relative error normalized as the percentage of the strain value, including the average error, upper and lower bounds of the error, and the 95% confidence interval of errors for the calculated strains in host matrix. The maximum relative error is less than 0.001%.

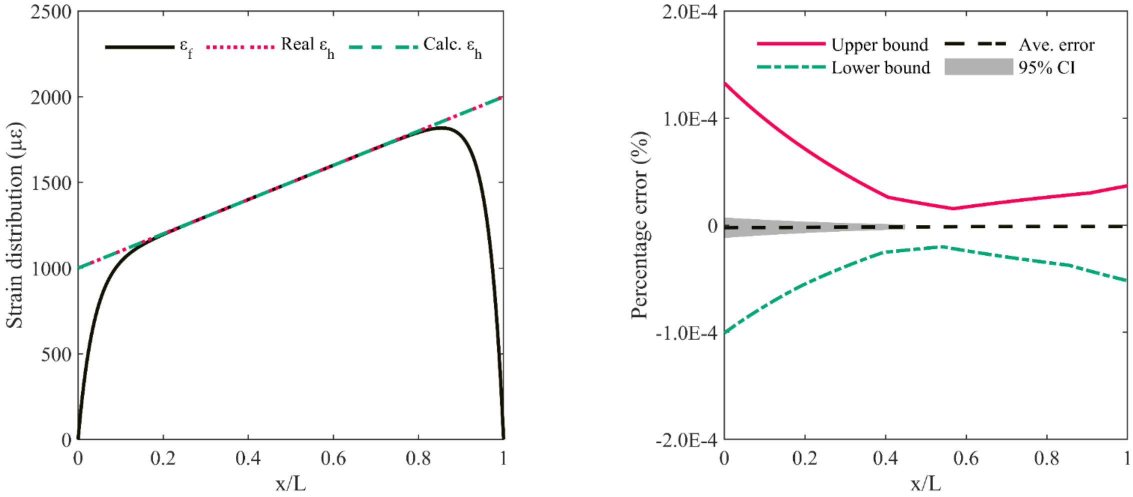

(a) (b)

Figure 2.2.22. Inverse analysis results of Case 2: (a) strain distributions; and (b) relative error along the DFOS. CI represents the confidence interval.

2.2.3.5.3. Case 3: Bi-linear strain field

The proposed method is used to estimate a strain field composed of two linear segments: (1) The strain linearly decreases from 1500 με to 1000 με as x increases from -0.5L to 0. (2) The strain linearly increases from 1000 με to 2000 με as x increases from 0 to 0.5L. The intersection point is at x = 0; hence, a = 0.5L. To solve the inverse problem, the number of search agents is set to 50.

Figure 2.2.23 shows the convergence of the investigated algorithms. Table 2.2.3 lists the computational results. Overall, the particle swarm optimization has demonstrated the best performance, because it achieves the smallest values of “Average error”, “Maximum error”, and “Standard deviation”, which indicate the highest effectiveness, precision, and stability, respectively. The average execution time of the particle swarm algorithm is comparable with the other algorithms.

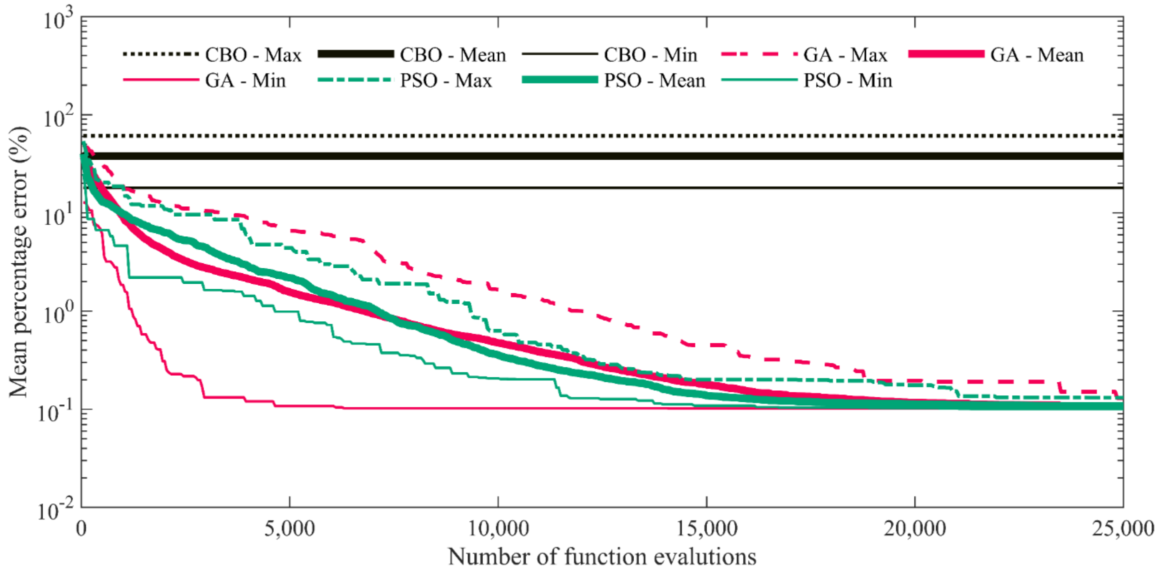

Figure 2.2.23. Convergence of the metaheuristic algorithms on case study 3. CBO, GA, and PSO represent colliding bodies optimization, genetic algorithm, and the particle swarm optimization.

Table 2.2.3. Computational results of the metaheuristics in solving case study 3

Optimization algorithm	Minimum error (%)	Average error (%)	Maximum error (%)	Standard deviation (%)	Average execution time (s)
Colliding bodies optimization	18	38	61	0.86	0.47
Genetic algorithm	0.10	0.11	0.13	0.01	0.50
Particle swarm optimization	0.10	0.11	0.13	0.01	0.50

Figure 2.2.24 shows the results of the particle swarm optimization. Figure 2.2.24(a) plots the strain distributions in DFOS (ε_{f}), the real strain distribution in host matrix ($\varepsilon_{\mathrm{hr}}$), and the calculated strain distribution in host matrix ($\varepsilon_{\mathrm{hc}}$). The calculated strain distribution corresponds to the optimization result with the lowest objective function. The calculated and measured strain distributions in host matrix are in good agreement. Figure 2.2.24(b) plots the relative error normalized as the percentage of the strain value, including the average error, upper and lower bounds of the error, and the 95% confidence interval of errors for the calculated strains in host matrix. The maximum relative error is less than 0.1%.

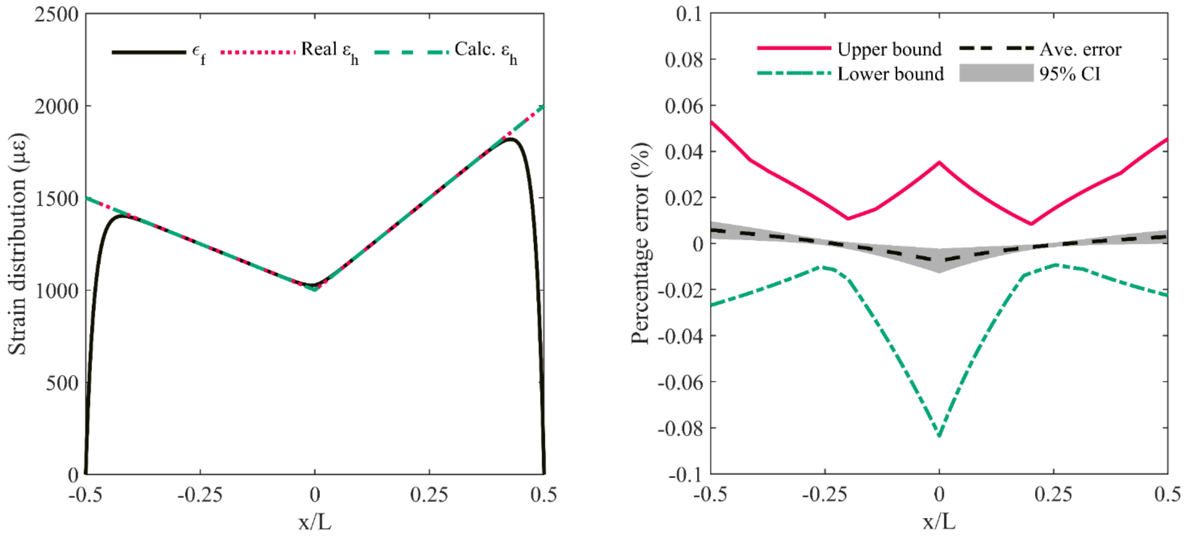

(a) (b)

Figure 2.2.24. Inverse analysis results of Case 3: (a) strain distributions; and (b) relative error along the DFOS. CI represents the confidence interval.

2.2.3.5.4. Case 4: Discontinuous strain field

The proposed method is used to estimate a strain field composed of two linear segments with an abrupt strain change: (1) The strain linearly decreases from 750 με to 500 με as *x* increases from -0.5L to 0. (2) The strain linearly increases from 750 με to 1500 με as *x* increases from 0 to 0.5L. The intersection point is at $x = 0$; hence, $a = 0.5$L. To solve the inverse problem, the number of search agents is set to 50. Figure 2.2.25 shows the convergence of the investigated algorithms.

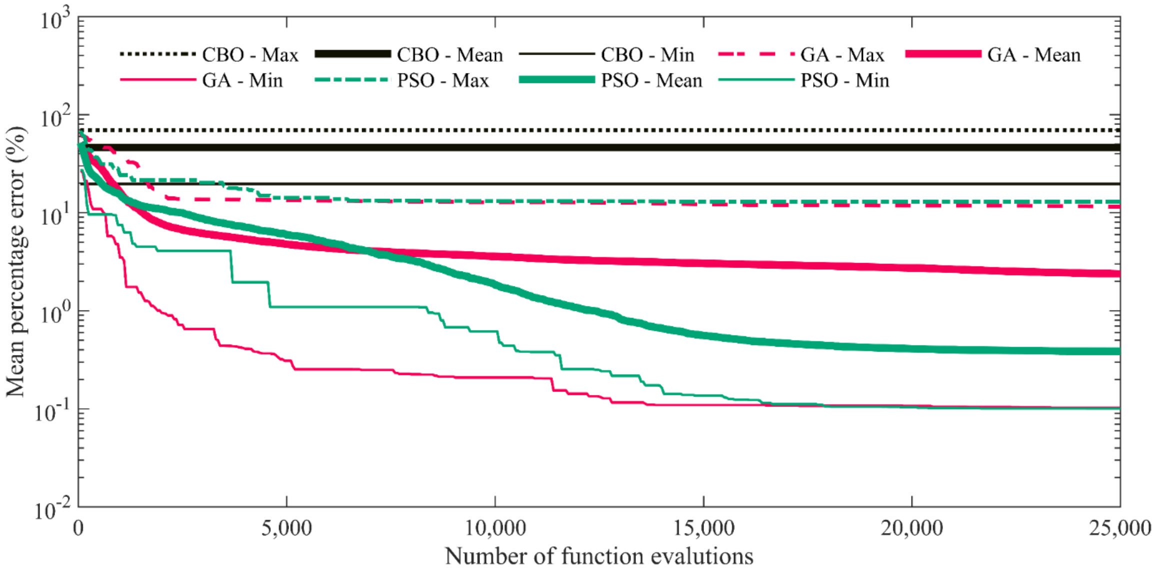

Figure 2.2.25. Convergence of the metaheuristic algorithms on case study 4. CBO, GA, and PSO represent colliding bodies optimization, genetic algorithm, and the particle swarm optimization.

Table 2.2.4 lists the results. Overall, the particle swarm optimization has demonstrated the best performance, because it achieves the smallest values of “Average error”, “Maximum error”, and “Standard deviation”, which respectively indicate the highest effectiveness, precision, and stability. The average execution time of the particle swarm algorithm is comparable with the other algorithms, meaning that the computational efficiency of these algorithms are comparable.

Table 2.2.4. Computational results of the metaheuristics in solving case study 4

Optimization algorithm	Minimum error (%)	Average error (%)	Maximum error (%)	Standard deviation (%)	Average execution time (s)
Colliding bodies optimization	19.70	46.30	69.30	9.52	0.97
Genetic algorithm	0.10	2.38	11.50	2.83	0.99
Particle swarm optimization	0.10	0.39	12.90	1.81	1.01

Figure 2.2.26 shows the results of the particle swarm optimization. Figure 2.2.26(a) plots the strain distributions in DFOS (ε_f), the real strain distribution in host matrix (ε_{hr}), and the calculated strain distribution in host matrix (ε_{hc}). The calculated strain distribution corresponds to the optimization result with the lowest objective function. The calculated and measured strain distributions in host matrix are in good agreement. Figure 2.2.26(b) plots the relative error normalized as the percentage of the strain value, including the average error, upper and lower bounds of the error, and the 95% confidence interval of errors for the calculated strains in host matrix. The maximum relative error is less than 0.1%.

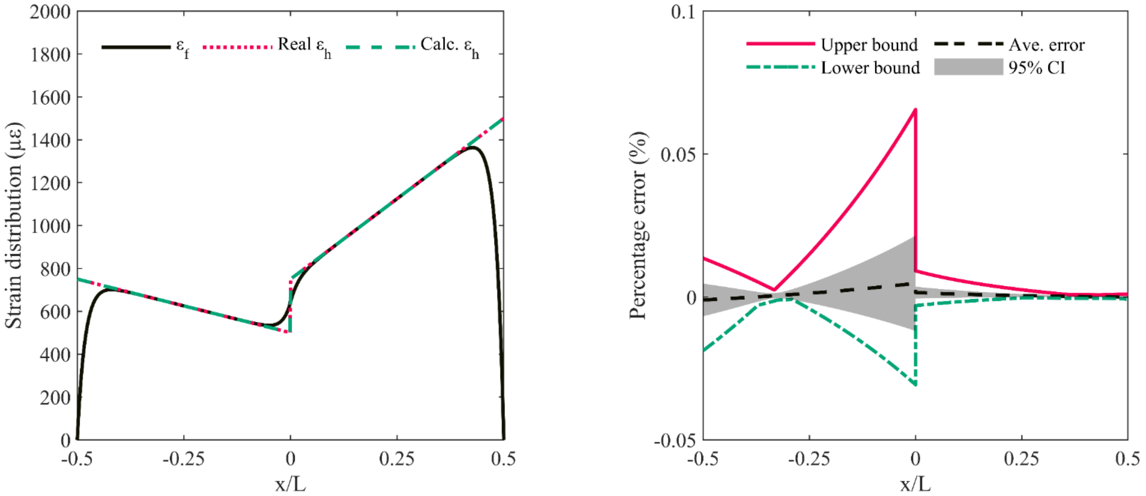

(a) (b)

Figure 2.2.26. Inverse analysis results of Case 4: (a) strain distributions; and (b) relative error along the DFOS. CI represents the confidence interval.

2.2.3.6. Case studies for scenario 2

This section presents two case studies to evaluate the performance of the proposed method when the type of strain field in host matrix is unknown. In each case, multiple concentrated loads are applied at arbitrary sections of a simply support beam instrumented with DFOS, as illustrated in Figure 2.2.27.

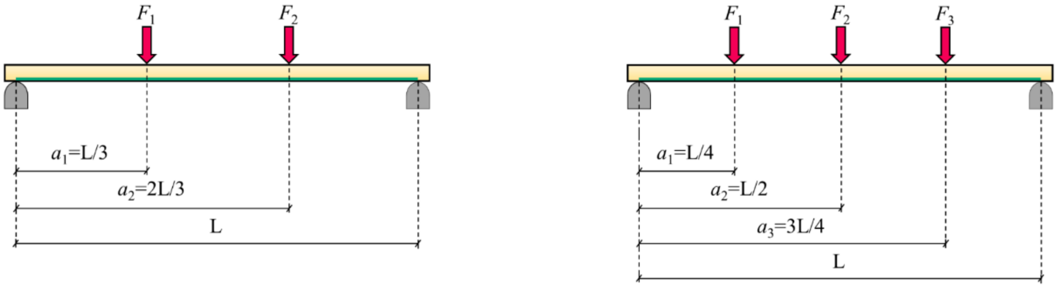

(a) (b)

Figure 2.2.27. Simply supported beam under: (a) two concentrated forces; (b) three concentrated forces.

Both the locations and magnitudes of the loads need to be determined through inverse analysis. Figure 2.2.27(a) shows a beam under two concentrated loads. Figure 2.2.27(b) shows a beam under three concentrated loads. The beams have a uniform cross section along the length. The strain distribution in host matrix caused by the i-th load (F_i) can be expressed as:

$$\varepsilon_{\mathrm{h}}(x) = \begin{cases} \varepsilon_i \left(\dfrac{x}{a_i}\right) & 0 \le x \le a_i \\ \varepsilon_i \left(\dfrac{L-x}{L-a_i}\right) & a_i \le x \le L \end{cases} \tag{2.2.67}$$

where ε_i is the maximum strain at the section where the i-th load is applied; a_i is the distance between the i-th load and the left support; and L is the span of the beam.

With Eq. (2.2.67), the strain distribution in the DFOS can be expressed as:

$$\varepsilon_{\mathrm{f}}(x) = \begin{cases} C_1 \cosh(kx) + C_2 \sinh(kx) + \varepsilon_i \left(\dfrac{x}{a_i}\right) & 0 \le x \le a_i \\ C_3 \cosh(kx) + C_4 \sinh(kx) + \varepsilon_i \left(\dfrac{L-x}{L-a_i}\right) & a_i \le x \le L \end{cases} \tag{2.2.68}$$

where C_1, C_2, C_3, and C_4 are the integration constants to be determined by the boundary conditions.

The boundary conditions are:

$$\varepsilon_{\mathrm{f}}(x=0) = 0 \tag{2.2.69a}$$
$$\varepsilon_{\mathrm{f}}(x={a_i}^-) = \varepsilon_{\mathrm{f}}(x={a_i}^+) \tag{2.2.69b}$$
$$\varepsilon_{\mathrm{f}}(x=L) = 0 \tag{2.2.69c}$$
$$\tau_{\mathrm{f}}(x={a_i}^-) = \tau_{\mathrm{f}}(x={a_i}^+) \tag{2.2.69d}$$

The integration constants are determined as:

$$C_1 = 0 \tag{2.2.70a}$$
$$C_2 = \frac{\varepsilon_i L}{k a_i (L-a_i)} \left[\frac{\sinh(k a_i)}{\tanh(kL)} - \cosh(k a_i)\right] \tag{2.2.70b}$$
$$C_3 = -\frac{\varepsilon_i L}{k a_i (L-a_i)} \sinh(k a_i) \tag{2.2.70c}$$
$$C_4 = \frac{\varepsilon_i L}{k a_i (L-a_i)} \left[\frac{\sinh(k a_i)}{\tanh(kL)}\right] \tag{2.2.70d}$$

For each load, there are two unknown parameters to be determined (ε_i and a_i). When the beam is divided into (N + 1) segments, there is a total of N loads. The total strain is equal to the sum of N number of ε_i, where i = 1, 2, ... , N. Therefore, the decision vector can be expressed as:

$$\phi = [\varepsilon_1, \varepsilon_2, \dots, \varepsilon_\alpha, a_1, a_2, \dots, a_\alpha, N]^T \tag{2.2.71}$$

where ε_i is the maximum strain in the host matrix caused by the i-th concentrated load (F_i); a_i is the location of F_i; and N is the number of applied concentrated loads.

A candidate solution is feasible when the following statement is satisfied:

$$1 \leq N \leq MN \tag{2.2.72}$$

where MN is the maximum number of concentrated loads. In this study, MN is set to 5.

To solve the inverse problem, each algorithm is executed for 50 independent runs to evaluate the algorithms. The computation for optimization is terminated as the number of objective function evaluations reaches 10 NS^2 where NS is the number of search agents which is set to 100.

2.2.3.6.1. Case 5: Two concentrated forces

The beam shown in Figure 2.2.27(a) is analyzed using the proposed method. The concentrated forces, F_1 and F_2, are applied at the third spans of the beam. The span length of the beam is 0.25 m. The strain distributions in the host structure are shown in Figure 2.2.28. $\varepsilon_{f,i}$ and $\varepsilon_{h,i}$ are the strains in optical fiber and host matrix caused by the i-th force, respectively. ε_f and ε_h are the total strains in optical fiber and host matrix, respectively.

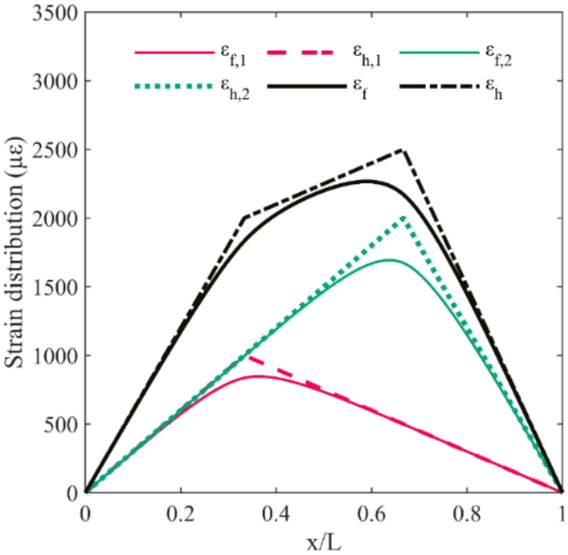

Figure 2.2.28. Strain distributions for two concentrated forces.

Figure 2.2.29 shows the convergence curves of the optimization algorithms. Table 2.2.5 lists the computational results. Overall, the genetic algorithm shows the best performance because it shows the smallest values of “Average error”, “Maximum error”, and “Standard deviation”. The different algorithms show comparable results for the average execution time.

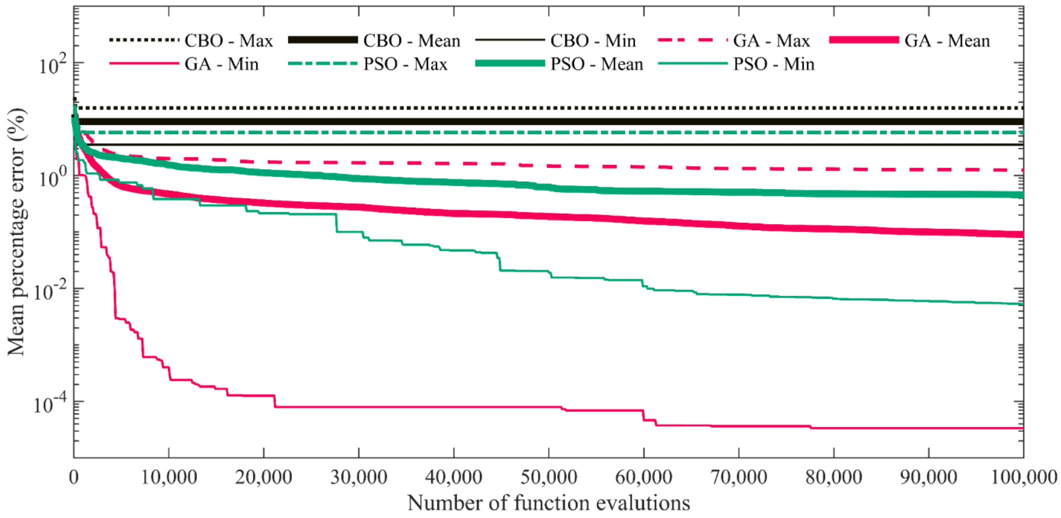

Figure 2.2.29. Convergence curves of the metaheuristic algorithms for Case 5.

Table 2.2.5. Computational results of the metaheuristics in solving case study 5

Optimization algorithm	Minimum error (%)	Average error (%)	Maximum error (%)	Standard deviation (%)	Average execution time (s)
Colliding bodies optimization	3.52	9.05	15.78	3.49	1.01
Genetic algorithm	0.000	0.09	1.26	0.24	1.17
Particle swarm optimization	0.005	0.46	5.79	1.46	1.38

The results from the genetic algorithm are plotted in Figure 2.2.30(a), showing that the real and the calculated strains in host matrix are in good agreement. Figure 2.2.30(b) shows the average error, upper and lower bounds of error, and the 95% confidence interval of the error. The absolute maximum error is less than 3% and the 95% confidence interval is in the range of (-1.5%, 1%).

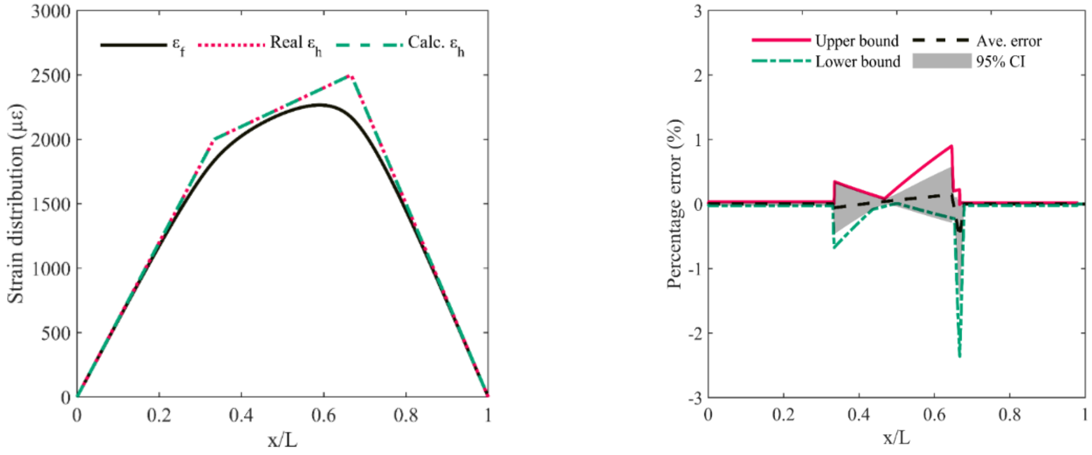

(a) (b)

Figure 2.2.30. Inverse analysis results of Case 5: (a) strain distributions; and (b) relative error along the DFOS. CI represents the confidence interval.

2.2.3.6.2. Case 6: Three concentrated forces

The beam shown in Figure 2.2.27(b) is analyzed using the proposed method. The concentrated forces, F_1 to F_3, are applied at the quarter and middle spans of the beam. The span length of the beam is 0.25 m. The strain distributions in the host structure are shown in Figure 2.2.31. Figure 2.2.32 shows the convergence curves of the optimization algorithms.

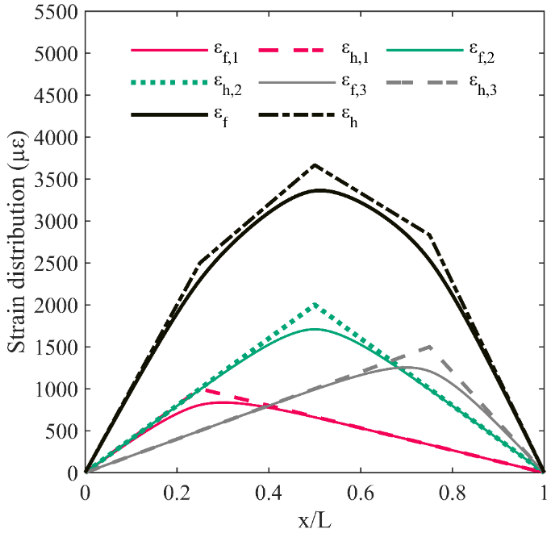

Figure 2.2.31. Strain distributions for three concentrated forces.

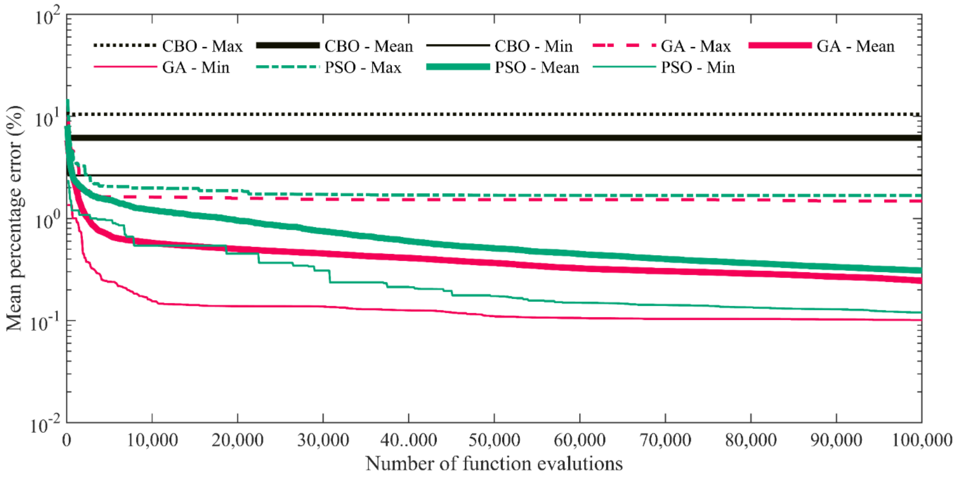

Figure 2.2.32. Convergence curves of the metaheuristic algorithms for Case 6.

Table 2.2.6 lists the computational results. Overall, the genetic algorithm shows the best performance since it has the smallest values of “Average error”, “Maximum error”, and “Standard deviation”. The different algorithms show comparable results for the average execution time.

The results of genetic algorithm are plotted in Figure 2.2.33(a), indicating that the real and the calculated strains in host matrix are in good agreement. Figure 2.2.33(b) shows the average error, upper and lower bounds of the error, and the 95% confidence interval of the error. The absolute maximum error is less than 5% and the 95% confidence interval is in the range of (-2%, 2%).

Table 2.2.6. Computational results of the metaheuristics in solving case study 6

Optimization algorithm	Minimum error (%)	Average error (%)	Maximum error (%)	Standard deviation (%)	Average execution time (s)
Colliding bodies optimization	2.64	6.16	10.46	1.80	2.36
Genetic algorithm	0.10	0.25	1.48	0.21	3.51
Particle swarm optimization	0.12	0.31	1.68	0.28	3.69

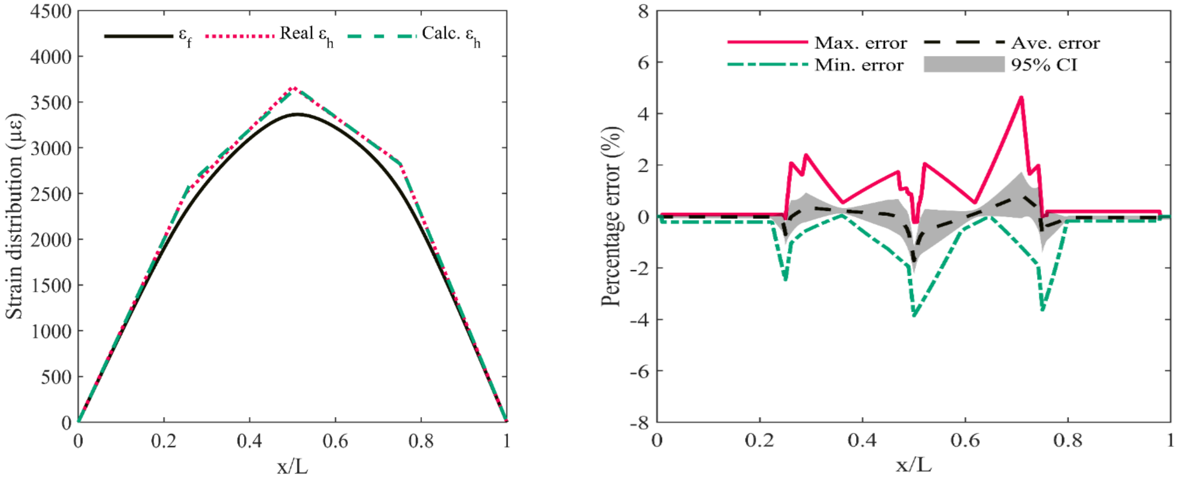

(a) (b)

Figure 2.2.33. Inverse analysis results of Case 6: (a) strain distributions; and (b) relative error along the DFOS. CI represents the confidence interval.

2.2.3.6.3. Case 7: A real-world application

A case study of the proposed method for a real-world application was conducted. A carbon-fiber-reinforced polymer (CFRP) post-tensioned fiber reinforced concrete beam, shown in Figure 2.2.34 [49], was tested, and the sensor data were analyzed using the developed method.

It is noted that beam specimens, rather than pipes, were tested because the beam specimens were available in the laboratory. The availability of the tests using pipe specimens was affected by COVID-19. To avoid delaying the research progress, we adopted beam specimens for validating the theoretical research results. The test results can be utilized to valid the developed theoretical methods because the proposed inverse strain transfer analysis method is independent of the specific material (e.g., API 5L grade steel, or reinforced concrete) and the specific geometry (e.g., pipe, or beam). The case study focuses on inverse mechanical analysis for the strain transfer behaviors and the optimization of the sensing results. Based on the above considerations, the following validation tests were designed and performed:

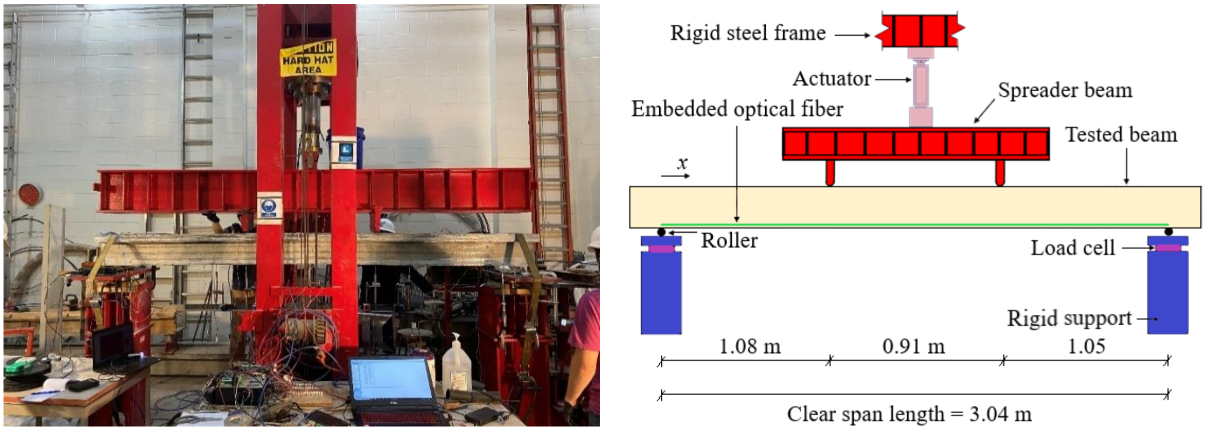

(a) (b)

Figure 2.2.34. Four-point bending test set-up of the CFRP post-tensioned fiber reinforced concrete beam: (a) photograph; and (b) the schematic illustration.

The beam was under four-point bending, and two concentrated forces were applied at 1.08 and 1.99 m away from the start point of the optical fiber. A DFOS was embedded in the concrete. The span length of the beam is 3.04 m. The strain distributions in the optical fiber and host structure are shown in Figure 2.2.35.

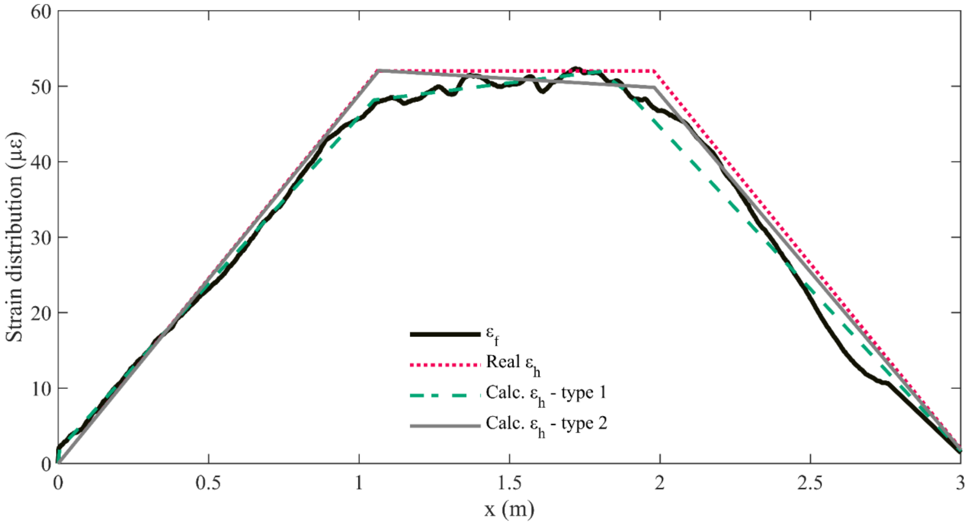

Figure 2.2.35. strain distribution in the host structure obtained by inverse analysis for Case 7.

The case study was conducted with two types of methods: (I) Type 1: Consider the number of applied loads, as well as their location and magnitude, as unknown parameters. (II) Type 2: Consider the magnitudes of the applied concentrated loads as the unknown parameters. Figure 2.2.36 shows the convergence curves of the optimization algorithms.

Table 2.2.7 and Table 2.2.8 list the computational results for type 1 and type 2. The genetic algorithm showed the best performance as it has the smallest values of “Average error”, “Maximum error”, and “Standard deviation”. The different algorithms show comparable results for the average execution time.

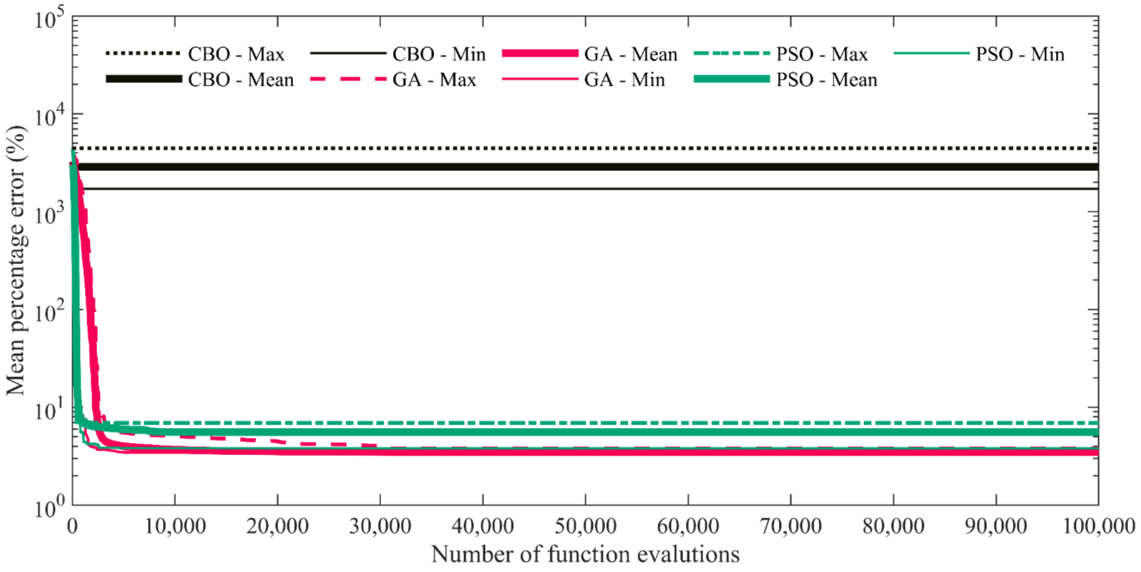

(a)

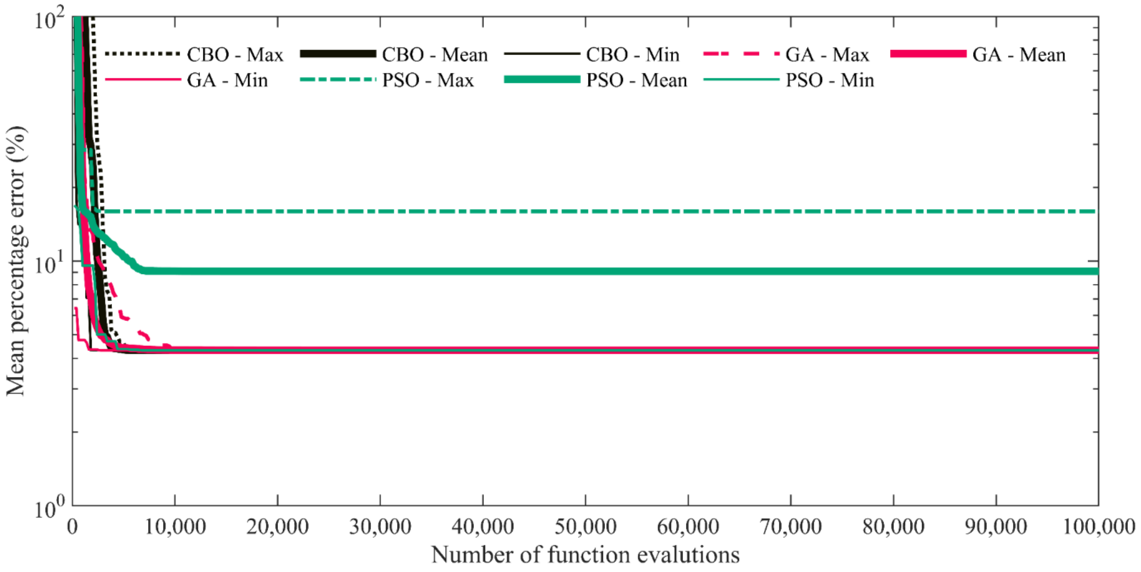

(b)

Figure 2.2.36. Convergence of the metaheuristic algorithms for Case 7: (a) type 1, and (b) type 2.

Table 2.2.7. Computational results of the metaheuristics in solving case 7 – type 1

Optimization algorithm	Minimum error (%)	Average error (%)	Maximum error (%)	Standard deviation (%)	Average execution time (s)
Colliding bodies optimization	1709.97	2877.93	4442.76	2084.57	2.88
Genetic algorithm	3.46	3.48	3.80	0.67	3.42
Particle swarm optimization	3.82	5.57	6.89	4.09	3.71

Table 2.2.8. Computational results of the metaheuristics in solving case 7 – type 2

Optimization algorithm	Minimum error (%)	Average error (%)	Maximum error (%)	Standard deviation (%)	Average execution time (s)
Colliding bodies optimization	4.32	4.33	4.33	0.081	2.07
Genetic algorithm	4.32	4.32	4.32	0.000	2.88
Particle swarm optimization	4.32	9.09	15.99	9.81	2.90

The results from the genetic algorithm are plotted in Figure 2.2.37, indicating that the real and the calculated strains in host matrix are in good agreement; the results of type 2 are more accurate than those of type 1. Figure 2.2.37 shows the average error, upper and lower bounds of the error, and the 95% confidence interval of the error for type 1 and type 2. The absolute maximum error for type 1 and type 2 is less than 10% and 7%; the 95% confidence interval for type 1 is in the range of (-10%, 15%); the 95% confidence interval for type 2 is in the range of (-5%, 1%).

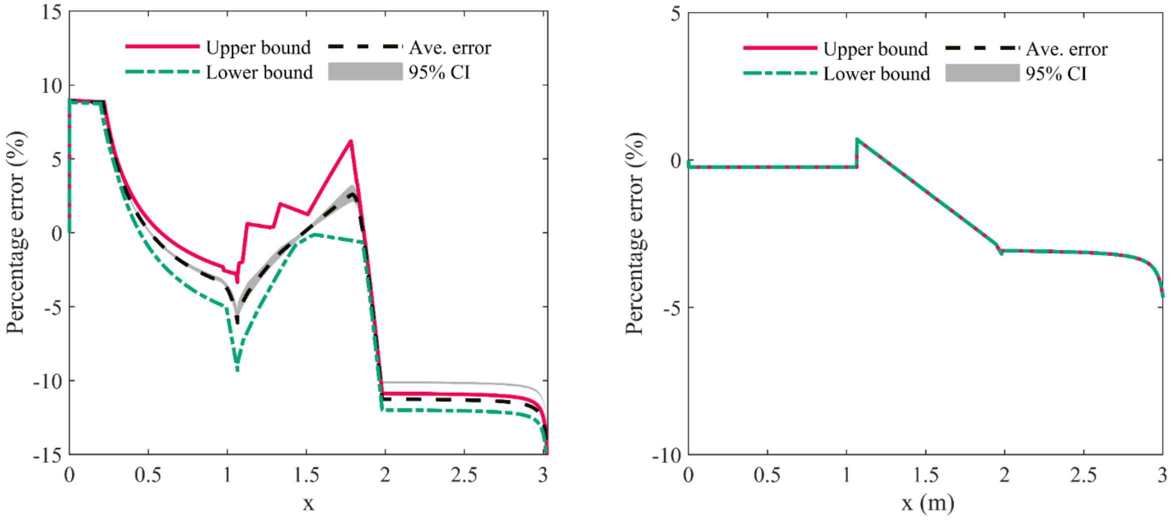

(a) (b)

Figure 2.2.37. Relative error along the DFOS for the results obtained for Case 7: (a) type 1, and (b) type 2. CI represents the confidence interval.

2.2.3.7. Summary

Strains measured by DFOS with protective coatings can be different from the real strains in host matrix due to strain transfer effect. In this project, forward and inverse strain transfer analysis methods were developed. The forward strain transfer analysis was conducted to derive the strain distributions sensed by the DFOS, and the inverse strain transfer analysis was conducted to determine the real strain distributions in host matrix using strain distributions measured from DFOS. Two different scenarios of strain distributions in host matrix are investigated, which have known and unknown types of strain fields, respectively. Three representative metaheuristic algorithms are respectively utilized in the inverse analysis. The performance of the proposed method was evaluated by analytical case studies and experimental testing of a prestressed concrete beam subjected to four-point bending. The results demonstrated high accuracy and efficiency of the proposed method.

2.3. Detection, localization, quantification, and visualization of cracks

2.3.1. Overview

Research was conducted to develop methods to quantify crack width at multiple scales with high accuracy. Specifically, this study has three main objectives: (1) develop a new method to evaluate crack width from micro to macro scales; (2) investigate the feasibility to monitor multiple cracks using a single DFOS; and (3) investigate the effects of three key parameters of DFOS, which are the coating thickness of optical fiber, the spatial resolution of strain measurement, and the spacing between adjacent cracks. To this end, a customized specimen was designed to manipulate cracks under precise displacement control. An optical fiber was attached to the specimen and served as a DFOS which measured strain distributions along the fiber based on OFDR. An algorithm was presented to analyze crack width based on the measured strain distribution. The crack width measured by the DFOS was compared with the crack width measured by an extensometer. Parametric studies were conducted to investigate the effects of the three key parameters on the measurement of crack width. This study is expected to significantly enhance the capability of detecting, locating, and quantifying cracks by using DFOS.

2.3.2. Experimental program

2.3.2.1. Specimen and test set-up

Figure 2.3.1 shows the specimen and the test set-up. The specimen consisted of two aluminum plates and two steel bars with a U-shaped cross section as the slideway of the plates. The aluminum plates, U-shaped bars, and optical fiber are shown in grey color, orange color, and green color, respectively. Under tension, the bars constrained the lateral movement of the plates but allow sliding along the length direction. Each plate measured 13 mm in width and 400 mm in length. The two ends of the specimen were gripped and loaded by the load frame under displacement control at the rate of 0.2 mm/min. As the aluminum plates slid along the U-shaped bars, a crack was generated at the interface between the two plates. The crack width was controlled by the load frame and measured by an extensometer which was clipped on the aluminum plates at the crack, as shown in Figure 2.3.1(a). The measurement of crack width from the extensometer was used as the ground truth in this study.

It is noted that aluminum plate specimens have been utilized in the validation testing, rather than using steel pipes, because aluminum plate specimens were available in the laboratory and easier to handle for reliable tests. The availability of the tests using pipe specimens was affected by COVID-19. To avoid further delaying the progress, we adopted plate specimens for developing the technology. The tests are acceptable because the developed technology for monitoring cracks does not rely on the specific material (e.g., API 5L grade steel, or aluminum) and the specific geometry of the structure (e.g., pipe, or plate). The research focuses on technology development. Based on the above considerations, the following validation tests were performed:

Optical fibers were attached to the surface of the specimen using adhesives, and each optical fiber served as a DFOS and the transmission line. In this research, two cracking scenarios were considered: single crack and multiple cracks. Figure 2.3.1(b) shows the set-up for two cracks. One end of the optical fiber was connected to the data acquisition system for measurement of strain distribution along the optical fiber, and the other end of the optical fiber was free. The optical fiber was passed through the crack two times to simulate the effect of two cracks crossing a DFOS. The spacing between adjacent cracks is simulated by changing the length of the optical fiber at the turning portion. In the scenario of single crack, the same set-up was employed, but the optical fiber was passed through the crack for one time.

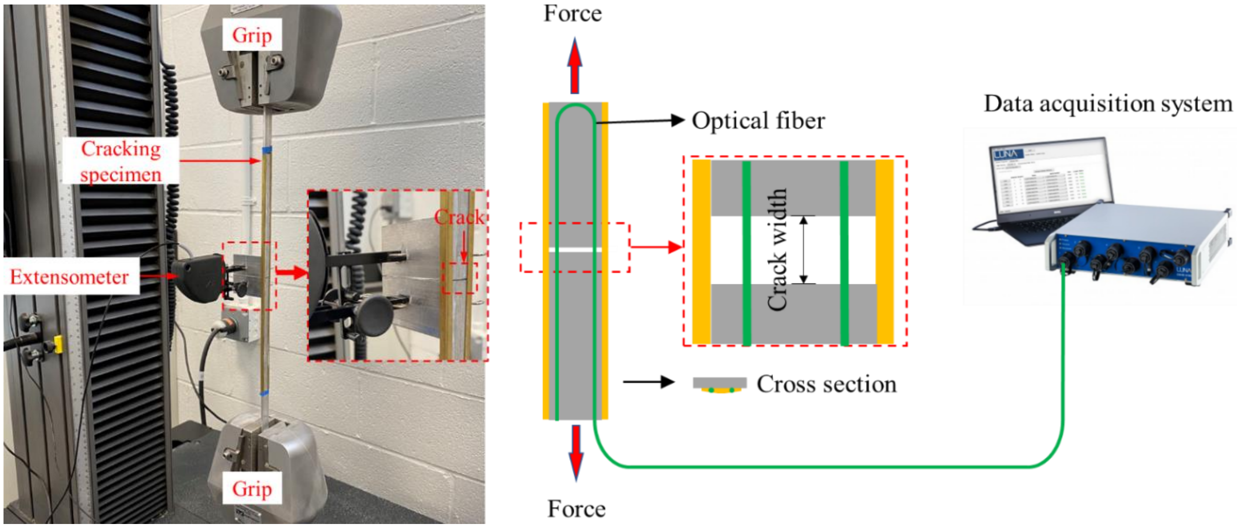

(a) (b)

Figure 2.3.1. Specimen and test set-up: (a) photography of the specimen on the load frame; and (b) the set-up for measurement using DFOS.

2.3.2.2. Loading protocol

Figure 2.3.2 shows the loading protocol of the tensile tests. Under the displacement control mode, the displacement applied by the load frame linearly increased with time. The measurement results from the extensometer installed at the crack width was almost the same as the displacement applied by the load frame. This is because the two aluminum plates were discontinuous except for the thin optical fiber bridging the crack between the two plates. The deformations of the aluminum plates are negligible. Therefore, the elongation represents the crack width of the specimen.

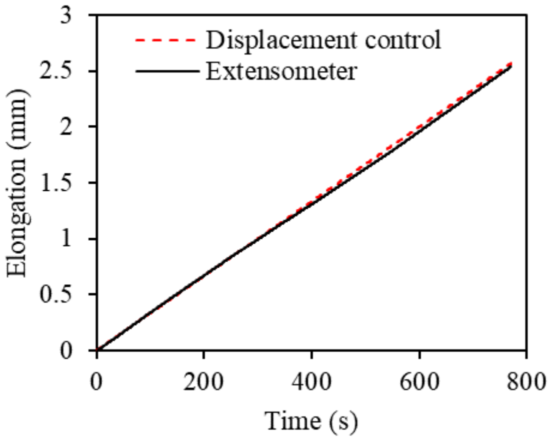

Figure 2.3.2. Comparison of the elongations measured by load frame and the extensometer.

2.3.2.3. Investigated cases

This research investigates the effects of the coating thickness, spatial resolution, and spacing between adjacent cracks. A total of 11 cases were investigated, as listed in Table 2.3.1, including 3 coating thicknesses (242 µm, 650 µm, and 900 µm), 3 spatial resolutions (0.65 mm, 1.3 mm, and 2.6 mm), and 6 spacings between adjacent cracks (100 mm, 150 mm, 200 mm, 300 mm, 400 mm, and 500 mm). The control case uses a bare fiber (coating thickness: 242 µm) and the spatial resolution of 0.65 mm. In each case, three tests were duplicated.

Table 2.3.1. Investigated cases

Cases	Coating thickness (µm)	Spatial resolution (mm)	Crack spacing (mm)
1 (control)	242	0.65	-*
2	650	0.65	-
3	900	0.65	-
4	242	1.30	-
5	242	2.60	-
6	242	0.65	500
7	242	0.65	400
8	242	0.65	300
9	242	0.65	200
10	242	0.65	150
11	242	0.65	100

* Note: Cases 1-5 investigated the effects of coating thickness and spatial resolution on measurement of single cracks. Therefore, the crack spacing is not applicable. Cases 6-11 investigated the effect of the spacing between two adjacent cracks.

2.3.2.4. Experimental results

Figure 2.3.3 shows the results of the strain distributions measured from the DFOS in the 11 cases. For each case, the strain distributions were measured under different crack widths. Representative strain distributions for selecting crack widths are included. Figures 2.3.3(a) to 2.3.3(e) show the strain distributions measured from the different DFOS in the single crack scenario. The legend shows the crack width.

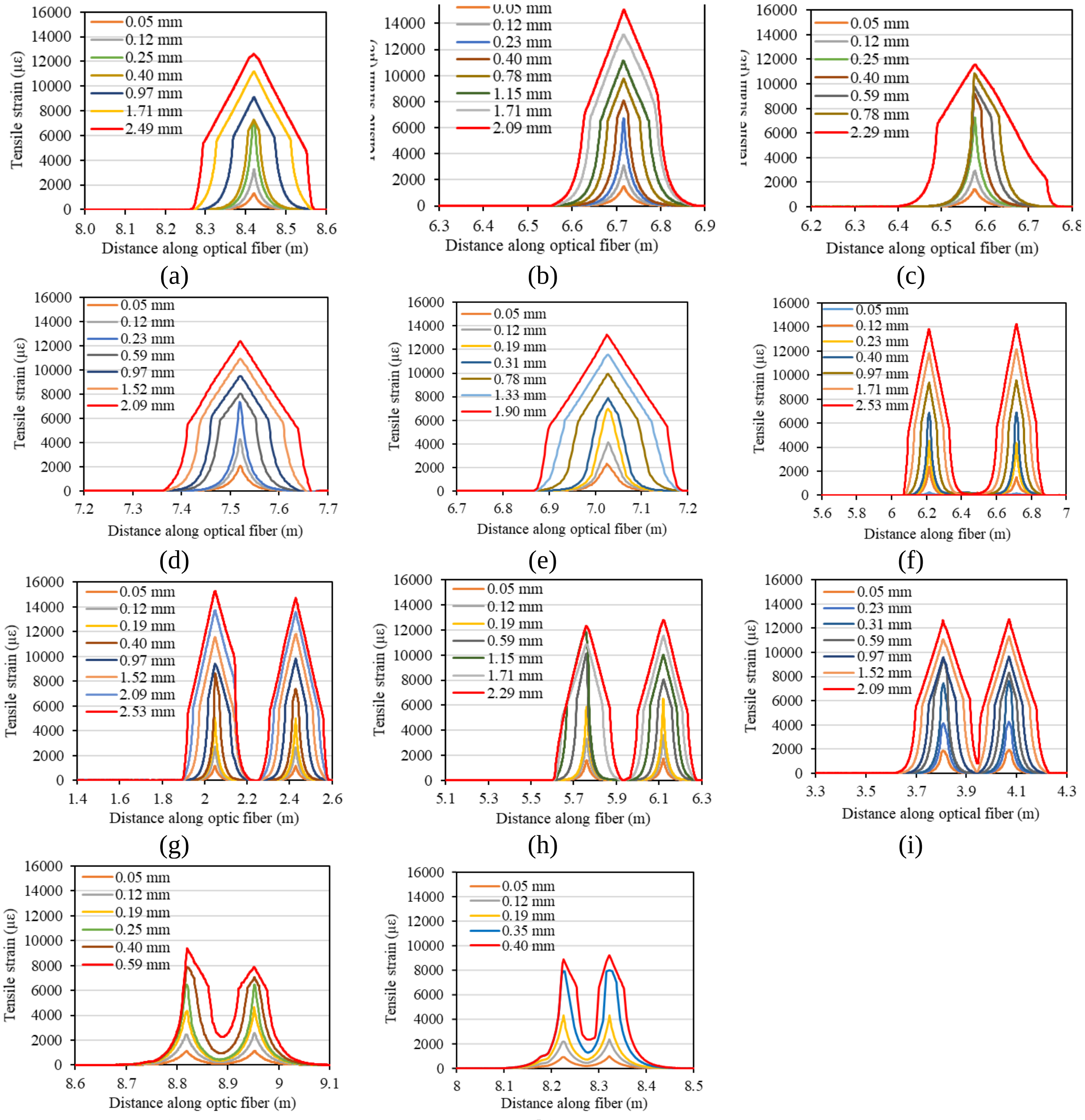

Figure 2.3.3. Representative strain distributions measured from DFOS: (a) Case 1; (b) Case 2; (c) Case 3; (d) Case 4; (e) Case 5; (f) Case 6; (g) Case 7; (h) Case 8; (i) Case 9; (j) Case 10; and (k) Case 11.

Figure 2.3.3(a) shows the measured strain distributions in the control case. The peak indicates the location of the crack. The strain distributions are symmetrical to the peak. The development of the strain distribution can be divided into three stages: (1) Crack initiation: a sharp peak is measured at the location of the crack, and the corresponding crack width is increased from 0 mm to 0.25 mm. (2) Debonding: the strain peak is widened with the increase of the crack width, due to debonding in the optical fiber. Due to debonding, the abrupt elongation of the optical fiber at the crack was averaged over a longer length, reducing the peak strain. The corresponding crack width ranges from 0.25 mm to 2.49 mm. (3) Slipping: The debonding length propagates along the fiber length. Eventually, after the debonding length is significantly developed, the DFOS fails to provide further measurement.

Figures 2.3.3(b) and 2.3.3(c) show the results of strain distributions measured from the fiber optic sensors with the coating thicknesses of 650 µm and 900 µm, respectively. The strain distributions measured from the sensor with a coating thickness of 650 µm are approximately symmetrical to the location of the crack, while the strain distributions measured from the sensor with a coating thickness of 900 µm are not symmetrical to the location of the crack after debonding occurs. That is because debonding in the sensor with a coating thickness of 900 µm is not symmetrical, which can be attributed to the interfacial properties associated with the fabrication of the optical fiber. The bond strength in the optical fiber at one side of the crack can be higher than the bond strength in the optical fiber at the other side of the crack.

Figures 2.3.3(d) and 2.3.3(e) show the results of strain distributions measured from bare fibers with spatial resolutions of 1.3 mm and 2.6 mm, respectively. Compared with the measurement results shown in Figure 2.3.3(f) for the spatial resolution of 0.65 mm, the change of the spatial resolution does not change the trend and the magnitude of the strain distribution at the crack.

Figures 2.3.3(f) to 2.3.3(k) show the strain distributions from bare fibers with a spatial resolution of 0.65 mm in the multiple crack scenario, and the spacing of the two adjacent cracks is 500, 400, 300 200, 150, and 100 mm, respectively. When the crack spacings are 500 mm (Figure 2.3.3(f)), 400 mm (Figure 2.3.3(g)) and 300 mm (Figure 2.3.3(h)), both cracks are detected in the strain distributions measured by the same optical fiber throughout the loading process. Two peaks are identified in the strain distribution along the fiber length, and there is no interference with each other as the crack width increases. When the spacing between the two cracks is reduced to 200 mm (Figure 2.3.3(i)), there is no interference between the two cracks when the crack width is small; however, after the crack width is increased to 2.09 mm, there is a small overlap at the edges of the lobes of the strain distributions corresponding to the two cracks. While a small overlap does not highly affect the measurement results of crack width, however, a large overlap may significantly influence the measurement results. When the spacing between the two cracks is reduced to 150 mm (Figure 2.3.3(j)), the strain distributions for the two cracks are affected by the presence of each other. Overlap of the peaks for the two cracks can be observed at a narrower crack width. Consistent observations can be obtained when the spacing between the two cracks is further reduced to 100 mm (Figure 2.3.3(k)). Therefore, the maximum crack width that can be measured by a single DFOS is dependent on the spacing between two adjacent cracks.

2.3.2.5. Discussions

2.3.2.5.1. Quantification of crack width

According to the definition of strain, the elongation of the optical fiber due to the crack opening is reflected by the strain distribution measured by the optical fiber, and the elongation of the aluminum plates can be described by the strain in the plates. In this case, the strain of the aluminum plate is negligible. Therefore, the crack width can be considered to be equivalent to the integration of the strain peak corresponding to the crack, as illustrated in Figure 2.3.4. The aluminum plates are shown in grey color. The optical fiber free of strain change is shown in green color, and the optical fiber subjected to strain change due to the crack is shown in purple color.

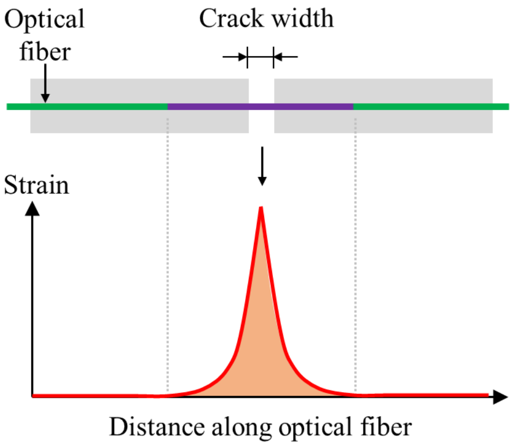

Figure 2.3.4. Illustration of the strain distribution in an optical fiber before debonding occurs.

Therefore, the crack width can be calculated based on the strain distributions measured from the DFOS. Figure 2.3.5(a) plots the crack widths calculated by the integration of strains, and compares the results against the crack widths measured from the extensometer. The results from the DFOS and the extensometer agree well with each other. A straight line can be used to fit the data, and the coefficient of determination is 0.9996, which indicates a high correlation. The measurement error of crack width by the DFOS is defined based on mean absolute deviation [50], as described in Eq. (2.3.1):

$$\text{Error} = \frac{1}{n}\sum_{i=1}^{n}\sqrt{\left(w_{\text{Measurement},i} - w_{\text{Real},i}\right)^2} \tag{2.3.1}$$

where n is the total number of data points; $w_{\text{Measurement},i}$ is the crack width measured from the DFOS; and $w_{\text{Real},i}$ is regarded as the real crack width measured from the extensometer. $w_{\text{Measurement},i}$ and $w_{\text{Real},i}$ are expressed as follows:

$$w_{\text{Measurement},i} = \frac{w_{\text{DFOS},i}}{k} \tag{2.3.2a}$$

$$w_{\text{Real},i} = w_{\text{E},i} \tag{2.3.2b}$$

where n is the total number of data points; $w_{\text{DFOS},i}$ is the crack width measured from the DFOS; and $w_{\text{E},i}$ is the crack width measured from the extensometer; and k is the slope of the linear fitting curve, which is 1.019, as shown in Figure 2.3.5(a).

A method proposed in prior research on quantifying crack width is introduced for comparison with the forementioned method. The magnitude of strain peak is correlated to the crack width [51], as shown in Figure 2.3.5(b). The data points show a transition behavior, which can be attributed to the occurrence of debonding in the optical fiber. At the crack widths about 0.3 mm, as marked by the green circle, the trend of the curve is significantly changed, because the strain transfer behavior between the matrix and the optical fiber is altered after debonding occurs.

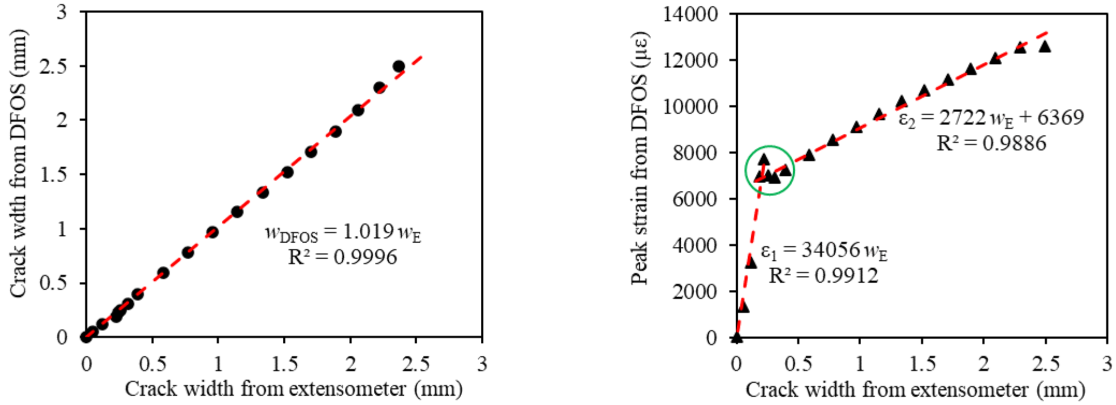

(a) (b)

Figure 2.3.5. Quantification of crack width: (a) correlation between the crack widths determined by the DFOS and the extensometer; and (b) correlation between the magnitude of peak strain and the crack width measured from the extensometer.

Due to the transition behavior, two lines are used to fit the data points [51]. The first line is used to describe the relationship before debonding, and the second line is used to describe the relationship after debonding. Eq. (2.3.2) is used to evaluate the measurement accuracy, where $w_{\mathrm{Measurement},i}$ and $w_{\mathrm{Real},i}$ are respectively expressed in Eq. (2.3.3a) and Eq. (2.3.3b):

$$w_{\mathrm{Measurement},i} = \frac{\varepsilon_{m,i}}{k_m} \tag{2.3.3a}$$

$$w_{\mathrm{Real},i} = w_{\mathrm{E},i} \tag{2.3.3b}$$

where n is the total number of data points; $\varepsilon_{m,i}$ is the peak strain measured from the DFOS; k_m is the slope of the fitting line, as shown in Figure 2.3.5(b); $w_{\mathrm{E},i}$ is the crack width measured from the extensometer; and m is the number of the segment for the bi-linear fitting curve (m = 1 for the first segment, and m = 2 for the second segment).

2.3.2.5.2. Effects of coating thickness

Figure 2.3.6(a) shows the crack widths measured from the DFOS with different coating thicknesses. The crack width was calculated by the integration of strain distributions. The measurement results follow linear trends, although the slopes of the different fibers are slightly different. Figure 2.3.6(b) compares the results of peak strains measured from the optical fibers with different coating thicknesses. A bi-linear correlation between the crack widths and the magnitude of the peaks is used to estimate the crack widths. Different optical fibers show different transition points, and the peak strain values are significantly different after the transition points. When the optical fibers have different coating thicknesses, the slopes of the first line are almost the same, but the slopes of the second line are different. The errors of the different optical fibers and methods are compared in Figure 2.3.6(c). With presented method for determining crack width, the measurement errors are 18 μm, 5.6 μm, and 19 μm for the coating thicknesses of 242 μm, 650 µm, and 900 µm, respectively. With prior method based on the peak strain, measurement errors are 47 µm, 39 µm, and 51 µm for the coating thicknesses of 242 µm, 650 µm, and 900 µm, respectively. At each coating thickness, the presented method shows higher accuracy.

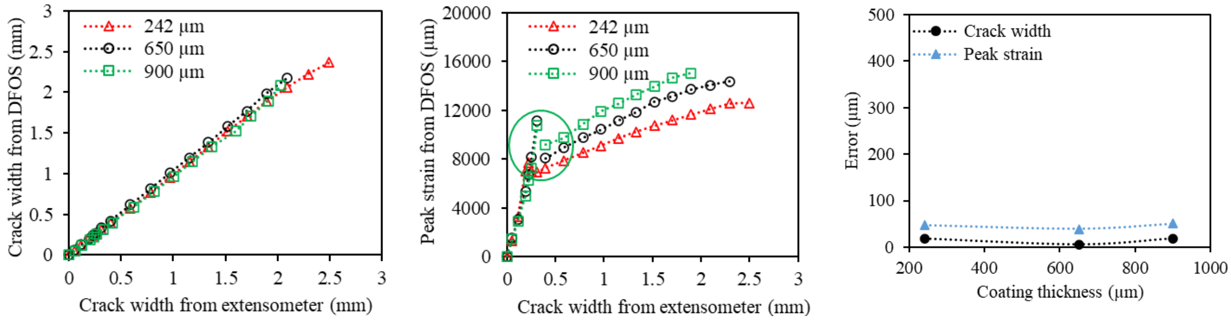

(a) (b) (c)

Figure 2.3.6. Effects of coating thickness: (a) comparison of measurement results of the crack width from the sensors with different coating thicknesses; (b) comparison of measurement results of the peak strain from the sensors with different coating thicknesses; and (c) measurement accuracy of the crack width.

2.3.2.5.3. Effects of spatial resolution

Figure 2.3.7(a) compares the crack widths measured from the DFOS with different spatial resolutions, and the crack widths were determined by the integration of the strain distributions. As the spatial resolution changes from 0.65 mm to 2.6 mm, the slope of the curve decreases from 1.0 to 0.8. Figure 2.3.7(b) compares the results of peak strains measured from the DFOS with different spatial resolutions. The different optical fibers show different transition points, and the peak strain values are different after the transition points.

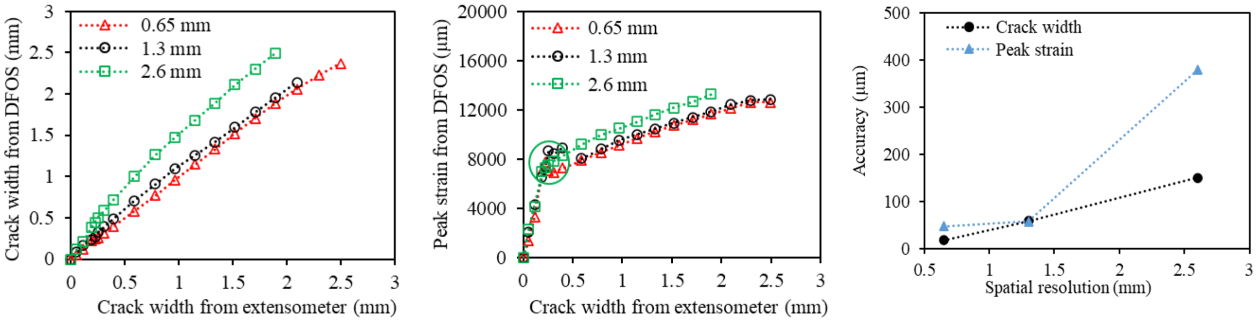

(a) (b) (c)

Figure 2.3.7. Parametric study of effects of spatial resolution: (a) relationship between integration results and the crack width detected with 0.65 mm, 1.3 mm, and 2.6 mm spatial resolution, respectively; and (c) measurement accuracy of crack width of different spatial resolutions.

Figure 2.3.7(c) shows that the accuracy of the crack width is dependent on the spatial resolution of the DFOS. With present method, as the spatial resolution changes from 0.65 mm to 2.6 mm, the error is increased from 18 µm to 151 µm. With the prior method based on the peak strain, as the spatial resolution changes from 0.65 mm to 2.6 mm, the error is increased from 47 µm to 379 µm.

2.3.2.5.4. Effects of crack spacing

When there are multiple cracks, different cracks may interfere with each other. With a small spacing between adjacent cracks, as the crack width increases, the peak strains corresponding to the two cracks can have an overlap in the middle. The overlap has adverse effects on the measurement accuracy of the crack width. Figure 2.3.8(a) shows the effects of the crack spacing on the accuracy. As the crack width increases, the accuracy of crack width is compromised, and the decrease of the spacing between cracks aggravates the accuracy.

Given a required accuracy of 50 µm, the maximum measurable crack width is determined, as plotted against the spacing between cracks in Figure 2.3.8(b). Overall, the maximum measurable crack width increases with the spacing between cracks. When the spacing is increased from 100 mm to 400 mm, the maximum measurable crack width is increased from 0.05 mm to 2.29 mm. The relationship between the maximum crack width and crack spacing can be fitted with a parabolic equation. However, after the spacing between cracks is larger than 400 mm, further increasing the spacing will not affect the maximum measurable crack width, because there will be no interference between cracks.

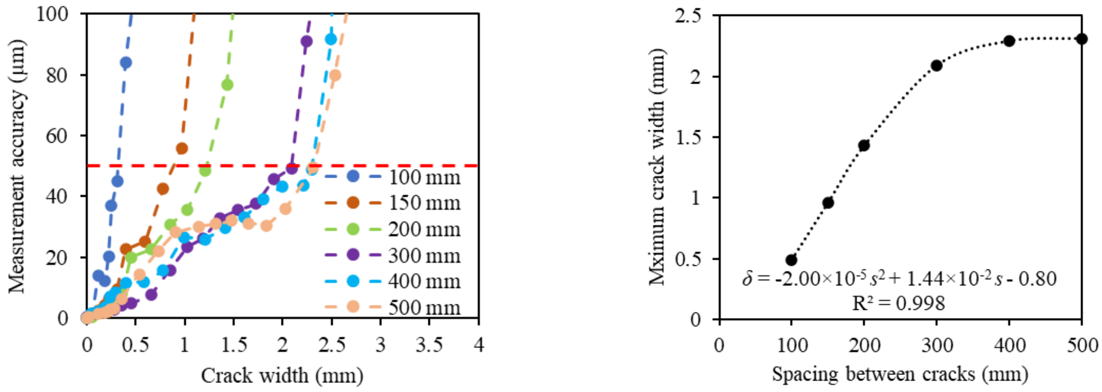

(a) (b)

Figure 2.3.8. Effect of crack spacing on: (a) measurement accuracy; and (b) measurable crack width. The crack spacing and measurable crack width are s and δ, respectively.

2.3.3. Summary

Based on the above investigations, the following findings can be drawn:

(1) Crack widths were measured using the proposed method at micro to macro scales in the cracking process. The initiation and development of cracks can be detected, located, and quantified by analyzing strain distributions measured from the DFOS. The measurement accuracy of crack width can be as high as 5.6 µm.

(2) The proposed measurement method provides better accuracy and linearity of crack width than the prior methods based on the correlation between the peak strain and crack width. The proposed method is not prone to possible debonding in the optical fibers and shows desired robustness in the measurement of crack width throughout the crack process.

(3) With the proposed method, the measurement accuracy of the crack width is less sensitive to the thickness of protective coatings of the different types of optical fibers with different packages, compared with the prior method based on the correlation between the peak strain and crack width. The measurement accuracy can be compromised by using optical fibers with thick coatings.

(4) The measurement accuracy of the crack width is dependent on the spatial resolution of the strain distribution. When the spatial resolution is increased from 0.65 mm to 1.3 mm, the error is increased from 18 μm to 151 μm. When the spatial resolution is increased from 1.3 mm to 2.6 mm, the error is increased from 47 μm to 379 μm.

(5) Multiple cracks can be located and quantified using a single DFOS. Increasing the spacing between the cracks tends to improve the measurement accuracy of crack width. Under a given accuracy of crack width, the derived parabolic equation can be used to assess the maximum measurable crack width.

The utilization of a distributed fiber optic sensor for monitoring cracks in a pipe subjected to various cracking mechanisms is illustrated in Figure 2.3.9. The method developed for monitoring cracks in this project is a general method based on strain measurements, which can be applied to different types of pipe cracks caused by different cracking mechanisms. When a distributed fiber optic sensor is installed in a helix pattern on the surface of the pipe, the sensor captures the various types of cracks, as long as the crack affects the strains in the distributed sensor. The cracks can be axial or circumferential cracks. The above research has shown that the distributed fiber optic sensor is sensitive to cracks from micro- to macro-scale because microcracks can also cause changes in the strain field of the pipe. Regarding the concerns about potential breakage of the sensor cable due to the tension force by pipe outside diameter expansion at a result of cracks formed in the pipe wall, packaged distributed fiber optic sensors have shown high performance in self-protection via a interfacial debonding mechanism, as elaborated in section 2.4.

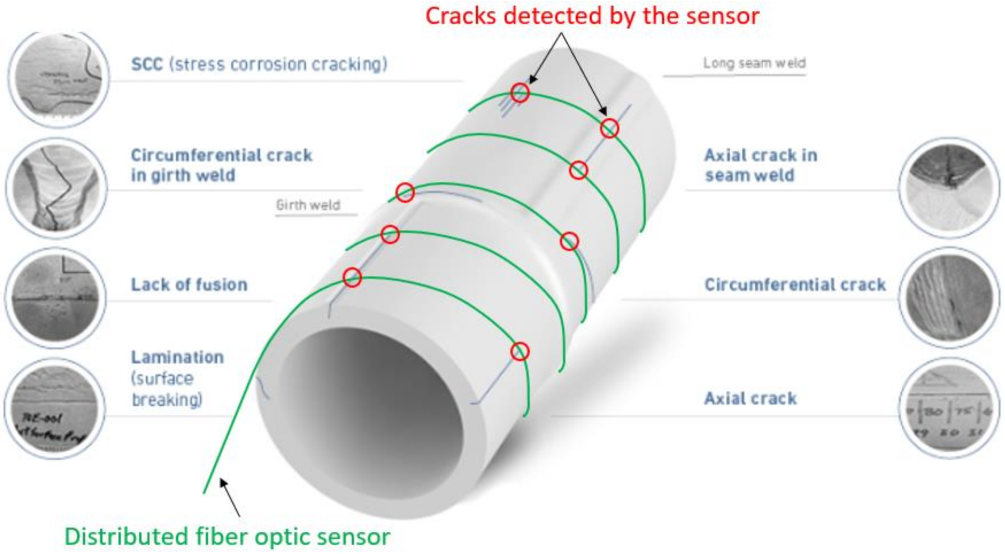

Figure 2.3.9. Monitoring of cracks in a pipe instrumented with distributed fiber optic sensor on the surface.

2.4. Interfacial mechanics of distributed sensors undergoing debonding

2.4.1. Interfacial debonding effect

Recent research showed that DFOS were applicable in the presence of fiber-coating interface debonding [52, 53], and the interface debonding showed benefits for fiber optic sensors [54]. Figure 2.4.1 shows a fiber optic cable embedded in a matrix subject to tensile forces. As the matrix is cracked, debonding occurs between the fiber and protective coating. The stresses in the fiber are re-distributed over a debonding length along the fiber to accommodate the localized deformation at the crack opening, thus reducing the peak tensile stress in the fiber and protecting the fiber from rupture [55]. The debonding helps avoid rupture of DFOS crossing cracks [52, 56]. Debonding is essential for using DFOS in structural health monitoring because the occurrence of discontinuity such as cracks [52, 56] and delamination [57] in host structures is unavoidable in practice.

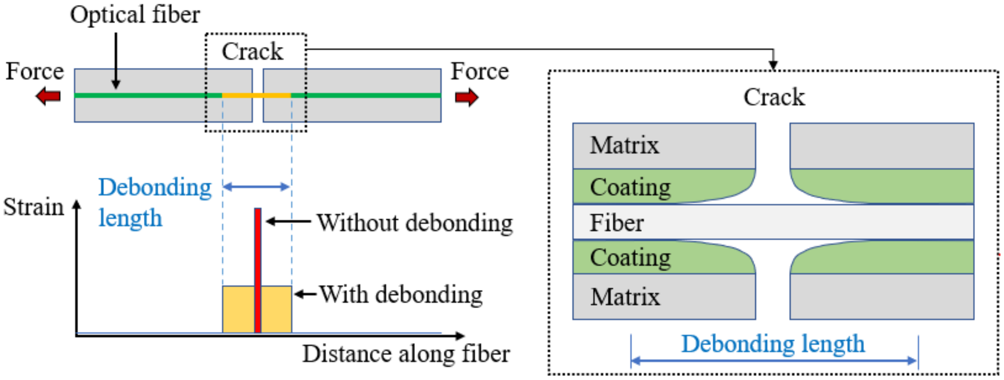

Figure 2.4.1. Debonding at fiber-coating interface to avoid the rupture of DFOS across a crack.

Currently, there is lack of knowledge on the fiber-coating interfacial behavior [48]. Previous research on the interfacial strain transfer of fiber optic sensors focused on the elastic stage, lacking consideration of interfacial debonding. The strain transfer of a fused silica fiber with polymeric coating was studied in references [24-26]. It was assumed that the fused silica fiber was exposed to constant shear stress at the fiber-coating interface when debonding occurred [48]. However, the derived strain distributions in fused silica fibers were inconsistent with the strain distributions measured from high-resolution distributed sensors [27]. Multiple challenges have been identified from previous research: (1) The fiber-coating interfacial behavior is unclear, hindering accurate interpretation of sensor data. (2) It is difficult to determine the interfacial properties of sensors. Existing research on the interface laws relies on trial-and-error methods with limited efficiency and accuracy. The parameters were manually selected in references [58, 59]. When there are many parameters, it will be challenging to obtain parameters using trial-and-error methods. In a nutshell, the interfacial bond-slip behavior of optical fibers is still unclear. When a distributed sensor is used to measure strains, the following questions need to be answered: (1) When will debonding be initiated between the fiber and coating? (2) How will the debonding propagate at the interface? (3) How will the debonding affect the strain distribution in fused silica fiber under the strain transfer effect? These knowledge gaps have stalled wider applications of distributed sensors because it is unknown how to properly interpret the distributed strain sensing data in the presence of cracks.

Motivated by the challenges, this research has three main objectives: (1) to develop a unified cohesive interface law (CIL) and a mechanical model to describe the interfacial behaviors; (2) to understand the fiber-coating interfacial behavior for DFOS; and (3) to utilize DFOS to measure the strain distributions in fused silica fiber in presence of interfacial debonding. To this end, this research performed a mechanical analysis on the fiber-coating interface based on the CIL and intrinsically linked the CIL to the force-slip results in the fiber pullout process. The link was then used to calibrate the parameters of the CIL perform through a metaheuristic inverse analysis. Strain distributions in the fused silica fiber were directly measured using a fully DFOS technology.

The novelties of this research include three aspects: (1) This research proposes a unified CIL to describe the fiber-matrix interface and derived closed-form solutions. (2) This research presents a metaheuristic inverse analysis to enable automatic determination of interfacial parameters. (3) The proposed CIL and analytical solutions are validated by measurements from DFOS. A unique feature of this research is that the research on interface mechanics and DFOS is integrated via metaheuristic inverse analysis.

2.4.2. Methods

2.4.2.1. Framework

Figure 2.4.2 shows the research framework. The black arrows show the flow of solving the problems in previous research, and the interface law is the key to addressing the challenges. The interface law is evaluated via fiber pullout response, and the relation is established through a forward mechanical analysis. This research presents a unified CIL and proposes to determine the interface law using fiber pullout test through metaheuristic inverse analysis.

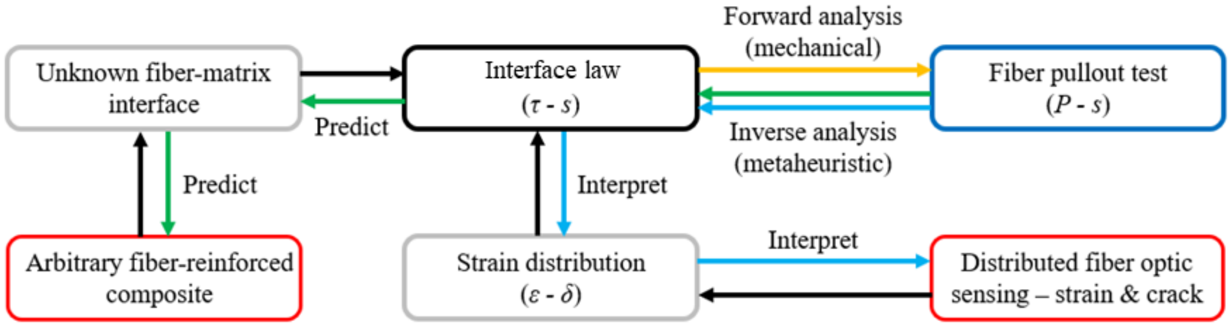

Figure 2.4.2. Framework integrating forward analysis, inverse analysis, and DFOS for strains and cracks.

With the interface law, on one hand, the interface law is utilized to interpret the bond-slip behavior of the fiber-coating interface for fiber optic sensors, thus enabling DFOS to measure cracks in presence of interfacial debonding. The interface law is utilized to predict the strain distributions in fused silica fiber during the fiber pullout process, and the prediction results are evaluated using a DFOS. On the other hand, the proposed CIL is independent of the specific materials and applicable to different types of composites to predict mechanical properties of the unknown fiber-reinforced interface, as marked by the green arrows.

2.4.2.2. Mechanical analysis

2.4.2.2.2. Governing equation

Figure 2.4.3 shows an infinitesimal segment of a fiber embedded in a host matrix, which can be the adhesive (e.g., epoxy) used to attach the fiber to the surface of a pipe. The representative types of matrices for structures include the cementitious matrix such as mortar and the polymetric matrix such as epoxy resin. The optical fiber is composed of a fused silica fiber core and polymeric coating. The coating of the optical fiber is in direct contact with the matrix.

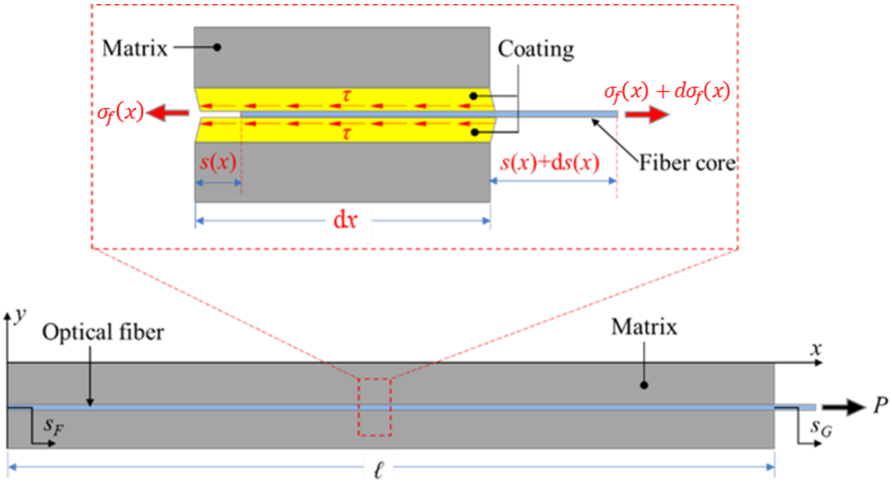

Figure 2.4.3. Infinitesimal segment of fiber embedded in a matrix and subjected to a pullout force.

When the matrix is fixed, the fused silica fiber is subjected to a pullout force P. The length of the optical fiber embedded in the matrix is ℓ (embedment length), and the diameter of the fused silica fiber core is D_f. The axial stress in the fiber core is $\sigma_f(x)$, where x is the coordinate along the fiber length. The interfacial slip between fiber core and coating is s. The elastic modulus and section area of the representative types of host matrix for engineering structures are often much larger than those of the fiber core and coating. Therefore, the matrix deformation is neglected. Since the interfacial slip varies along the fiber length, s is written as $s(x)$. The slip distances at the free end and the loaded end of the matrix are respectively denoted as $s_F = s(x = 0)$ and $s_G = s(x = \ell)$. The shear stress at the fiber-coating interface is a function of s and expressed as $\tau(s)$.

The equilibrium equation of the fused silica fiber along x direction is expressed as:

$$\sigma_f(x) \cdot A_f + \tau(s)dx \cdot p_f = \left[\sigma_f(x) + d\sigma_f(x)\right] \cdot A_f \tag{2.4.1a}$$

$$\sigma_c(x) \cdot A_c = \tau(s)dx \cdot p_f + [\sigma_c(x) + d\sigma_c(x)] \cdot A_c \tag{2.4.1b}$$

where $\sigma_c(x)$ and A_c are the axial stress in the coating and the cross-sectional area of coating, respectively; A_f and p_f are the cross-sectional area and perimeter of fiber core, respectively, which are expressed as:

$$A_f = \frac{1}{4}\pi {D_f}^2 \tag{2.4.2a}$$

$$p_f = \pi D_f \tag{2.4.2b}$$

Eq. (2.4.1) is rewritten as:

$$\frac{d\sigma_f(x)}{dx} = \frac{p_f}{A_f}\tau(s) \tag{2.4.3a}$$

$$\frac{d\sigma_c(x)}{dx} = -\frac{p_f}{A_c}\tau(s) \tag{2.4.3b}$$

According to the Hooke's Law, the relationship between the normal stress and strain along the fiber length is expressed in Eq. (2.4.4):

$$\sigma_f(x) = E_f\varepsilon_f(x) = E_f\frac{du_f(x)}{dx} \tag{2.4.4a}$$

$$\sigma_c(x) = E_c\varepsilon_c(x) = E_c\frac{du_c(x)}{dx} \tag{2.4.4b}$$

$$s(x) = u_f(x) - u_c(x) \tag{2.4.4c}$$

$$E_c = \frac{E_{ci}A_{ci} + E_{co}A_{co}}{A_{ci} + A_{co}} \tag{2.4.4d}$$

where E_f, E_{ci}, and E_{co} are the elastic moduli of the fiber core, inner coating, and outer coating, respectively; $u_f(x)$ and $u_c(x)$ are the displacement of fiber core and coating layers, respectively; A_{ci} and A_{co} are the cross-sectional areas of the inner and outer coatings, respectively.

Substituting Eq. (2.4.4) into Eq. (2.4.3) and Eq. (2.4.1), the governing equation is obtained:

$$\frac{d^2s(x)}{dx^2} - \lambda^2\tau(s) = 0 \tag{2.4.5a}$$

$$\frac{ds(x)}{dx} = \varphi\varepsilon_f(x) \tag{2.4.5b}$$

$$w_c = 2\left[u_f(\ell) - u_f(0)\right] = \frac{2}{\varphi}(s_G - s_F) = 2\int_0^{\ell}\varepsilon_f(x)dx \tag{2.4.5c}$$

where $\lambda = \sqrt{\frac{p_f\cdot\varphi}{E_fA_f}}$; $\varphi = \left(\frac{A_fE_f}{A_cE_c} + 1\right)$; and w_c refers to the crack width.

The boundary conditions at the free end are:

$$\varepsilon_f(x = 0) = 0 \tag{2.4.6a}$$

$$s(x = 0) = s_F \tag{2.4.6b}$$

The axial stress in the fiber core at the loaded end is expressed as:

$$\varepsilon_f(x = \ell) = \frac{P}{A_fE_f} \tag{2.4.7}$$

The governing equations describe the relationship between the interfacial slip and the shear stress [60]. Eq. (2.4.5c) provides a theoretical foundation for the quantification of crack widths using the interfacial slip or integration of the strain distribution in vicinity of the crack. The interfacial bond-slip law is needed to solve the governing equation of the interface law.

2.4.2.2.3. Unified CIL

This subsection presents a CIL to unify the bond-slip models of shear-softening and shear-hardening interfaces, as shown in Figure 2.4.4. The CIL has three main stages: (i) a linear-elastic stage, (ii) a yielding stage, and (iii) a debonding stage. In the linear-elastic stage, as the slip increases from 0 to αs_f $(0 < \alpha < 1)$, the shear stress linearly increases from 0 to $\beta\tau_f$. In the yielding stage, as the slip increases from αs_f to s_f, the shear stress linearly changes from $\beta\tau_f$ to τ_f. If $\beta > 1$, the CIL describes a linear softening behavior, meaning that the interfacial shear stress deceases in the yielding stage. If $\beta = 1$, the CIL describes a constant behavior. If $0 < \beta < 1$, the CIL describes a linear hardening behavior, meaning that the interfacial shear stress increases in the yielding stage. Finally, after the slip is larger than s_f, the debonding stage occurs, and the shear stress decreases with the interface slip exponentially.

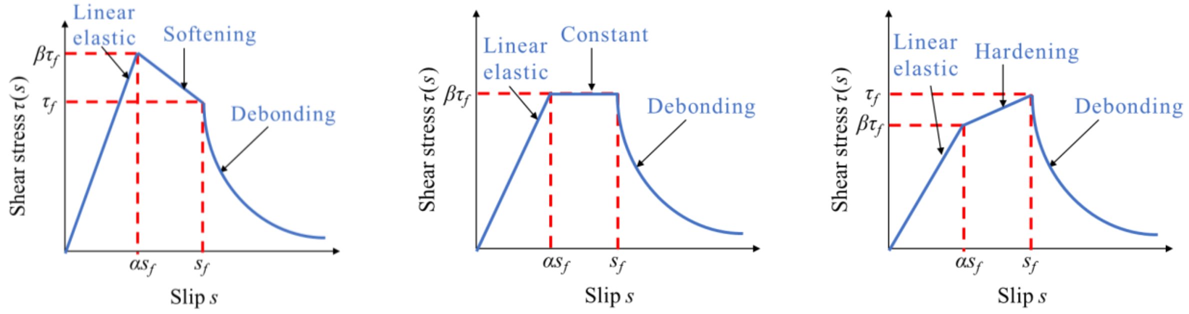

(a) (b) (c)

Figure 2.4.4. Illustration of CIL: (a) softening interface ($\beta > 1$)*; (b) constant interface* ($\beta = 1$)*; and (c) hardening interface* ($0 < \beta < 1$)*.*

The CIL is expressed as:

$$\tau(s) = \begin{cases} \dfrac{\beta\tau_f}{\alpha s_f}s & , \quad 0 \le s \le \alpha s_f \\ \dfrac{\tau_f}{1-\alpha}\left[\dfrac{(1-\beta)s}{s_f} + (\beta - \alpha)\right], & \quad \alpha s_f < s \le s_f \\ \tau_f e^{\frac{-\tau_f(s-s_f)}{k}} & , \quad s_f \le s \end{cases} \tag{2.4.8}$$

where τ_f, s_f, α, β, and k are the unknown parameters of the CIL to be calibrated; τ_f, s_f, and k are the bond strength, the slip corresponding to the bond strength, and interfacial fracture energy, respectively; α and β determine the separating point in the linear elastic ascending part of the CIL; β is of crucial importance in the CIL because β determines the type of the interface. With equation (2.4.8), the governing equation shown in Eq. (2.4.5) has been solved.

2.4.2.3. Metaheuristic inverse analysis

This section presents the metaheuristic inverse analysis method to accurately calibrate the parameters of the CIL, as illustrated in Figure 2.4.5. Past research showed that the force-slip curves of pullout tests were determined when a CIL was given through a forward analysis. However, the calibration of the model parameters is an inverse problem, which was usually solved through the trial-and-error method. Nevertheless, the trial-and-error method is inefficient and inaccurate, especially when there are multiple parameters that involve coupling effects. Inaccurate model parameters highly affect the analysis accuracy of interfacial behaviors.

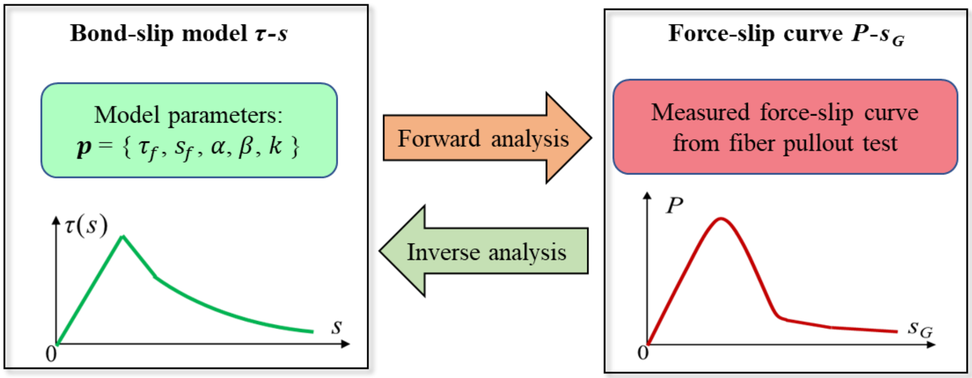

Figure 2.4.5. Comparison of the forward and inverse problems of the fiber pullout behavior.

This study proposes to solve the inverse problem using the hypotrochoid spiral algorithm. A set of initial values are assigned to the model. With the initial values, the analytical solutions of force-slip data are calculated based on the forward analysis. The calculation results are compared with the fiber pullout test results. The discrepancy between the calculation results and test results are obtained, and the hypotrochoid spiral algorithm is used to minimize the discrepancy by optimizing the model parameters. The objective function in the minimization is defined as $f(X)$:

$$f(X) = \frac{1}{n}\sum_{i=1}^{n} \mathrm{RMSE}[P(\ell_i, X), \Upsilon_i(s_{G_i})] \tag{2.4.9}$$

where X is the vector composed of the five parameters of CIL; the fiber embedded in the matrix is divided into n segments, and ℓ_i is the i-th length; $P(\ell_i, X)$ is the calculated pullout force corresponding to ℓ_i; s_{G_i} is the slip corresponding to ℓ_i; Υ_i is a fitted model to estimate the magnitude of the tested pullout force; and the root mean square error (RMSE) is defined as:

$$\mathrm{RMSE}(P, \Upsilon_i) = \sqrt{\frac{\sum_{i=1}^{n}(p_i - \nu_i)^2}{n}} \tag{2.4.10}$$

where $P = [p_1, p_2, \ldots, p_N]$ and $A = [\nu_1, \nu_2, \ldots, \nu_N]$ are the vectors for the calculated and tested values of the pullout forces, respectively.

The coefficient of determination (R^2) and the maximum absolute error (MAE) are also used to evaluate the accuracy of the inverse analysis:

$$\mathrm{R}^2 = 1 - \frac{\sum_{i=1}^{n}(p_i - \nu_i)^2}{\sum_{i=1}^{n}[\nu_i - \mathrm{mean}(\nu_i)]^2} \tag{2.4.11a}$$

$$\mathrm{MAE}(P, Y_i) = \frac{1}{n}\sum_{i=1}^{n}|p_i - \nu_i| \tag{2.4.11b}$$

The optimization algorithm was executed for 20 independent runs. The number of search agents was set to 50, and the optimization process was terminated when the number of iterations reached 500. After the five parameters α, β, τ_f, s_f, and k are determined through the inverse analysis, the CIL is determined and used to derive the force-slip curve, the slip distribution and shear stress distribution at the fiber-matrix interface, as well as the axial strain distribution of the fiber at an arbitrary slip level.

2.4.3. Analytical studies

Previous research showed that the fiber pullout process and the failure mode were dependent on the fiber length (ℓ) embedded in the matrix, and there was a critical embedment length (ℓ_0) for the fiber. The critical embedment length is the minimum length necessary to completely activate the whole CIL along embedded fiber length (ℓ) in the matrix.

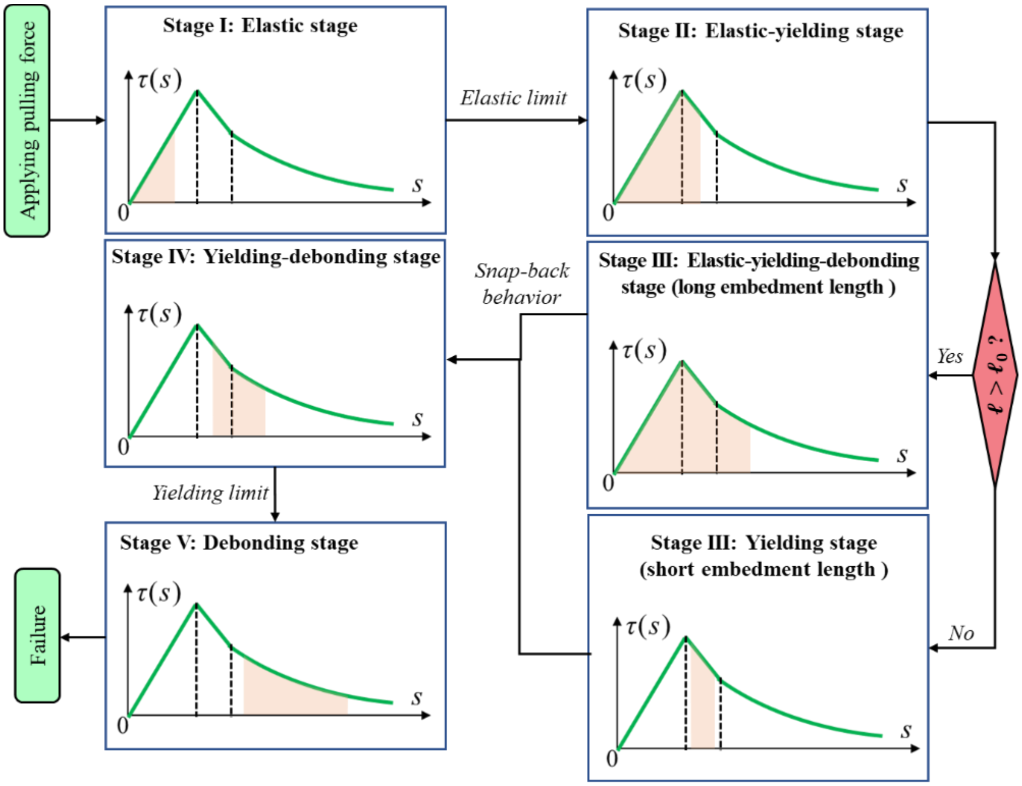

Figure 2.4.6. Five main stages of the fiber-matrix damage in the single fiber pullout process.

Based on the critical embedment length (ℓ_0), the pullout behavior is investigated in two cases: (1) Case 1: the embedment length is longer than the critical length ($\ell > \ell_0$). The pullout process in Case 1 included five stages, which are the elastic stage, elastic-yielding stage, elastic-yielding-debonding stage, yielding-debonding stage, and debonding stage. (2) Case 2: the embedment length is shorter than the critical length ($\ell < \ell_0$). The pullout process in Case 2 included five stages, which are the elastic stage, elastic-yielding stage, yielding stage, yielding-debonding stage, and debonding stage. The difference between the two cases is that the elastic-yielding-debonding stage in Case 1 is replaced by the yielding stage in Case 2.

Long embedment lengths enable the complete development of the interface capacity. Short embedment lengths undergo lower strain and load levels. Therefore, evaluation of the critical embedment length ℓ_0 is critical, considering that the failure mode of the fiber pullout test is fiber slip. Figure 2.4.6 shows the five main stages of the fiber-matrix interface damage in the single fiber pullout process. The mechanical behavior is related to the bonding length (ℓ), which is equal to the embedment length of the optical fiber in the matrix.

2.4.3.1. Case 1: Long embedment length ($\ell > \ell_0$)

With the CIL in Figure 2.4.4, the governing equation was solved to determine the slip, shear stress, and axial strain distributions along the embedded fiber length, as summarized in Table 2.4.1. ℓ_{el} and ℓ_{yd} are the elastic length and the yielding length, respectively, which are determined by the boundary conditions. The constants λ_1, λ_2, λ_3 and C_1 to C_6 were used to simplify the formulae.

The elastic, yielding, and debonding stages occur at the fiber-coating interface simultaneously only when the embedment length (ℓ) is longer than the critical embedment length (ℓ_0):

$$\ell_0 = \begin{cases} \dfrac{1}{\lambda_2}\cosh^{-1}\left(\dfrac{1}{\beta}\right), & \beta \neq 1 \\ \dfrac{1}{\lambda}\sqrt{\dfrac{2(1-\alpha)s_f}{\tau_f}}, & \beta = 1 \end{cases} \tag{2.4.18}$$

The elastic stage (Stage I) ends when $\tau(\ell) = \beta\tau_f$. The load and the corresponding loaded end slip at the end of the elastic stage are:

$$P_A = A_f E_f \frac{1}{\varphi}\lambda_1 \tanh(\lambda_1 \ell)\,\alpha s_f \tag{2.4.19a}$$

$$s_{G,A} = \alpha s_f \tag{2.4.19b}$$

The elastic-yielding stage (Stage II) ends when $\tau(\ell) = \tau_f$. The load and the corresponding loaded end slip at the end of the elastic-yielding stage are:

$$P_C = \begin{cases} A_f E_f \dfrac{1}{\varphi}\lambda_2 \dfrac{(1-\alpha)\beta s_f}{1-\beta}\sinh(\lambda_2 \ell), & \beta \neq 1 \\ A_f E_f \dfrac{1}{\varphi}\lambda^2 \tau_f \ell, & \beta = 1 \end{cases} \tag{2.4.20a}$$

$$s_{G,C} = \begin{cases} \dfrac{(1-\alpha)\beta s_f}{1-\beta}\cosh(\lambda_2 \ell) - \dfrac{\beta-\alpha}{1-\beta}s_f, & \beta \neq 1 \\ \dfrac{1}{2}\lambda^2 \tau_f \ell^2 + \alpha s_f, & \beta = 1 \end{cases} \tag{2.4.20b}$$

The elastic-yielding-debonding stage (Stage III) ends when $\tau(0) = \beta\tau_f$. The load and the loaded end slip at the end of elastic-yielding-debonding stage are:

$$P_D = A_f E_f \frac{1}{\varphi} \frac{2k}{\tau_f} \lambda_3 \sqrt{C_1} \tanh\left[\lambda_3 \sqrt{C_1} (\ell - C_2)\right], \quad (\text{when } \ell_{yd} = \ell_0) \tag{2.4.21a}$$

$$s_{G,D} = \frac{2k}{\tau_f} \ln\left\{\cosh\left[\lambda_3 \sqrt{C_3} (\ell - C_4)\right]\right\} - \frac{k}{\tau_f} \ln(C_3), \quad (\text{when } \ell_{yd} = \ell_0) \tag{2.4.21b}$$

The yielding-debonding stage (Stage IV) ends when $\tau(0) = \tau_f$. The load and the corresponding loaded end slip at the end of the elastic stage are shown in Eq. (2.4.22).

Table 2.4.1. Analytical solutions for long embedment length ($\ell < \ell_0$)

Stage	Analytical solutions
I	$s(x) = s_F \cosh(\lambda_1 x)$ (2.4.13a) $\tau(x) = \frac{\beta \tau_f}{\alpha s_f} s_F \cosh(\lambda_1 x)$ (2.4.13b) $\varepsilon_f(x) = \frac{1}{\varphi} \lambda_1 s_F \sinh(\lambda_1 x)$ (2.4.13c)
II	The solution at the region of $0 \le x \le \ell_{el}$: $s(x) = \alpha s_f \frac{\cosh(\lambda_1 x)}{\cosh(\lambda_1 \ell_{el})}$ (2.4.14a) $\tau(x) = \beta \tau_f \frac{\cosh(\lambda_1 x)}{\cosh(\lambda_1 \ell_{el})}$ (2.4.14b) $\varepsilon_f(x) = \frac{1}{\varphi} \lambda_1 \alpha s_f \frac{\sinh(\lambda_1 x)}{\cosh(\lambda_1 \ell_{el})}$ (2.4.14c) The solution at the region of $\ell_{el} \le x \le \ell$: $s(x) = \begin{cases} \frac{(1-\alpha)\beta s_f}{1-\beta} \cosh[\lambda_2(\ell_{el} - x)] - \frac{\lambda_1 \alpha s_f}{\lambda_2} \tanh(\lambda_1 \ell_{el}) \sinh[\lambda_2(\ell_{el} - x)] - \frac{\beta - \alpha}{1-\beta} s_f \;, & \beta \neq 1 \\ \frac{1}{2} \lambda^2 \tau_f (\ell_{el} - x)^2 - \lambda_1 \alpha_f \tanh(\lambda_1 \ell_{el}) \cdot (\ell_{el} - x) + \alpha s_f \;, & \beta = 1 \end{cases}$ (2.4.14d) $\tau(x) = \begin{cases} \beta \tau_f \cosh[\lambda_2(\ell_{el} - x)] - \frac{\alpha(1-\beta)\lambda_1 \tau_f}{(1-\alpha)\lambda_2} \tanh(\lambda_1 \ell_{el}) \sinh[\lambda_2(\ell_{el} - x)] \;, & \beta \neq 1 \\ \tau_f \;, & \beta = 1 \end{cases}$ (2.4.14e) $\varepsilon_f(x) = \begin{cases} \frac{1}{\varphi} \lambda_1 \alpha s_f \tanh(\lambda_1 \ell_{el}) \cosh[\lambda_2(\ell_{el} - x)] - \frac{1}{\varphi} \lambda_2 \frac{(1-\alpha)\beta s_f}{1-\beta} \sinh[\lambda_2(\ell_{el} - x)] \;, & \beta \neq 1 \\ -\frac{1}{\varphi} \lambda^2 \tau_f (\ell_{el} - x) + \frac{1}{\varphi} \lambda_1 \alpha_f \tanh(\lambda_1 \ell_{el}) \;, & \beta = 1 \end{cases}$ (2.4.14f)
III	The solution at the region of $0 \le x \le \ell_{el}$: $s(x) = \alpha s_f \frac{\cosh(\lambda_1 x)}{\cosh(\lambda_1 \ell_{el})}$ (2.4.15a) $\tau(x) = \beta \tau_f \frac{\cosh(\lambda_1 x)}{\cosh(\lambda_1 \ell_{el})}$ (2.4.15b) $\varepsilon_f(x) = \frac{1}{\varphi} \lambda_1 \alpha s_f \frac{\sinh(\lambda_1 x)}{\cosh(\lambda_1 \ell_{el})}$ (2.4.15c) The solution at the region of $\ell_{el} \le x \le \ell_{el} + \ell_{yd}$: $s(x) = \begin{cases} \frac{(1-\alpha)\beta s_f}{1-\beta} \frac{\sinh\left[\lambda_2\left(\ell_{el} + \ell_{yd} - x\right)\right]}{\sinh\left(\lambda_2 \ell_{yd}\right)} - \frac{(1-\alpha)s_f}{1-\beta} \frac{\sinh[\lambda_2(\ell_{el} - x)]}{\sinh\left(\lambda_2 \ell_{yd}\right)} - \frac{\beta - \alpha}{1-\beta} s_f, & \beta \neq 1 \\ \frac{1}{2} \lambda^2 \tau_f (\ell_{el} - x)\left(\ell_{el} + \ell_{yd} - x\right) - \frac{(1-\alpha)s_f}{\ell_{yd}} (\ell_{el} - x) + \alpha s_f, & \beta = 1 \end{cases}$ (2.4.15d)

Table 2.4.1. Analytical solutions for long embedment length ($\ell < \ell_0$)

Stage	Analytical solutions	
	$\tau(x) = \begin{cases} \beta\tau_f \frac{\sinh[\lambda_2(\ell_{el}+\ell_{yd}-x)]}{\sinh(\lambda_2\ell_{yd})} - \tau_f \frac{\sinh[\lambda_2(\ell_{el}-x)]}{\sinh(\lambda_2\ell_{yd})}, & \beta \neq 1 \\ \tau_f \quad , & \beta = 1 \end{cases}$	(2.4.15e)
	$\varepsilon_f(x) = \begin{cases} -\frac{1}{\varphi}\lambda_2 \frac{(1-\alpha)\beta s_f}{1-\beta} \frac{\cosh[\lambda_2(\ell_{el}+\ell_{yd}-x)]}{\sinh(\lambda_2\ell_{yd})} + \frac{1}{\varphi}\lambda_2 \frac{(1-\alpha)s_f}{1-\beta} \frac{\cosh[\lambda_2(\ell_{el}-x)]}{\sinh(\lambda_2\ell_{yd})}, & \beta \neq 1 \\ -\frac{1}{\varphi}\lambda^2\tau_f(\ell_{el}-x) - \frac{1}{2}\frac{1}{\varphi}\lambda^2\tau_f\ell_{yd} + \varphi\frac{(1-\alpha)s_f}{\ell_{yd}} \quad , & \beta = 1 \end{cases}$	(2.4.15f)
	The solution at the region of $\ell_{el}+\ell_{yd} \leq x \leq \ell$:	
	$s(x) = \frac{2k}{\tau_f}\ln\{\cosh[\lambda_3\sqrt{C_1}(x-C_2)]\} - \frac{k}{\tau_f}\ln(C_1)$	(2.4.15g)
	$\tau(x) = \frac{C_1\tau_f \cdot e^{\frac{\tau_f s_f}{k}}}{\cosh^2[\lambda_3\sqrt{C_1}(x-C_2)]}$	(2.4.15h)
	$\varepsilon_f(x) = \frac{1}{\varphi}\frac{2k}{\tau_f}\lambda_3\sqrt{C_1}\tanh[\lambda_3\sqrt{C_1}(x-C_2)]$	(2.4.15i)
IV	The solution at the region of $0 \leq x \leq \ell_{yd}$:	
	$s(x) = \begin{cases} \frac{1-\alpha}{1-\beta}s_f\frac{\cosh(\lambda_2 x)}{\cosh(\lambda_2\ell_{yd})} - \frac{\beta-\alpha}{1-\beta}s_f, & \beta \neq 1 \\ \frac{1}{2}\lambda^2\tau_f(x^2-{\ell_{yd}}^2)+s_f \quad , & \beta = 1 \end{cases}$	(2.4.16a)
	$\tau(x) = \begin{cases} \tau_f\frac{\cosh(\lambda_2 x)}{\cosh(\lambda_2\ell_{yd})}, & \beta \neq 1 \\ \tau_f \quad , & \beta = 1 \end{cases}$	(2.4.16b)
	$\varepsilon_f(x) = \begin{cases} \frac{1}{\varphi}\lambda_2\frac{1-\alpha}{1-\beta}s_f\frac{\sinh(\lambda_2 x)}{\cosh(\lambda_2\ell_{yd})}, & \beta \neq 1 \\ \frac{1}{\varphi}\lambda^2\tau_f x \quad , & \beta = 1 \end{cases}$	(2.4.16c)
	The solution at the region of $\ell_{yd} \leq x \leq \ell$:	
	$s(x) = \frac{2k}{\tau_f}\ln\{\cosh[\lambda_3\sqrt{C_3}(x-C_4)]\} - \frac{k}{\tau_f}\ln(C_3)$	(2.4.16d)
	$\tau(x) = \frac{C_3\tau_f \cdot e^{\frac{\tau_f s_f}{k}}}{\cosh^2[\lambda_3\sqrt{C_3}(x-C_4)]}$	(2.4.16e)
	$\varepsilon_f(x) = \frac{1}{\varphi}\frac{2k}{\tau_f}\lambda_3\sqrt{C_3}\tanh[\lambda_3\sqrt{C_3}(x-C_4)]$	(2.4.16f)
V	$s(x) = \frac{2k}{\tau_f}\ln\{\cosh[\lambda_3\sqrt{C_5}(x-C_6)]\} - \frac{k}{\tau_f}\ln(C_5)$	(2.4.17a)
	$\tau(x) = \frac{C_5\tau_f \cdot e^{\frac{\tau_f s_f}{k}}}{\cosh^2[\lambda_3\sqrt{C_5}(x-C_6)]}$	(2.4.17b)
	$\varepsilon_f(x) = \frac{1}{\varphi}E_f\frac{2k}{\tau_f}\lambda_3\sqrt{C_5}\tanh[\lambda_3\sqrt{C_5}(x-C_6)]$	(2.4.17c)

$$P_E = A_f E_f \frac{1}{\varphi}\frac{2k}{\tau_f}\lambda_3 e^{-\left(\frac{\tau_f s_f}{2k}\right)} \tanh\left(\lambda_3 e^{-\left(\frac{\tau_f s_f}{2k}\right)} \ell\right) \tag{2.4.22a}$$

$$s_{G,E} = \frac{2k}{\tau_f}\ln\left[\cosh\left(\lambda_3 e^{-\left(\frac{\tau_f s_f}{2k}\right)} \ell\right)\right] + s_f \tag{2.4.22b}$$

2.4.3.2. Case 2: Short embedment length ($\ell < \ell_0$)

When the embedment length of fiber is shorter than the critical embedment length ($\ell < \ell_0$), the elastic-yielding-debonding stage in Case 1 is replaced by a yielding stage. The other stages in Cases 1 and 2 are the same, so they are not duplicated. This section only elaborates the yielding stage (Stage III), and the corresponding formulae of slip, shear stress, and axial strain distributions along the embedded fiber length are summarized in Table 2.4.2.

Table 2.4.2. Analytical solutions for short embedment length ($\ell < \ell_0$)

Stage	Analytical solutions	
III	$s(x) = \begin{cases} \left(s_F + \frac{\beta - \alpha}{1 - \beta} s_f\right)\cosh(\lambda_2 x) - \frac{\beta - \alpha}{1 - \beta} s_f\,, & \beta \neq 1 \\ \frac{1}{2}\lambda^2 \tau_f x^2 + s_F\,, & \beta = 1 \end{cases}$	(3.23a)
	$\tau(x) = \begin{cases} \left[\frac{(1 - \beta)\tau_f}{(1 - \alpha)s_f} s_F + \frac{\beta - \alpha}{1 - \alpha}\tau_f\right]\cosh(\lambda_2 x)\,, & \beta \neq 1 \\ \tau_f\,, & \beta = 1 \end{cases}$	(3.23b)
	$\varepsilon_f(x) = \begin{cases} \varphi\lambda_2\left(s_F + \frac{\beta - \alpha}{1 - \beta} s_f\right)\sinh(\lambda_2 x)\,, & \beta \neq 1 \\ \varphi\lambda^2 \tau_f x\,, & \beta = 1 \end{cases}$	(3.23c)

The yielding stage (Stage III) is ended when $s_{G,D} = s_f$. The corresponding load at the end of the yielding stage is:

$$P_D = \begin{cases} \varphi A_f E_f \left(\frac{1 - \alpha}{1 - \beta}\right) s_f \lambda_2 \tanh(\lambda_2 \ell)\,, & \beta \neq 1 \\ \varphi A_f E_f \lambda^2 \tau_f \ell\,, & \beta = 1 \end{cases} \tag{2.4.24}$$

2.4.3.3. Analytical results

Based on the unified CIL and analytical solutions, the shear stress distributions along the interface are obtained by solving the governing equation at each loading stage. Figure 2.4.7 illustrates the evolution of the interfacial shear stress when the embedment length is longer than the critical embedment length ($\ell > \ell_0$).

The evolution of the interfacial shear stresses for a long embedment length is characterized by five stages. In the first stage, the load-displacement response is linear elastic. The shear stress distributions along the interface are shown in Figure 2.4.7(a) and Figure 2.4.7(b). At the end of the elastic stage, a portion of the interface enters the yielding stage, while the remaining portion is still in the elastic stage. The corresponding shear stress distributions along the interface are depicted in Figure 2.4.7(c) and Figure 2.4.7(d). Specifically, the parameter β has a significant effect on the shear stress distribution. When $\beta > 1$, the shear stress distribution shows a softening effect for the portion of interface in the yielding stage; when $\beta = 1$, the shear stress distribution is constant; and when $0 < \beta < 1$, the shear stress distribution shows a hardening effect. At the end of the elastic-yielding stage, a portion of the interface enters the debonding stage, while the remaining part is still in the elastic-yielding stage. The corresponding shear stress distributions along the interface are depicted in Figure 2.4.7(e) and Figure 2.4.7(f). In the elastic-yielding-debonding stage, the applied force increases due to the debonding at the interface. At the end of the elastic-yielding-debonding stage, there is no elastic stage at the interface. The shear stress distributions are shown in Figure 2.4.7(g) and Figure 2.4.7(h). At the end of the yielding-debonding stage, the shear stress is equal to the bond strength (τ_f) at the free end. Finally, Figure 2.4.7(i) depicts the shear stress distribution at debonding stage.

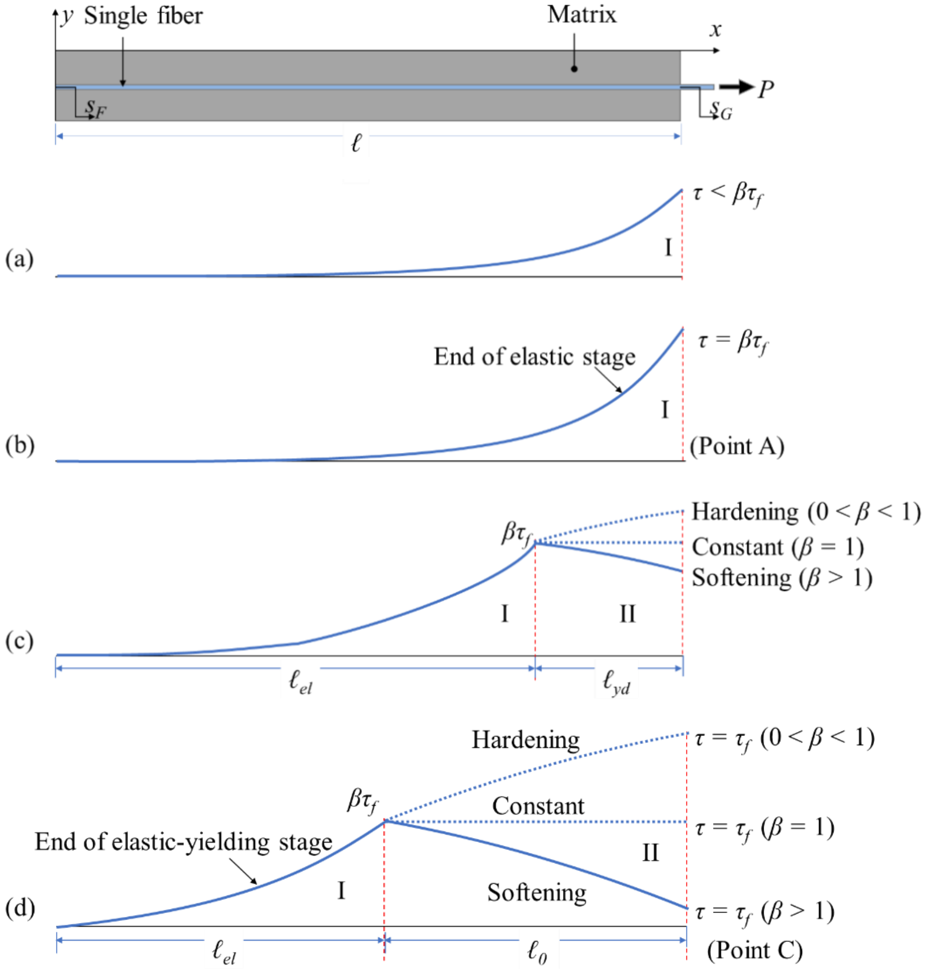

Figure 2.4.7. Evolution of interfacial shear stresses for a long embedment length and propagation of debonding: (a, b) elastic stage; (c, d) elastic-yielding stage; (e, f) elastic-yielding-debonding stage; (g, h) yielding-debonding stage; and (i) debonding stage. I, II and III represent elastic, yielding and debonding stress state, respectively.

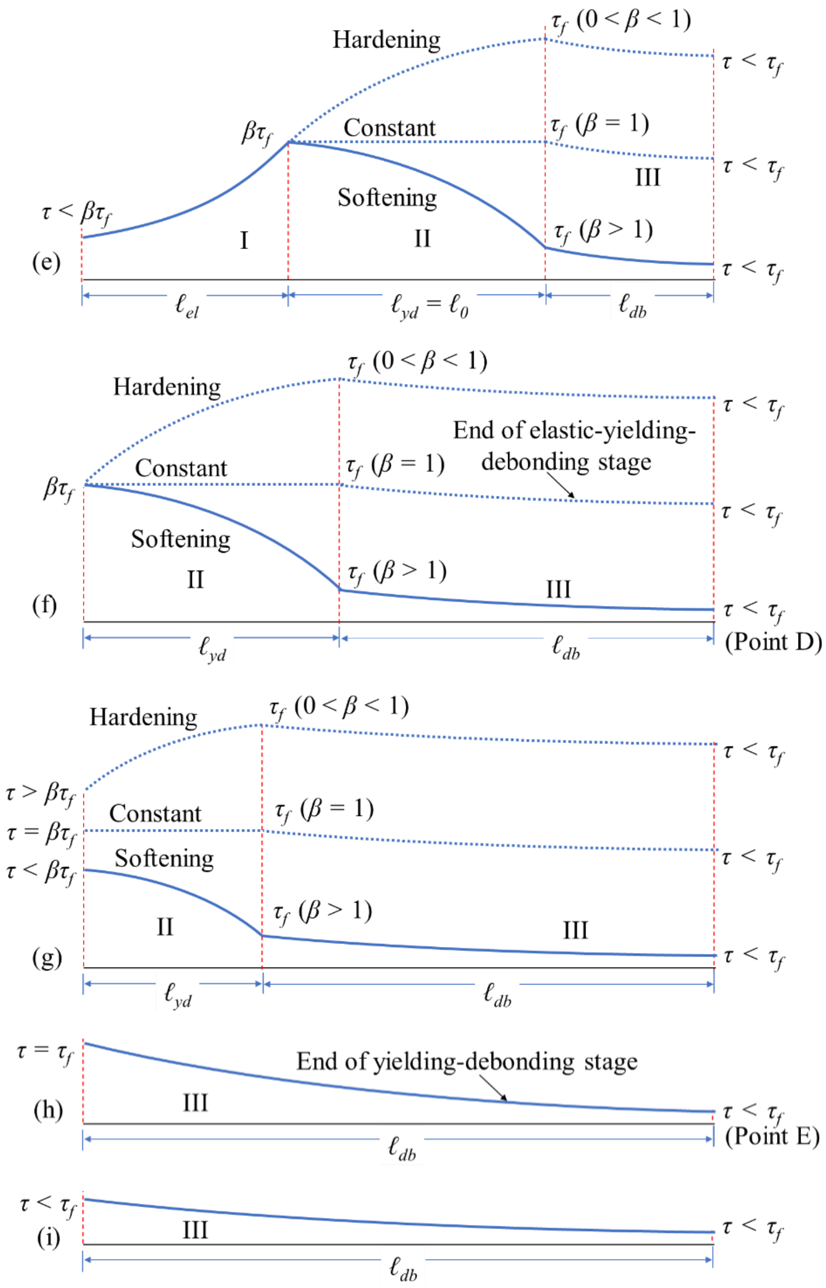

Figure 2.4.7. Evolution of interfacial shear stresses for a long embedment length and propagation of debonding: (a, b) elastic stage; (c, d) elastic-yielding stage; (e, f) elastic-yielding-debonding stage; (g, h) yielding-debonding stage; and (i) debonding stage. I, II and III represent elastic, yielding and debonding stress state, respectively.

When the embedment length is shorter than the critical embedment length ($\ell < \ell_0$), the shear stress distribution at the end of the elastic-debonding stage is shown in Figure 2.4.8(a). There is no elastic stage along the fiber, and the interface is in the softening stage along the whole fiber length. At the end of the softening phase, the shear distribution is shown in Figure 2.4.8(b). Then, the shear stress distribution evolves to the yielding-debonding stage.

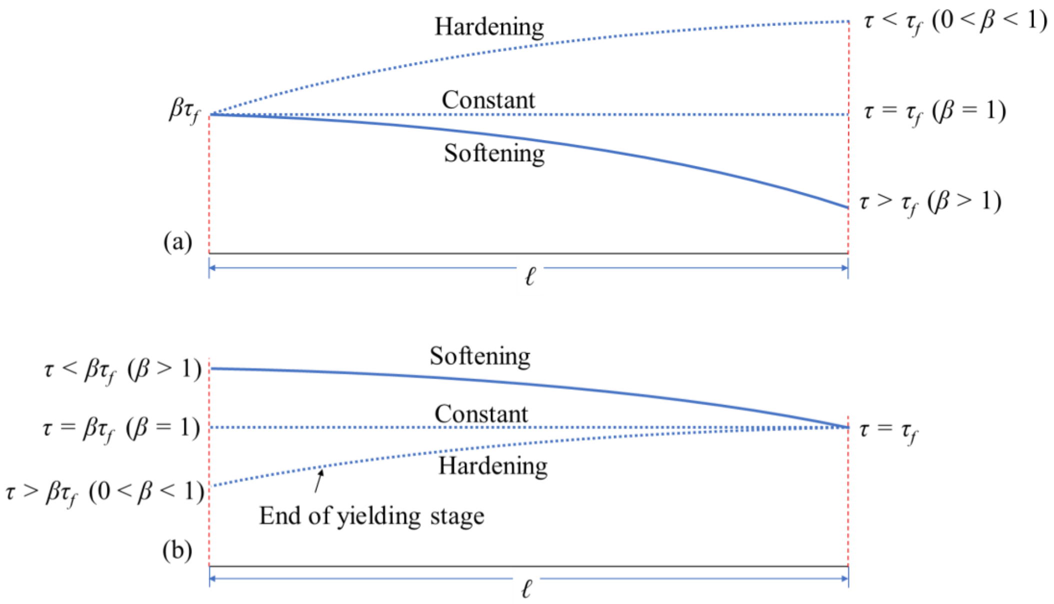

Figure 2.4.8. Evolution of interfacial shear stress distribution of yielding stage for a short embedment length and propagation of debonding.

2.4.4. Implementation

The presented interface law and analysis is implemented into optical fibers that were used to validate the approaches. The validation of the approaches took advantage of the unique sensing capability of the DFOS. The proposed CIL and derivation of analytical formulae are independent of specific materials (e.g., fiber optic cables) and applicable to other composites.

2.4.4.1. Pullout tests

Single fiber pullout tests were carried out as shown in Figure 2.4.9(a). In each test, an optical fiber was attached using adhesive (ethyl cyanoacrylate super glue) on two aluminum plates (length × width × thickness: 200 mm × 30 mm × 5 mm). The coating of the fiber was stripped off using a stripper at crack position. The aluminum plate was gripped by a low-capacity load frame (load capacity: 1 kN; accuracy: ±0.2 N). The embedment fiber length with the coating was $\ell = 160$ mm. The test was repeated eight times. The embedded silica fiber was pulled out under displacement control at a constant rate of 0.5 mm/min. The applied force was measured from the load cell embedded in the load frame. The pullout displacement was measured using an extensometer attached to the two aluminum plates. Representative results are shown in Figure 2.4.9(b). The curves indicate that the pullout behavior is dependent on the embedded fiber length. An extensometer measured the relative displacement between the two aluminum plates representing the crack width increase. Figure 2.4.9(c) shows the representative strain distribution curves with crack width opening.

It is noted that plate specimens have been utilized in the pull-out testing, rather than using steel pipes, because plate specimens were available in the laboratory and easier to handle for reliable tests. The availability of the tests using pipe specimens was affected by COVID-19. To avoid delaying the progress, we adopted plate specimens for validating the theoretical studies. The validation tests are acceptable because the theoretical analysis does not rely on the specific material (e.g., API 5L grade steel, or aluminum) and the specific geometry (e.g., pipe, or plate). The validation focuses on mechanical analysis and equation derivation.

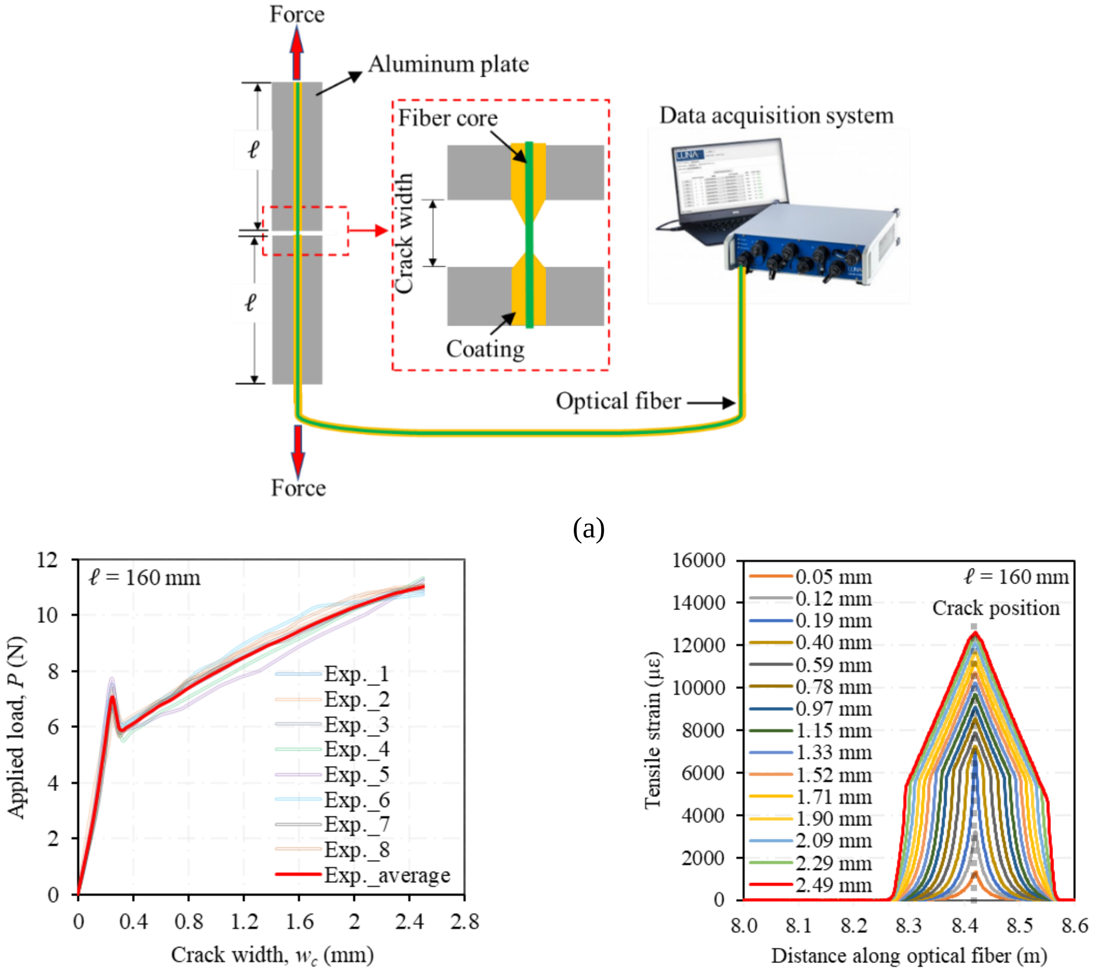

(b) (c)

Figure 2.4.9. Fiber pullout test: (a) test set-up (b) representative pullout load versus crack width curves; and (c) representative experimental strain distribution curves with crack width opening.

2.4.4.2. Metaheuristic inverse analysis

The model parameters α, β, τ_f, s_f, and k were determined through the metaheuristic inverse analysis based on the fiber pull-out test results. Figure 2.4.10 shows the optimization convergence curves for the 20 independent runs of the inverse analysis. The curves indicate that the adopted algorithm effectively minimizes the objective function and avoids premature convergence.

Table 2.4.3 lists the results of the parameters of the presented CIL and performance metrics. The results indicate that the force-slip results obtained from the inverse analysis agree with the test results. Figure 2.4.11(a) compares the experimental and analytical results of the force-crack width curves based on inverse analysis.

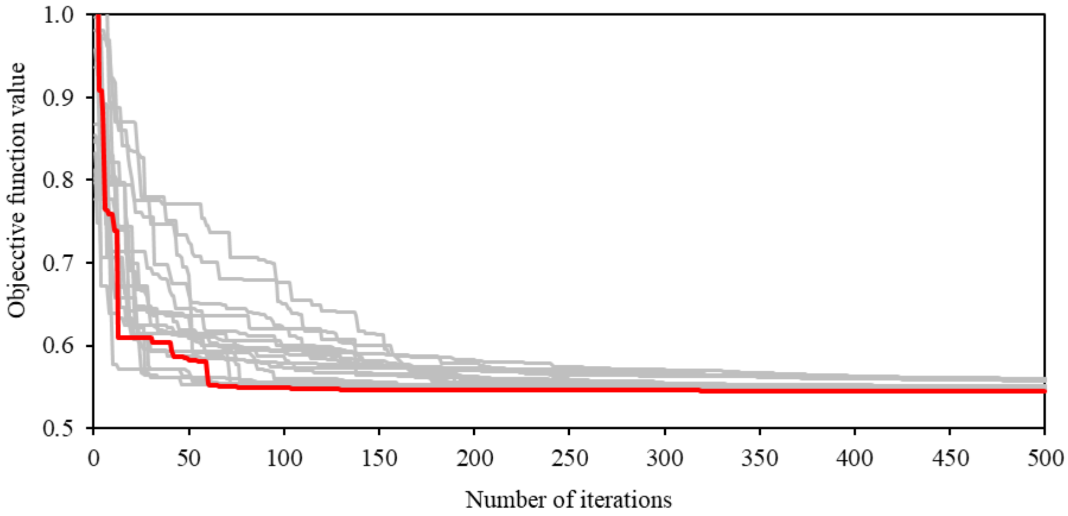

Figure 2.4.10. Convergence of the hypotrochoid spiral optimization algorithm for 20 independent runs. The red line represents the best result, and the gray lines represent the other results.

Table 2.4.3. Parameters of the bond-slip relationships

Samples (ℓ = 160mm)	s_f (mm)	τ_f (MPa)	α	β	k (N/mm)	RMSE	R^2	MAE
Exp._1	1.092	0.1158	0.3689	5.6786	1621.54	0.1225	0.984	0.0901
Exp._2						0.1032	0.991	0.0715
Exp._3						0.1009	0.994	0.0791
Exp._4						0.1102	0.992	0.0804
Exp._5						0.1231	0.995	0.1002
Exp._6						0.1068	0.987	0.0787
Exp._7						0.1242	0.993	0.1013
Exp._8						0.1097	0.989	0.0925
Exp._average						0.1125	0.991	0.0867

2.4.4.3. Distributed fiber optic sensing

With the model parameters, the mechanical model was used to derive the slip distribution and the shear stress distribution at the fiber-coating interface and the strain distribution in the fiber along the fiber length at an arbitrary crack width opening. Figure 2.4.11 plots nine selected crack width levels at the loaded end, w_c = [0.05 mm, 0.12 mm, 0.22 mm, 0.32 mm, 0.59 mm, 0.78 mm, 1.33 mm, 1.89 mm, 2.49 mm], in the pullout force-crack width curve when the embedment length is 160 mm. The nine crack width levels were selected to represent nine stages of the pullout process. This analytical analysis provides a theoretical foundation for measuring the crack widths using the empirical relationship between the magnitude of strain peak measured from DFOS and crack width.

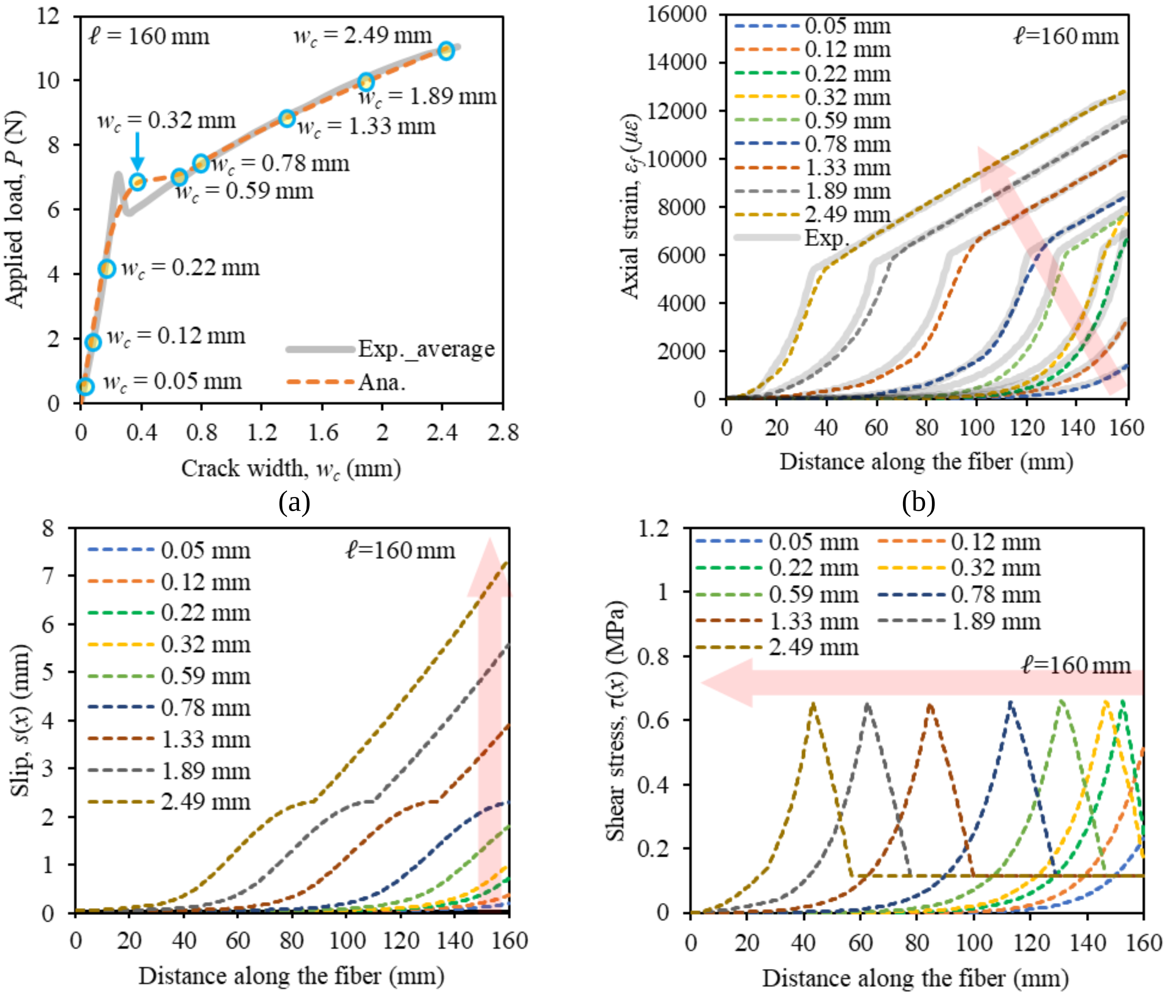

(a) (b)

(c) (d)

Figure 2.4.11. Assessment of the analytical solution for nine levels of crack width: (a) the crack widths at nine loading levels; (b) comparison of the analytical and experimental results of axial strain distributions; (c) slip distributions; and (d) shear stress distributions.

Figure 2.4.11(b) compares the analysis results of the strain distributions in the fused silica fiber against the measurements from the DFOS based on OFDR. The analysis and measurement results of the strain distributions agree, indicating that the presented interface law and inverse analysis are effective in analyzing the interfacial behavior. The understanding of the interfacial behavior enables the operation of DFOS and the interpretation of the sensing data in the presence of debonding at the fiber-coating interface. In the presence of cracks, the theoretical formula that relates the slip of the optical fiber and the crack opening width is determined according to the governing equation Eq. (2.4.5), and the crack width is calculated by the integration of the tensile strains in the vicinity of the crack. This analytical analysis also paves the theoretical way to quantify the crack widths using strain distributions measured from DFOS, and the developed approaches enable accurate interpretation of the results from the DFOS.

Figure 2.4.11(c) shows the slip distributions along the fiber at different crack width openings. The slip reaches the maximum value at the loaded end ($x = \ell$) and gradually decreases towards the free end ($x = 0$) of the fiber. When the slip is small (s_G < 0.284 mm or w_c < 0.12 mm), the entire interface is elastic. When s_G increases from 0.284 mm to 1.746 mm (or 0.12 mm < w_c < 0.59 mm), the interface is in the elastic-yielding stage. When s_G increases from 1.746 mm to 7.310 mm (or 0.59 mm < w_c < 2.49 mm), the fiber core-cladding interface is in the elastic-yielding-debonding stage.

Figure 2.4.11(d) shows the shear stress distributions along the fiber length at different crack width openings. When the crack width opening is small (w_c < 0.12 mm), the shear stress reaches the maximum value at the loaded end and gradually decreases towards the free end of the fiber. When the crack width opening increases from 0.12 mm to 0.59 mm, the maximum shear stress reaches the peak shear, the maximum shear stress reaches the peak at the intersection between the elastic and yielding sections. The position of maximum shear stress moves toward the free end of the embedded section when the crack width opening increases. When the crack width opening is larger than 0.59 mm, the loaded end of the embedded section reaches the debonding section, and the position of peak shear stress moves further toward the free end of the embedded fiber.

2.4.5. Summary

This study presents a unified cohesive interface law to describe the bond-slip behavior of fused silica fiber with polymeric coating in the fiber pullout process, performs a mechanical analysis on fiber pullout responses based on the presented interface law, develops a metaheuristic inverse analysis to calibrate the model parameters, and applies a DFOS technology based on optical frequency domain reflectometry to measure the strain distributions in optical fibers. The following findings are drawn:

(1) The presented CIL reasonably reflected the bond-slip behavior for fused silica fiber with polymeric coating and has the potential for other types of fiber-matrix interface. With the proposed CIL, the mechanical analysis on the fiber-coating interface can establish the intrinsic relationship between the CIL and the fiber pullout force-crack width response.

(2) The parameters of the unified CIL were automatically determined via the metaheuristic inverse analysis with high efficiency and accuracy. For the investigated embedment fiber lengths, the RMSE is lower than 0.13, R^2 is higher than 0.98, and MAE is lower than 0.11.

(3) The presented method provides reasonable predictions of the slip distribution and shear stress distribution at the fiber-coating interface as well as the strain distributions in the fused silica fiber. The results of the strain distributions agreed with the strain distributions measured from the DFOS throughout the pullout process.

(4) This research advances the understanding of the fiber-coating interfacial behavior, and the understanding enables DFOS to be operated in presence of debonding at the fiber-coating interface at cracks, as well as accurate measurement of crack width by interpretation results obtained from DFOS.

2.5. Detection, localization, quantification, and visualization of buckling/dent

2.5.1. Overview

This research aims to address the challenges by developing an effective and practical method for buckling detection and shape reconstruction using strain profiles measured from a DFOS. This study has three main research objectives: (1) to develop a practical method to detect buckling and reconstruct the detailed buckling shape for thin-walled plates subjected to eccentric buckling loads, mimicking realistically complex buckling deformations; (2) to investigate the effects of spatial resolution and sensor deployment of DFOS on the performance in shape reconstruction; and (3) to develop a method to visualize the strain distributions and buckling deformations of monitored structures for practical engineers.

To achieve the above objectives, this research tested two types of specimens, including a bar specimen under uniaxial compression and a plate specimen under eccentric compression. Both specimens were instrumented with DFOS and monotonically loaded until buckling occurred. A practical method was proposed to determine the full-field strain contours in the specimens throughout the loading process and to reconstruct the deformed shape based on the relationship between strain and deformation. Furthermore, a depth camera was used to monitor the specimens throughout the loading process, and the point cloud were used to evaluate the buckling deformations obtained from the proposed method. Finally, a parametric study was conducted to investigate the effects of spatial resolution and sensor deployment on shape reconstruction.

Compared with existing research, this research has four novelties: (1) This research addresses buckling deformation of plates under eccentric loads, rather than simple deflections of beams or cantilever plates. (2) This research focuses on the development of practical yet efficient solutions to detect, locate, trace, visualize, and quantify three-dimensional (3D) buckling deformations. (3) This research measures experimental deformations directly by computer vision method to validate the shape reconstruction approach. (4) This research evaluates important parameters of DFOS and sensor deployment scheme.

2.5.2. Methods

The framework of this research on buckling detection and shape reconstruction is shown in Figure 2.5.1. The DFOS was deployed on thin walls to measure strain distributions. The measured strains are used to determine the strain distribution function, which was then used to determine the deformed shape of the structure through an inverse analysis. Finally, computer vision measurement is performed to obtain three-dimensional point clouds for measuring structural deformations and validating the developed method. This research developed a method to determine the strain distribution function through data regression, and presented a shape reconstruction method to determine the deformed shape based on strain distributions.

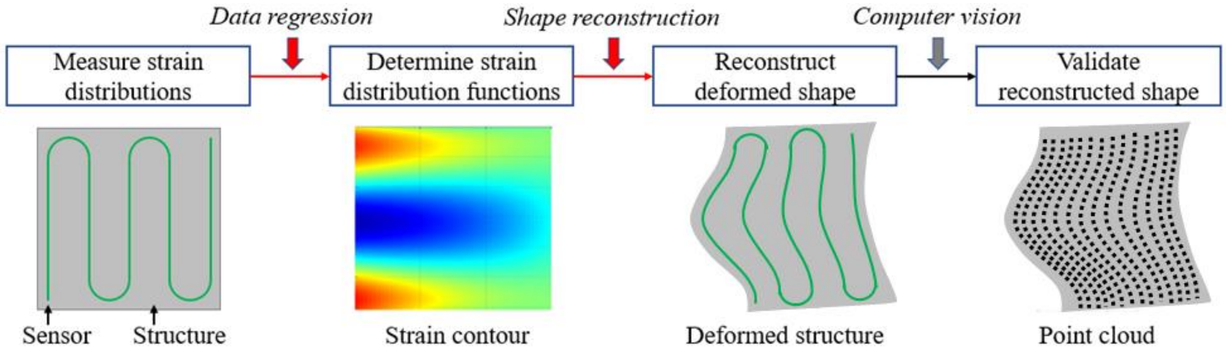

Figure 2.5.1. Research framework integrating DFOS, shape reconstruction, and computer vision.

2.5.2.1. Shape reconstruction

2.5.2.1.1 Strain distribution function

Since a DFOS measures strains at many points along the sensor, each measurement from the sensor is a series of strain data that can be expressed as a strain vector $\boldsymbol{\varepsilon}_p$:

$$\boldsymbol{\varepsilon}_p = \left[\varepsilon_{p1} \cdots \varepsilon_{pi} \cdots \varepsilon_{pN}\right]^T \tag{2.5.2}$$

where ε_{pi} is the strain measured from point i (i = 1, 2, ..., N), and N is the total number of data points. The subscript p is the direction (x or y) of the strain component, consistent with the direction of the distributed sensor.

The coordinates of measurement points in the DFOS are expressed as:

$$[\boldsymbol{X}, \boldsymbol{Y}] = \begin{bmatrix} x_1 & y_1 \\ \vdots & \vdots \\ x_i & y_i \\ \vdots & \vdots \\ x_N & y_N \end{bmatrix} \tag{2.5.3}$$

where x_i and y_i are respectively the x and y coordinate values of point i.

With the strain vector and the coordinate matrix, the strain and coordinate of each point along the DFOS can be described using the following matrix:

$$[\boldsymbol{X}, \boldsymbol{Y}, \boldsymbol{\varepsilon}_p] = \begin{bmatrix} x_1 & y_1 & \varepsilon_{p1} \\ \vdots & \vdots & \vdots \\ x_i & y_i & \varepsilon_{pi} \\ \vdots & \vdots & \vdots \\ x_N & y_N & \varepsilon_{pN} \end{bmatrix} \tag{2.5.4}$$

Although the DFOS covers a large area of the monitored structure, the DFOS does not provide measurement at every point because there are gaps between adjacent paths of the DFOS. This study proposes to determine the full-field strain distributions of the monitored structure through regression analysis of the strain distribution function using a surface fitting method. The strain component at an arbitrary point (x, y) is expressed as:

$$\varepsilon_p(x,y) = \sum_{k=1}^{M} m_k f_k(x,y) \tag{2.5.5}$$

where m_k is the coefficient of the k-th fitting function (k = 1, 2, ..., M), and M is the total number of the fitting functions. Then, the strain vector $\boldsymbol{\varepsilon}_p$ can be expressed as:

$$\boldsymbol{\varepsilon}_p = \begin{bmatrix} f_1(x_1,y_1) & \cdots & f_k(x_1,y_1) & \cdots & f_M(x_1,y_1) \\ \vdots & \ddots & \vdots & \ddots & \vdots \\ f_1(x_i,y_i) & \cdots & f_k(x_i,y_i) & \cdots & f_M(x_i,y_i) \\ \vdots & \ddots & \vdots & \ddots & \vdots \\ f_1(x_N,y_N) & \cdots & f_k(x_N,y_N) & \cdots & f_M(x_N,y_N) \end{bmatrix} \begin{bmatrix} m_1 \\ \vdots \\ m_k \\ \vdots \\ m_M \end{bmatrix} = \boldsymbol{F}^{\varepsilon}\boldsymbol{m}^{\varepsilon} \tag{2.5.6}$$

If polynomial functions are used to fit the profiles of strain distributions, the strain component at an arbitrary point (x,y) is expressed as:

$$\varepsilon_p(x,y) = \sum_i \sum_j m_{ij} x^i y^j \tag{2.5.7}$$

where m_{ij} is the coefficient; i and j are the orders of polynomial functions.

The coefficients are determined by minimizing the following objective function based on the least-square residual method:

$$\Phi^{\varepsilon} = \min\left\{\left[\boldsymbol{\varepsilon}_p - \boldsymbol{F}^{\varepsilon}\boldsymbol{m}^{\varepsilon}\right]^T \boldsymbol{W}^R \left[\boldsymbol{\varepsilon}_p - \boldsymbol{F}^{\varepsilon}\boldsymbol{m}^{\varepsilon}\right]\right\} \tag{2.5.8}$$

where the weight matrix $\boldsymbol{W}^R$ is composed of weights for each data point as expressed by:

$$\boldsymbol{W}^R = \mathrm{diag}\left[W_1^R \cdots W_i^R \cdots W_N^R\right] \tag{2.5.9}$$

where weight W_i^R is the relative data reliability of point i, which can be determined by:

$$W_i^R = \begin{cases} 1, & \text{Point } i \text{ at straight sensor lengths} \\ 0, & \text{Point } i \text{ at curved sensor lengths} \end{cases} \tag{2.5.10}$$

where the weight value $W_i^R = 1$ is assigned to the data point that is located in the straight sensor lengths; and the data point that is located in the curved sensor lengths is not used in the shape reconstruction. Thus, it became possible to consider the influence of acute curvature of sensor deployment profile using the relative data reliability of distributed strain data.

2.5.2.1.2. Strain-deformation relationship

The equation that governs the relationship between strain and out-of-plane deformation of a surface is determined based on the elastic theory, as shown in Eq. (2.5.11):

$$\varepsilon_p(x,y) = -z\frac{\partial^2 v_p(x,y)}{\partial p^2}, \qquad (p = x \text{ or } y) \tag{2.5.11}$$

where z is the distance from the neutral axis of the cross section.

Given a specific y-coordinate, the governing equation can be rewritten as:

$$\varepsilon_p(x, y_i) = -z\frac{d^2 v_x(x, y_i)}{dx^2} \tag{2.5.12}$$

where $v_x(x, y_i)$ is the deflection of the structure along y_i.

When the length of the buckled region of the structure is detected, the boundary conditions of the governing equation can be described in Eq. (2.5.13):

$$v_x(\mathrm{x} = 0, y_i) = v_x(x = L, y_i) = 0 \tag{2.5.13a}$$

$$\left.\frac{dv_x(x, y_i)}{dx}\right|_{x=0} = \left.\frac{dv_x(x, y_i)}{dx}\right|_{x=L} = 0 \tag{2.5.13b}$$

$$\left.\frac{d^2 v_x(x, y_i)}{dx^2}\right|_{x=0} = \left.\frac{d^2 v_x(x, y_i)}{dx^2}\right|_{x=L} = 0 \tag{2.5.13c}$$

where L is the length of the buckled region. The starting and end points of the buckled area are expressed as x = 0 and x = L, respectively.

According to Eq. (2.5.7), the strain distribution surface is expressed using polynomial functions, so the deflection can be expressed in Eq. (2.5.14), and the integration constants are determined by boundary conditions.

$$v_x(x, y_i) = \sum_i \sum_j M_{ij} x^{i+2} {y_i}^j \tag{2.5.14a}$$

$$M_{ij} = -\frac{1}{z}\frac{m_{ij}}{i(i-1)} \tag{2.5.14b}$$

2.5.2.1.3 Computer vision

Computer vision measurement was performed using a depth camera with a pair of camaras (model: Intel d455), and the data were processed using commercial software (Intel RealSense View®). The depth camera used stereo vision to determine the distance between the camera and specimens. For shape reconstruction, the two cameras were synchronized to capture photos of the specimen. Since the distance between left and right cameras is known, depth values for each pixel in the image can be calculated by correlating points of paired photos [61]. The depth pixel values were processed to generate a depth frame. Subsequent depth frames created a depth video stream for shape reconstruction. The ideal range of the adopted depth camera was 0.3 m to 3 m. The depth resolution was up to 1280 px × 720 px, and the depth accuracy was finer than 2% [62]. In this study, the depth camera captured videos for one side of each specimen, and the measurement was synchronized with the DFOS system.

2.5.3. Experimental studies

2.5.3.1. Buckling test

2.5.3.1.1. Specimen and test set-up

Buckling testing was conducted to assess the buckling behaviors of bar and plate specimens, respectively. The bar specimen represented one-dimensional (1D) buckling deformations, and the plate specimen represented two-dimensional (2D) buckling deformations. The tested specimens are shown in Figure 2.5.2.

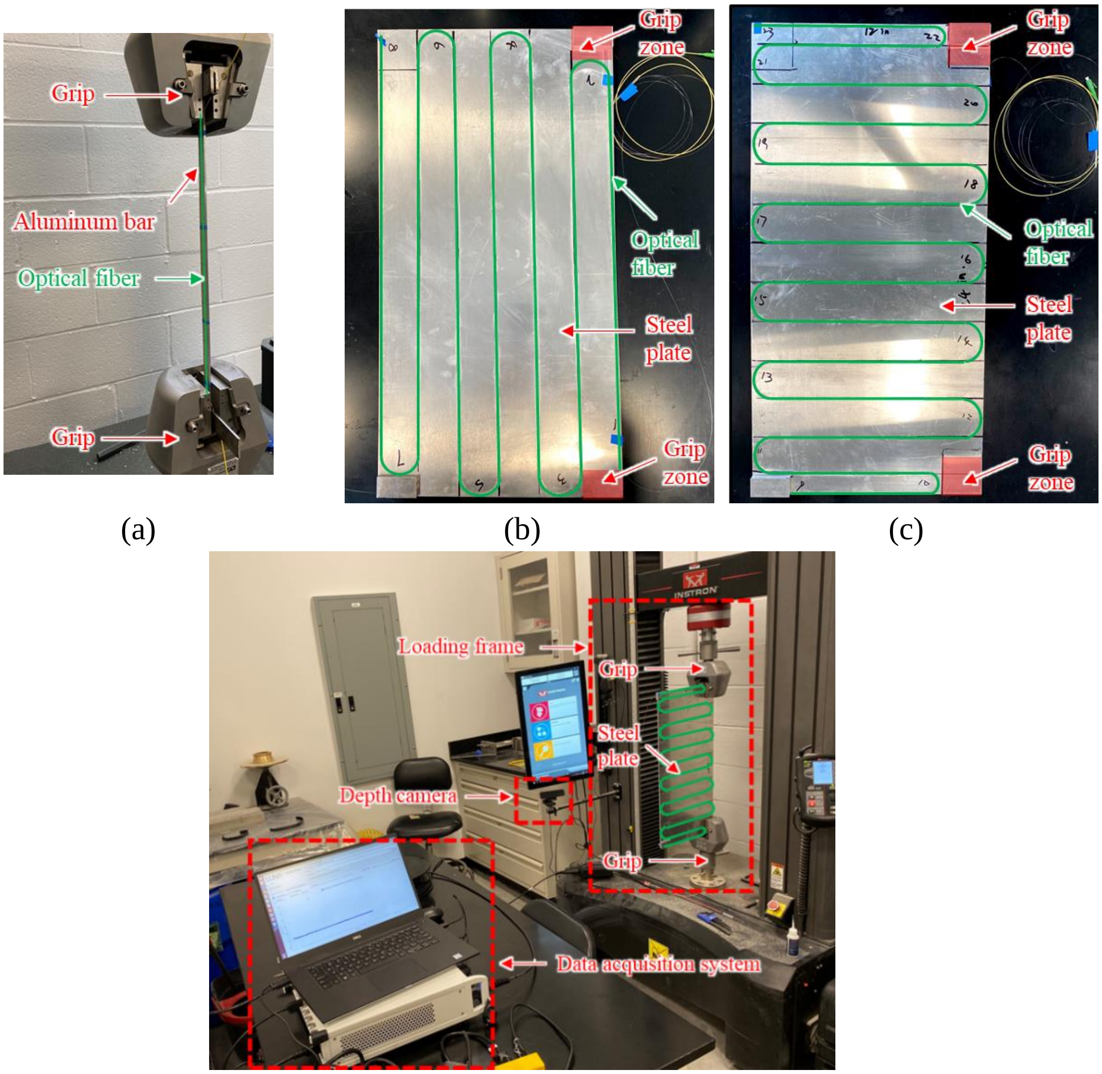

(a) (b) (c)

(d)

Figure 2.5.2. Specimen preparation and test set-up: (a) photograph of the bar specimen on the load frame; (b) installation of the optical fiber on side A of the plate specimen; (c) installation of the optical fiber on side B of the plate specimen; and (d) photograph of the plate specimen.

It is noted that plate specimens were utilized in experimental testing, rather than pipes, because plate specimens were available in the laboratory and easier to handle for reliable tests. The availability of the tests using pipe specimens was affected by COVID-19. To avoid delaying the progress, we adopted plate specimens to develop the technology for monitoring dents or local buckling. The technology is developed based on strain measurements. The method is independent of the specific geometry of specimens (e.g., pipe, or plate).

The length and cross section of the bar specimen were 500 mm and 12.7 mm × 2.54 mm, respectively. Two optical fibers were deployed as a DFOS on two surfaces of the bar specimen along its length. The attached length of each optical fiber was $L = 400$ mm, as depicted in Figure 2.5.2(a). The thickness and area of the plate specimen were 2.54 mm and 609.6 mm × 304.8 mm, respectively. Two optical fibers were attached as a DFOS on the two surfaces (side A and side B) of the plate specimen following the designed zigzag patterns, as shown in Figure 2.5.2(b) and Figure 2.5.2(c), respectively. On both sides of the plate, the spacing between two adjacent paths of the DFOS was 50.8 mm. The bar specimen was made of aluminum. The plate specimen was made of structural steel.

Before the optical fibers were installed, the specimens were cleaned to remove grease and rust from the surfaces. The purpose of the surface cleaning effort is to ensure the bond between epoxy and specimens. Then, the optical fibers were attached to the specimens via tapes at discrete spots following the pattern designed to cover the majority area of the specimens. The tape was used to hold optical fibers in place during the installation. Next, a fast-setting glue was used to attach the optical fibers to the specimens at discrete points between the taped spots. Once the glue was set, the tape was removed. The removal of tape must be careful to prevent damage to the optical fibers. Finally, a two-part epoxy was applied to the optical fibers for strong attachment and reliable strain transfer between the specimen and optical fiber. The thickness of epoxy should be minimized to alleviate the effect of epoxy on the buckling of specimens. In this study, the thickness of epoxy was about 0.25 mm, which was around one tenth of the thickness of the specimens. The width of epoxy strips was about 5 mm. The epoxy was cured in air at room temperature (22 ºC ± 2 ºC) and normal humidity (50% ± 5%).

After the epoxy was cured for 24 hours, the specimens were tested under mechanical loading using a load frame (model: Instron 8813, load capacity: 100 kN), as shown in Figure 2.5.2(a) and Figure 2.5.2(d). Each specimen was loaded under compression by the load frame until buckling occurred. The bar specimen was loaded along the center to generate symmetrical deformation, while the plate specimen was loaded with an eccentricity to generate unsymmetrical deformation. For each DFOS, one end was connected to the data acquisition system for measurement, and the other end was free. The resolution of the DFOS was set at 0.65 mm. The compression tests were performed under displacement control with a displacement rate of 0.2 mm/min. The applied load was measured by a load cell embedded in the load frame, and the displacement was measured by a displacement sensor of the load frame.

2.5.3.1.2. Load-displacement curves and visual inspection

Figure 2.5.3 shows the load-displacement curves and buckling deformations of the tested specimens. The specimens showed similar curves with three stages: (1) Stage 1: from "O" to "A", where the compressive load approximately linearly increases with the displacement; (2) Stage 2: from "A" to "B", where the compressive load increases with the displacement with a decreasing slope until reaching the peak load at point B; and (3) Stage 3: from "B" to "C", where the load decreases with the displacement.

The bar specimen under uniaxial compression exhibited a typical buckling deformation. The lateral deformation increased with the applied displacement. The plate specimen under eccentric compression exhibited a representative out-of-plane buckling deformation that is unsymmetrical to the loading axis and increased with the applied displacement.

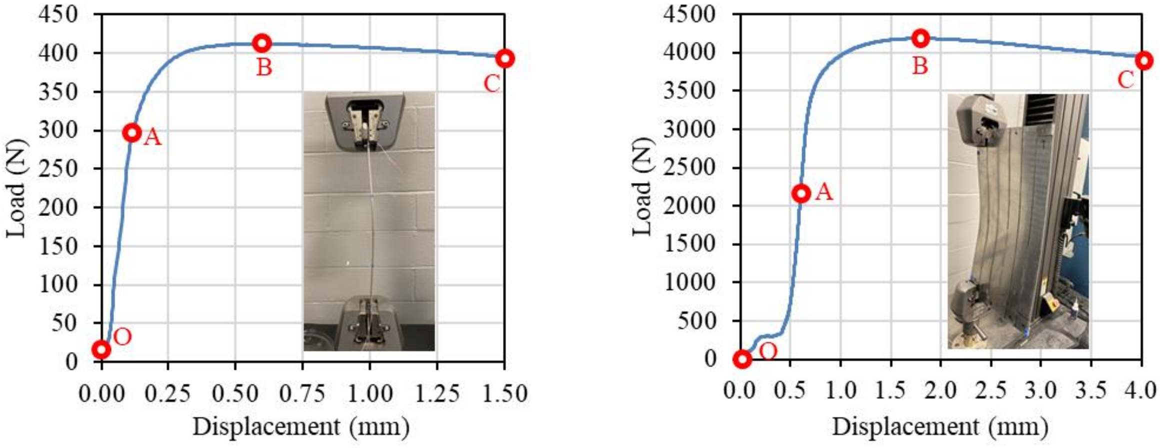

(a) (b)

Figure 2.5.3. Load-displacement of the specimens under compression: (a) the bar, and (b) the plate.

2.5.3.2. Strain distributions

2.5.3.2.1. Bar specimen

The strain distributions measured from the DFOS installed on the bar specimen under different loads are shown in Figure 2.5.4. The vertical axis represents the strains caused by buckling, and the horizontal axis represents the distance along the DFOS, with the zero distance at the connector of the data acquisition system.

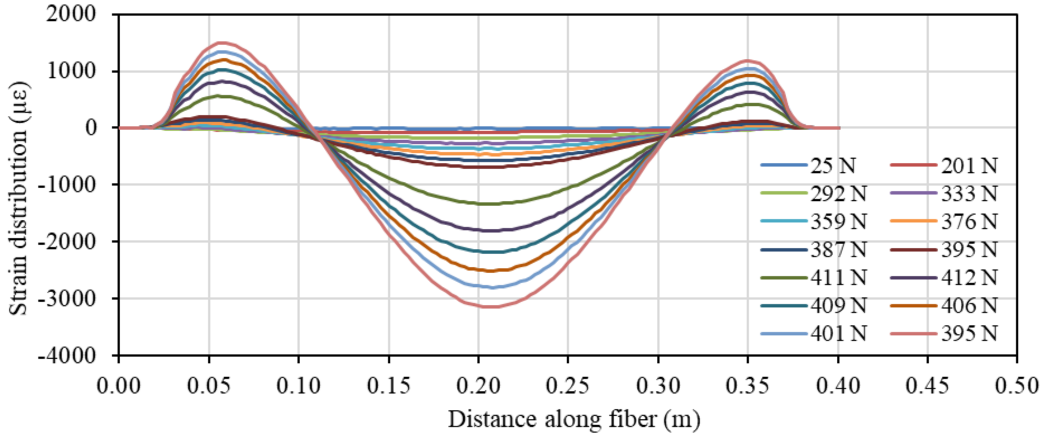

Figure 2.5.4. Strain distributions measured from the DFOS deployed on the bar.

The length range of the DFOS is selected to show the strain distributions within the length of fiber optic cable installed on the bar. When the load increased from 0 to 292 N (Stage 1), the strains along the entire fiber length were compressive strains (negative), and the peak strain increased with the load. When the load increased from 292 N to 412 N (Stage 2), the strains in the middle region of the specimen were negative, while the strains at the two ends of the specimen were changed to positive values. The strains in both positive and negative regions increased with the load. When the load decreased from 412 N to 395 N (Stage 3), the shapes of strain distributions and curvature distributions are similar to those in Stage 2. The magnitudes of strain distributions increased with the decrease of the load due to the further increase of buckling deformations.

2.5.3.2.2. Plate specimen

Similar to the bar specimen, the strain distributions measured from the DFOS installed on the two surfaces of plate specimen under different loads are shown in Figure 2.5.5. The vertical axis represents the strains caused by buckling, and the horizontal axis represents the distance along the DFOS, with the zero distance at the connector of the data acquisition system. In each figure, the length range of the DFOS is selected to show the strain distributions within the length of fiber optic cable installed on the plate specimen.

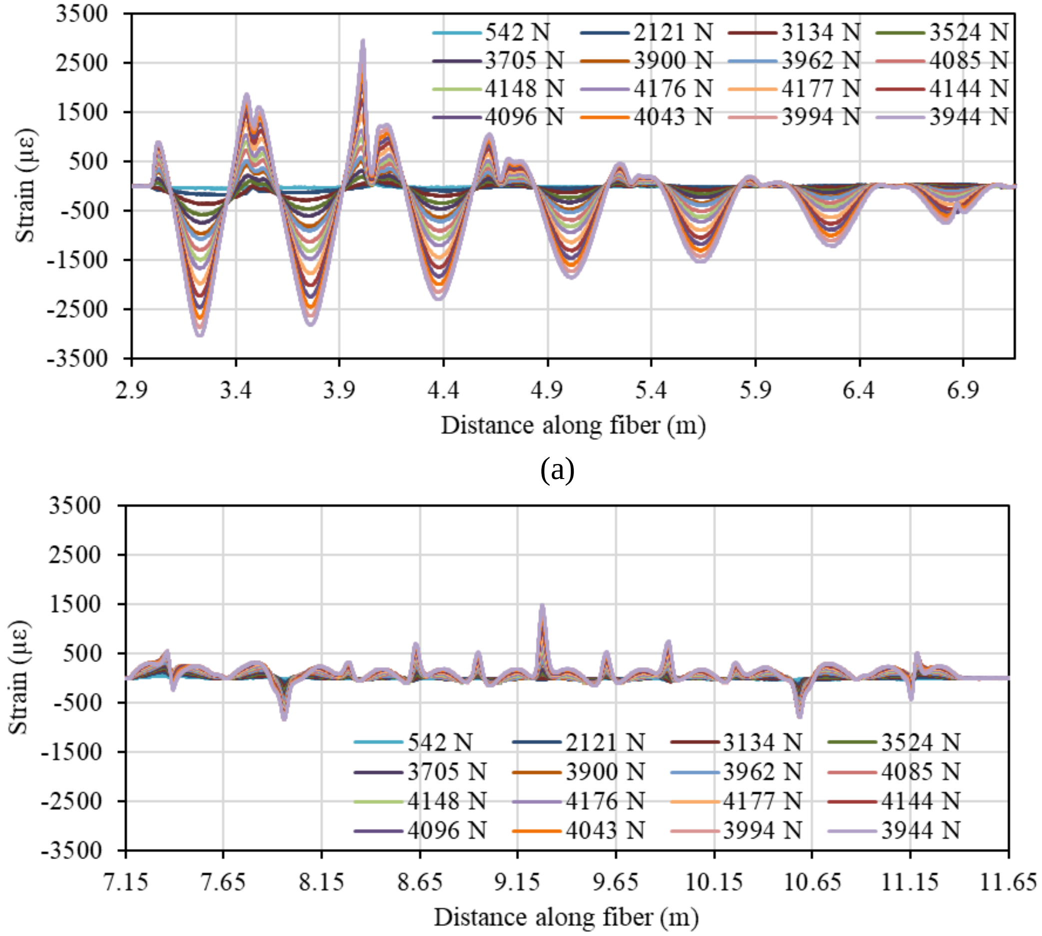

(a)

(b)

Figure 2.5.5. Strain distributions measured from the DFOS deployed on the plate specimen under different loads: (a) side A; and (b) side B.

Figure 2.5.5(a) shows strain distributions measured from side A of the specimen in Stage 1 to Stage 3. In Stage 1, when the load increased from 0 to 2121 N, the strains along the entire length were negative, and the peak strains increased with the load. In Stage 2, when the load increased from 2121 N to 4183 N, strains in the middle region of the plate were negative, while the strains at the two end regions of the plate were changed to positive values. The peak strains in both positive and negative regions increased with the loads. In Stage 3, when the load decreased from 4183 N to 3944 N, the shapes of strain distributions were similar to those in Stage 2. The magnitudes of strains increased with the decrease of the loads due to the increase of the buckling deformation. Similar trends of evolution of strains were observed from side B in Figure 2.5.5(b), while the magnitudes of strains were much lower than those from side A.

2.5.3.2.3. Strain contour

To use the strain data for visualization and shape reconstruction, 2D coordinates were assigned to each point via coordinate transform as described in Section 2. The measured strain distributions are re-plotted by coordinate transform. Then, the strain distributions measured from the discrete lines were used to generate continuous 2D strain contours via interpolation, as illustrated in Figure 2.5.6.

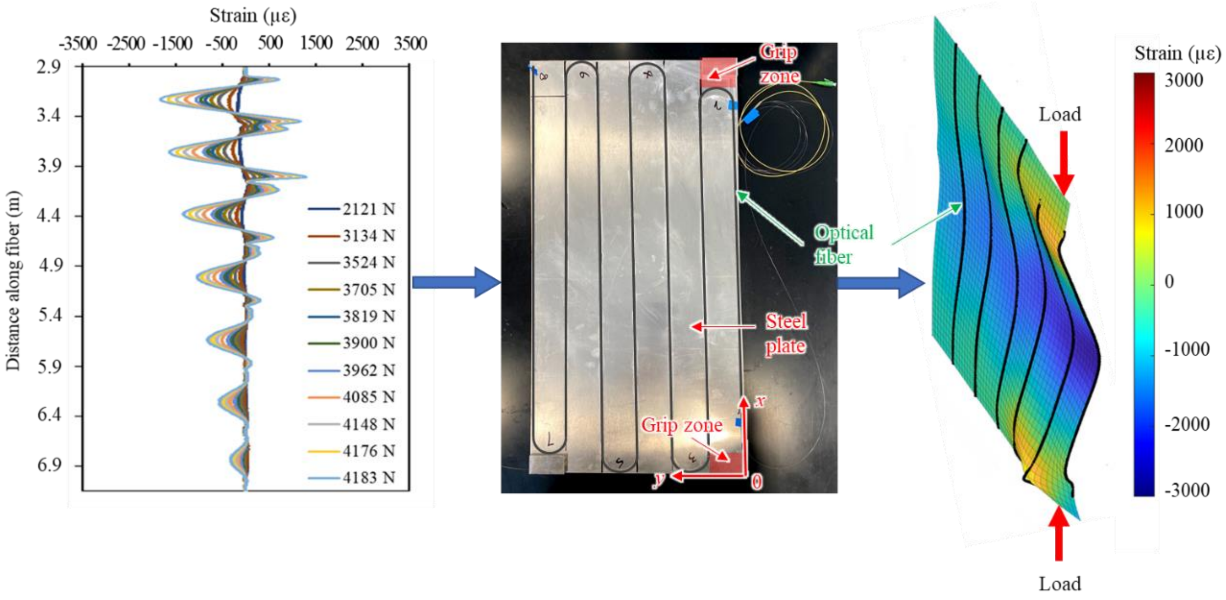

Figure 2.5.6. Mapping of strain distributions on the plate for visualization of buckling deformation.

Figure 2.5.7 plots the different orders of polynomial surfaces employed to fit the strain distributions measured from the DFOS deployed on side A of the plate specimen. The directions of x and y coordinates are introduced in Figure 2.5.6.

The measurement results of strain distributions are represented by the black curves, and the polynomial fitting surfaces are shown by the colored contours. Red color stands for the areas subjected to high tensile strains, and blue color marks the areas subjected to high compressive strains. As the order of the polynomial fitting surface was increased, the spatial distribution and the magnitude of the strain distributions of the buckled plate were reasonably represented.

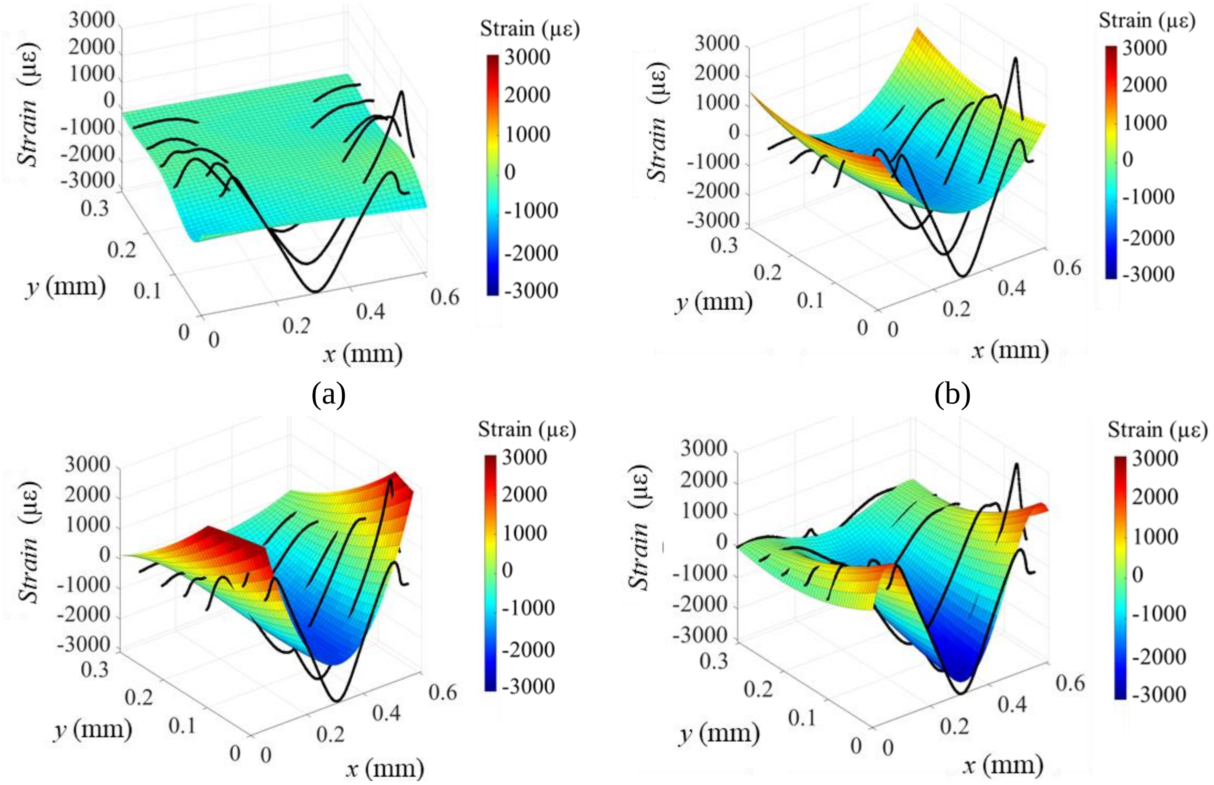

(a) (b)

(c) (d)

Figure 2.5.7. Strain polynomial fitting in the load direction (ε_x): (a) x (1-order) and y (5-order); (b) x (2-order) and y (2-order); (c) x (3-order) and y (2-order); and (d) x (5-order) and y (3-order).

A sensitivity analysis was performed to investigate the appropriate orders of the polynomial fitting surfaces. The evaluation results are listed in Table 2.5.1. Three performance metrics were adopted, which are the sum of squares due to error (SSE), coefficient of determination (R^2), and the RMSE.

$$\mathrm{SSE} = \sum_{i=1}^{n} (p_i - \nu_i)^2 \tag{2.5.15}$$

$$R^2 = 1 - \frac{\sum_{i=1}^{n} (p_i - \nu_i)^2}{\sum_{i=1}^{n} [\nu_i - \mathrm{mean}(\nu_i)]^2} \tag{2.5.16}$$

$$\mathrm{RMSE} = \sqrt{\frac{\sum_{i=1}^{n} (p_i - \nu_i)^2}{n}} \tag{2.5.17}$$

where $P = [p_1, p_2, \ldots, p_N]$ and $A = [\nu_1, \nu_2, \ldots, \nu_N]$ are the vectors for the fitted and tested values of the strain profiles, respectively.

Table 2.5.1. Sensitivity analysis for polynomial fitting of strain surface

SSE ($\mu\varepsilon^2$)		Order of *x*				
		1	2	3	4	5
Order of *y*	1	7.03×10^9	3.27×10^9	1.45×10^8	7.13×10^7	3.38×10^7
	2	7.04×10^9	3.29×10^9	2.30×10^8	4.21×10^7	$\mathbf{6.44\times10^6}$
	3	7.02×10^9	7.65×10^7	1.23×10^8	4.89×10^7	3.35×10^7
	4	6.97×10^9	7.99×10^7	8.60×10^7	3.43×10^7	9.54×10^7
	5	6.94×10^9	9.12×10^7	1.21×10^8	2.96×10^7	2.99×10^7
R^2		Orders of *x*				
		1	2	3	4	5
Order of *y*	1	0.014	0.528	0.979	0.990	0.995
	2	0.016	0.525	0.967	0.994	**0.997**
	3	0.013	0.989	0.982	0.993	0.995
	4	0.006	0.989	0.988	0.995	0.996
	5	0.001	0.987	0.983	0.996	0.996
RMSE ($\mu\varepsilon$)		Orders of *x*				
		1	2	3	4	5
Order of *y*	1	1.05×10^3	716.50	150.80	105.80	72.8
	2	1.05×10^3	718.90	190.00	81.30	**31.80**
	3	1.05×10^3	109.60	138.70	87.26	72.59
	4	1.05×10^3	112.00	116.20	73.44	38.73
	5	1.04×10^3	119.70	137.80	68.23	68.61

The pentomic-square fitting (5-order in x axis and 2-order in y axis) had the highest accuracy, in terms of the lowest SSE and RMSE as well as the highest R^2. Both the global and local fitting performance of the fitting surface must be considered. When the polynomial order is too high, the fitting surface will overfit input strain, producing unrealistic estimations. The discrepancy between the pentomic-square fitting surface and the measured distributions is plotted in Figure 2.5.8(a). Large discrepancy is found from the data points near the edges of the plate specimen.

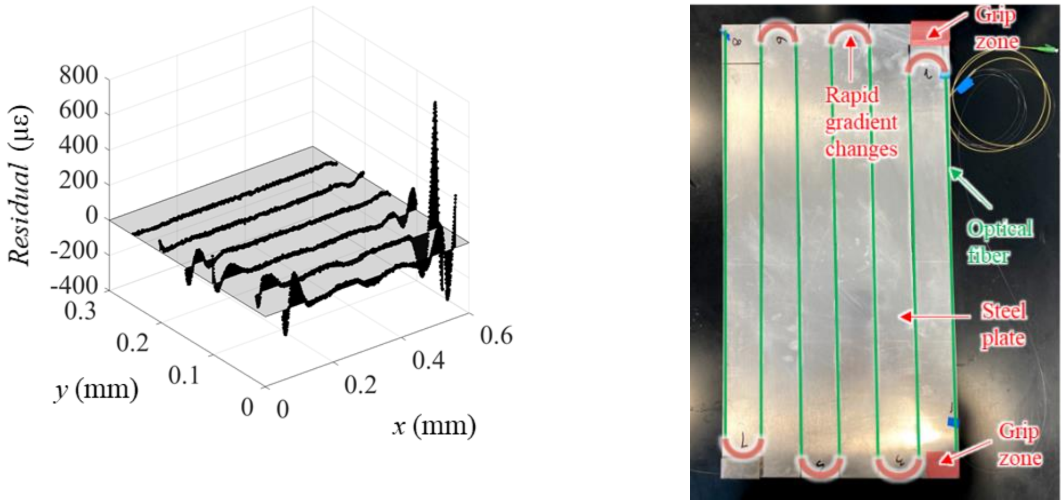

(a) (b)

Figure 2.5.8. Residual profile of strain polynomial fitting surface caused by the bending deformation of the DFOS at the edges.

This is because the optical fiber near the edges was subjected to acute curvatures, as shown in Figure 2.5.8(b). Such results suggest that it is inappropriate to use the strains measured from the lengths of curved sensor lengths deployed near the edges. As indicated in Eq. (2.5.10), those lengths should be assigned with low weights to minimize their impact on the results.

Figure 2.5.9 compares the contours of strain distributions of the two sides of the plate specimen under four load levels (3900 N, 4085 N, 4183 N, and 3944 N). Figure 2.5.9(a) shows the contours of side A of the plate specimen. The areas subjected to high tensile strains are shown in red color, and the areas subjected to high compressive strains are shown in blue color.

As the applied load increased from 0 to 3900 N, there was no obvious change in the contours. As the applied load increased from 3900 N to 4183 N, obvious changes were shown in the contours. As the applied load decreased from 4183 N to 3944 N, the magnitudes of strains increased with the decrease of the loads. Figure 2.5.9(b) shows the contours of side B of the plate specimen. No obvious change was observed until the load decreased from 4183 N to 3944 N, when the magnitudes of strains increased with the decrease of the loads, consistent with the contours from side A. The strains measured from side B were lower than those measured from side A, because the DFOS deployed on the two sides of the plate were in different directions. The sensor of side A was along the loading direction and thus subjected to higher deformations under buckling of the plate. The sensor of side B was in the width direction of the plate and subjected to smaller deformations.

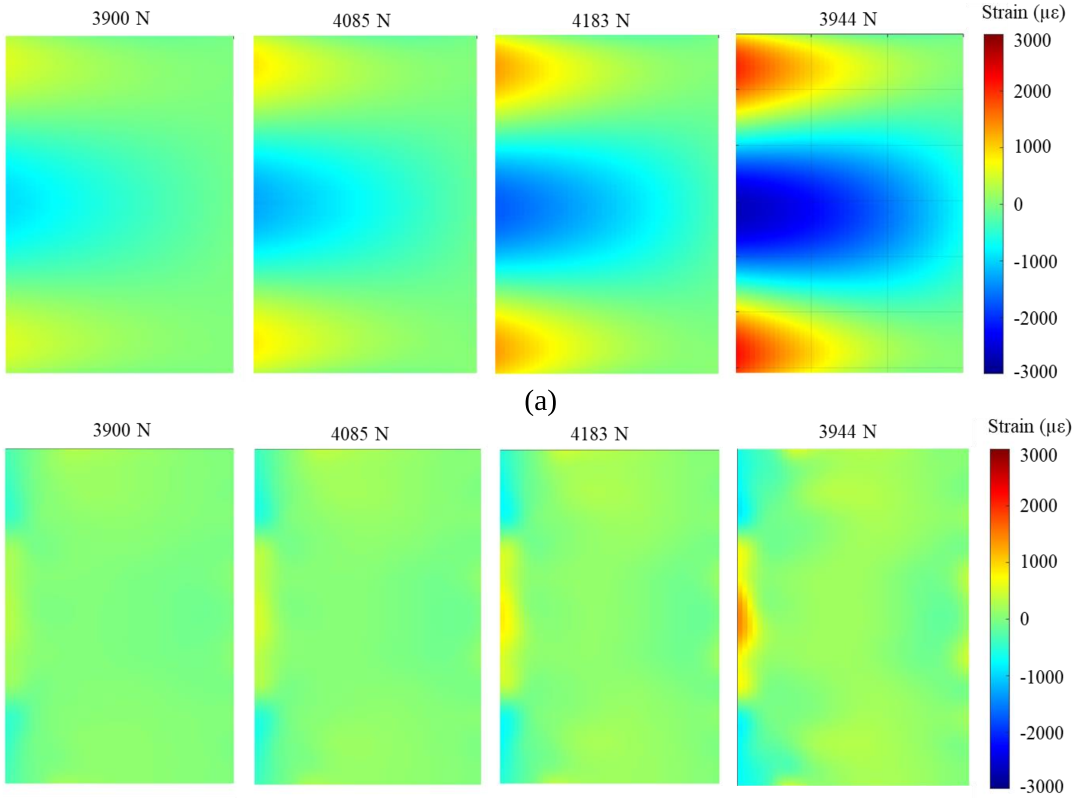

(a)

(b)

Figure 2.5.9. Mapping contours of strain distributions for the plate: (a) side A, and (b) side B.

2.5.3.3. Shape reconstruction

<u>2.5.3.3.1. Bar specimen</u>

The buckling deformation of the bar specimen was reconstructed and compared with the point cloud data from the computer vision system, as shown in Figure 2.5.10. The considered load increased from 292 N to 406 N and then decreased to 395 N. The deformed shapes obtained from the two methods agree well with each other, validating the shape reconstruction method for 1D buckling problems. The discrepancy between the buckling deformations obtained from the two methods was attributed to inherent inaccuracy of the sensors such as the DFOS and deep camara, data acquisition systems, and positions of the DFOS, as well as boundary conditions.

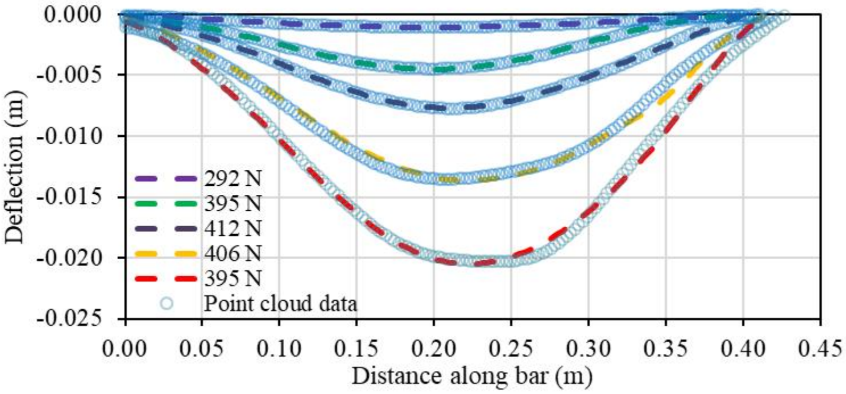

Figure 2.5.10. Deformation of the bar obtained from shape reconstruction and computer vision.

<u>2.5.3.3.2. Plate specimen</u>

Figure 2.5.11 compares the shape reconstruction results obtained from the proposed method and the computer vision method for the plate. The colorful surface represents the shape of the buckled plate obtained from the proposed method, and the black dots represent the point cloud data obtained from computer vision.

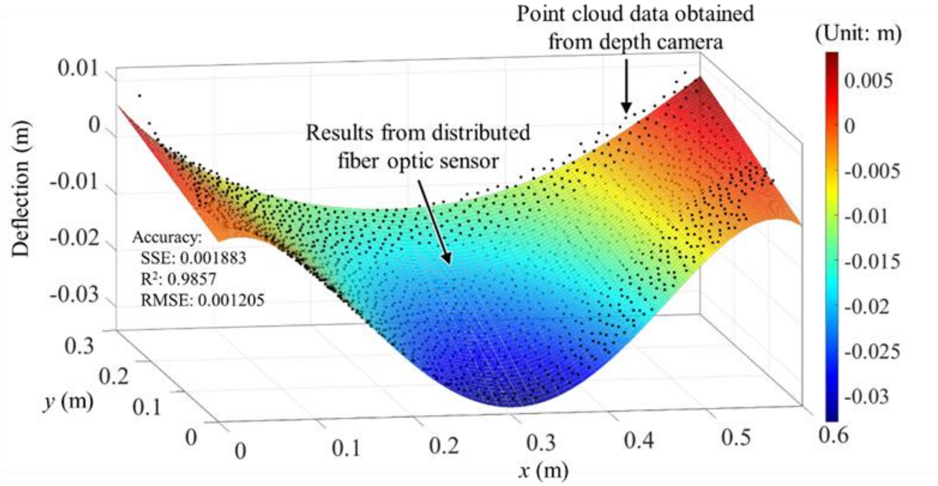

Figure 2.5.11. Comparison of plate deformations obtained from the shape reconstruction method and computer vision method.

Overall, the reconstructed shape fitted with the measured deformation. The values of SSE, R^2, and RMSE are 1.88×10^{-3}, 0.986, and 1.21×10^{-3}, respectively. These values indicate that the accuracy of the proposed shape reconstruction is high. The discrepancy was mainly at the edges due to the inaccurate strains as shown in Figure 2.5.8.

2.5.3.3.3. Accuracy

Figure 2.5.12 shows the performance metrics of the shape reconstruction results evaluated against the computer vision results. When the specimens were loaded until buckling occurred, the accuracy of the shape reconstruction method was reduced. The reduction was attributed to the large local deformation because the adopted strain-deflection relationship in Eq. (2.5.10) was based on the small deformation assumption, which is inapplicable for large deformations.

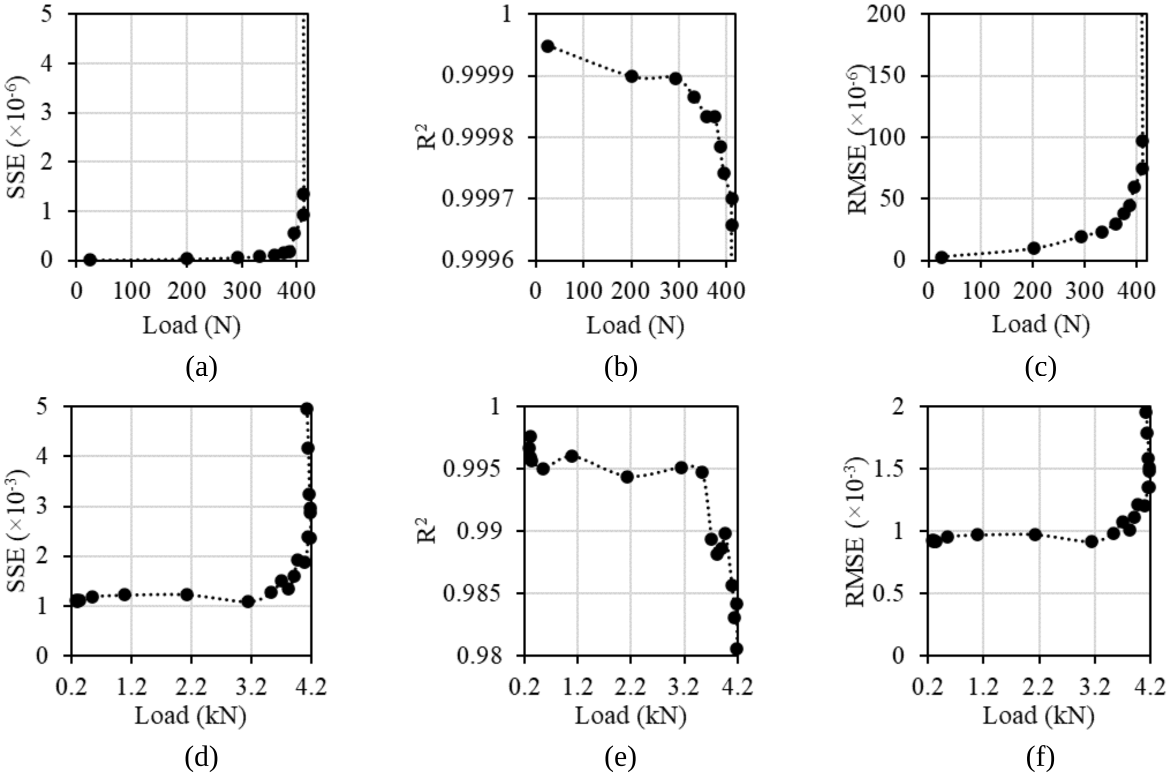

Figure 2.5.12. Performance metrics of shape reconstruction of the bar and plate specimens in the buckling process: (a) SSE of the bar; (b) R^2 of the bar; (c) RMSE of the bar; (d) SSE of the plate; (e) R^2 of the plate; and (f) RMSE of the plate.

2.5.4. Parametric study

2.5.4.1. Spatial resolution

Figure 2.5.13 shows the effect of the spatial resolution of the DFOS deployed on the plate specimen. As the spatial resolution changed from 0.65 mm to 2.6 mm, the changes of SSE, R^2, and RMSE were negligible. As the spatial resolution changed from 2.6 mm to 20.8 mm, the values of SSE and RMSE rapidly increased, and R^2 decreased.

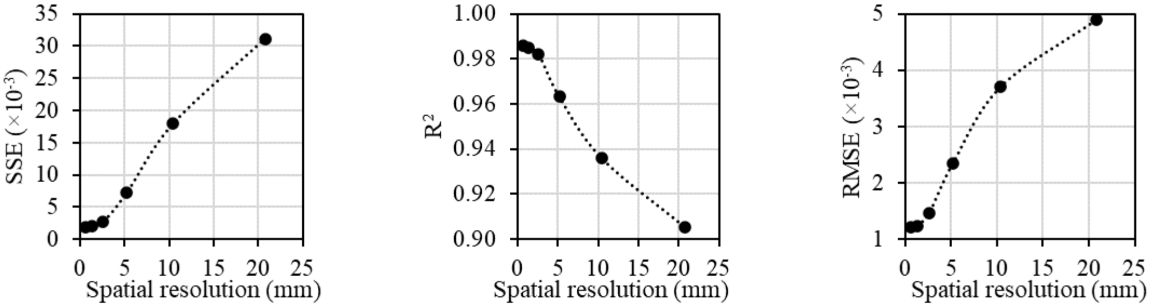

(a) (b) (c)

Figure 2.5.13. Effect of the spatial resolution for the plate specimen when the load was 4 kN: (a) SSE; (b) R^2; and (c) RMSE.

The results indicated that the spatial resolution had a significant effect on the measurement accuracy. In real applications, selection of an appropriate spatial resolution is critical to achieve high accuracy and data efficiency. If the spatial resolution is too high, a big dataset will be recorded. It is recommended to use 2.6 mm as the optimal spatial resolution for buckling detection and shape reconstruction. The corresponding values of SSE, R^2, and RMSE are 1.98×10^{-3}, 0.98, and 1.23×10^{-3} respectively.

2.5.4.2 Sensor deployment

Figure 2.5.14 shows the effect of the sensor deployment scheme on shape reconstruction accuracy of the plate specimen. The spacing between adjacent sensor paths was used to characterize the deployment scheme. As the spacing between adjacent strips increased from 50.8 mmm to 304.8 mm, the values of SSE and RMSE were significantly increased, and R^2 were highly reduced. The results indicated that fine spacing benefited the accuracy. To balance the accuracy and sensor deployment efficiency, the recommended spacing is 100 mm or finer.

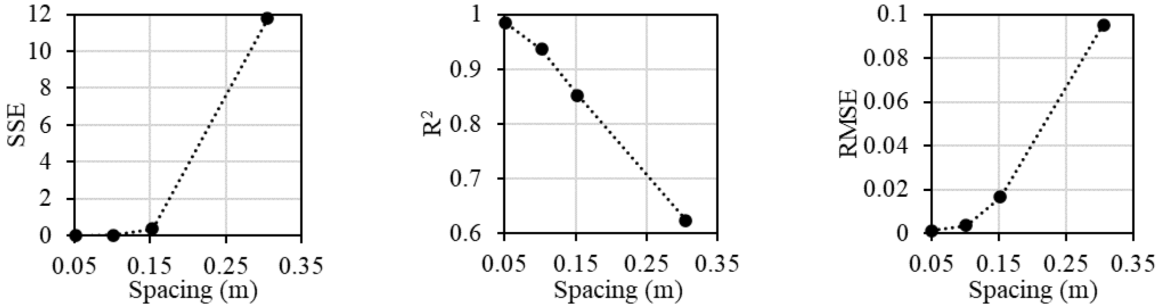

(a) (b) (c)

Figure 2.5.14. Effect of the sensor deployment scheme for the plate specimen when the load was 4 kN: (a) SSE; (b) R^2; and (c) RMSE.

2.5.5. Summary

This research develops an approach to detect, measure, visualize, and quantify 3D buckling of thin-walled structures using DFOS with sub-mm spatial resolutions in real time. An effective and practical shape reconstruction method was developed to derive the deformed shape based on the strain distributions. The reconstructed shape was validated using a computer vision method that measured point cloud from the specimens. A parametric study was conducted to investigate the effects of key sensing parameters such as the spatial resolution and sensor deployment scheme on the performance of the shape reconstruction method, and used to optimize the resolution and deployment of DFOS. Based on the above investigations, the following conclusions are drawn:

(1) DFOS can be used to measure detailed strain distributions of thin-walled structures subjected to buckling. The measured strain distributions can be used to detect, visualize, and quantify 3D buckling deformation. The capabilities of visualization and quantification enable engineers to immediately assess the structural condition.

(2) The proposed shape reconstruction method achieved adequate accuracy in bar and plate structures subjected to buckling. The deformed shape of the plate specimen was complex due to the eccentric loading condition. The complex shape was reconstructed using the proposed method. The shape reconstruction results were comparable with the computer vision method but did not require visibility of cameras for the monitored structure.

(3) The spatial resolution and sensor installation pattern showed significant effects on the accuracy of shape reconstruction. Fine spatial resolution and spacing of DFOS benefited the accuracy. It is recommended to use 2.6 mm as the spatial resolution and 100 mm as the spacing in practical applications.

(4) This research focuses on investigation of the feasibility of the proposed method for bar and plate specimens. The performance of the proposed method for pipes is still unknown, but it is envisioned that comparable performance can be achieved from pipes since the method is based on strains. Buckling/dents will be detected as long as the strain field of the pipe is changed. In this research, modification of the strain-deflection relationship for large local deformations was not considered. It is envisioned that the accuracy will be improved by considering large deformations. Future research will be performed to improve the shape reconstruction method and validate the performance in real pipes.

The research in section 2.5 reveals that distributed fiber optic sensors can be used to monitor dents via measuring strain distributions, as illustrated in Figure 2.5.15. The dents can be caused by third-party activities such as excavation. This dent monitoring capability is similar to the crack monitoring capability, while the deformation is different which causes different strain profiles. The layout of the sensor can be straight or spiral (Figure 2.3.9), depending on the specific use case.

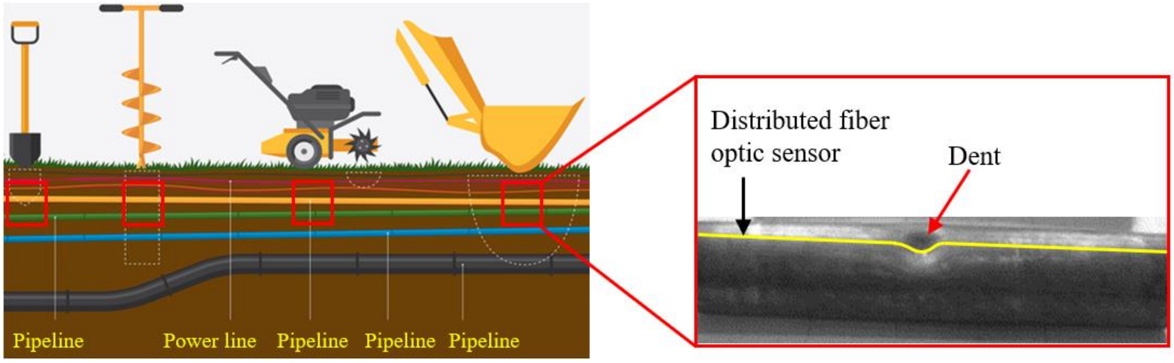

Figure 2.5.15. Monitoring of dents in pipelines subjected to third-party excavation or other impacts.

2.6. Detection, localization, quantification, and visualization of corrosion

2.6.1. Overview

In previous research on distributed fiber optic corrosion sensors, the emphasis was mainly placed on feasibility of using DFOS to detect corrosion. Although the results showed a good promise, some challenges concerning real-life applications have been identified: (1) It is a challenge for pipeline engineers and stakeholders to understand and accurately interpret the unique sensor data measured from DFOS in practice. Skilled sensor experts are needed to process and explain the sensor data, thus increasing the operation cost of DFOS. (2) It is unclear how the corrosion condition of pipeline can be quantitatively evaluated using the data measured from the distributed sensors. In general, the DFOS data are associated with the severity of corrosion. However, there is lack of effective tools to quantify the relationship and generate warning for the severity of corrosion. (3) It is unknown how corrosion assessment using distributed sensors is affected by key parameters of the fiber optic cable, sensing parameters, and sensor deployment methods. These challenges hinder a wider application of DFOS for enhancing the capability of pipeline monitoring and improving safety.

This paper presents a distributed monitoring method for detection, localization, visualization, quantification, and warning for pipe corrosion based on the measurement from a DFOS. This paper has three main contributions: (1) development of a distributed sensing method to detect, locate, and visualize corrosion of pipes; (2) development of a meso-scale analytical model to quantify mass loss due to corrosion and provide warning; and (3) investigation of the effects of important influencing factors on the assessment of pipe corrosion. To validate the developed method, steel pipes were prepared and instrumented with distributed sensors, and immersed in a sodium chloride solution (concentration: 3.5 wt.%) for corrosion tests. Strain distributions were measured from the distributed sensors based on OFDR. Mass loss of pipes was evaluated using a high-precision microbalance. A meso-scale analytical model was developed and presented to correlate the measured strains with mass loss of pipes due to corrosion. The effects of optical fiber type, spatial resolution of strain measurement, and sensor deployment pattern on corrosion assessment were investigated. Finally, a threshold-based warning method was developed based on corrosion assessment data for real-time alarming of pipe corrosion condition.

2.6.2. Experimental program

2.6.2.1. Materials and specimen preparation

Figure 2.6.1 shows the dimensions of the investigated pipes that were made using low-carbon and stainless steel, respectively. Low-carbon steel is commonly used in transmission pipelines for oil and gas, following standards ASTM A733 and ASTM A269. Stainless steel with high corrosion resistance was used as reference to evaluate corrosion. The outer diameter and wall thickness were 25.4 mm and 3 mm, respectively. Although this research was conducted using these pipes with limited types of materials and dimensions, the approach is applicable to various pipes with different sizes and materials because the developed approach is based on strain measurement. Corrosion of pipes will be monitored as long as corrosion causes strain changes.

(a) (b)

Figure 2.6.1. Pipe specimens: (a) a low-carbon steel pipe; and (b) a stainless steel pipe.

A fiber optic cable was installed on the pipe after cleaning the rust on pipe surface in three steps. First, the fiber optic cable was attached to a pipe at discrete spots using tape. Second, the fiber optic cable was fixed on the pipe at discrete points using a fast-curing glue. Third, the tape at discrete spots on the pipe was removed, and a two-part epoxy was applied along the fiber optic cable to ensure a reliable attachment of fiber and effective strain transfer between outer coating or tight buffer and pipe. The epoxy only covered the fiber optic cable and the cable line on the pipe. Any epoxy that flowed away from the fiber optic cable was cleaned to avoid potential effect on pipe corrosion. The installation of sensor for monitoring a continuous length of 1 m took less than 10 minutes by one person. The time and labor requirements are reasonably low compared with the existing sensor technologies for pipeline inspection. Figure 2.6.2 shows the deployment pattern of fiber optic cables. The fiber optic cable was installed on the pipe following a helix pattern. Different spacings between adjacent spirals were investigated to optimize the deployment.

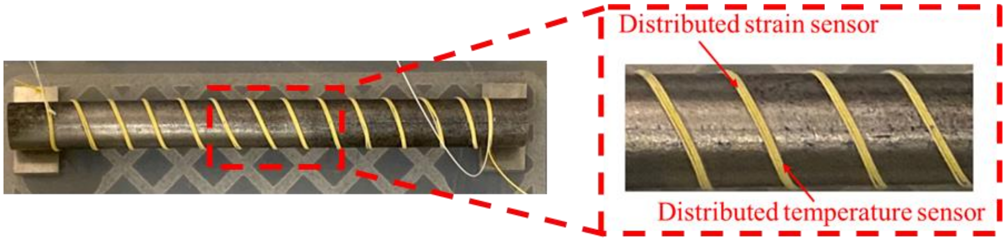

Figure 2.6.2. Deployment of a coated fiber optic cable as a sensor on a pipe specimen.

2.6.2.2. Investigated cases

A total of 14 different cases were investigated, as listed in Table 2.6.1. The pipe specimens were grouped into four categories, designated as P0 to P3. P0 was the control specimen made using stainless steel.

Group P1 includes three specimens which were designed for low-carbon steel pipes used to investigate the effects of three different coating thicknesses of fiber optic cable (242 μm, 650 μm, and 900 μm). Group P2 includes one specimen that was designed to investigate the effect of five different measurement spatial resolutions of DFOS (0.65 mm, 1.30 mm, 2.60 mm, 10.40 mm, and 20.80 mm). Group P3 has five specimens to investigate five different helix spacings (10 mm, 20 mm, 40 mm, 60 mm, and 80 mm) for the sensor deployment.

Table 2.6.1. Investigated cases of corrosion testing

Cases	Pipe group	Cable diameter (μm)	Spatial resolution (mm)	Spacing (mm)
1	P0	900	0.65	20
2	P1	242	0.65	20
3		650	0.65	20
4		900	0.65	20
5	P2	900	0.65	20
6		900	1.30	20
7		900	2.60	20
8		900	10.40	20
9		900	20.80	20
10	P3	242	0.65	10
11		242	0.65	20
12		242	0.65	40
13		242	0.65	60
14		242	0.65	80

2.6.2.3. Experimental set-up

After the epoxy was hardened after 24 hours (h), the pipes were put in a plastic container and immersed in a sodium chloride solution (concentration: 3.5% by mass) for corrosion tests at room temperature (25 ºC ± 2 ºC). Figure 2.6.3(a) shows the test set-up.

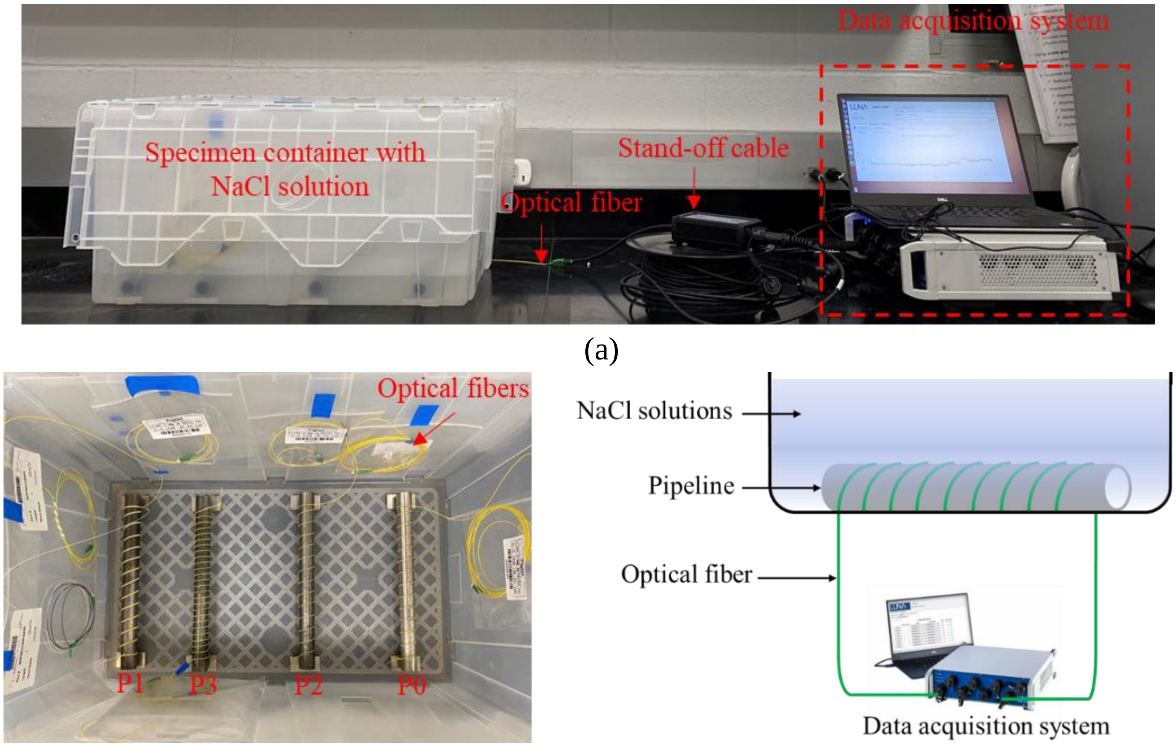

(a)

(b) (c)

Figure 2.6.3. Corrosion test of steel pipes: (a) test set-up; (b) four pipe specimens; and (c) illustration of a pipe instrumented with DFOS.

The fiber optic cable was connected to the distributed sensing system for data acquisition. Each measurement took about 20 s to 40 s, and the measurement frequency was 2 Hz. A distributed temperature sensor was used for temperature compensation, which could eliminate the effect of temperature variation on the measurement of strain distributions from the distributed strain sensor. The pipes were supported by plastic blocks at the two ends to fully expose the bottom of the pipes to the sodium chloride solution as shown in Figure 2.6.3(b) and Figure 2.6.3(c) as an example.

2.6.3. Experimental results

2.6.3.1. Visual inspection

Figure 2.6.4 shows an example of representative visual inspection results from one specimen in each testing group. No rust was observed on the control pipe (P0) made of stainless steel. Rust grew on the external surfaces of pipes in groups P1 to P3. As the immersion time increased, the thickness of rust increased. Most rust was attached to the surface of the pipes, and only a small volume of rust was transported off the pipes. Since the corrosion products are expansive and have a lower density compared with intact steel, the diameter of the corroded pipe was increased.

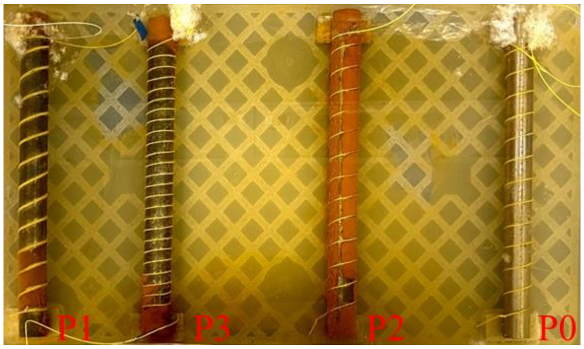

Figure 2.6.4. Four pipes immersed in a sodium chloride solution for corrosion experiments.

2.6.3.2. Strain distributions

The increase of the pipe diameter caused strain changes in the DFOS on the pipes. Figure 2.6.5 shows the strain distributions measured from the DFOS at different immersion times (30 h, 60 h, 114 h, 134 h, 184 h, 208 h, 280 h, 472 h, 640 h, 912 h, and 1080 h). The vertical axis represents the tensile strain induced by corrosion, and the horizontal axis represents the distance along the DFOS, with the zero distance at the connector of the data acquisition system.

In each figure, the length range of the DFOS is selected to show the strain distributions within the length of fiber optic cable wrapped on the pipes. As shown in Figure 2.6.5(a), for the control specimen, a small strain change was measured, indicating negligible corrosion, which is consistent with visual inspection. The small strain change can be attributed to the expansion of the coatings of fiber optic cables due to water absorption. Although the coatings had a high water resistance and negligible degradation with presence of water, as specified by the manufacturer, the coating could absorb water and expand slightly. The effect of the expansion due to water absorption on the strains measured from the fiber optic cable should be calibrated and subtracted from the strain distributions used to evaluate corrosion of the pipe specimens.

Figures 2.6.5(b) to 2.6.5(d) show the strain distributions measured from the DFOS deployed on the specimens in groups P1 to P3. Obvious strain changes along the pipes can be observed. Compared with results of P0 shown in Figure 2.6.5(a), the values of strain distributions for P1 to P3 at the same immersion durations are much larger because rust was generated on the surfaces of the specimens in groups P1 to P3. Non-uniform strain distributions are observed because corrosion is uneven, which can be attributed to the different material defects and surface conditions. Compared with P1 and P2, the non-uniform strain distributions for P3 shown in Figure 2.6.5(d) are more obvious, which might be attributed to the smaller helix spacing.

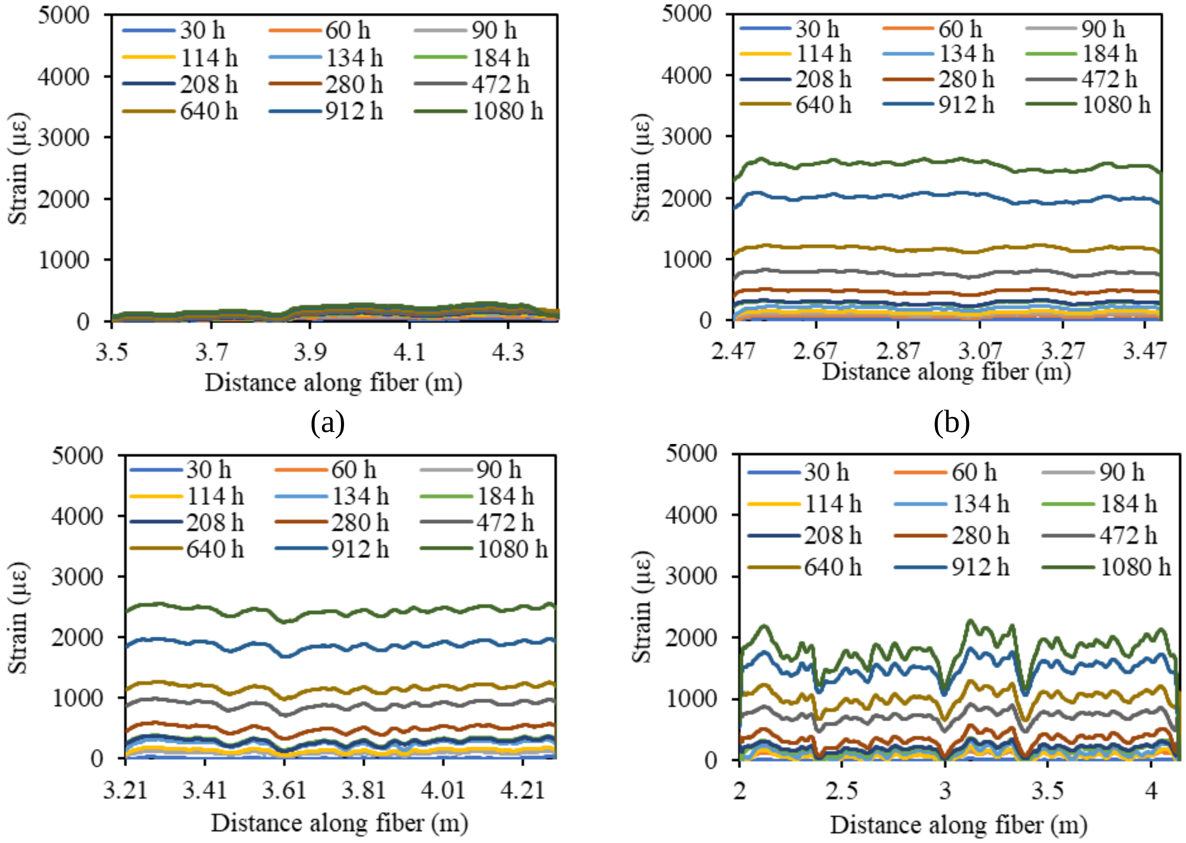

(a) (b)

(c) (d)

Figure 2.6.5. Strain distributions measured from the DFOS deployed along the pipe specimens: (a) Case 1 in group P0; (b) Case 2 in group P1; (c) Case 5 in group P2; and (d) Case 10 in group P3.

2.6.3.3. Visualization

The expansion induced by corrosion of a pipe was detected by the change of strains sensed by a DFOS. With the location of the DFOS installed on the pipe, the distance along the DFOS can be correlated with the position of the pipe surface. With the correlation, the strain distributions measured from the DFOS can be replotted via a coordinate transform, as shown in Figure 2.6.6.

The position of the DFOS on the pipes is described in a polar coordinate system, which can be transformed into coordinated in a Cartesian coordinate system. The specimen is cut along the pipe, and the circumference is unfolded to a flat plane (Figure 2.6.6). The circumference of the pipe becomes the width of the plane, and the length of the pipe remains the length of the plane. The strain distributions measured from the DFOS is plotted in the plane to show a 2D contour, which can be used for visualization of corrosion in real time. The data between adjacent paths of fiber optic cable were obtained via biharmonic spline interpolant using MATLAB curve fitting tool function. The different paths of the DFOS show the strain variations.

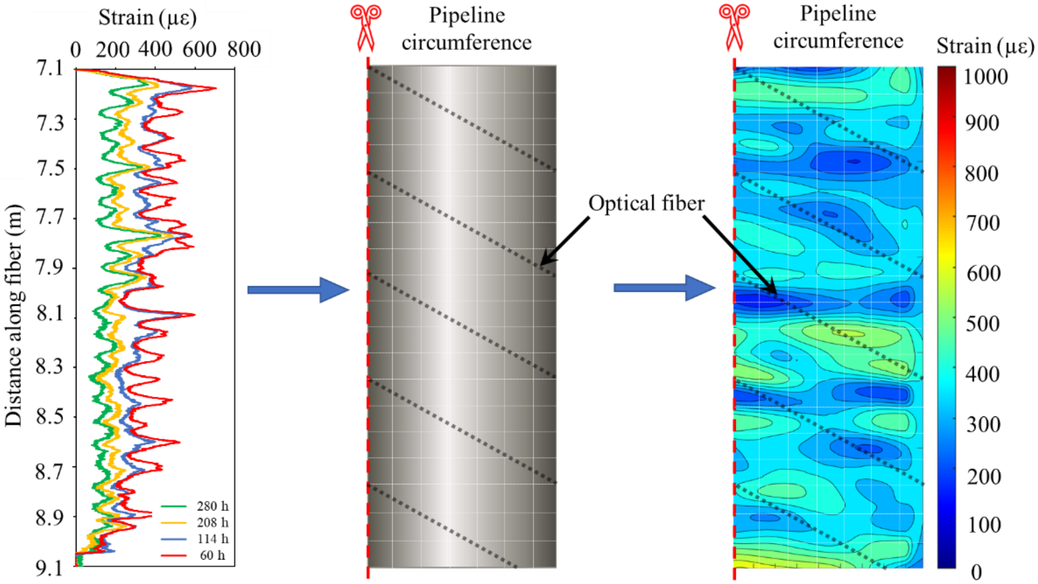

Figure 2.6.6. Method of mapping strain distributions on a pipe for visualization of corrosion.

Figure 2.6.7 shows the mapping of corrosion at different immersion times (30 h, 472 h, 912 h, and 1080 h). The areas of pipes subjected to high strains are shown in red color, indicating that the areas have more severe corrosion.

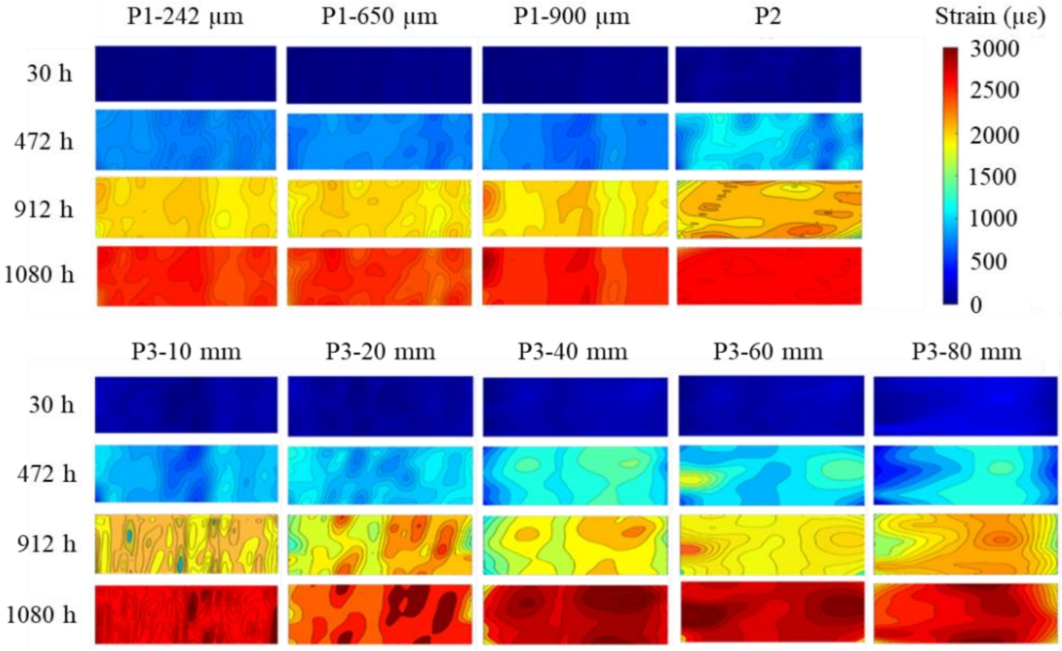

Figure 2.6.7. Mapping of corrosion for specimens with a measurement spatial resolution of 0.65 mm.

Figure 2.6.8(a) shows the measurement of corrosion from specimens in group P2. As the spatial resolution changed from 0.65 mm to 2.6 mm, there was no obvious difference in the images. As the spatial resolution changed from 2.6 mm to 10.4 mm, obvious difference could be seen from the pictures. As the spatial resolution changed from 10.4 mm to 20.8 mm, the corrosion distribution could not be reasonably assessed, indicating that the spatial resolution had a significant effect on corrosion visualization. Figure 2.6.8(b) plots the monitored corrosion condition from specimens in group P3 with different helix spacings. As the spacing increased from 10 mm to 80 mm, the visualization results were highly changed, indicating a sensitivity to the helix spacing, which can be attributed to uneven corrosion distribution. A coarse helix spacing miss critical information.

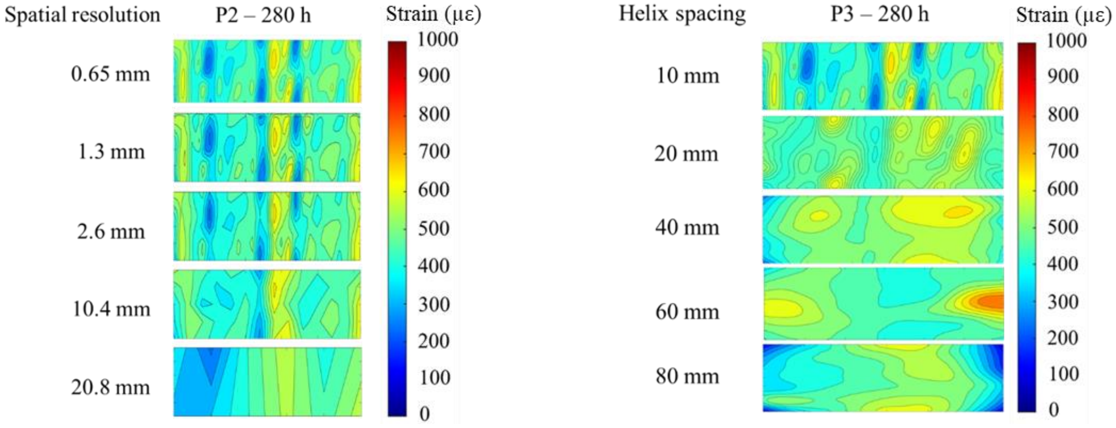

(a) (b)

Figure 2.6.8. Corrosion condition of: (a) P2 specimens at 280 h; and (b) P3 specimens at 280 h.

2.6.3.4. Quantification

<u>2.6.3.4.1. Mass loss evaluation</u>

Mass loss evaluation is a common method used to evaluate corrosion of pipelines. A reference sample of a pipe under consideration is prepared and placed near the pipe under corrosion. The mass loss of reference sample is measured to evaluate the mass loss of the pipe, assuming that the sample is subjected to the same corrosion rate as the pipe. This study used short pipes as reference samples for mass loss evaluation, as shown in Figure 2.6.9(a).

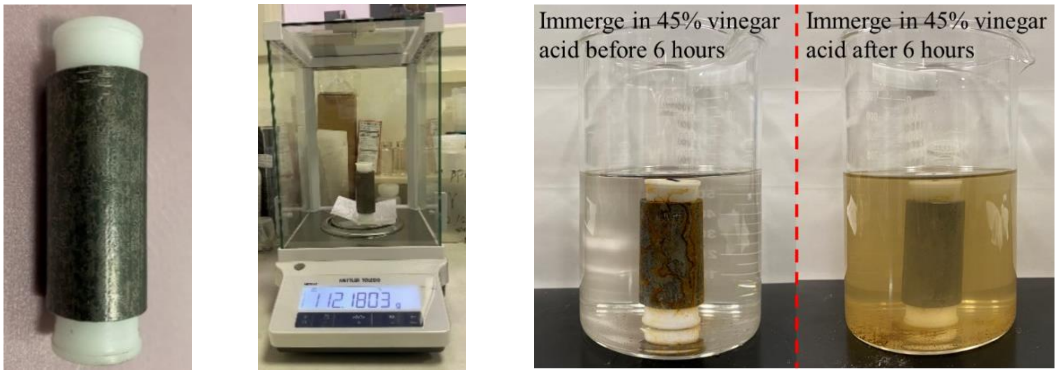

(a) (b) (c)

Figure 2.6.9. Evaluation of mass loss: (a) reference pipe; (b) high-precision microbalance; and (c) reference pipe in a vinegar acid solution for removing surface rust.

The reference pipes measured 60 mm in length, and their two ends were sealed using plastic corks to prevent ingress of sodium chloride. Before the corrosion test, the reference pipes were cleaned, and the initial mass was measured using a high-precision microbalance (model: Mettler-Toledo Balance ME204E, USA), as shown in Figure 2.6.9(b). The readability of the high-precision microbalance was 0.1 mg. Then, the reference pipes were immersed in the same sodium chloride solution as the test pipes with DFOS. For every 12 h, one reference pipe was taken out of the solution to evaluate the mass loss, so the corrosion condition of pipes can be assessed over time. Before mass measurement, the reference pipe was immersed in a vinegar acid (concentration: 45% by mass) for 6 h to remove corrosion products from the surface, as shown in Figure 2.6.9(c). Then, the reference pipe was rinsed under running water. Next, it was placed in an oven at 70 °C for 15 min to get dried. After the reference pipe was cooled in air to room temperature, its mass was measured again using the high-precision microbalance. The mass of the reference was compared with its initial mass, and the mass difference is the mass loss (Δm) due to corrosion.

2.6.3.4.2. Pipe corrosion model

Figure 2.6.10 shows a meso-scale model of a steel pipe with corrosion. A fiber optic cable was installed on the surface in a helix pattern. Due to symmetry, only half of the cross section of pipe is shown. Since the fiber optic cable is winded on the surface of the pipe, the cut section of the cable has an ellipse shape in an arbitrary section perpendicular to the pipe length. The uncorroded section of the pipe is shown in orange color; the corrosion products (rust) that grow on the surface of the steel is shown in red color; the buffer of the fiber optic cable is shown in green color; and the fiber core is shown in white color. The rust is porous and has a larger volume than the steel, thus exerting pressure to the fiber optic cable. The pressure causes elongation of the fiber optic cable, and thus results in tensile strains in the fiber optic cable. Therefore, the strain change in the fiber optic cable reflects the corrosion process of the pipe. Figure 2.6.10(b) shows the geometry of the pipe after it is cut and unfolded to a flat plane. The round circumference is turned to a straight line. In the course of corrosion, the length of the fiber optic cable and the pipe perimeter are elongated, while the spacing (s) of adjacent fiber paths is retained.

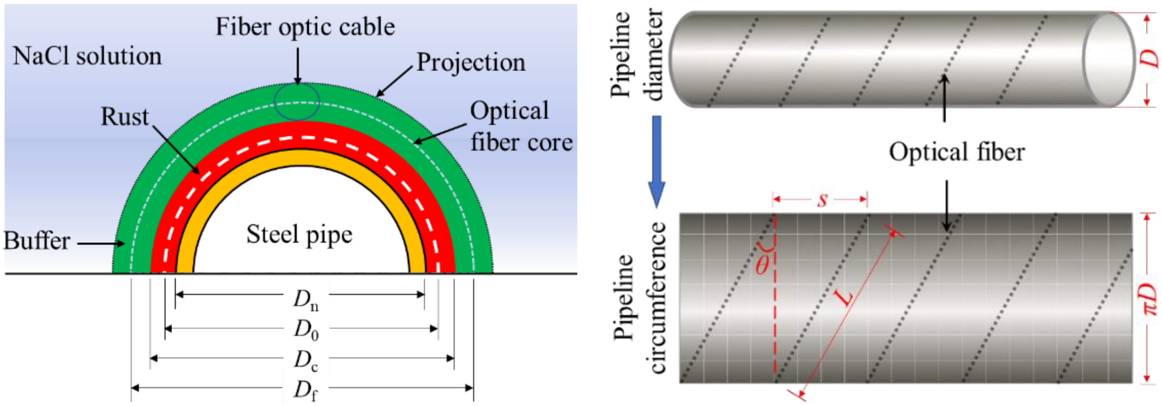

(a) (b)

Figure 2.6.10. Meso-scale corrosion model of a steel pipe with a DFOS: (a) Diameter change due to the corrosion; and (b) the geometry of the pipe after cut and unfolded to a flat plane.

To derive formulae for evaluating mass loss due to corrosion using the DFOS, the following assumptions are adopted:

(1) All pipe corrosion products remain on the pipe surface. When pipes are embedded in soil or exposed to air, most corrosion products will stay on the pipe surface. Only a small amount of rust was transported to the solution.

(2) The cross section of the pipe is circular throughout the corrosion process.

In Figure 2.6.10, the outer diameter of the pipe is D_0 (D_0 = 25.4 mm) before corrosion and D_n after corrosion, the diameter including the rust layer is D_c, and the diameter including the rust layer and a half thickness of fiber optic cable is D_f. Thus, the cross-sectional area (A_p) and volume (V_p) of the corroded steel of the pipe and the volume of rust (V_r) can be expressed as:

$$A_p = \frac{1}{4}\pi\left({D_0}^2 - {D_n}^2\right) \tag{2.6.4}$$

$$V_p = \frac{1}{4}\pi\left({D_0}^2 - {D_n}^2\right)L \tag{2.6.5}$$

$$V_r = \frac{1}{4}\pi\left({D_c}^2 - {D_n}^2\right)L \tag{2.6.6}$$

Therefore, the mass loss of the pipe (Δm) due to corrosion can be expressed as:

$$\Delta m = \frac{1}{4}\pi\left({D_0}^2 - {D_n}^2\right)\rho L \tag{2.6.7}$$

where L is the pipe length subjected to corrosion (L = 300 mm in this study); and ρ is the density of pipe material (ρ = 7850 kg/m^3 in this study).

In Figure 2.6.10(b), the original fiber length (l_0) and fiber length after corrosion (l_f) are:

$$l_0 = \sqrt{(\pi D_0)^2 + s^2} \tag{2.6.8a}$$

$$l_\mathrm{f} = \sqrt{(\pi D_\mathrm{f})^2 + s^2} \tag{2.6.8b}$$

Therefore, the average strain in the fiber optic sensor can be calculated as:

$$\varepsilon = \frac{l_\mathrm{f} - l_0}{l_0} = \sqrt{\frac{(\pi D_\mathrm{f})^2 + s^2}{(\pi D_0)^2 + s^2}} - 1 \tag{2.6.9a}$$

Since the thickness of the fiber optic cable is negligible compared with the diameter of the pipe, D_f can be replaced by D_c in Eq. (2.6.9a), and the equation can be rewritten as:

$$\varepsilon = \sqrt{\frac{(\pi D_c)^2 + s^2}{(\pi D_0)^2 + s^2}} - 1 \tag{2.6.9b}$$

The volume expansion coefficient (k) of the rust will be defined as:

$$k = \frac{V_r}{V_p} = \frac{{D_c}^2 - {D_n}^2}{{D_0}^2 - {D_n}^2} \tag{2.6.10}$$

With Eq. (2.6.9) and Eq. (2.6.10), Eq. (2.6.7) can be converted into Eq. (2.6.11):

$$\Delta m = \frac{\pi \rho L {D_0}^2}{4(k-1)}\left[(1+\alpha^2)(2\varepsilon+\varepsilon^2)\right] \tag{2.6.11a}$$

$$\alpha = \frac{s}{\pi D_0} \tag{2.6.11b}$$

The volume expansion coefficient of rust is approximately equal to k = 2 for steel corrosion. By assuming k = 2, Eq. (2.6.11) can be rewritten as:

$$\Delta m = \frac{\pi \rho L {D_0}^2}{4}\left[(1+\alpha^2)(2\varepsilon+\varepsilon^2)\right] \tag{2.6.12}$$

Eq. (2.6.12) describes the relationship between the mass loss of the pipe and the strain measured from the DFOS, and considers the effect of the helix spacing on the strain measurement from the DFOS. In other words, once the strain distribution is measured from the DFOS, the mass loss of the pipe can be estimated using Eq. (2.6.12). According to Eq. (2.6.12), Figure 2.6.11 plots the estimated mass loss results of the tested pipes obtained from the strains measured from the DFOS for groups P0 to P3, respectively. Except Figure 2.6.11(a), each figure of Figures 2.6.11(b) to 2.6.11(d) summarizes the results of multiple specimens in the group.

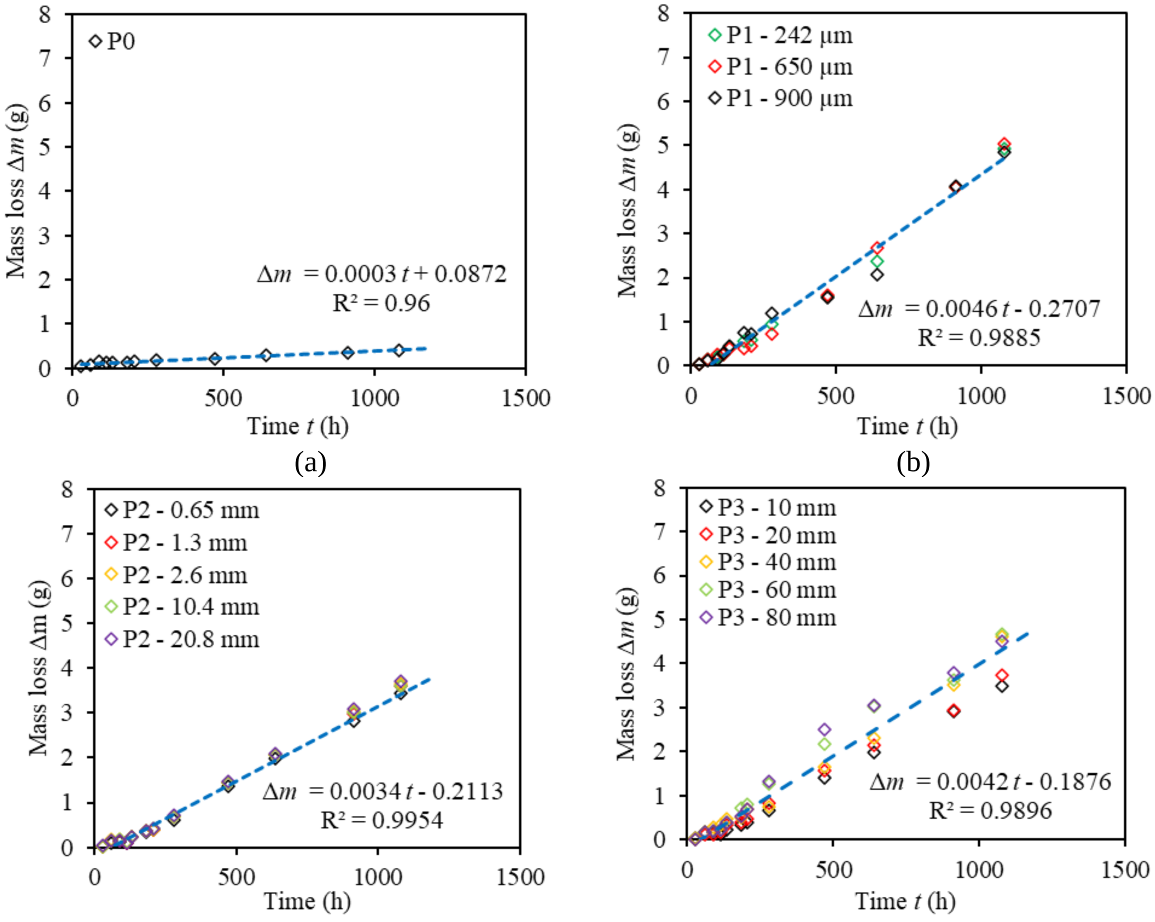

(a) (b)

(c) (d)

Figure 2.6.11. Results of mass loss of the pipe specimens: (a) P0; (b) P1; (c) P2; and (d) P3.

2.6.3.4.3. Calibration of corrosion expansion coefficient

To validate the mass loss measurement using DFOS, Figure 2.6.12 summarizes the results from specimens P1, P2, and P3. The data are fitted using a linear equation through a regression analysis. The obtained R^2 is 0.993, indicating a good correlation. However, the slope of the fitting line is 1.718, meaning that there is a factor between the estimated mass loss using the DFOS and the reference mass loss using microbalance. The factor can be attributed to the assumed value of k in Eq. (2.6.13).

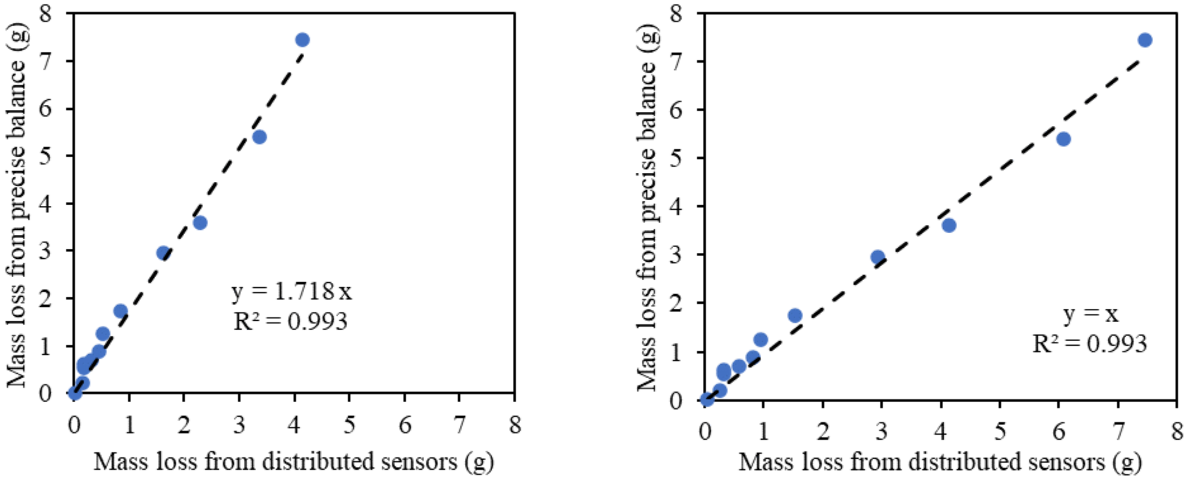

(a) (b)

Figure 2.6.12. Comparison of measured and calculated mass loss of pipes: (a) k = 2; (b) k = 1.582.

According to the slope in Figure 2.6.12(a), the k value can be revised to k = 1.582 for the laboratory tests performed in this paper. Thus, Eq. (2.6.12) can be rewritten as Eq. (2.6.13). By applying Eq. (2.6.13), the mass loss is re-estimated and plotted in Figure 2.6.12(b). The slope changed to 1.000, indicating that the proposed calibration method provides reasonable evaluation of the mass loss of the pipe under corrosion.

$$\Delta m \approx \frac{\pi \rho L {D_0}^2}{2.328}\left[(1+\alpha^2)(2\varepsilon+\varepsilon^2)\right] \tag{2.6.13}$$

2.6.3.4.4. Accuracy

With the corrosion assessment described using the mass loss of pipe (Δm) measured from the DFOS and high-precision microbalance, respectively, measurement error is defined based on mean absolute deviation [63], as described in Eq. (2.6.14):

$$\text{Error} = \frac{1}{n}\sum_{i=1}^{n}\sqrt{\left(\Delta m_{\text{calculating},i} - \Delta m_{\text{fitting},i}\right)^2} \tag{2.6.14}$$

where n is the total number of data points; $\Delta m_{\text{calculating},i}$ is mass loss calculated using Eq. (2.6.13) based on the measurement of strain distribution from the DFOS; and $\Delta m_{\text{fitting},i}$ is mass loss determined from the linear fitting as shown in Figure 2.6.13(b).

Figure 2.6.13 shows the effects of the coating thickness, spatial resolution, and helix spacing on the accuracy of the proposed method for corrosion assessment. Figure 2.6.13(a) shows the effect of coating thicknesses. As the coating thickness increased from 242 µm to 900 µm, there is only slight change of error within 5%, meaning that the coating thickness does not significantly affect the accuracy. Therefore, fiber optic cables with a thick coating can be used to enhance the mechanical strength. Figure 2.6.13(b) shows the effect of spatial resolution. As the spatial resolution changed from 0.65 mm to 20.8 mm, the error was approximately linearly increased from 0.116 g to 0.273 g, indicating that a fine spatial resolution benefits the measurement accuracy.

In real application for pipeline monitoring, an appropriate spatial resolution is critical to achieve a reasonable accuracy for the evaluation of mass loss while retaining a desired data efficiency. On one hand, if the spatial resolution is too low, the accuracy will be compromised. On the other hand, if the spatial resolution is too high, a big data set with unnecessary data will be recorded. Figure 2.6.13(c) shows the effect of the helix spacing. As the helix spacing increased from 10 mm to 80 mm, the error was approximately linearly increased from 0.112 g to 0.317 g, indicating that a fine spacing of fiber optic cable could benefit the measurement accuracy. When the spacing is small, more detailed information of the corrosion distribution on the surface of pipeline can be captured. This is particularly important in the cases where the corrosion distribution on pipeline is significantly nonuniform, because a coarse spacing of the distribution fiber optic sensor may miss some critical corrosion spots. While the measured strain distributions slightly changed with the coating thickness, the spatial resolution and helix spacing showed significant effects on the contours of corrosion and quantification of mass loss. Based on these results, it is recommended to use the following parameters for the investigated pipes: (1) outer diameter: 25.4 mm; (2) coating thickness: 900 µm; (3) spatial resolution: 10.4 mm; and (4) helix spacing: 40 mm. Further research is needed for pipes with larger diameters.

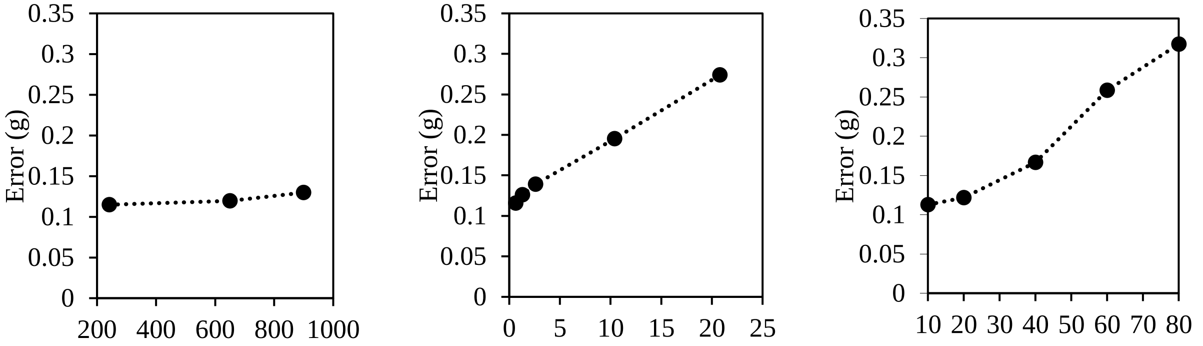

Figure 2.6.13. Evaluation of measurement accuracy of mass loss due to corrosion under different: (a) coating thicknesses; (b) spatial resolutions; and (c) helix spacings.

2.6.3.5 Corrosion warning

The mass loss of pipeline can be used to estimate the average corrosion rate (CR unit in mm/y = millimeter per year), as shown in Eq. (2.6.15):

$$CR = \frac{\Delta m \times 365 \times 1000}{ATD} \tag{2.6.15}$$

where Δm is the mass loss (g); A is the initial exposed surface area (mm^2); T is exposure time (days); and D is density of metal (g/cm^3).

According to the specifications in NACE SP0775-2018 [64], the average corrosion rate is ranked “low” when CR is less than 0.025 mm/y; the average corrosion rate is ranked “moderate” when CR is between 0.025 mm/y and 0.12 mm/y; the average corrosion rate is ranked “high” when CR is between 0.12 mm/y and 0.25 mm/y; and the average corrosion rate is ranked “severe” when CR is larger than 0.25 mm/y. Figure 2.6.14 summarizes the results from specimens P1, P2, and P3. After the pipe was exposed to the sodium chloride solution for 3 days, the value of CR exceeded 0.25 mm/y, indicating a “severe” corrosion. A warning message was generated for the corrosion rate of the monitored pipeline.

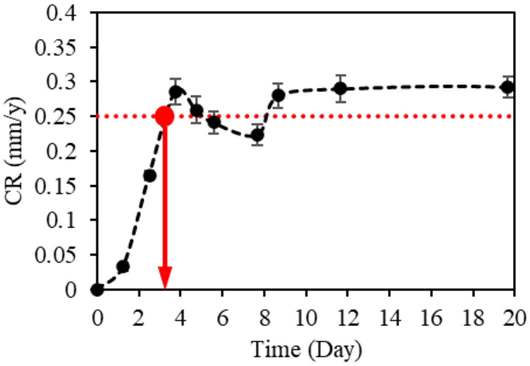

Figure 2.6.14. Warning of pipeline corrosion condition based on the threshold of corrosion rate (CR).

2.6.4. Summary

This chapter presents a real-time monitoring method for detection, localization, visualization, quantification, and warning of pipeline corrosion using a single-mode telecommunication-grade fiber optic cable as a fully-distributed sensor. Corrosion tests of pipes instrumented with different DFOS have been conducted to investigate the effects of package thickness, deployment pattern, and spatial resolution of the sensors on corrosion assessment. A meso-scale analytical model is developed to correlate the measured strains with the mass loss of pipe under corrosion and utilized for corrosion quantification. A threshold-based warning method is proposed for pipeline corrosion management. The experimental results indicate that the presented method is promising for real-time monitoring of pipeline corrosion without influence on normal operation of pipeline. Based on above investigations, the following findings can be drawn:

(1) Corrosion of pipes can induce strain change in DFOS deployed on the surface of pipes. As corrosion is developed, the tensile strain in DFOS is increased. The strains measured from DFOS can be used to detect corrosion on pipes. Strain distribution along a DFOS can be used to locate corrosion on the pipe. With the correlation between DFOS length and position on the pipe, the strains measured from DFOS can be used to locate and visualize corrosion on pipes.

(2) The proposed meso-scale analytical model can be used to describe the dimensional changes in the course of pipe corrosion and elucidate the mechanisms of monitoring pipe corrosion using the DFOS. With the model, the strain measured from the DFOS can be used to quantify the mass loss of pipe due to corrosion. With the measurement results of mass loss of pipes, a rust expansion coefficient in the analytical model could be calibrated and enable reasonable predictions of mass loss using the strains measured from the DFOS. It is recommended to use 1.582 as the rust expansion coefficient in future development and applications. Based on the capability of quantifying pipe corrosion, corrosion warning can be provided by the threshold of corrosion rate.

(3) The strain and corrosion measurement results are dependent on the coating thickness, spatial resolution, and helix spacing of the DFOS. While the measured strain distributions slightly changed with the coating thickness, the spatial resolution and helix spacing showed significant effects on the contours of corrosion and the quantification of mass loss. It is recommended to use the following parameters for pipelines with 25.4-mm outer diameter: coating thickness of 900 µm, spatial resolution of 10.4 mm, and helix spacing of 40 mm. Further research is needed for the appropriate parameters in other sizes of pipes.

Based on this research, the following research needs have been identified:

(1) In this study, the pipe specimens were immersed in sodium chloride solution for corrosion tests. The corrosion rate and microstructures of rusts are different from those of corrosion in air and soil. Further research is needed to test the performance of the proposed method in scenarios of corrosion in air and soil.

(2) This study was focused on laboratory research and development using pipes with a limited length and diameter. The performance of the proposed approach in real-life applications with large pipes remains unclear. Further research is needed to evaluate the performance of the proposed approach. A life-cycle assessment is needed to understand the economic impact of the DFOS on intelligent management of pipelines.

(3) In this study, the use of epoxy in the installation of the fiber optic cables on pipe specimens could slightly affect the corrosion of the pipes because the epoxy could affect the contact of pipe to water and oxygen, given the relatively small pipe surface area. Further research can be conducted using large pipes because the area covered by epoxy can be reduced, so that the effect of epoxy on the corrosion and monitoring performance can be evaluated.

2.7. Measurement of interactive deformations and cracks

2.7.1. Overview

The above research has shown that individual anomalies such as cracks and corrosion can be well measured based on the measurements of strain distributions. When the type of anomalies is known and limited to a single type, the methods developed in the above sections can be utilized to detect, locate, and quantify the anomalies. However, in fact, the real practices often involve many types of anomalies that may occur simultaneously. For example, pipelines are often subject to strain changes. When a pipe has a crack, both the crack and the strains in the pipe are reflected in the strain distributions measured from the DFOS. It is essential to develop effective methods to differentiate the effect of strains and cracks on the strain distributions measured from the DFOS deployed on pipelines.

To address the above challenge, this study aims to: (1) develop a mechanical model to analyze the strain distributions sensed by DFOS subject to both strain changes and cracks; and (2) investigate the interactive effects of strains and cracks that occur simultaneously using DFOS.

2.7.2. Theoretical studies

2.7.2.1. Governing equation

Figure 2.7.1 shows the schematic view of an optical fiber adhered to the substrate in symmetry with a crack with a width of 2δ occurs in the substrate material. By considering symmetry, only a half-segment of the optical fiber has been analyzed.

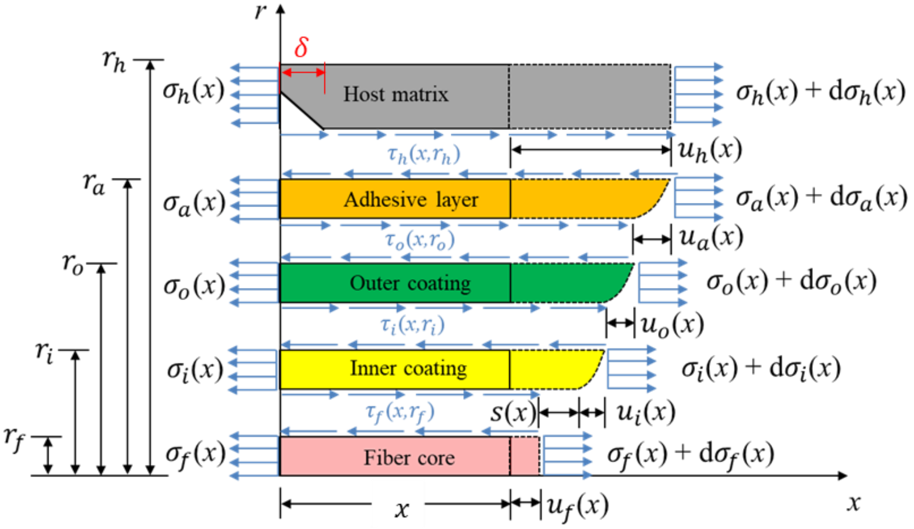

Figure 2.7.1. Illustration of stress and deformation of an optical fiber embedded in a matrix.

$$u_h(x) = u_f(x) + s(x) + u_i(x) + u_o(x) + u_a(x) \tag{2.7.1}$$

$$\varepsilon_f(x) = \frac{du_f(x)}{dx} = u_f'(x) \tag{2.7.2}$$

$$u_h(x) = \int_0^x \varepsilon_h(x)\,dx + \delta \qquad \text{for } x \ \geq 0 \tag{2.7.3}$$

$$u_i(x) + u_o(x) + u_a(x) = -\frac{E_f\, r_f^2}{2}\left[\frac{In\left(\frac{r_i}{r_f}\right)}{G_i} + \frac{In\left(\frac{r_o}{r_i}\right)}{G_o} + \frac{In\left(\frac{r_a}{r_o}\right)}{G_a}\right]\frac{d\varepsilon_f(x)}{dx} \tag{2.7.4}$$

According to Eq. (2.7.1) to Eq. (2.7.4), we can obtain:

$$s(x) = \frac{1}{k^2} u_f''(x) - u_f(x) + u_h(x) \tag{2.7.5a}$$

$$k^2 = \frac{2}{E_\mathrm{f}\, r_\mathrm{f}^2 \left[\frac{In(r_i/r_f)}{G_i} + \frac{In(r_o/r_i)}{G_o} + \frac{In(r_a/r_o)}{G_a}\right]} \tag{2.7.5b}$$

Besides, based on equation of equilibrium, we also have:

$$\tau_f(x, r_f) = -\frac{E_f\, r_f}{2} \frac{d\varepsilon_f(x)}{d\, x} \tag{2.7.6}$$

Based on Eq. (2.7.6), we can obtain:

$$u_f''(x) = \varepsilon_f'(x) = -\frac{2}{E_f\, r_f} \tau_f(x, r_f) \tag{2.7.7}$$

Based on the cohesive interface law proposed by previous study [28], τ_f is also the function of interfacial slip s:

$$\tau_f(s) = \begin{cases} \frac{\beta \tau_f}{\alpha s_f} s & , \quad 0 \le s \le \alpha s_f \\ \frac{(1-\beta)\tau_f}{(1-\alpha)s_f} s + \frac{(\beta-\alpha)\tau_f}{1-\alpha}, & \quad \alpha s_f < s \le s_f \\ \tau_f e^{\frac{-\tau_f (s - s_f)}{q}} & , \quad s_f \le s \end{cases} \tag{2.7.8}$$

According to the previous study [28], the third stage of cohesive interface law can be replaced by the constant curve τ_f when the value of q is large, which is illustrated in Figure 2.7.2. Therefore, Eq. (2.7.8) is simplified as:

$$\tau_f(s) = \begin{cases} \frac{\beta \tau_f}{\alpha s_f} s & , \quad 0 \le s \le \alpha s_f \\ \frac{(1-\beta)\tau_f}{(1-\alpha)s_f} s + \frac{(\beta-\alpha)\tau_f}{1-\alpha}, & \quad \alpha s_f < s \le s_f \\ \tau_f & , \quad s_f \le s \end{cases} \tag{2.7.9}$$

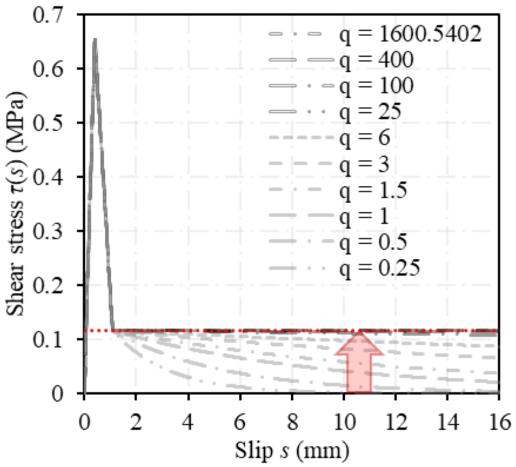

Figure 2.7.2. Parametric study of effect of q to the third stage of cohesive interface law.

Plugging Eq. (2.7.9) into Eq. (2.7.7), the relationship between $s(x)$ and $\varepsilon_f(x)$ is established:

$$s(x)=\begin{cases}-\dfrac{E_f\,r_f}{2}\dfrac{\alpha s_f}{\beta\tau_f}u_f''(x) & , \quad 0\le s\le\alpha s_f\\ -\dfrac{E_f\,r_f}{2}\dfrac{(1-\alpha)s_f}{(1-\beta)\tau_f}\left[u_f''(x)+\dfrac{2}{E_f\,r_f}\dfrac{(\beta-\alpha)\tau_f}{1-\alpha}\right], & \alpha s_f< s\le s_f\end{cases} \tag{2.7.10a}$$

$$\frac{ds(x)}{dx}=\begin{cases}-\dfrac{E_f\,r_f}{2}\dfrac{\alpha s_f}{\beta\tau_f}\varepsilon_f''(x) & , \quad 0\le s\le\alpha s_f\\ -\dfrac{E_f\,r_f}{2}\dfrac{(1-\alpha)s_f}{(1-\beta)\tau_f}\varepsilon_f''(x), & \alpha s_f< s\le s_f\end{cases} \tag{2.7.10b}$$

Substituting Eq. (2.7.10a) into Eq. (2.7.5a), we are able to obtain the governing equation that only contains $u_f(x)$ and $\varepsilon_h(x)$:

$$\begin{cases}\left[1+k^2\dfrac{E_f\,r_f}{2}\dfrac{\alpha s_f}{\beta\tau_f}\right]u_f''(x)-k^2u_f(x)+k^2[u_h(x)]=0, & 0\le s\le\alpha s_f\\ \left[1+k^2\dfrac{E_f\,r_f}{2}\dfrac{(1-\alpha)s_f}{(1-\beta)\tau_f}\right]u_f''(x)-k^2u_f(x)+k^2\left[u_h(x)+\dfrac{(\beta-\alpha)s_f}{1-\beta}\right]=0, & \alpha s_f< s\le s_f\\ u_f''(x)+\dfrac{2}{E_fr_f}\tau_f=0, & s_f\le s\end{cases} \tag{2.7.11}$$

Eq. (2.7.11) can be re-written in the form of:

$$\begin{cases}u_f''(x)-{k_1}^2u_f(x)+{k_1}^2[u_h(x)]=0, & 0\le s\le\alpha s_f\\ u_f''(x)-{k_2}^2u_f(x)+{k_2}^2\left[u_h(x)+\dfrac{(\beta-\alpha)s_f}{1-\beta}\right]=0, & \alpha s_f< s\le s_f\\ u_f''(x)+\dfrac{2}{E_fr_f}\tau_f=0, & s_f\le s\end{cases} \tag{2.7.12a}$$

$${k_1}^2=\frac{k^2}{1+k^2\dfrac{E_f\,r_f}{2}\dfrac{\alpha s_f}{\beta\tau_f}} \tag{2.7.12b}$$

$${k_2}^2=\frac{k^2}{1+k^2\dfrac{E_f\,r_f}{2}\dfrac{(1-\alpha)s_f}{(1-\beta)\tau_f}} \tag{2.7.12c}$$

The general solution of the first and second stage of Eq. (2.7.12a) can be expressed as:

$$\begin{cases}u_{f,I}(x)=C_1\,cosh(\,k_1x)+C_2\,sinh(\,k_1x)+u_h(x), & 0\le s\le\alpha s_f\\ u_{f,II}(x)=C_3\,cosh(\,k_2x)+C_4\,sinh(\,k_2x)+u_h(x)+\dfrac{(\beta-\alpha)s_f}{1-\beta}, & \alpha s_f< s\le s_f\\ u_{f,III}(x)=-\dfrac{\tau_f}{E_fr_f}x^2+C_5x+C_6, & s_f\le s\end{cases} \tag{2.7.13}$$

where C_1, C_2, C_3, C_4, C_5, and C_6 are constants for each stage, respectively.

2.7.2.2. Uniform strain fields

In uniform strain fields, $\varepsilon_h(x)=\varepsilon_0$, the deformation can be expressed as:

$$u_h(x) = \int_0^x \varepsilon_h(x)\,dx + \delta = \varepsilon_0 x + \delta \qquad \text{for } x \geq 0 \tag{2.7.14}$$

The development length of crack effect is ℓ_{cr} (Segment A-C). The development length of uniform strain field is ℓ_{st} (Segment D-B). L is a half-length of the matrix, as shown in Figure 2.7.3.

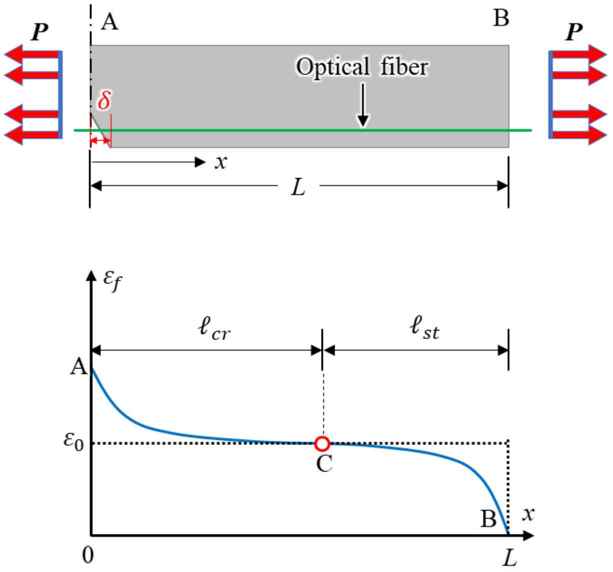

Figure 2.7.3. Distributed fiber optic sensor under a uniform strain field in the cracked host matrix.

2.7.2.2.1. Stage I: Elastic phase

In Stage I, the crack width in the substrate is small, and the interface between the fiber and fiber coating remains intact, and the bond stress increases linearly as the interfacial deformation increases ($0 < x < l_{cr}$). It is important to note that no debonding occurs between the epoxy resin and the concrete substrate, even if cracks occur in the epoxy resin. Stage I ends when the crack width reaches a critical value of $2\delta_{cr}$, and the interface at the crack begins to yield, which marks the start of Stage II. When the interface model of the fiber and the coating layer is completely elastic, Eq. (2.7.14) can be substituted into the first stage of Eq. (2.7.13) to derive the differential equation expression of the fiber deformation, normal strain, shear stress, and fiber slip:

$$u_{f,I}(x) = C_{1,I}\cosh(k_1 x) + C_{2,I}\sinh(k_1 x) + \varepsilon_0 x + \delta \tag{2.7.15a}$$

$$\varepsilon_{f,I}(x) = C_{1,I}k_1\sinh(k_1 x) + C_{2,I}k_1\cosh(k_1 x) + \varepsilon_0 \tag{2.7.15b}$$

$$\tau_{f,I}(x) = -\frac{E_f\, r_f}{2}\left[C_{1,I}{k_1}^2\cosh(k_1 x) + C_{2,I}{k_1}^2\sinh(k_1 x)\right] \tag{2.7.15c}$$

$$s_I(x) = -\frac{E_f\, r_f}{2}\frac{\alpha s_f}{\beta\tau_f}\left[C_{1,I}{k_1}^2\cosh(k_1 x) + C_{2,I}{k_1}^2\sinh(k_1 x)\right] \tag{2.7.15d}$$

where $C_{1,I}$ and $C_{2,I}$ are the integration constants to be determined by the boundary conditions.

The boundary conditions are different for different segments:

$$u_{f,I}(x = 0) = 0, \qquad 0 \leq x \leq \ell_{cr} \tag{2.7.16a}$$

$$\varepsilon_{f,I}(x = \ell_{cr}^{-}) = \varepsilon_{f,I}(x = \ell_{cr}^{+}), \qquad 0 \le x \le \ell_{cr} \tag{2.7.16b}$$

$$\tau_{f,I}(x = \ell_{cr}^{-}) = \tau_{f,I}(x = \ell_{cr}^{+}), \qquad \ell_{cr} \le x \le L \tag{2.7.16c}$$

$$\varepsilon_{f,I}(x = L) = 0, \qquad \ell_{cr} \le x \le L \tag{2.7.16f}$$

By substituting Eq. (2.7.16) into Eq. (2.7.15), the constants C_1 and C_2 are determined:

$$C_{1,I} = \begin{cases} -\delta, & 0 \le x \le \ell_{cr} \\ \dfrac{\varepsilon_0}{k_1}[sinh(k_1 L) - tanh(k_1 \ell_{cr})\, cosh(k_1 L)], & \ell_{cr} \le x \le L \end{cases} \tag{2.7.17a}$$

$$C_{2,I} = \begin{cases} \delta\, tanh(k_1 \ell_{cr}), & 0 \le x \le \ell_{cr} \\ \dfrac{\varepsilon_0}{k_1}[tanh(k_1 \ell_{cr})\, sinh(k_1 L) - cosh(k_1 L)], & \ell_{cr} \le x \le L \end{cases} \tag{2.7.17b}$$

2.7.2.2.2. Stage II: Elastic-yielding phase

Once the crack width exceeds the critical value, the interfacial yielding takes place and leads to a softening region at the interface between the fiber core and coating. Consequently, the fiber-coating interface becomes elastic far away from the crack and softened near its location. In this scenario, two equations of deformation compatibility are necessary to describe the strain transfer mechanism accurately. To obtain the differential equation of deformation for the optical fiber, Eq. (2.7.14) is inserted into the first two stages of Eq. (2.7.13):

$$u_{f,II}(x) = \begin{cases} C_{1,II}\, cosh(k_1 x) + C_{2,II}\, sinh(k_1 x) + \varepsilon_0 x + \delta, & \ell_{yd} \le x \le L \\ C_{3,II}\, cosh(k_2 x) + C_{4,II}\, sinh(k_2 x) + \varepsilon_0 x + \delta + \dfrac{(\beta - \alpha) s_f}{1 - \beta}, & 0 \le x \le \ell_{yd} \end{cases} \tag{2.7.17a}$$

$$\varepsilon_{f,II}(x) = \begin{cases} C_{1,II} k_1\, sinh(k_1 x) + C_{2,II} k_1\, cosh(k_1 x) + \varepsilon_0, & \ell_{yd} \le x \le L \\ C_{3,II} k_2\, sinh(k_2 x) + C_{4,II} k_2\, cosh(k_2 x) + \varepsilon_0, & 0 \le x \le \ell_{yd} \end{cases} \tag{2.7.17b}$$

$$\tau_{f,II}(x) = \begin{cases} -\dfrac{E_f\, r_f}{2}\left[C_{1,II} {k_1}^2\, cosh(k_1 x) + C_{2,II} {k_1}^2\, sinh(k_1 x)\right], & \ell_{yd} \le x \le L \\ -\dfrac{E_f\, r_f}{2}\left[C_{3,II} {k_2}^2\, cosh(k_2 x) + C_{4,II} {k_2}^2\, sinh(k_2 x)\right], & 0 \le x \le \ell_{yd} \end{cases} \tag{2.7.17c}$$

$$s_{II}(x) = \begin{cases} -\dfrac{E_f\, r_f}{2}\dfrac{\alpha s_f}{\beta \tau_f}[C_{1,II} {k_1}^2\, cosh(k_1 x) + C_{2,II} {k_1}^2\, sinh(k_1 x)], & \ell_{yd} \le x \le L \\ -\dfrac{E_f\, r_f}{2}\dfrac{(1-\alpha) s_f}{(1-\beta)\tau_f}\left[C_{3,II} {k_2}^2\, cosh(k_2 x) + C_{4,II} {k_2}^2\, sinh(k_2 x) + \dfrac{2}{E_f\, r_f}\dfrac{(\beta - \alpha)\tau_f}{1 - \alpha}\right], & 0 \le x \le \ell_{yd} \end{cases} \tag{2.7.17d}$$

where $C_{1,II}$, $C_{2,II}$, $C_{3,II}$, and $C_{4,II}$ are the integration constants to be determined by the boundary conditions.

The boundary conditions are different for different segments:

$$u_{f,II}(x = 0) = 0, \qquad 0 \le x \le \ell_{yd} \tag{2.7.18a}$$

$$\varepsilon_{f,II}\left(x = \ell_{yd}^{-}\right) = \varepsilon_{f,II}\left(x = \ell_{yd}^{+}\right), \qquad 0 \le x \le \ell_{yd} \tag{2.7.18b}$$

$$\tau_{f,II}\left(x = \ell_{yd}^{-}\right) = \tau_{f,II}\left(x = \ell_{yd}^{+}\right), \qquad \ell_{yd} \le x \le \ell_{cr} \tag{2.7.18c}$$

$$\varepsilon_{f,II}(x = \ell_{cr}^{-}) = \varepsilon_{f,II}(x = \ell_{cr}^{+}), \qquad \ell_{yd} \le x \le \ell_{cr} \tag{2.7.18d}$$

$$\tau_{f,II}(x = \ell_{cr}^{-}) = \tau_{f,II}(x = \ell_{cr}^{+}), \qquad \ell_{cr} \le x \le L - \ell_{st} \tag{2.7.18e}$$

$$\varepsilon_{f,II}(x = (L - \ell_{st})^-) = \varepsilon_{f,II}(x = (L - \ell_{st})^+), \qquad \ell_{cr} \le x \le L - \ell_{st} \tag{2.7.18f}$$

$$\tau_{f,II}(x = (L - \ell_{st})^-) = \tau_{f,II}(x = (L - \ell_{st})^+), \qquad \ell_{cr} \le x \le L \tag{2.7.18g}$$

$$\varepsilon_{f,II}(x = L) = 0, \qquad \ell_{cr} \le x \le L \tag{2.7.18h}$$

By substituting Eq. (2.7.18) into Eq. (2.7.17), the constants $C_{1,II}$, $C_{2,II}$, $C_{3,II}$, and $C_{4,II}$ are determined:

$$C_{1,II} = \begin{cases} \dfrac{2\beta\tau_f(e^{2k_1L} - 1)}{{k_1}^2 E_f r_f [e^{k_1\ell_{yd}} - e^{2k_1(L-\ell_{yd})}]}, & \ell_{yd} \le x \le \ell_{cr} \\ \dfrac{\varepsilon_0}{k_1}[sinh(k_1L) - tanh(k_1\ell_{cr})\, cosh(k_1L)], & L - \ell_{cr} \le x \le L \end{cases} \tag{2.7.19a}$$

$$C_{2,II} = \begin{cases} \dfrac{-2\beta\tau_f(e^{2k_1L} + 1)}{{k_1}^2 E_f r_f [e^{k_1\ell_{yd}} - e^{2k_1(L-\ell_{yd})}]}, & \ell_{yd} \le x \le \ell_{cr} \\ \dfrac{\varepsilon_0}{k_1}[tanh(k_1\ell_{st})\, sinh(k_1L) - cosh(k_1L)], & L - \ell_{cr} \le x \le L \end{cases} \tag{2.7.19b}$$

$$C_{3,II} = -\left(\delta + \frac{\beta - \alpha}{1 - \beta} s_f\right), \qquad 0 \le x \le \ell_{yd} \tag{2.7.19c}$$

$$C_{4,II} = \left(\delta + \frac{\beta - \alpha}{1 - \beta} s_f\right) coth\left(k_2\ell_{yd}\right) - \frac{2\beta\tau_f}{E_f r_f {k_2}^2} csch\left(k_2\ell_{yd}\right), \qquad 0 \le x \le \ell_{yd} \tag{2.7.19d}$$

Once the crack width exceeds the critical width for debonding, the interface between the fiber and its coating at the crack begins to debond. The interfacial shear stress at the crack, denoted as $\tau_{f,II}(x = 0)$, becomes equal to the initial interfacial shear stress τ_f. To calculate the half crack width δ_s at which optical fiber debonding from the substrate initiates, the following equation needs to be solved:

$$\tau_f = \frac{E_f r_f}{2}\left(\delta_s + \frac{\beta - \alpha}{1 - \beta} s_f\right) {k_2}^2 \tag{2.7.20}$$

Therefore, the critical half crack width (δ_s) is expressed as follows:

$$\delta_s = \frac{2\tau_f}{E_f r_f {k_2}^2} - \frac{\beta - \alpha}{1 - \beta} s_f \tag{2.7.21}$$

2.7.2.2.3. Stage III: Elastic-yielding-debonding phase

As the crack width further increases, the interface between the fiber core and coating can be categorized into three regions: the debonding region near the crack ($0 \le x < \ell_{db}$), the yielding region in the middle, and the elastic region at the end. Within the debonding region, the interfacial shear stress is mainly caused by the friction between the fiber and coating, and it remains constant.

$$\tau_f(x) = \tau_f \tag{2.7.22}$$

The strain induced in the optical fiber is expressed as a constant within the debonding region. The differential equation expression of the fiber deformation, normal strain, shear stress, and fiber slip are obtained:

$$u_{f,III}(x) = \begin{cases} C_{1,III}\,cosh(\,k_1x) + C_{2,III}\,sinh(\,k_1x) + \varepsilon_0x + \delta, & \ell_{db} + \ell_{yd} \le x \le L \\ C_{3,III}\,cosh(\,k_2x) + C_{4,IIII}\,sinh(\,k_2x) + \varepsilon_0x + \delta + \dfrac{(\beta-\alpha)s_f}{1-\beta}, & \ell_{db} < x \le \ell_{db} + \ell_{yd} \\ -\dfrac{\tau_f}{E_fr_f}x^2 + C_{5,III}x + C_{6,III}, & 0 \le x \le \ell_{db} \end{cases} \tag{2.7.23a}$$

$$\varepsilon_{f,III}(x) = \begin{cases} C_{1,III}k_1\,sinh(\,k_1x) + C_{2,III}k_1\,cosh(\,k_1x) + \varepsilon_0, & \ell_{db} + \ell_{yd} \le x \le L \\ C_{3,III}k_2\,sinh(\,k_2x) + C_{4,III}k_2\,cosh(\,k_2x) + \varepsilon_0, & \ell_{db} < x \le \ell_{db} + \ell_{yd} \\ -\dfrac{2\tau_f}{E_fr_f}x + C_{5,III}, & 0 \le x \le \ell_{db} \end{cases} \tag{2.7.23b}$$

$$\tau_{f,III}(x) = \begin{cases} -\dfrac{E_f\,r_f}{2}[C_{1,III}k_1\,sinh(\,k_1x) + C_{2,III}k_1\,cosh(\,k_1x) + \varepsilon_0], & \ell_{db} + \ell_{yd} \le x \le L \\ -\dfrac{E_f\,r_f}{2}[C_{3,III}k_2\,sinh(\,k_2x) + C_{4,III}k_2\,cosh(\,k_2x) + \varepsilon_0], & \ell_{db} < x \le \ell_{db} + \ell_{yd} \\ \tau_f, & 0 \le x \le \ell_{db} \end{cases} \tag{2.7.23c}$$

$$s_{III}(x) = \begin{cases} -\dfrac{E_f\,r_f}{2}\dfrac{\alpha s_f}{\beta\tau_f}[C_{1,II}{k_1}^2\,cosh(\,k_1x) + C_{2,II}{k_1}^2\,sinh(\,k_1x)], & \ell_{db} + \ell_{yd} \le x \le L \\ -\dfrac{E_f\,r_f}{2}\dfrac{(1-\alpha)s_f}{(1-\beta)\tau_f}\left[C_{3,II}{k_2}^2\,cosh(\,k_2x) + C_{4,II}{k_2}^2\,sinh(\,k_2x) + \dfrac{2}{E_f\,r_f}\dfrac{(\beta-\alpha)\tau_f}{1-\alpha}\right], & \ell_{db} < x \le \ell_{db} + \ell_{yd} \end{cases} \tag{2.7.23d}$$

where $C_{1,III}$, $C_{2,III}$, $C_{3,III}$, $C_{4,III}$, $C_{5,III}$, and $C_{6,III}$ are the integration constants to be determined by the boundary conditions.

The boundary conditions are different for different segments:

$$u_{f,III}(x=0) = 0, \qquad 0 \le x \le \ell_{db} \tag{2.7.24a}$$

$$\varepsilon_{f,II}(x=\ell_{db}^-) = \varepsilon_{f,II}(x=\ell_{db}^+), \qquad 0 \le x \le \ell_{db} \tag{2.7.24b}$$

$$\tau_{f,II}(x=\ell_{db}^-) = \tau_{f,II}(x=\ell_{db}^+), \qquad \ell_{db} \le x \le \ell_{yd} \tag{2.7.24c}$$

$$\varepsilon_{f,II}\left(x=\left(\ell_{db}+\ell_{yd}\right)^-\right) = \varepsilon_{f,II}\left(x=\left(\ell_{db}+\ell_{yd}\right)^+\right), \qquad \ell_{db} \le x \le \ell_{yd} \tag{2.7.24d}$$

$$\tau_{f,II}\left(x=\left(\ell_{db}+\ell_{yd}\right)^-\right) = \tau_{f,II}\left(x=\left(\ell_{db}+\ell_{yd}\right)^+\right), \qquad \ell_{yd} \le x \le \ell_{cr} \tag{2.7.24e}$$

$$\varepsilon_{f,II}(x=\ell_{cr}^-) = \varepsilon_{f,II}(x=\ell_{cr}^+), \qquad \ell_{yd} \le x \le \ell_{cr} \tag{2.7.24f}$$

$$\tau_{f,II}(x=\ell_{cr}^-) = \tau_{f,II}(x=\ell_{cr}^+), \qquad \ell_{cr} \le x \le L-\ell_{st} \tag{2.7.24g}$$

$$\varepsilon_{f,I}(x=(L-\ell_{cr})^-) = \varepsilon_{f,I}(x=(L-\ell_{cr})^+), \qquad \ell_{cr} \le x \le L-\ell_{st} \tag{2.7.24h}$$

$$\tau_{f,I}(x=(L-\ell_{cr})^-) = \tau_{f,I}(x=(L-\ell_{cr})^+), \qquad \ell_{cr} \le x \le L \tag{2.7.24i}$$

$$\varepsilon_f(x=L) = 0, \qquad \ell_{cr} \le x \le L \tag{2.7.24j}$$

By substituting Eq. (2.7.24) into Eq. (2.7.23), constants $C_{1,III}$, $C_{2,III}$, $C_{3,III}$, and $C_{4,III}$, $C_{5,III}$, and $C_{6,III}$ are determined:

$$C_{1,III} = \begin{cases} \dfrac{-2\beta\tau_f(e^{2k_1L}+1)}{{k_1}^2E_fr_f[e^{k_1(\ell_{yd}+\ell_{db})} - e^{2k_1\left(L-(\ell_{yd}-\ell_{db})\right)}]}, & \ell_{yd} \le x \le \ell_{cr} \\ \dfrac{\varepsilon_0}{k_1}[sinh(\,k_1L) - tanh(k_1\ell_{cr})\,cosh(\,k_1L)], & L-\ell_{cr} \le x \le L \end{cases} \tag{2.7.25a}$$

$$C_{2,III} = \begin{cases} \dfrac{2\beta\tau_f(e^{2k_1L}-1)}{{k_1}^2E_fr_f[e^{k_1(\ell_{yd}+\ell_{db})} - e^{2k_1\left(L-(\ell_{yd}-\ell_{db})\right)}]}, & \ell_{yd} \le x \le \ell_{cr} \\ \dfrac{\varepsilon_0}{k_1}[tanh(k_1\ell_{cr})\,sinh(\,k_1L) - cosh(\,k_1L)], & L-\ell_{cr} \le x \le L \end{cases} \tag{2.7.25b}$$

$$C_{3,III}=\frac{-2\beta\tau_f(e^{2k_2\ell_{db}}+1)}{{k_2}^2E_fr_f[e^{k_2(\ell_{yd}+\ell_{db})}-e^{k_2(\ell_{db}-\ell_{yd})}]},\qquad \ell_{db}\le x\le \ell_{yd} \tag{2.7.25c}$$

$$C_{4,III}=\frac{2\beta\tau_f(e^{2k_2\ell_{db}}-1)}{{k_2}^2E_fr_f[e^{k_2(\ell_{yd}+\ell_{db})}-e^{k_2(\ell_{db}-\ell_{yd})}]},\qquad \ell_{db}\le x\le \ell_{yd} \tag{2.7.25d}$$

$$C_{5,III}=\frac{-2\beta\tau_f(e^{2k_2\ell_{db}}+1)\sinh(k_2\ell_{db})}{k_2E_fr_f[e^{k_2(\ell_{yd}+\ell_{db})}-e^{k_2(\ell_{db}-\ell_{yd})}]}+\frac{2\beta\tau_f(e^{2k_2\ell_{db}}-1)\cosh(k_2\ell_{db})}{k_2E_fr_f[e^{k_2(\ell_{yd}+\ell_{db})}-e^{k_2(\ell_{db}-\ell_{yd})}]}+\varepsilon_0+\frac{2\tau_f\ell_{db}}{E_fr_f},\qquad 0\le x\le \ell_{db} \tag{2.7.25e}$$

$$C_{6,III}=\frac{-2\beta\tau_f(e^{2k_2\ell_{db}}+1)\,cosh(\,k_2\ell_{db})}{{k_2}^2E_fr_f[e^{k_2(\ell_{yd}+\ell_{db})}-e^{k_2(\ell_{db}-\ell_{yd})}]}+\frac{2\beta\tau_f(e^{2k_2\ell_{db}}-1)\,sinh(\,k_2\ell_{db})}{{k_2}^2E_fr_f[e^{k_2(\ell_{yd}+\ell_{db})}-e^{k_2(\ell_{db}-\ell_{yd})}]}+\varepsilon_0\ell_{db}+\delta+\frac{(\beta-\alpha)s_f}{1-\beta}+\frac{\tau_f}{E_fr_f}{\ell_{db}}^2-C_{5,III}\ell_{db},\qquad 0\le x\le \ell_{db} \tag{2.7.25f}$$

2.7.3. Experimental studies

In the previous section, a three-stage crack-strain transfer model was developed to describe the process by which substrate cracking leads to strain in a DFOS. In order to evaluate this model, experimental testing was conducted to validate strain distribution of uniform tensile strain field.

2.7.3.1. Instrumentation, testing setup and loading protocol

Experimental testing was carried out to validate the iterative effects of crack and tensile deformation occurred in the same position on the specimen. Specifically, a notched plate specimen was used to represent the combination effects of crack and uniform tension of two-dimensional specimens, as shown in Figure 2.7.4.

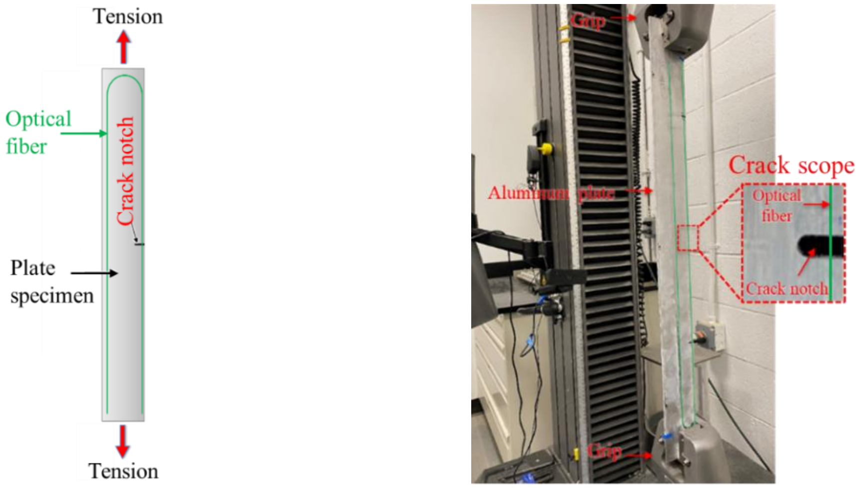

(a) (b)

Figure 2.7.4. Specimen preparation, instrumentation, and test set-up: (a) illustration of test set-up; and (b) photograph of the plate specimen on the load frame.

Although this research was conducted using plate specimens, this research was conducted to validate the theoretical method which is applicable to various pipes because the method is based on strain measurement. The combined strain and cracks in pipelines will lead to the same strain distributions in the distributed fiber optic sensor.

The plate specimen measured 812.8 mm (32 inches) in length, 76.2 mm (3 inches) in width and 2.54 mm (0.1 inch) in thickness. A notch was manually fabricated on one edge of the specimen to represent crack, and length and width of the notch were 5 mm and 2 mm, respectively. Two optical fibers were attached on the two surfaces of plate specimen in the designed layout (green lines on the plate). The optical fiber was passed through the crack at both sides of plate to measure the iterative effects of crack and uniform tension occurred in the same position crossing a DFOS. For each optical fiber, one end was connected to the data acquisition system for the DFOS, and the other end of the optical fiber was free. On each surface of the specimen, the distance between two adjacent paths of the optical fiber alignment was 38.1 mm (1.5 inches).

2.7.3.2. Strain distribution results

This section presents the results of strain distributions obtained from the DFOS installed on the specimen under varying loads, as shown in Figure 2.7.5. The strain values, resulting from the interaction between crack and tensile deformation, are plotted on the vertical axis, while the horizontal axis represents the distance along the DFOS, with the zero distance indicating the connector of the data acquisition system. The length range of the DFOS is chosen to display the strain distributions within the fiber optic cable installed on the plate specimen.

Based on the test results and analytical study, Figure 2.7.5 compares half of measurement results symmetrical to cracking position against the strain distribution obtained from analytical study. Overall, the results measured from the DFOS, and the analytical results agree well with each other. Overall, the strain in the DFOS prohibits obvious strain transfer effect within the critical embedment length at crack and uniform strain field end of the DFOS. The discrepancy can be attributed to the operational error of measuring crack width using crack scope and the stress concentration at the grip end of specimen.

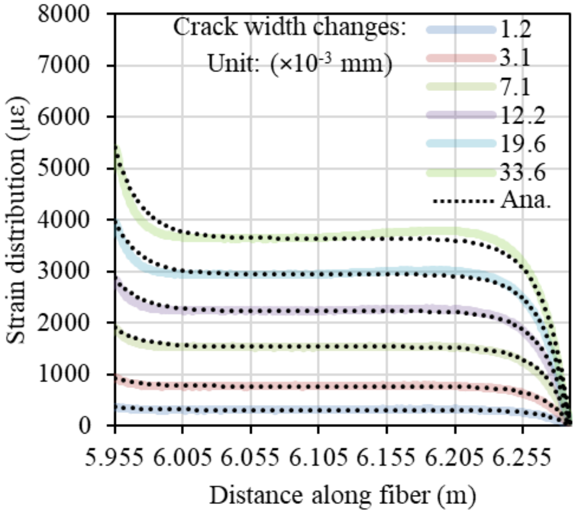

Figure 2.7.5. Comparison of measurement results of the strain distribution from the DFOS with analytical results. (Ana. refers to analytical results).

2.7.4. Summary

This project conducted theoretical and experimental studies on the measurement of combined strains and cracks using DFOS. The strain distributions caused by loads and cracks were superimposed in the measured strain distribution results. The combined results can be decomposed using the methods developed in this project. After the strain distributions are decomposed, the strain distributions caused by an individual effect can be analyzed to support the measurement of strain fields as well as the detection, localization, and quantification of cracks.

2.8. Measurement of interactive dent and corrosion

2.8.1. Overview

The above research has shown that the combinations of strain changes and cracks can be well measured and differentiated using a DFOS based on the measurements of strain distributions. The research motivated further research on the combinations of other types of anomalies. In real practice, cracks are relatively rare compared with dent and corrosion, which exist in most in-service pipelines more or less. When a pipe has both dent and corrosion which happen to occur at the same position of the pipe, both dent and corrosion can significantly affect the strain distributions measured from a DFOS passing through the position of dent and corrosion. It is essential to develop effective methods to detect and differentiate the effect of dent and corrosion on the strain distributions measured from DFOS deployed on pipelines. To address the above challenge, this study aims to: (1) develop an approach to measuring both dent and corrosion that occur at the same position of a pipe; and (2) investigate the interactive effects of dent and corrosion that occur simultaneously using DFOS data.

2.8.2. Methods

2.8.2.1. Materials and specimen preparation

Experimental testing was carried out to evaluate and differentiate the iterative effects of corrosion and dent that occurred in the same position on the pipe specimen, as shown in Figure 2.8.1. The pipe specimen was made of steel, which is commonly used for transmission natural gas and hydraulic fluid. The length, outer diameter, and wall thickness of the pipe specimen were 250 mm, 38.1 mm (1.5 inch) and 1.65 mm (0.065 inch) respectively, which is shown in Figure 2.8.1(a).

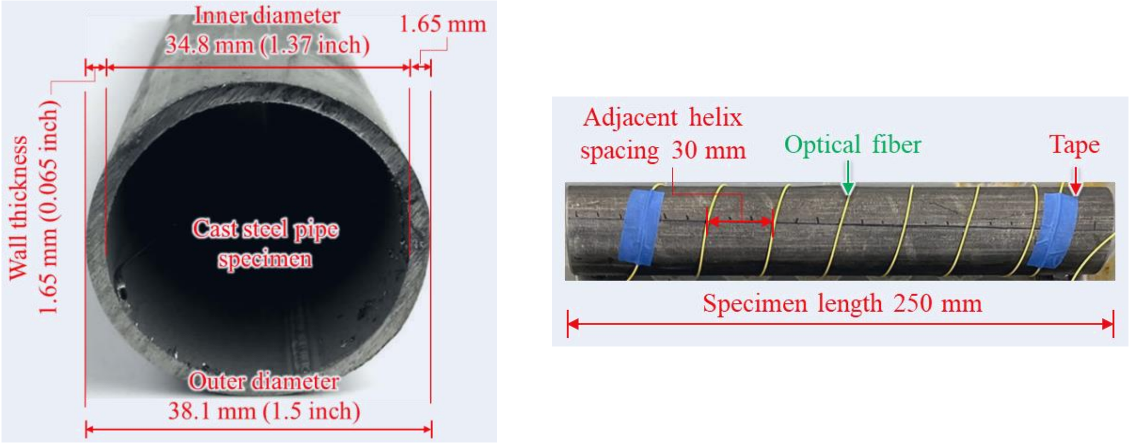

(a) (b)

Figure 2.8.1. Dimensions of pipe specimen and installation of fiber optic cable: (a) dimensions of the pipe; and (b) installation of fiber optic cable on the pipe.

DFOS were attached on the surface of pipe specimens in the designed layout (yellow lines on the pipes), which is shown in Figure 2.8.1(b). To prepare the specimen for optical fiber installation, it was first immersed in a 5% concentration acetic acid solution to remove surface rust and then wiped clean using alcohol wipes. The optical fibers were then attached to discrete spots on the specimen according to a pre-designed layout aimed at covering a large area. Tape was used to secure the optical fibers in place during installation. Subsequently, fast-setting glue was applied to attach the optical fibers to the specimen at discrete points between the tape spots. After the glue had set, the tape was removed with caution to prevent damage to the fibers or the glue. Finally, a two-part epoxy was applied to the optical fiber for a robust attachment and reliable strain transfer between the specimen and the optical fiber. Any excess epoxy on the fiber optic cable was removed to prevent the impact on corrosion. The thickness of the epoxy layer was about 250 µm, which is around one tenth of the pipe thickness. The width of the epoxy was about 4-6 mm. The epoxy was cured at room temperature (22 ºC ± 2 ºC) and normal humidity (50% ± 5%) for 24 hours.

2.8.2.2. Test set-up, instrumentation, and loading protocol

The specimens were loaded under three-point bending to generate dent deformation at mid-span using a universal load frame. The span length between two supports is 210 mm. The dent test was conducted under displacement control at a rate of 1 mm/min. The applied load was recorded by the load cell of universal testing machine, and an extensometer was instrumented to record the mid-span deflection of pipe specimens. Specifically, the optical fiber was passed through the dent region to measure the iterative effects of dent and corrosion. One end of optical fiber was connected to the data acquisition system for the DFOS, and the other end of the optical fiber was free. The details of the test set-up and instrumentation are shown in Figure 2.8.2.

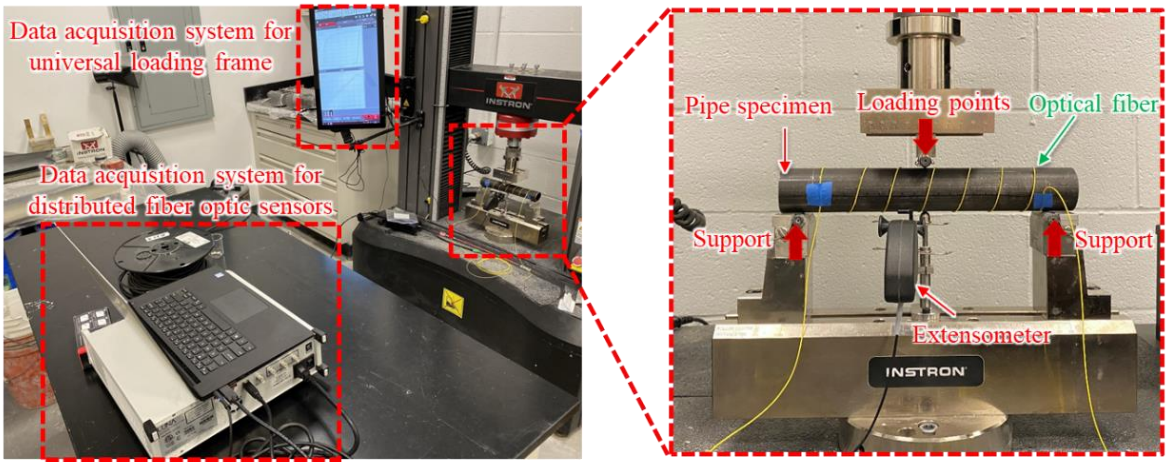

Figure 2.8.2. Photograph for instrumentation, and test set-up of pre-dent test.

In this study, we used a data acquisition system (model: Luna ODiSi 6) to perform the OFDR measurement. The measurement accuracy specified by the manufacturer is ±5 µε for strain and ± 2.2 °C for temperature. The range of spatial resolution was 0.65 mm to 10.4 mm.

The pipe specimens were immersed in a 3.5% sodium chloride solution at room temperature (25 °C ± 2 °C) for corrosion tests after the dent testing. Figure 2.8.3(a) illustrates the setup used for the corrosion tests. Plastic blocks were used to support the pipes at both ends, exposing the bottom of the pipes to the sodium chloride solution, as exemplified in Figure 2.8.3(b).

To compensate for temperature variation, a distributed fiber optic temperature sensor was utilized, which could eliminate the influence of temperature on the measurement of strain distributions from the distributed fiber optic strain sensor, as depicted in Figure 2.8.3(c). The distributed sensing system was connected to the fiber optic cable for data acquisition, with Rayleigh backscattering signals measured and converted into strain distributions along the sensor. Each measurement took 20 seconds approximately, and the measurement frequency was 2 Hz.

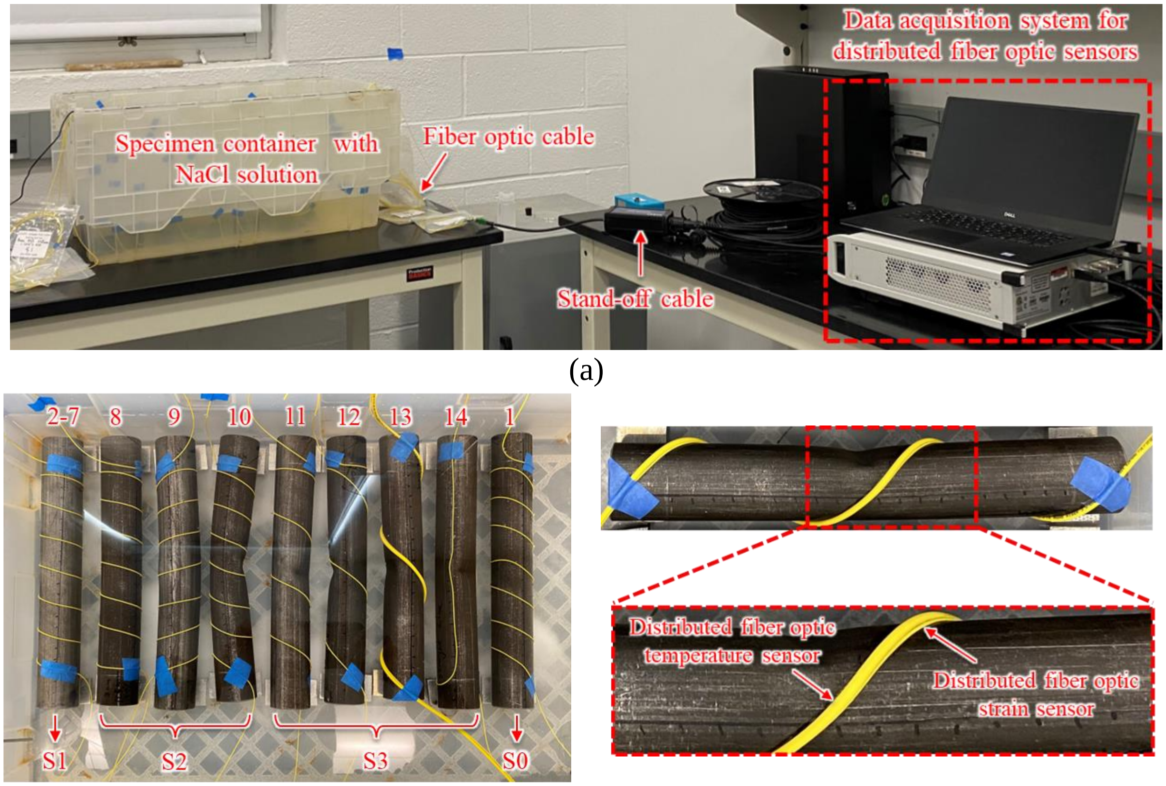

(a)

(b) (c)

Figure 2.8.3. Corrosion test of steel pipes: (a) test set-up; (b) investigated specimens; and (c) illustration of a pipe instrumented with DFOS.

2.8.2.3. Investigated cases

Table 2.8.1 presents a summary of the 14 cases studied in this research. The pipe specimens were divided into four categories: S0, which was the control specimen without dent deformation, S1 consisting of one specimen used to investigate the impact of five different measurement spatial resolutions of the DFOS (0.65 mm, 1.30 mm, 2.60 mm, 10.40 mm, and 20.80 mm), S2 consisting of three specimens used to study the effects of four different dent deformations (15%, 30%, 45%, and 60% of pipe outer diameter), and S3 containing four specimens to examine five different helix spacings (30 mm, 60 mm, 90 mm, 120 mm, and Straight line) for different sensor deployments.

The impact of coating thickness was not investigated in this study since previous research [30] found that it did not significantly affect accuracy.

Table 2.8.1. Investigated cases of testing for dent and corrosion interactive effect

Group	Cases	Spatial resolution (mm)	Sensor deployment pattern	Adjacent helix spacing (mm)	Degree of deformation
S0 (Ref.)	1	0.65	Helix	30	0
S1	2	0.65	Helix	30	30% of OD
	3	1.3	Helix	30	30% of OD
	4	2.6	Helix	30	30% of OD
	5	5.2	Helix	30	30% of OD
	6	10.4	Helix	30	30% of OD
	7	20.8	Helix	30	30% of OD
S2	8	0.65	Helix	30	15% of OD
	9	0.65	Helix	30	45% of OD
	10	0.65	Helix	30	60% of OD
S3	11	0.65	Helix	60	30% of OD
	12	0.65	Helix	90	30% of OD
	13	0.65	Helix	120	30% of OD
	14	0.65	Straight line	-	30% of OD

Note: "Degree of deformation" refers to the ratio of dent depth over pipe outer diameter; "OD" refers to pipe outer diameter.

2.8.3. Results and discussions

2.8.3.1. Load-displacement curve and visual inspection

Figure 2.8.4 shows the load-displacement curves and dent deformations of the pipe specimens. The pipe specimen under three-point bending exhibited a representative dent deformation with the applied displacement. The dent deformation increased with the applied displacement. All load-displacement curves consist of the loading part and the unloading part.

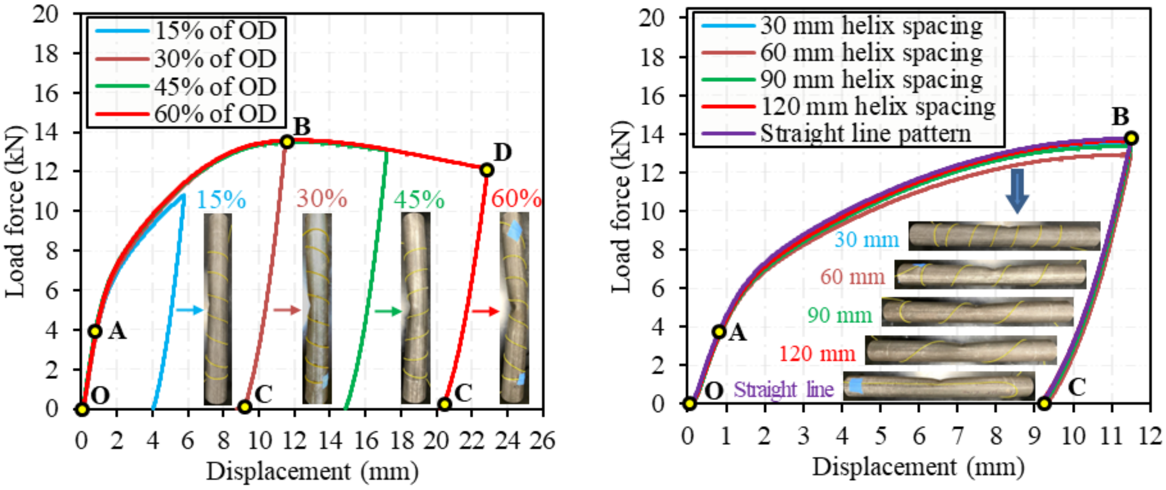

(a) (b)

Figure 2.8.4. Load-displacement of the pipe specimens under three-point bending: (a) Cases 1 to 10; and (b) Cases 1 and 11 to 14.

When the extent of dent deformation is smaller than 30% of the outer diameter of the pipes, the pipes showed similar load-displacement curves with three stages: (1) Stage 1: from “O” to “A”, where the bending load approximately linearly increases with the displacement. (2) Stage 2: from “A” to “B”, where the bending load increases with the displacement with a decreasing slope until reaching the peak load at point B. Both Stages 1 and 2 belong to the loading part. (3) Stage 3: from “B” to “C”, belonging to the unloading part, where the unloading force decreases with the unloading displacement.

When the degree of dent deformation is greater than 30% of pipe outer diameter, the specimens showed similar curves with four stages: (1) Stage 1: from “O” to “A”, where the bending load approximately linearly increases with the displacement. (2) Stage 2: from “A” to “B”, where the bending load increases with the displacement with a decreasing slope until reaching the peak load at point B. (3) Stage 3: from “B” to “D”, where the load decreases with the increasing displacement. Stages 1 to 3 belong to the loading part. (3) Stage 4: from “D” to “C” belonging to the unloading part, where the unloading force decreases with the unloading displacement.

Figure 2.8.5 shows an example of representative visual inspection results from one specimen in each testing group. Rust was generated on the external surfaces of pipes in groups S0 to S3. As the immersion time increased, the thickness of rust increased. Most rust was attached to the surface of the pipes, and only a small volume of rust was transported off the pipes. Since the corrosion products are expansive and have a lower density compared with intact steel, the diameter of the corroded pipe was increased.

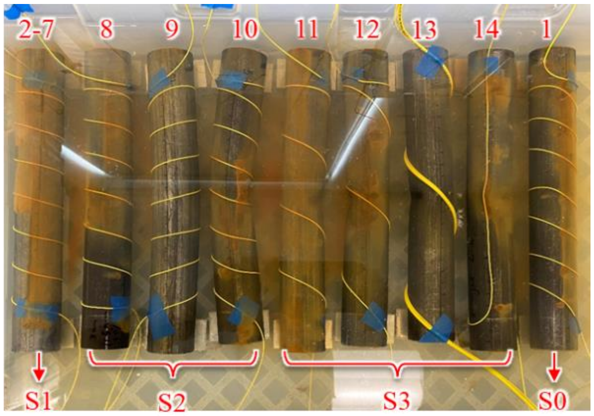

Figure 2.8.5. Photograph for pipe specimens immersed in the sodium chloride solution (3.5 wt. %) for corrosion experiments.

2.8.3.2. Strain distribution results for pre-dent

The dent tests were conducted using displacement control with a constant displacement rate of 1 mm/min. The applied load and displacement were measured by a load cell embedded in the load frame and an extensometer, respectively. Figure 2.8.6 shows the strain distributions measured by the DFOS installed on the pipe specimens under different loads. The vertical axis represents the strains resulting from dent deformation, while the horizontal axis represents the distance along the DFOS, with the zero distance at the data acquisition system's connector. Each figure's length range is chosen to display the strain distributions within the fiber optic cable's installed length on the pipe specimens.

The strain magnitudes increase with the dent deformations during loading. During unloading, the magnitudes of strain distributions decreased to a certain level due to the residual dent deformations. Based on the cases in groups S1 and S2, the peak strain and residual peak strain magnitudes near the dent position increased with increasing dent deformations, which is consistent with visual observations. In contrast, the peak strain and residual peak strain magnitudes near the dent position decreased with increasing adjacent helix spacing, as observed in the cases of groups S1 and S3.

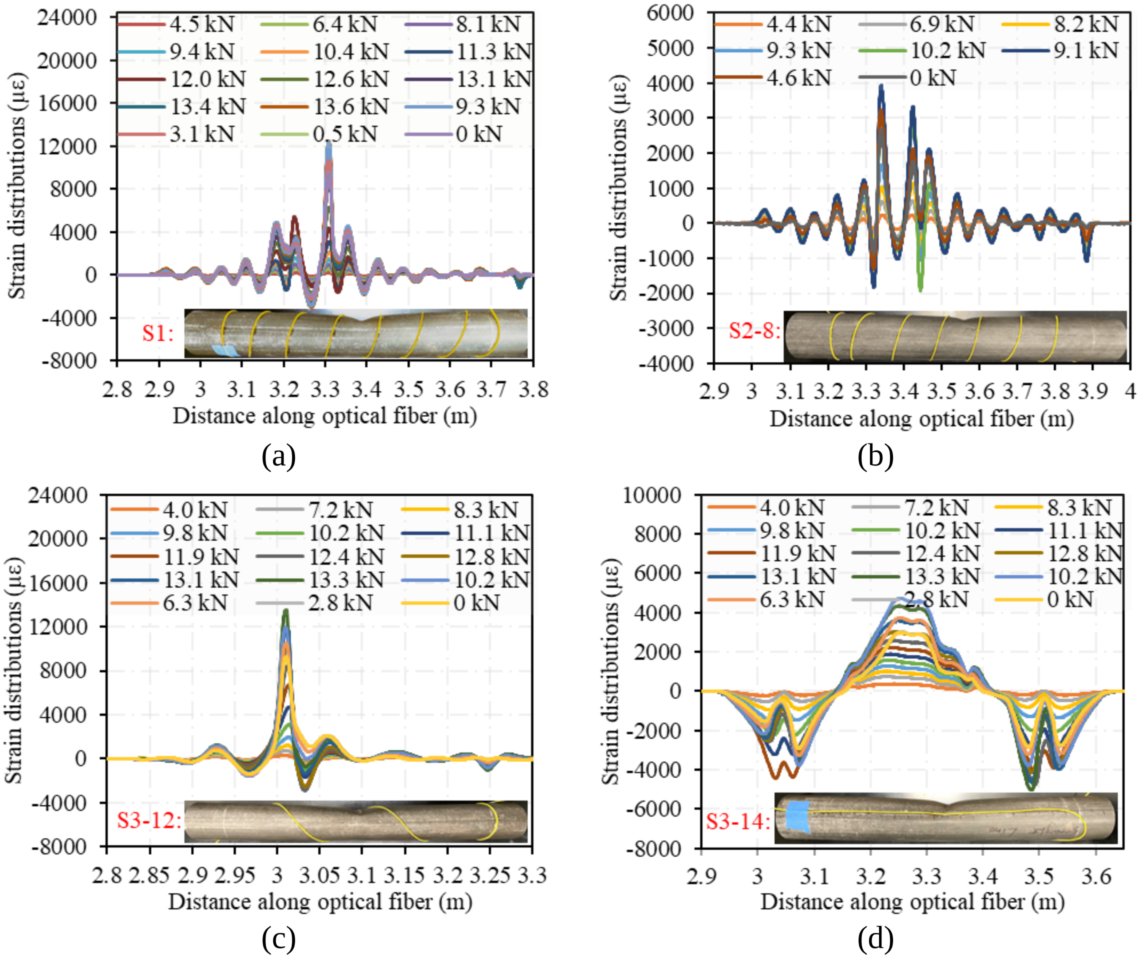

(a)

(b)

(c)

(d)

Figure 2.8.6. Strain distributions measured from the distributed fiber optic strain sensors deployed along the pipe specimens: (a) Cases 2-7 in group S1; (b) Case 8 in group S2; (c) Case 12 in group S3; and (d) Case 14 in group S3.

2.8.3.3. Strain distribution results for dent-corrosion interactive effect

The increase of the pipe diameter caused strain changes in the DFOS on the pipes. Figure 2.8.7 shows the strain distributions measured from the DFOS at different immersion times (23 h, 114 h, 268 h, 384 h, 504 h, 624 h, 744 h, 864 h, and 982 h). As shown in Figure 2.8.7(a), for the control specimen, uniform strain expansions were measured due to the individual corrosion effect, which is consistent with visual inspection. Figure 2.8.7(b) shows representative strain distributions measured from the DFOS deployed on the specimens in group S1-2. Compared with results of S0 at the same immersion durations, the values of strain distributions for S1-2 are much larger near dent region due to a dent-corrosion interactive effect. Non-uniform strain distributions are observed in interactive regions. The range of interactive regions is consistent with the residual strain distribution caused by dent effect.

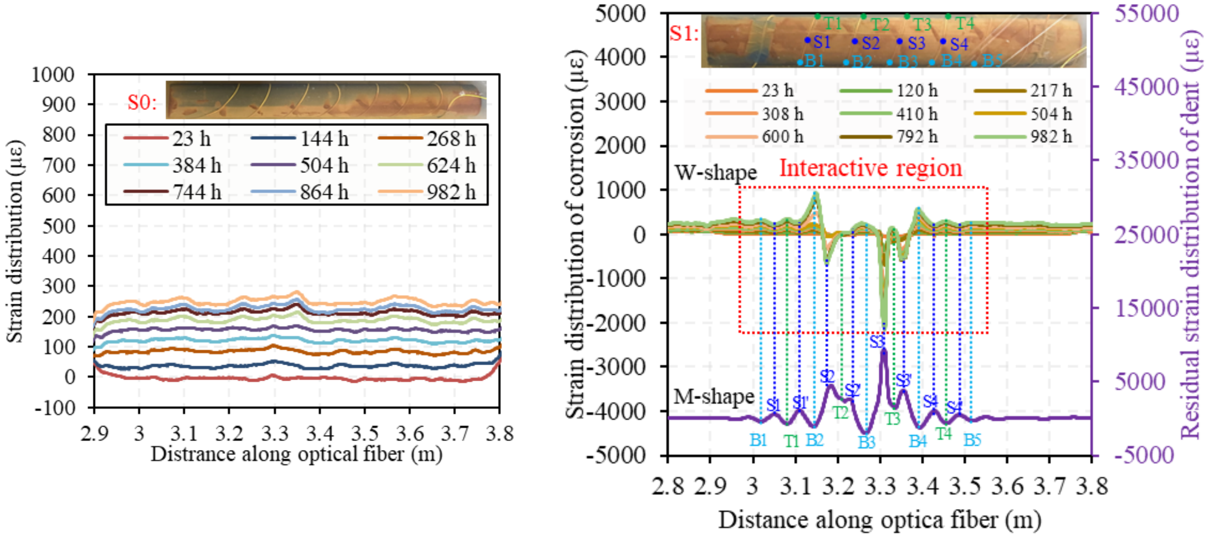

(a) (b)

Figure 2.8.7. Strain distributions of pipe specimens under different immersion times: (a) Case 1 in group S0; (b) Cases 2-7 in group S1.

With the coordinate of optical fiber correlated to the position of optical fiber on the pipe, the strain distribution along optical fiber can be converted to the strains on the helix layout on pipe. In one cycle of helix (B1-S1-T1-S1'-B2), it was found that the strain distribution due to residual dent follows a representative "M" shape: strains near the neutral axis reached the maximum positive value, and strains near the top and bottom reached the maximum negative value. It is consistent with the result of finite element analysis in Figure 2.8.8(a). The strain distribution due to corrosion-dent interactive effect showed a representative "W" shape: strains near the neutral axis are troughs, and strains near the top and bottom are peaks.

Besides, according to von Mises stress field of pipe shown in Figure 2.8.8(b), residual stress concentration occurs mainly on the top and bottom of pipe, but residual stresses on two side of pipe are close to zero. This result is also consistent with the corrosion strain distribution within interactive region: side points (S1, S1', S2, S2', S3, S3', S4, and S4') are located at the lowest points on the curve, but top and bottom points (T1, T2, T3, and T4; B1, B2, B3, and B4) are corresponding to the peak points on the curve. This results indicates that the interactive effect of dent to corrosion has a strong correlation with the residual von Mises stress in the pipe.

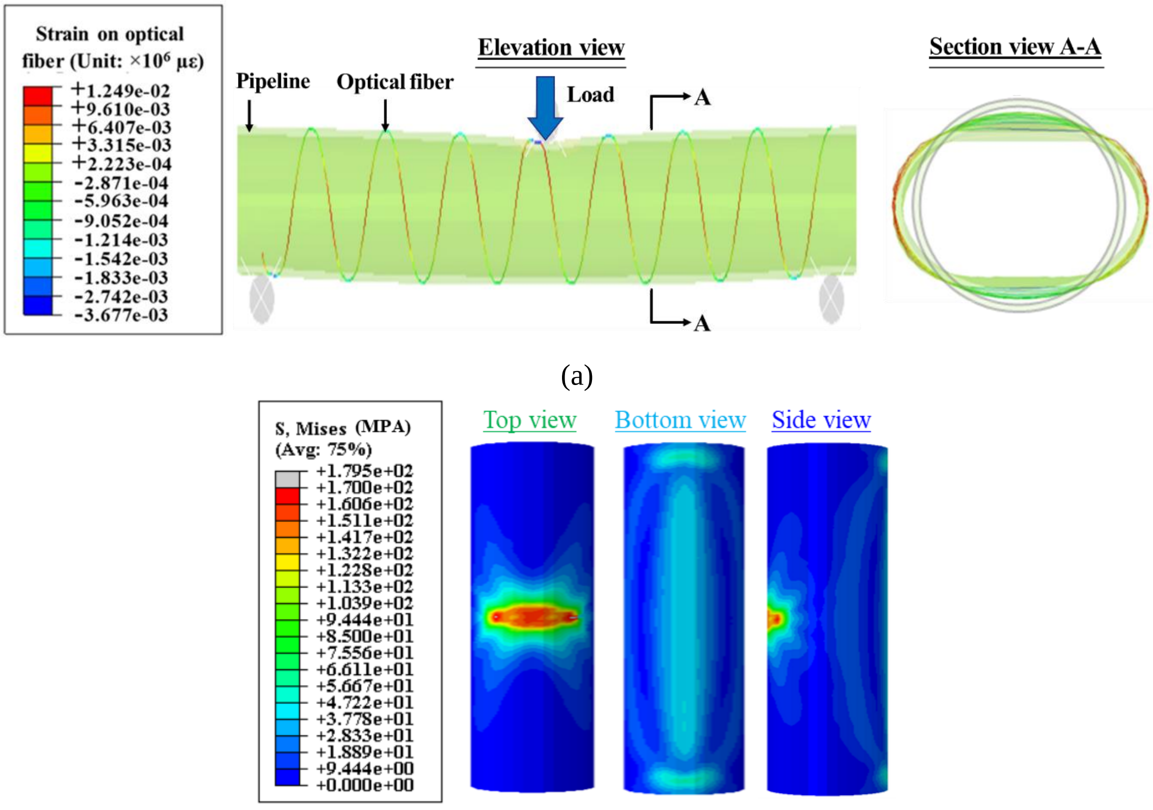

(a)

(b)

Figure 2.8.8. Finite element analysis results for optical fiber installed on pipe under three-point bending: (a) residual strain on optical fiber; (b) von Mises stress field of pipe.

2.9. Measurement of interactive deformations and dent

2.9.1. Overview

The above research has motivated research on the combinations of global and local deformations, which are very often in real practice. A pipe can be subject to global deformations due to ground motions such as earthquakes and sliding, and local deformations such as dents can be caused by excavations and local defects. When a pipe has both global and local deformations which occur at the same position of the pipe, both global and local deformations can significantly affect the strain distributions measured from a DFOS passing through the position of local deformations. It is essential to develop effective methods to detect and differentiate the effect of global and local deformations on the strain distributions measured from the DFOS deployed on pipelines. To address the above challenge, this study aims to: (1) develop an approach to measuring global and local deformations that occur at the same position of a pipe; and (2) investigate the interactive effects of global and local deformations that occur simultaneously using DFOS data.

2.9.2. Experimental program

2.9.2.1. Materials and specimen preparation

Experimental testing was carried out to evaluate and differentiate the iterative effects of bending, dent, notch, and dent that occurred at the same position of each pipe specimen. The pipe specimen was made of carbon steel, which is commonly used for transmission natural gas and hydraulic fluid according to the standard ASTM A500 Grade B. The length, outer diameter, and wall thickness of the pipe specimen were 2550 mm, 114.3 mm, and 6.02 mm, respectively.

The surface of pipe specimens were instrumented with DFOS network following a designated layout, which aimed to cover a significant area of the specimens. Prior to the installation of the optical fibers, the specimen was submerged in a 5% concentration of acetic acid solution to eliminate rust on the surfaces. The tape was used to secure the optical fibers in place during the installation process. Once in place, a fast-setting adhesive was used to attach the optical fibers to the specimens at specific points between the tape spots. After the adhesive had been set, the tape was carefully removed to prevent any damage to the optical fibers or adhesive. Finally, a two-part epoxy was applied to the optical fiber to ensure a sturdy attachment that would facilitate reliable strain transfer between the test specimen and the optical fiber. Any epoxy that spilled from the fiber optic cable was cleaned to prevent possible effects on pipe corrosion.

In this study, the thickness of epoxy was about 250 μm (0.25 mm), which was about 1/10 of the thickness of specimens. The width of epoxy path was about 4-6 mm. The epoxy was cured in air at room temperature (22 ºC ± 2 ºC) and normal humidity (50% ± 5%) for 24 hours. The sensor installation for a continuous length of 1 m took less than 10 min by one person.

2.9.2.1.2. Experimental set-up

The specimens were loaded under four-point bending to generate dent deformation at the middle span using a universal load frame. The length between two loading points was 750 mm. The dent test was conducted under displacement control at a rate of 1 mm/min. The applied load was recorded by the load cell, and an LVDTs were instrumented to record the support and mid-span deflections of pipe specimens. A high-resolution camera was used to capture the deformation of pipelines. The optical fiber was passed through the dent region to measure the iterative effects of bending and dent, bending and notch, and bending and dent/notch. One end of optical fiber was connected to the data acquisition system for the DFOS, and the other end of the optical fiber was free. In this study, a data acquisition system (model: Luna ODiSi 6) was employed to perform OFDR measurements. The measurement accuracy specified by the manufacturer is ±5 με for strain and ±2.2 °C for temperature. The details of testing setup and optical fiber layout is shown in Figure 2.9.1. A total of 2 pipe specimens were investigated, designated as S1 and S2.

Path-1 to Path-3 were installed along the length direction of pipe specimen. Path-1 was installed at the bottom of the pipe; Path-2 was installed along the neutral axis of the pipe; Path-3 was installed near the top of the pipe; Path-4 was installed in helix layout along the circumference direction of pipe specimen, and the distance between adjacent helix is 101.6 mm.

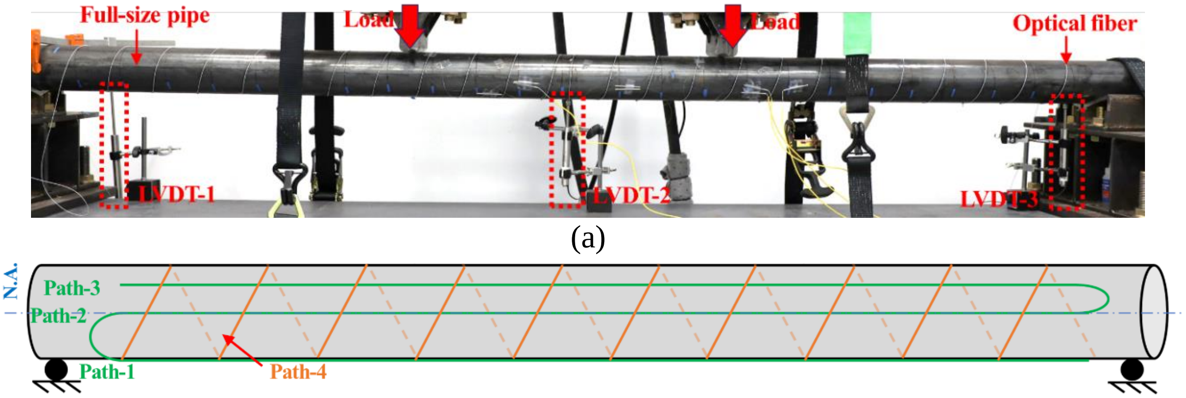

(a)

(b)

Figure 2.9.1. Instrumentation and test set-up: (a) Photograph of test set-up; and (b) Illustration of the deployment of DFOS on the specimens.

2.9.3. Results and discussions

2.9.3.1. Load-displacement curves and visual inspection

Figure 2.9.2 shows the load-displacement curves and visual inspection results of the pipes. The specimens showed similar curves with two stages: (1) Stage 1: elastic stage: the bending load increases with the displacement approximately linearly. (2) Stage 2: inelastic stage: the bending load increases with the displacement with a decreasing slope. In Stage 2, the pipes exhibited a representative interactive effect involving both local dent deformation and global bending deformation. Both dent deformation and global bending increased with the applied displacement.

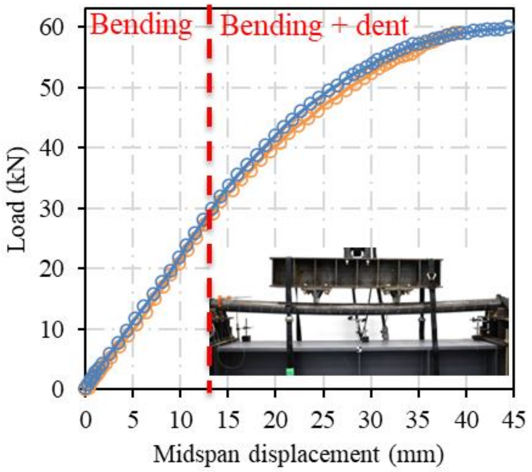

Figure 2.9.2. Load-displacement curves of specimens under four-point bending.

2.9.3.2. Strain distributions

Figure 2.9.3 shows the strain distributions measured from DFOS on the pipe under different loads. The vertical axis is the measured strains. The horizontal axis is the distance along the DFOS, with zero distance at the data acquisition system connector. Only the lengths of the DFOS installed on the pipe are displayed. The magnitudes of strain profiles increased as dent deformations increased during the loading process.

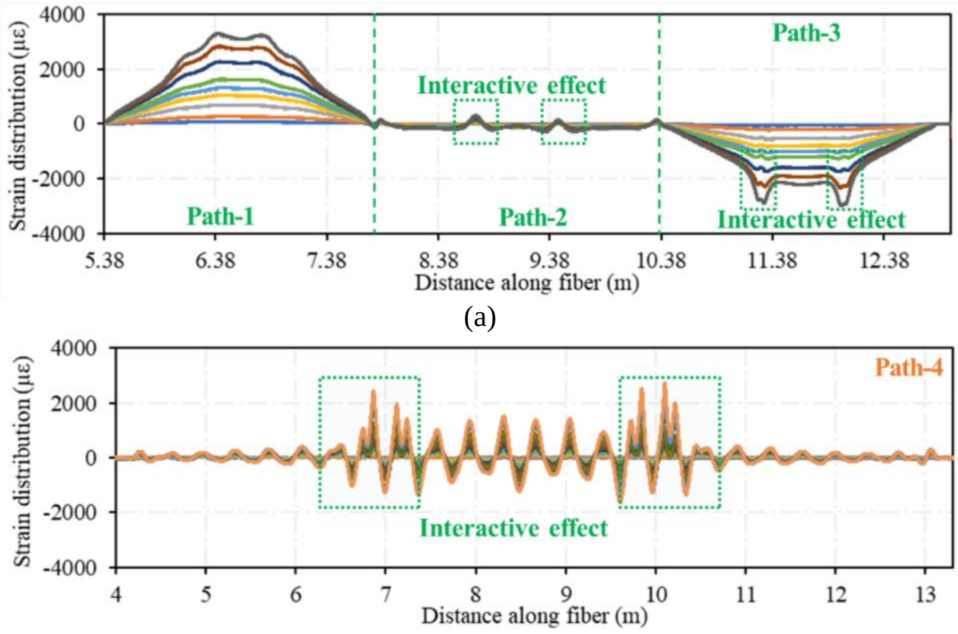

(a)

(b)

Figure 2.9.3. Strain distributions measured from the DFOS: (a) Path-1 to Path-3; (b) Path-4.

According to Figure 2.9.3(a), strain distributions on Path-1 (bottom of pipe) mainly showed global bending effect. However, for Path-2 (neutral axis of pipe) and Path-3 (near top of pipe), obvious interactive effect was observed at two loading points, which makes it easy and straight forward to detect and locate and interactive effect of local dent and global bending deformation. According to Figure 2.9.3(b), strain distributions near two loading points showed obvious "M" shape in one period of the curve. By integrating DFOS Path-1 to Path-4, the interactive region is determined along both longitudinal direction and circular direction.

2.9.3.3. Discussions

The strain distributions on Path-4 can be further used to differentiate the interaction between global bending and local dent. Under a certain load, the corresponding strain distribution can be regarded as a one-dimensional signal along the space domain. The spatial frequency within the interactive region and out of interactive region are different: the spatial frequency of global bending effect is relatively low, and the spatial frequency of local dent effect is relatively high. By using fast Fourier transform, the signal from its space domain was converted to a representation in the frequency domain. With the increase of applying load value, strain distributions under different loads were converted to frequency domain and then replotted into a three-dimensional power spectrum, which is shown in Figure 2.9.4(a).

The magnitude of power at the maximum load level is normalized to one and represented by color. It is observed that global bending effect occurred from the beginning of the test, but the local dent effect became obvious until the loading value larger than 30 kN, which is also consistent with the load-displacement curve. Moreover, if the normalization strategy is changed to: The magnitudes of powers at each load level are normalized to one (Figure 2.9.4(b)), it is observed that local stress concentration effect is detected almost from the beginning of the test, which is much earlier than the occurring of local dent effect. Such early detection capability is promising to enhance the safety and operational management of pipelines.

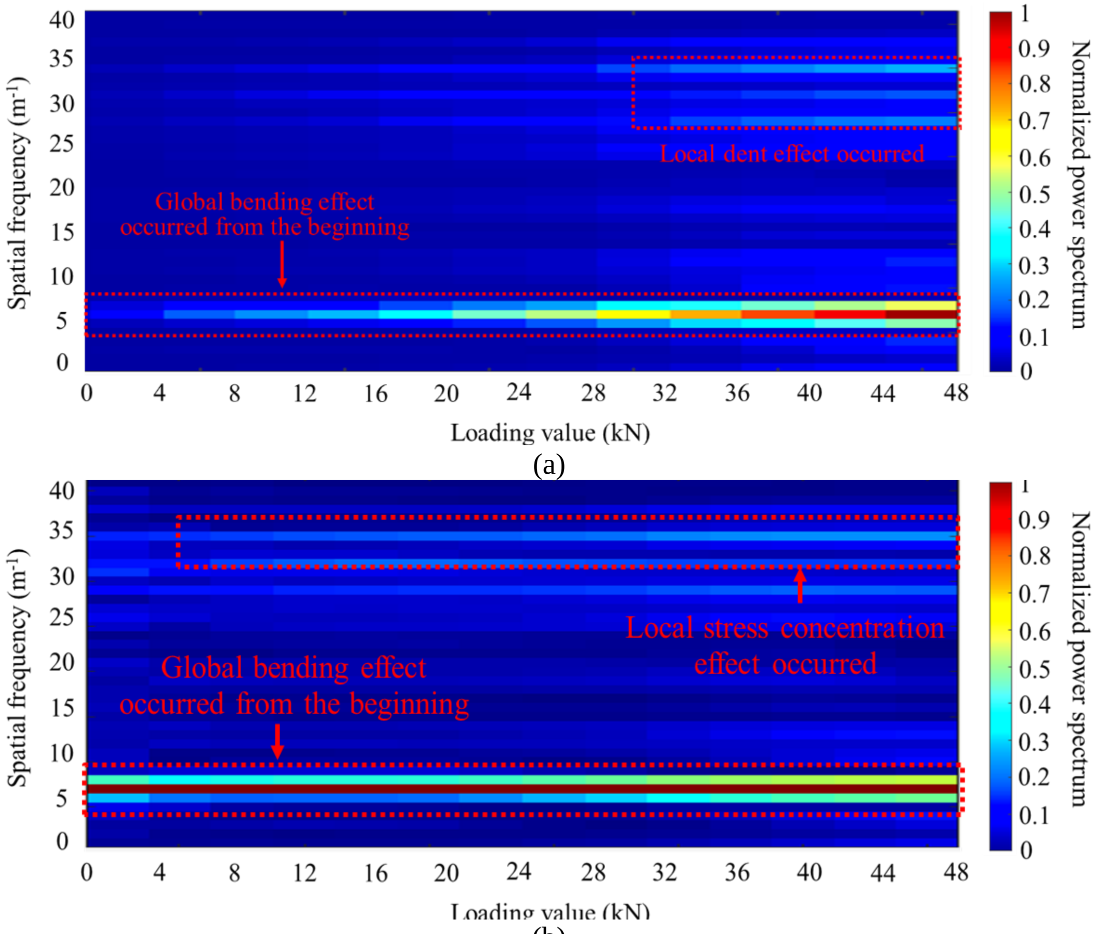

(a)

(b)

Figure 2.9.4. Normalized power spectrum of strain distribution: (a) the magnitude of power at the maximum load level is normalized to one; and (b) the magnitudes of powers at each load level are normalized to one.

2.10. Measurement of interactive impact loads and corrosion

2.10.1. Overview

This paper presents an experimental investigation on the behavior of steel plates under the combination effects of impact loads and corrosion using discrete and distributed fiber optic sensors. A systematic assessment strategy is developed to estimate corrosion severity and structural response of steel plates under impact loads and corrosion. The steel plates were coated with epoxy and instrumented with FBG and OFDR sensors. The tested scenarios include impact loads, corrosion, and their combination. In all scenarios, the fiber optic sensors monitored the structural response of the steel plates. This research provides insights into the complex interaction between impact loads and corrosion in steel plates.

2.10.2. Methods

2.10.2.1. FBG sensor

FBG refers to a periodic and permanent modification of the refractive index within the core of an optical fiber [65]. FBG sensors measure alterations in the reflected signal originating from the grating structure, which is influenced by external parameters such as temperature and strain. The reflected wavelength, known as the Bragg wavelength (λ_B), is expressed as [66]:

$$\lambda_B = 2n_{eff}\wedge \tag{2.10.1}$$

where n_{eff} is the effective refractive index; and $\wedge$ is the grating period corresponding to the distance between two adjacent grating planes.

When a wide spectrum light is projected to an FBG, the gratings selectively reflect a narrow band spectrum according to Eq. (2.10.1). The constructive interference between the light and the grating period causes a shift in the Bragg wavelength ($\Delta\lambda_B$) under temperature or strain changes. This Bragg wavelength shift can be expressed as [67]:

$$\Delta\lambda_B = \lambda_B[(1 - P_e)\Delta\varepsilon + (\alpha + \xi)\Delta\mathrm{T}] \tag{2.10.2}$$

where λ_B is the Bragg wavelength; P_e is the photo elastic coefficient of the fiber; $\Delta\varepsilon$ is strain change; α and ξ are the respective thermal expansion coefficient and the thermo-optic coefficient of the fiber and are dependent on the material of fiber; and ΔT is the temperature change. After implementing temperature compensation, strain changes are correlated with changes in Bragg wavelength, enabling the measurement of corrosion-induced strains.

2.10.2.2. Corrosion monitoring

Distributed sensing systems can provide continuous and spatially resolved measurements, allowing for the detection of strain changes at multiple points along the entire length of the fiber. This enables comprehensive coverage and monitoring of large areas without the need for numerous individual sensors. However, it is important to note that distributed sensing typically does not provide the same high acquisition frequency as discrete FBG sensors. FBG sensors can offer very fast acquisition rates, making them suitable for capturing dynamic events and rapid changes in strain. Since this study aims to investigate the simultaneous effects of corrosion and impact loads, high-frequency measurements are crucial. Thus, FBG sensors are well-suited for the assessment of the dynamic response and effects under the combined action.

2.10.2.3. Simplified sensing model for corrosion detection

Pitting corrosion is usually characterized by the formation of localized cavities beneath the metal surface, serving as a site for rust accumulation, resulting in stress concentration at the corroded area [68]. To simulate the corresponding corrosion-induced strain, it is assumed that the growth of corrosion product primarily develops in the vertical direction. This assumption allows to model the effect of corrosion as an equivalent concentrated load applied to the surface where corrosion occurs. The FBG demonstrates the ability to accurately synchronize real-time changes in Bragg wavelength, thereby enabling the detection and monitoring of strain changes induced by applied dynamic load and localized corrosion with high sensitivity. A sensing model is constructed to generalize the FBG-based method for detecting and monitoring corrosion phenomena. To reasonably evaluate pitting corrosion using the FBG-based sensing model, it is assumed that all corrosion products remain on the substrate and that the sensor is perfectly bonded to the metal surface. Consequently, the Bragg grating period can be simplified to a fixed support beam model. Figure 2.10.1 shows the simplified sensing model depicting the deformations of the FBG sensor under pitting corrosion and impact loading conditions. In Figure 2.10.1(a), when an equivalent upward force F_c caused by corrosion is applied to the bottom of the optical fiber, the sensor will be stretched and protruding of corrosion product above the steel surface will lead to an upward displacement (Δ_c). Similar downward bending deformation at the top of the fiber due to external loads will occur, as indicated in Figure 2.10.1(b).

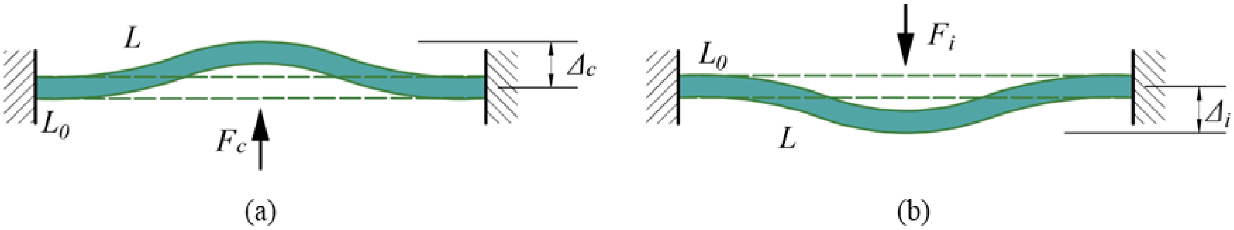

Figure 2.10.1. Deformations of a beam model under (a) pitting corrosion, and (b) impact load.

The deformation of the FBG sensor ΔL either induced by pitting corrosion or impact loading can be calculated as:

$$\Delta L = L - L_0 \tag{2.10.4}$$

where L is the deformed length of the FBG sensor; and L_0 is the original length of the FBG sensor. Then, the stain in the FBG sensor, $\Delta\varepsilon$, is expressed as:

$$\Delta\varepsilon = \frac{\Delta L}{L_0} = \frac{L - L_0}{L_0} \tag{2.10.5}$$

According to Eq. (2.10.2), $\Delta\varepsilon$ can be estimated by the Bragg wavelength change, $\Delta\lambda_B$:

$$\Delta\varepsilon = \frac{\Delta\lambda_B}{\lambda_B(1 - P_e)} \tag{2.10.6}$$

Integrating Eq. (2.10.6) into Eq. (2.10.5), ΔL is estimated by the Bragg wavelength change:

$$\Delta L = L_0 \cdot \frac{\Delta\lambda_B}{\lambda_B(1 - P_e)} \tag{2.10.7}$$

For a triangular deformation, based on Eq. (2.10.4), the upward displacement, Δ_c, is:

$$\Delta_c = \frac{1}{2}\sqrt{L^2 - L_0^2} = \frac{1}{2}\sqrt{\Delta L \cdot (\Delta L + 2L_0)} \tag{2.10.8}$$

Plugging Eq. (2.10.7) into Eq. (2.10.8), Δ_c is expressed by the Bragg wavelength change $\Delta\lambda_B$:

$$\Delta_c = \frac{L_0}{2}\sqrt{\alpha\Delta\lambda_B \cdot (\alpha\Delta\lambda_B + 2)} \tag{2.10.9}$$

where $\alpha = \frac{1}{\lambda_B(1-P_e)}$. Δ_c can be used as an indicator to assess the severity of pitting corrosion.

2.10.2.4. Pit depth estimation

Pits can exhibit various shapes and geometrics. ASTM-G46 stipulates standard visual charts for various shapes of pits, as shown in Figure 2.10.2 [69]. Figure 2.10.2(a) shows trough pitting corrosion, which is characterized by the formation of small, elongated pits parallel to the surface. These pits can deepen and elongate gradually, leading to the formation of channels or grooves. On the other hand, sideway pitting corrosion are pits on the vertical or inclined surfaces of a substrate. These pits can appear as localized depressions or craters along the sidewalls, as shown in Figure 2.10.2(b). One of the inherent risks associated with pitting corrosion is the misleading nature of surface pit openings as an indicator of sub-surface corrosion. This poses a significant challenge in accurately assessing the structural condition of components. Despite the appearance of minimal surface damage, the presence of substantial sub-surface corrosion can undermine the stability and performance of the affected structures. To ensure a thorough and reliable evaluation, it is imperative to employ a comprehensive technique and method that can penetrate beyond the surface, enabling an accurate assessment of the extent and influence of pitting corrosion on structural integrity.

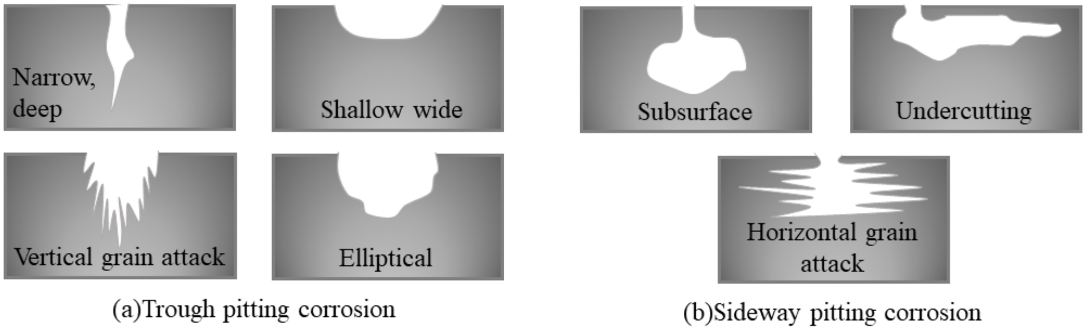

(a)Trough pitting corrosion (b)Sideway pitting corrosion

Figure 2.10.2. Standard cross-sectional shapes of pits.

The modeling of pit depth can be simplified as a two-dimensional (2D) problem, focusing on the penetration that poses a significant threat to critical structural elements by perforating the steel substrate. For the coated steel substrate, pitting corrosion is expected to occur beneath coatings, allowing the ingress of environmental agents. As discussed in reference [66], in order to facilitate the estimation of pit depth in corrosion assessment, a generalized shape model is proposed by capturing the geometric characteristics of various pitting shapes, which is able to represent most cases, as illustrated in Figure 2.10.3.

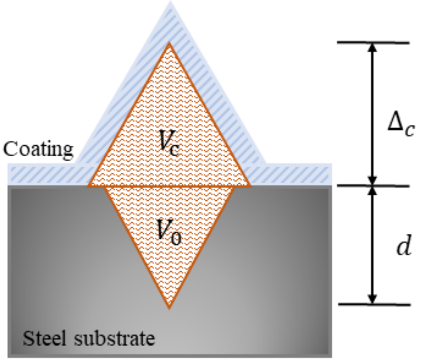

Figure 2.10.3. Generalized shape of pitting corrosion.

The total volume of corrosion product V of various cross-sectional shapes of pitting corrosion can be calculated as [66]:

$$V = V_0 + V_c = \int_0^d A_i h_i + \int_0^{\Delta_c} A_j h_j \tag{2.10.10}$$

where V_0 is the volume of original steel; V_c is the volume of the corrosion product above the steel surface; A_i and h_i are the area and height of element of original steel, respectively; A_j and h_j are the area and height of the element of corrosion product above the steel surface, respectively. If a triangle needle cross-sectional shape of the pit is assumed, Eq. (2.10.10) can be expressed as:

$$V = V_0 + V_c = \frac{A_0 d}{3} + \frac{A_c \Delta_c}{3} \tag{2.10.11}$$

where A_0 and A_c are the area of the corrosion product above the steel surface and the pit, respectively; d is the pit depth; and Δ_c is the upward displacement caused by corrosion protruding. Based on our previous study, it can be assumed that A_c is approximately 1.2 times larger than A_0, where $A_c = 1.2A_0$. Thus, Eq. (2.10.11) can be rewritten as:

$$V = \frac{A_0}{3}(d + 1.2\Delta_c) \tag{2.10.12}$$

Pitting corrosion leads to the formation of protrusions on the steel surface as corrosion product accumulates and covers the pits. The volume of the corrosion build-up varies depending on its constituents and differs from that of the original steel $\alpha\text{-}F_e$. Table 2.10.1 shows the volume ratio c, revealing that the corrosion product can expand by a factor of 1.5 to 6 compared to the volume of the original iron. Thus, the total volume of corrosion product V can be estimated as:

$$V = cV_0 \tag{2.10.13}$$

Table 2.10.1. Volume ratio ***c*** of corrosion product with different constituents

Rust	$\alpha\text{-}F_e$	F_eO	F_eO_4	$\alpha,\gamma\text{-}F_{e_2}O_3$	$\alpha,\gamma,\delta,\beta\text{-}F_eOOH$	$F_e(OH)_2$	$F_e(OH)_3$	$F_{e_2}O_3 \cdot 3H_2O$
Volume ratio, *c*	1.0	1.5-1.8	2.0	2.0-2.1	2.8-3.5	3.8	3.0	6.0

Combining Eq. (2.10.12) and Eq. (2.10.13), the pit depth d is expressed as:

$$d = \frac{1.2\Delta_c}{c - 1} \tag{2.10.14}$$

Thus, by integrating Eq. (2.10.9) into Eq. (2.10.14), the pit depth d can be estimated by monitoring the Bragg wavelength change as:

$$d = \frac{0.6L_0 \cdot \sqrt{\alpha\Delta\lambda_B \cdot (\alpha\Delta\lambda_B + 2)}}{c - 1} \tag{2.10.15}$$

where $\alpha = \frac{1}{\lambda_B(1-P_e)}$.

2.10.2.5.Corrosion rate assessment

The total mass loss m caused by corrosion can be calculated by:

$$m = \rho V \tag{2.10.16}$$

where ρ is the density of corrosion product, and V is the total volume of corrosion product.

Assuming that pitting corrosion product mainly develops vertically, the total volume of corrosion product V is proportional to the upward displacement Δ_c, so V can be expressed as:

$$V = k_1 \cdot \Delta_c \tag{2.10.17}$$

where k_1 is the linear scaling factor between the volume of corrosion product and the induced upward displacement. Combining Eq. (2.10.16) and Eq. (2.10.17), the total mass loss can be estimated as:

$$m = \rho k_1 \cdot \Delta_c \tag{2.10.18}$$

The CR is defined as the derivative of the total mass loss of a metal with respect to time. Thus, CR can be expressed as:

$$CR = \frac{dm}{dt} = \rho k_1 \frac{d\Delta_c}{dt} \tag{2.10.19}$$

Thus, by integrating Eq. (2.10.9) into Eq. (2.10.19), the average CR can be estimated from the measured Bragg wavelength change of the FBG sensor:

$$CR = \frac{\rho k_1 L_0}{2} \cdot \frac{d\sqrt{\alpha\Delta\lambda_B \cdot (\alpha\Delta\lambda_B + 2)}}{dt} \tag{2.10.20}$$

where $\alpha = \frac{1}{\lambda_B(1-P_e)}$.

2.10.3. Experimental program

2.10.3.1. Materials and specimens

Steel plates specimens made of ASTM A36 hot-rolled steel were adopted, with dimensions of 170mm×170mm×3mm. Four holes with a diameter of 13mm were punched on the four corners of each steel plate to fasten it on a test table, as shown in Figure 2.10.4(a). Before installing the fiber optic sensors, the surfaces of steel plates were cleaned with acetone to enhance the bond between epoxy and steel. Then, FBG sensors and DFOS were deployed on the steel plates, as depicted in Figure 2.10.4(b). The DFOS covered a large area of the plate. Therefore, for each plate, a 2-meter OFDR-based DFOS and an FBG sensor were deployed to monitor the growth and distribution of corrosion, as well as the dynamic response.

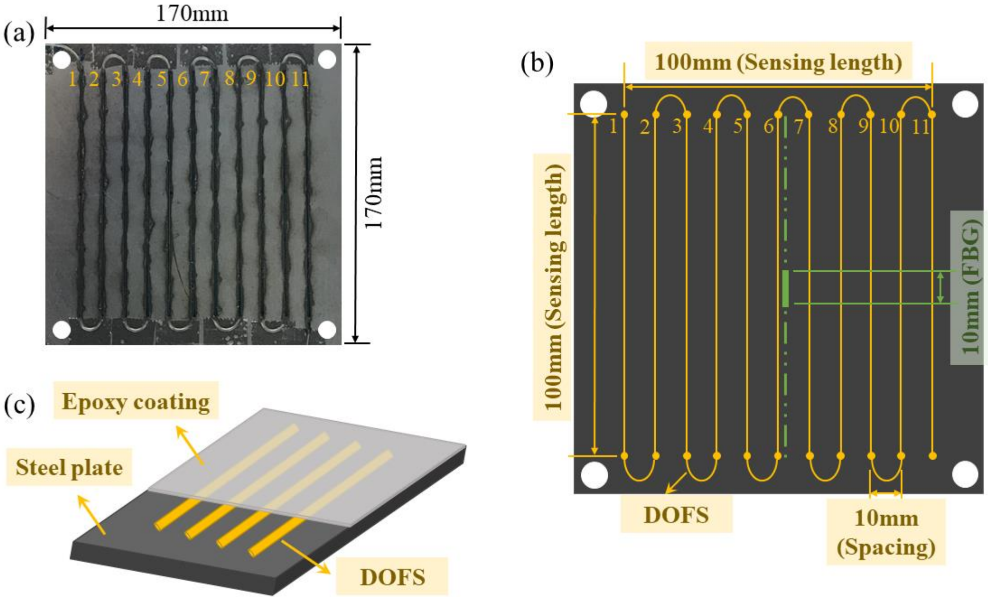

Figure 2.10.4. Test specimens and instrumentation: (a) An example of the test specimen, (b) schematic diagram of the test instrumentations, and (c) schematic diagram of the specimen structure.

The DFOS was arranged in a serpentine pattern with 11 sensing segments, measuring 100 mm in length and spaced 10 mm apart, creating a square sensing area of 100mm x 100mm. Super glue was used to attach each sensing segment and Bragg grating period, and tape was also utilized to secure the U-turn points. To differentiate the multiple distributed sensing segments for each specimen, they were labeled numerically from 1 to 11. The DFOS was connected to a distributed interrogator (ODiSi 6100 series) manufactured by LUNA using a stand-off cable. The gauge pitch of the DFOS was set to a minimum value of 0.65 mm. The FBG sensor was mounted at the center of the specimen using super glue, positioned adjacent to the intermediate (No. 6) distributed sensing segment, where impact loads were expected to be applied. The FBG sensors were connected to an FBG high-frequency interrogator (si155 series) manufactured by LUNA, with an acquisition frequency of 500 Hz. Following the instrumentation of FOS, Duralco^{TM} 4461 adhesive epoxy, a free-flowing liquid adhesive, was applied to the test specimens to simulate common conditions adopted in industrial applications, as shown in Figure 2.10.4(c). To protect the optical fibers and prevent premature failure due to applied impact loads, the thickness of epoxy coating was controlled at 1.5 mm using a professional drawdown bar. Then, the specimens were left to cure for 72 hours at an ambient temperature of approximately 24-27℃, ensuring that the epoxy coating reached the necessary hardness for subsequent corrosion and impact loading tests.

2.10.3.2. Test setup

To investigate the interaction between corrosive environments and dynamic loading on epoxy-coated steel, a series of tests were conducted in three groups: individual impact load, individual corrosion, and combined impact load and corrosion. In the impact load tests, a repetitive impact cycle was implemented. A 2-kg calibration weight was dropped freely to apply an impact load onto the center of the test specimens, as shown in Figure 2.10.5(a).

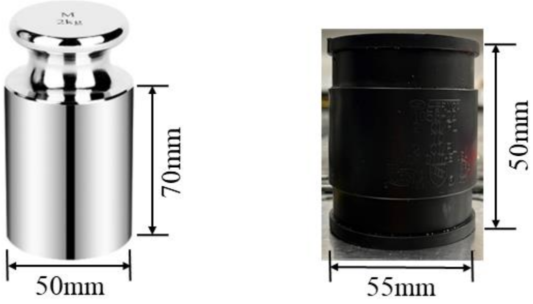

(a) Calibration weight (b) Rubber tube

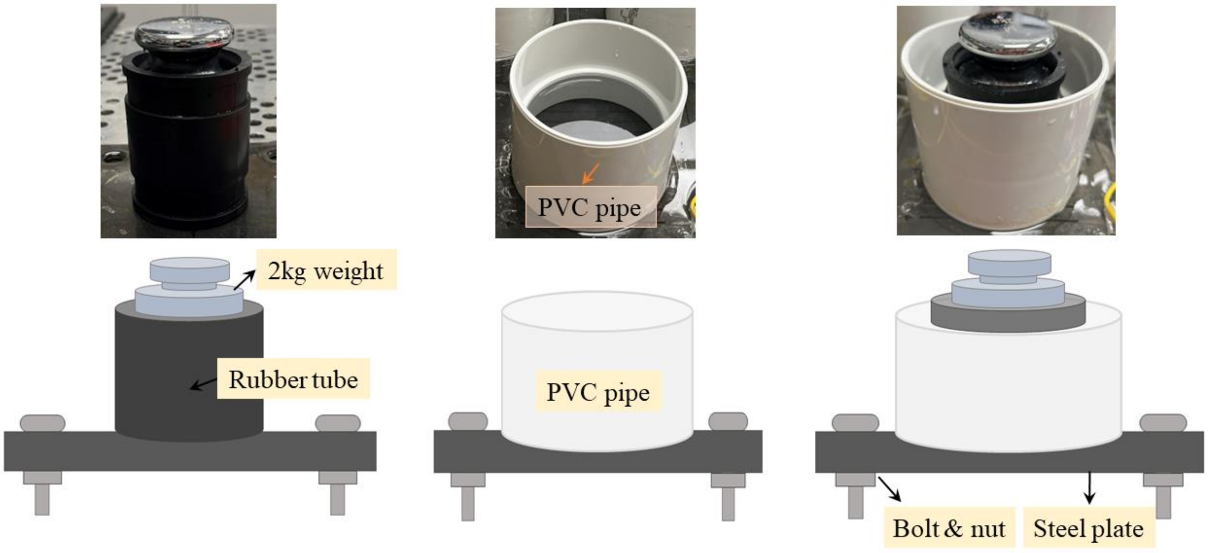

(c) Impact loading test setup (d) Corrosion test setup (e) Combined test setup

Figure 2.10.5. Photos and schematic of the test setups.

The setup for the impact loading tests also involved the placement of a rubber tube in the central area of each specimen to ensure consistent positioning of the weight during impact tests, as shown in Figure 2.10.5(b) and Figure 2.10.5(c). Within each impact cycle, sequential impact tests were conducted at 10-minute intervals with varying impact heights (12.5mm, 25mm, and 50mm). The contact time between the weight and the test specimen during each impact test was 5 seconds. The impact velocities and forces for each impact condition are listed in Table 2.10.2. In the corrosion tests, a 100mm diameter PVC pipe was affixed to the central sensing area of each specimen using epoxy resin, as shown in Figure 2.10.5(d). The pipe was then filled with a 3.5% NaCl solution to create a corrosive environment. To expedite the corrosion process, an artificial crack measuring 20mm in length was introduced using a soft grinding wheel with a diameter of 25mm. The crack was positioned 2mm away from the FBG sensor to facilitate corrosion beneath the sensor, enabling detection and further exploration of the interaction between corrosion and impact. The corrosion tests were carried out for a duration of 43 days (1032 hours). The test setup, illustrated in Figure 2.10.5(e), allowed for the assessment of the combined effects of impact loading and corrosion. The impact load cycle was repeated every six days, resulting in a total of six impact load cycles throughout the 43-day corrosion process, until sensor failure occurred.

Table 2.10.2. Impact parameters

Impact height (mm)	Velocity (m/s)	Force (N)
12.5	0.5	30
25.0	0.7	35
50.0	1.0	40

A total of 12 plates were tested, with 4 specimens in each group, including one specimen for temperature compensation. The plates subject to impact tests and combined tests were divided into three working conditions, according to the heights of impact tests. A comprehensive investigation encompassing 21 test cases was conducted, as indicated in Table 2.10.3.

Table 2.10.3. Investigated cases under three working conditions

Working condition	Case	Corrosion time (h)	Impact height (mm)
Corrosion	C1	1032	-
	C2	1032	-
	C3	1032	-
Impact loading	I1-1	-	12.5
	I1-2	-	25.0
	I1-3	-	50.0
	I2-1	-	12.5
	I2-2	-	25.0
	I2-3	-	50.0
	I3-1	-	12.5
	I3-2	-	25.0
	I3-3	-	50.0
Corrosion & impact loading	C&I1-1	1032	12.5
	C&I1-2	1032	25.0
	C&I1-3	1032	50.0
	C&I2-1	1032	12.5
	C&I2-2	1032	25.0
	C&I2-3	1032	50.0
	C&I3-1	1032	12.5
	C&I3-2	1032	25.0
	C&I3-3	1032	50.0

2.10.4. Results and discussion

2.10.4.1. Specimen resistance to corrosion under impact loads

2.10.4.1.1. Effect of impact load on corrosion development

Figure 2.10.6 shows the changes in Bragg wavelength resulting from individual corrosion and combined corrosion with impact. As the FBG sensor was limited to a sensing length of 10mm and installed at the center of the test specimen, it primarily reflected the corrosion and impact response in that central area. In Figure 2.10.6(a), the total wavelength changes of the three test specimens during the corrosion process were very close, indicating similar severity of corrosion in the central regions. They exhibited consistent trends in three phases of wavelength variation, as observed in previous studies [70, 71]. Phase 0 represented the initial stage of corrosion, where rust began to fill the poses between the adhesive and FBG sensors; Phase 1 denoted the rapid development period characterized by a high corrosion rate; Phase 2 signified the stabilized corrosion progression, where the accumulation of corrosion products hindered oxygen diffusion and further contact with the steel, resulting in a slower corrosion rate. The remaining wavelength changes primarily reflected residual strain. Throughout the total 1032 hours of corrosion exposure, phase 0, phase 1, and phase 2 lasted about 290 hours, 175 hours, and 567 hours, respectively.

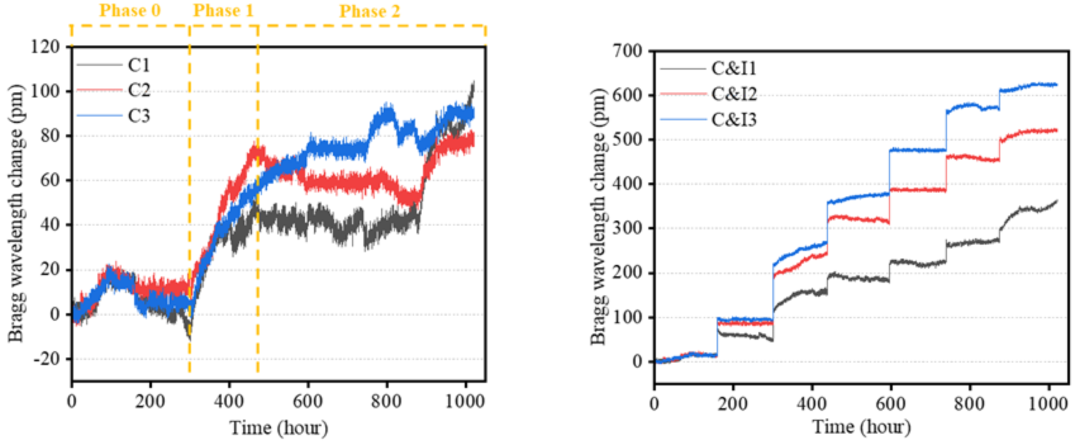

(a) (b)

Figure 2.10.6. Bragg wavelength change: (a) corrosion test, and (b) combined corrosion and impact test.

Compared with Figure 2.10.6(a), Figure 2.10.6(b) shows the combined Bragg waveforms. The corrosion phases showed relatively gradual wavelength changes, whereas the impact responses demonstrated sudden increases in wavelength, indicating that impact loads exacerbated corrosion. Additionally, when comparing the total Bragg wavelength changes between individual corrosion and combined scenarios, it can be found that the applied impacts significantly promoted corrosion growth. For instance, the total wavelength changes of specimens C3 and C&I3 were 90.93 pm and 627.45 pm, respectively, representing a 6.9-fold increase in wavelength after impact loading. Corrosion was accelerated to varying degrees under the influence of impacts. In Figure 2.10.6(a), C1, C2, and C3 exhibited similar overall wavelength changes with values of 101.33 pm, 80.73 pm, and 90.93 pm, respectively. However, the wavelength changes of C&I1, C&I2, and C&I3 at the end of the tests were 362.92 pm, 522.95 pm, and 627.45 pm, respectively, with significant differences, as shown in Figure 2.10.6(b). This can be attributed to differences in coating porosity or bonding properties between the coating and steel, resulting in diverse effects of impact loads on corrosion.

To overcome the limitations of FBG sensors, DFOS offered real-time monitoring of corrosion development and distribution. Figure 2.10.7 to Figure 2.10.9 show the corrosion distribution before and after each impact cycle for specimens C&I1, C&I2, and C&I3, respectively. These figures show the locations and values that exhibit the maximum strain changes.

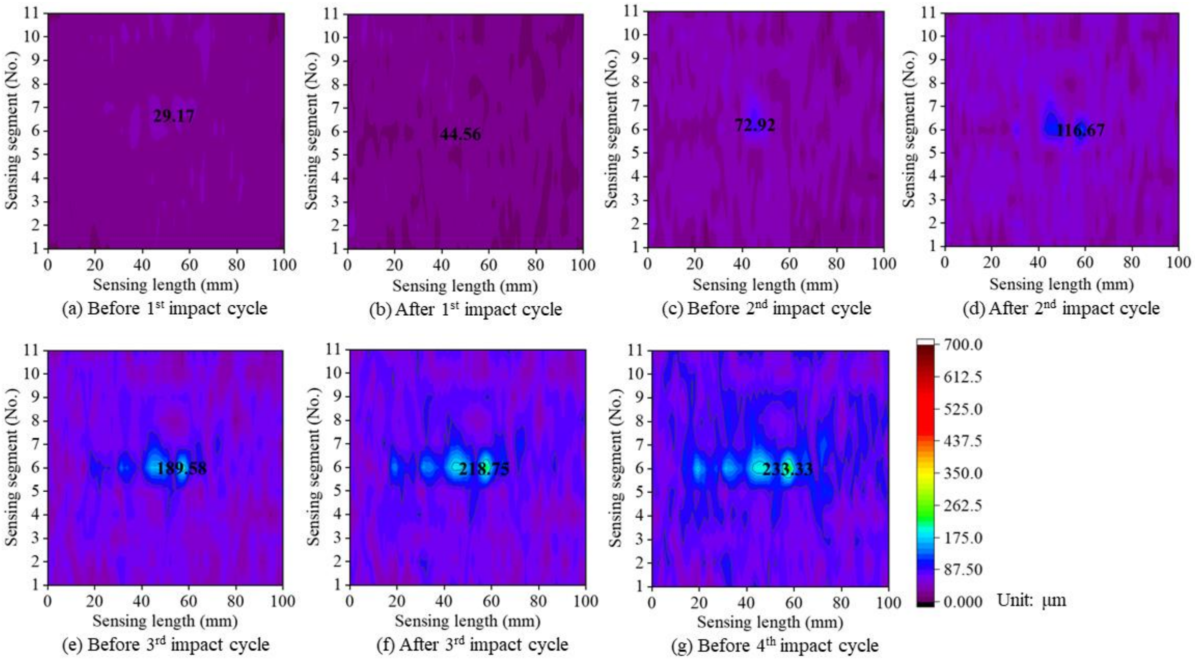

(a) Before 1st impact cycle (b) After 1st impact cycle (c) Before 2nd impact cycle (d) After 2nd impact cycle

(e) Before 3rd impact cycle (f) After 3rd impact cycle (g) Before 4th impact cycle

Figure 2.10.7. Effect of impact on corrosion distribution for specimen C&I1.

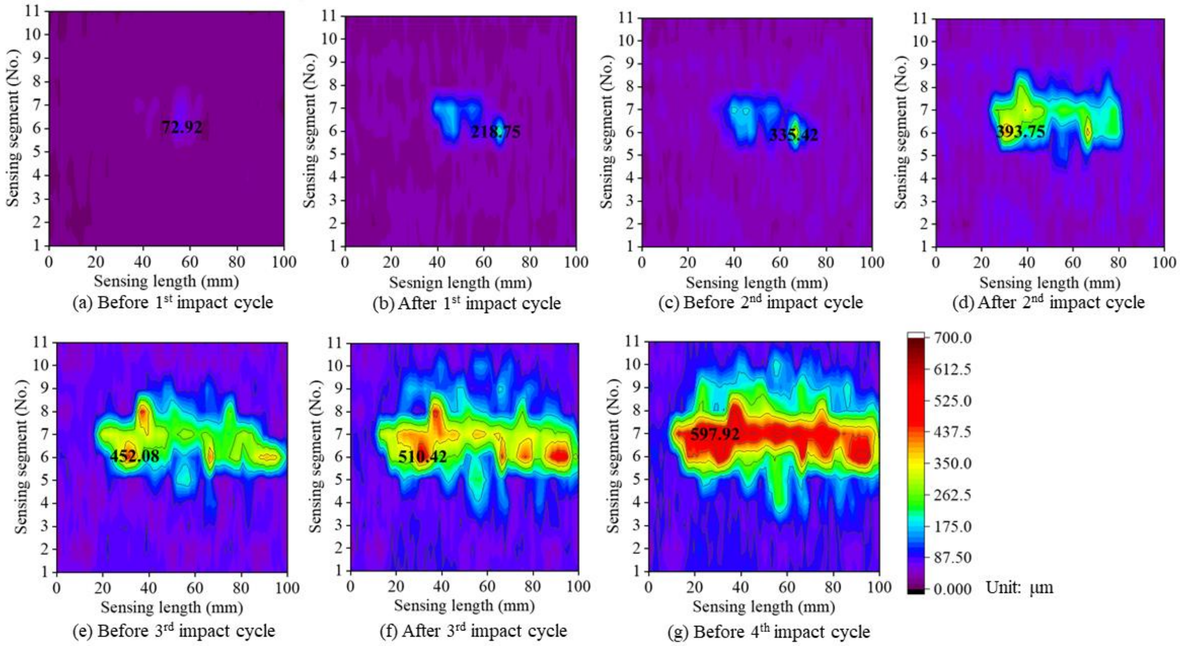

(a) Before 1st impact cycle (b) After 1st impact cycle (c) Before 2nd impact cycle (d) After 2nd impact cycle

(e) Before 3rd impact cycle (f) After 3rd impact cycle (g) Before 4th impact cycle

Figure 2.10.8. Effect of impact on corrosion distribution for specimen C&I2.

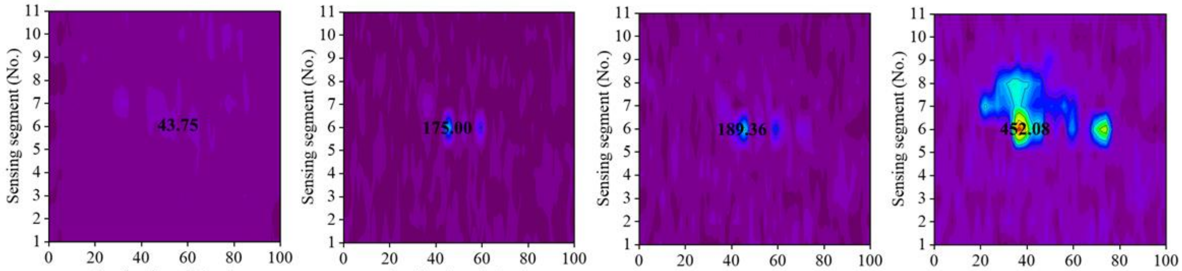

(a) Before 1st impact cycle (b) After 1st impact cycle (c) Before 2nd impact cycle (d) After 2nd impact cycle

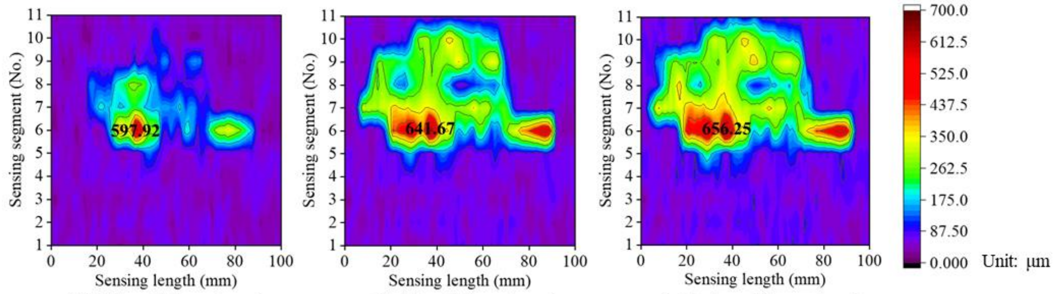

(e) Before 3rd impact cycle (f) After 3rd impact cycle (g) Before 4th impact cycle

Figure 2.10.9. Effect of impact on corrosion distribution for specimen C&I3.


(a) C&I1 (b) C&I2 (c) C&I3

Figure 2.10.10. Visual inspection of specimens after rust removal.

Corrosion originated from the areas where cracks were introduced in the epoxy coating. As time progressed, corrosion intensified and spread outward from these initial points. The strain distributions measured by DFOS provided a visual depiction of the gradual expansion of corrosion damage. However, due to the brittle and easily damaged nature of DFOS, the DFOS suffered premature damage before the 4th impact cycle test. Although DFOS could not complete the monitoring of the entire corrosion process, the corrosion distribution profile detected by DFOS closely aligned with the profiles observed in the visual inspection pictures shown in Figure 2.10.10.

Furthermore, the strain changes measured at adjacent sensing points where FBG and DFOS were installed were nearly identical, as indicated in Figure 2.10.11. This validates the effectiveness and accuracy of DFOS in detecting corrosion distribution and severity. Moreover, a comparison of the corrosion area and severity before and after each impact clearly demonstrates that impact loading exacerbated corrosion, consistent with the abrupt increases in Bragg wavelength changes in Figure 2.10.6(b). Additionally, from Figure 2.10.7(g), Figure 2.10.8(g), and Figure 2.10.9(g), C&I1 experienced the least severe corrosion, as indicated by the maximum strain change of 233.33 μm, while C&I3 exhibited the most extensive corrosion, with a maximum strain change of 656.25

μm, resulting in the smallest and largest corroded areas, respectively. These findings suggest that the bonding performance of the coating was disrupted to varying degrees. Hence, the corrosion rate and severity are directly influenced by the performance of the coating.

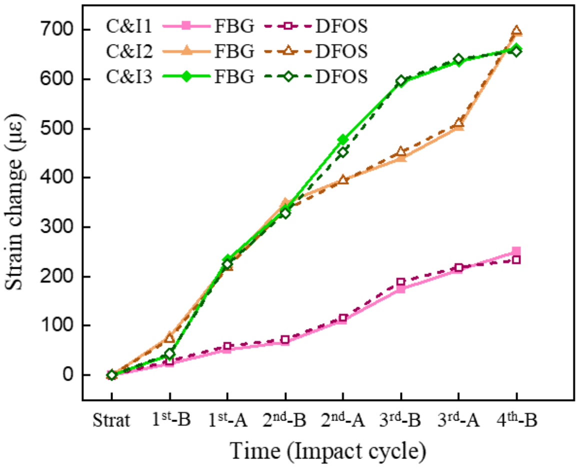

Figure 2.10.11. Strain changes of FBG and DFOS before and after each impact cycle. B denotes before impact cycles, and A denotes after impact cycles.

2.10.4.1.2. Effect of impact loads on pit depth

The pit depth of the test specimens was estimated using the developed generalized model, as described by Eq. (2.10.15). In addition, to assess the effect of impact loading on corrosion, the impact magnification index (η_d) is defined as:

$$\eta_d = d_{c\&i}/d_c \tag{2.10.21}$$

where $d_{c\&i}$ is the pit depth under the combined corrosion-impact test, and d_c is the pit depth under the corrosion test. Based on the test results discussed in Section 5.1.1, impact loads have the potential to increase the pit depth. This suggests that the impact magnification index should be greater than 1, and a higher impact magnification index signifies a stronger influence of impact loading on corrosion development.

Figure 2.10.12(a) shows the pit depth under both the corrosion test and the combined corrosion-impact test. At the end of the tests, the pit depth of the test specimens was also scanned using a Keyence Digital Microscope. The specimens subject to the combined action of corrosion and impact load exhibited greater pit depths compared with the specimens exposed to corrosion alone. The acceleration of impact load on corrosion progression was predominantly observed during the initial 450 hours, after which its influence gradually diminished. This behavior aligns with the pit depth development mechanism, where the early exposure phase is characterized by high growth rates (kinetic phase), followed by a phase controlled by oxygen concentration, resulting in slower development [72]. Specifically, specimens C2 and C&I2 displayed rapid pit depth development, reaching 262 μm and 525 μm, respectively, after approximately 450 hours of corrosion exposure. Subsequently, the pit depths increased gradually to 295 μm and 593 μm until the end of the test. Similar patterns were also observed for specimens C&I1 and C&I3.

Figure 2.10.12(b) shows the impact magnification index, η_d, according to Eq. (2.10.21). η_d was above 2 consistently, and up to 4.35, showing a high influence of impact loads on corrosion, particularly during the initial stage of approximately 300 hours. Beyond this stage, the changing trend of η_d gradually stabilized. Additionally, η_d for specimens C&I2 vs. C2 and C&I3 vs. C3 exhibited rapid increases in the early stage. In contrast, η_d for specimens C&I1 vs. C1 was relatively stable throughout the corrosion process. The effect of impact loads on corrosion was influenced by the extent of damage to the performance of epoxy coating, as indicated by the contour of corrosion distribution in Figure 2.10.7 to Figure 2.10.9 and the visual inspection in Figure 2.10.10. Specimens C&I2 and C&I3 exhibited larger corrosion areas and more severe coating damage than C&I1, allowing for a more extensive interaction between corrosive agents and the steel substrate. Hence, the extent to which impact loading affected corrosion was influenced by the performance and damage of the coating.

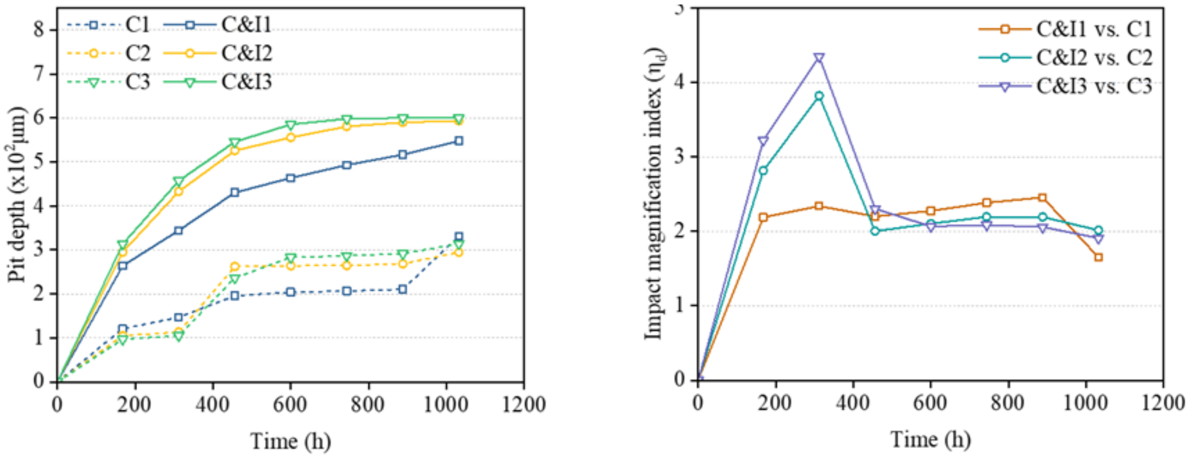

(a)　(b)

Figure 2.10.12. (a) Development of pit depth (d), and (b) variation of impact magnification index (η_d).

Figure 2.10.13 compares the estimated and scanned pit depths. The scanned pit depth was close to the estimated pit depth, with a maximum difference of 1%, validating the accuracy of the proposed pit depth model. Notably, the scanned pit depths were slightly smaller than the calculated values, which could be attributed to the presence of residual corrosion products within the pits.

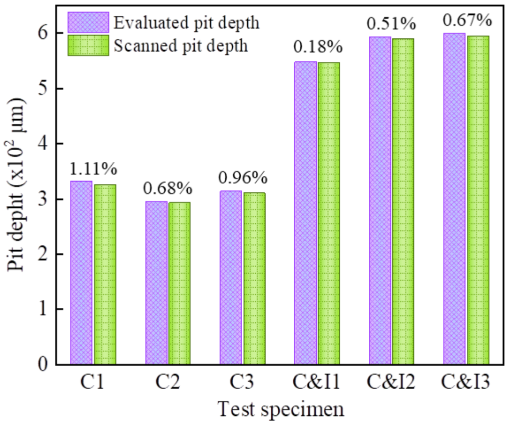

Figure 2.10.13. Validation of pit depth estimation. Symbol % means the error of the estimated pit depth.

2.10.4.1.3. Effect of impact loads on corrosion rate

Based on Eq. (2.10.18), the mass loss of the test specimens was evaluated from the measured Bragg wavelength change. Figure 2.10.14 shows a comparison of the mass loss between specimens under the corrosion test and those under the combined corrosion-impact test. The specimens subject to the combined condition exhibited greater mass loss compared to the specimens under the individual corrosion condition.

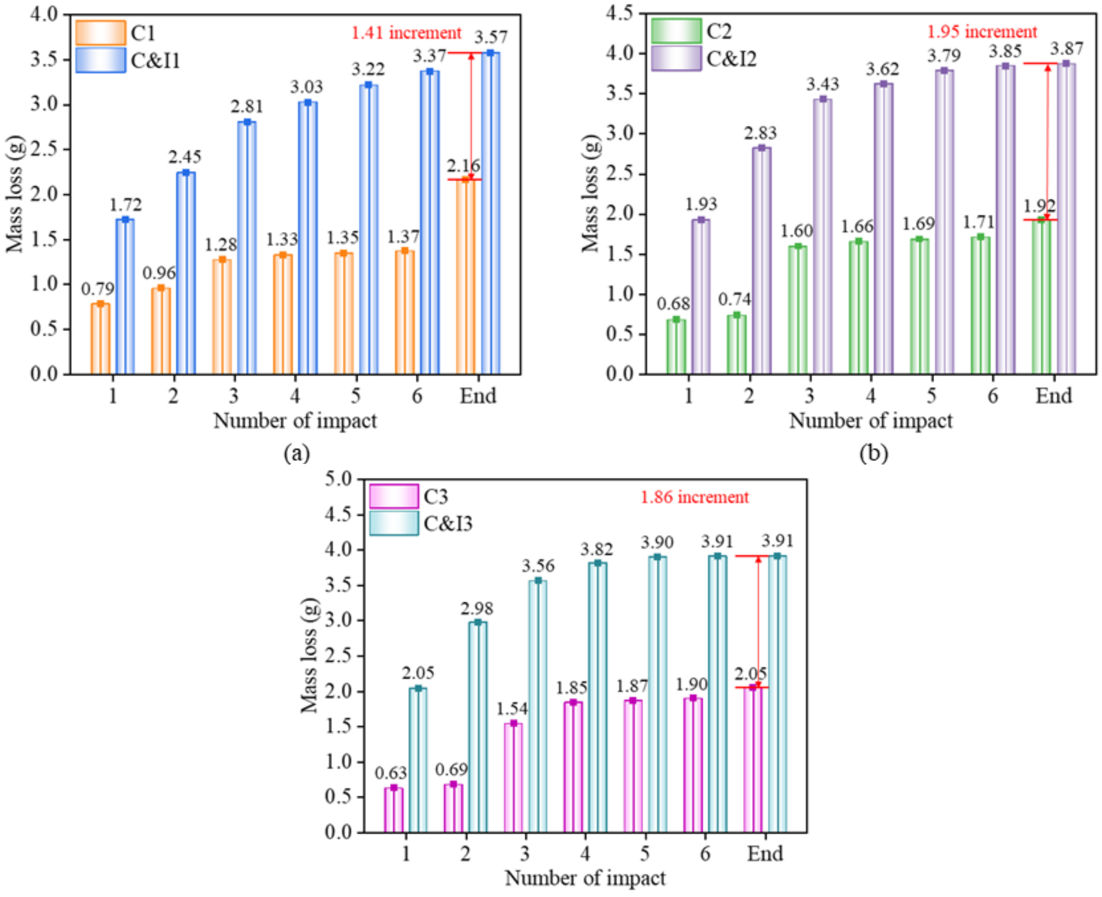

(a) (b) (c)

Figure 2.10.14. Mass loss under individual corrosion and combined corrosion-impact conditions.

When the total mass loss of the specimens under corrosion was similar, the specimens subject to the corrosion-impact condition showed notable differences in total mass loss. Specifically, the difference in total mass loss between C&I1 and C1 was much smaller than that between C&I2 and C2, and C&I3 and C3, with values of 1.41 g, 1.95 g, and 1.86 g, respectively. This discrepancy can be attributed to the lower severity of coating damage in C&I1, which hindered the corrosion solution from penetrating and interacting with the steel. In addition, it is worth noting that the mass loss increased rapidly during the first three cycles of impact loading and then gradually stabilized, aligning with the kinetic phase and concentration-controlled phase of corrosion development.

An average CR can be calculated by Eq. (2.10.20) to assess corrosion. Figure 2.10.15 shows the variation of CR in the corrosion process. At the end of the test, the CR of the specimens subject to the combined condition was noticeably higher than those under the individual corrosion condition. Specifically, C&I3 displayed the highest corrosion rate at 112 μm/year, while C3 had a corrosion rate of 16 μm/year. This pattern was also observed in other specimens, indicating that impact loading accelerated the corrosion rate. The rapid increase in corrosion rate due to the application of impact load was prominent during the initial approximately 450 hours of exposure and gradually declined thereafter. Furthermore, it is found that the promotional effect of impact load on the corrosion rate varied significantly among the specimens. In line with the findings from mass loss evaluation, specimens with more severe coating damage exhibited a more pronounced effect of impact loading on the corrosion rate. Moreover, referring to the NACE specification for pitting corrosion severity [73], it is categorized into four levels: low, moderate, high, and severe, with corrosion rates below 127 μm/year, 127-201 μm/year, 203-381 μm/year, and above 381 μm/year, respectively. In Figure 2.10.15, the average corrosion rates of C&I2 and C&I3 exceeded 127 μm/year, indicating a moderate corrosion severity, while the remaining specimens had corrosion rates below 127 μm/year, representing a low corrosion severity.

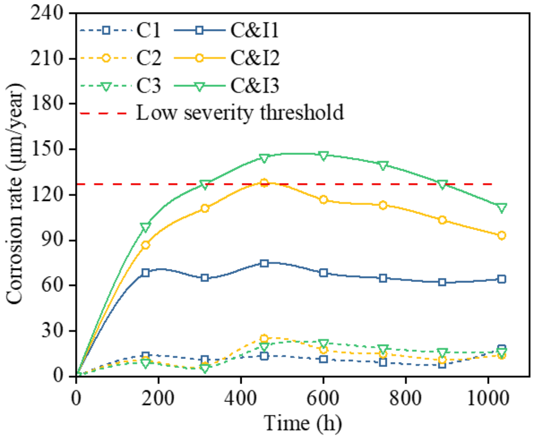

Figure 2.10.15. Pitting corrosion warning according to NACE specification.

2.10.4.2. Specimen resistance to impact loads under corrosion

2.10.4.2.1. Effect of impact parameters on dynamic response

Figure 2.10.16 to Figure 2.10.18 show the Bragg waveforms of impact loads monitored by FBG sensors under combined corrosion and impact loading conditions at three different impact heights (h): 12.5mm, 25.0mm, and 50.0mm, respectively. Six cycles of impact loads were applied throughout the corrosion process. In these figures, 0 represents the impact response without corrosion, while the 6th represents the last impact applied during the late stage of corrosion. The Bragg wavelength response exhibited three distinct phases of impact behavior across all cases:

- Loading phase: At the initial application of the impact load, a triangle waveform of tensile deformation was observed, lasting about 1 to 1.5 seconds.
- Stable phase: Following the loading phase, a stable period occurred as the load transitioned from dynamic to static. This phase typically lasted an average of 3.5 seconds.
- Unloading phase: During impact unloading, a larger triangle waveform of compression deformation was formed, resulting in a residual Bragg wavelength.

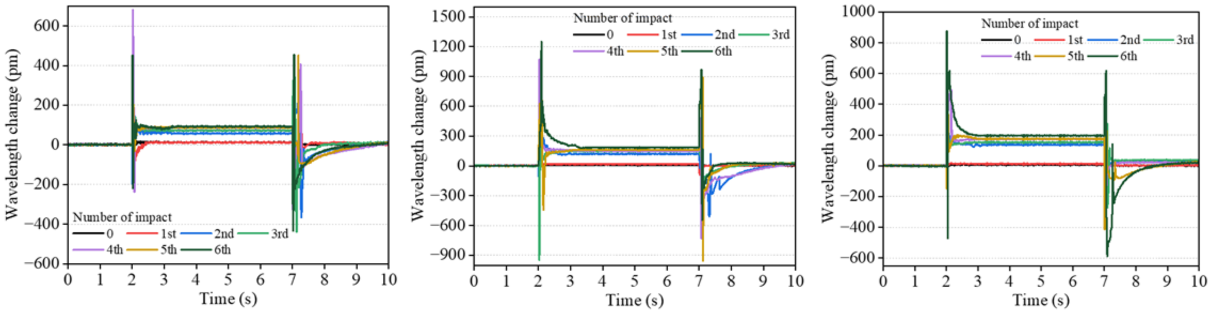

(a) C&I1-1 (b) C&I2-1 (c) C&I3-1

Figure 2.10.16. Impact response detected by FBG (h=12.5mm).

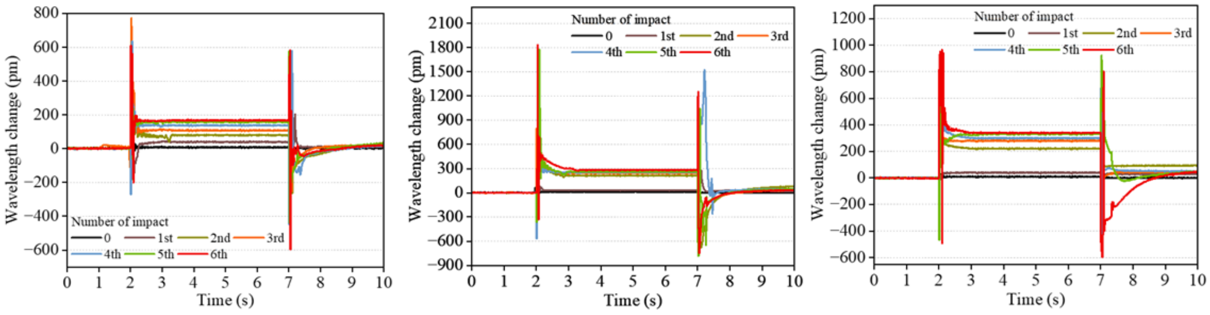

(a) C&I1-2 (b) C&I2-2 (c) C&I3-2

Figure 2.10.17. Impact response detected by FBG (h=25.0mm).

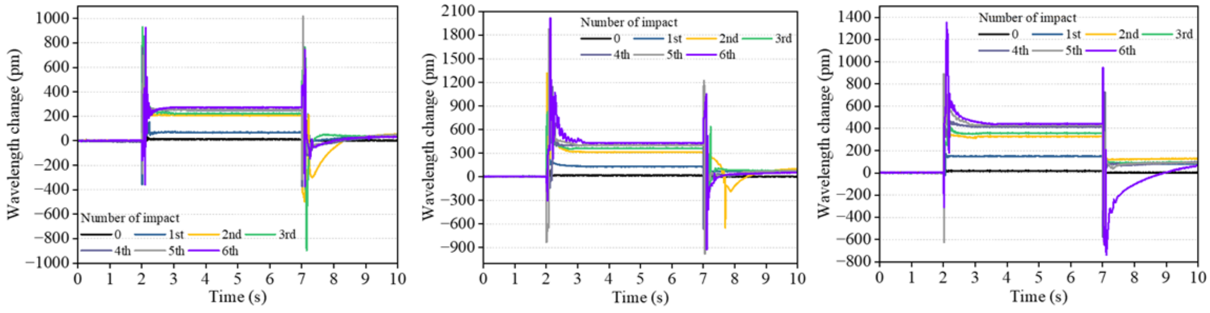

(a) C&I1-3 (b) C&I2-3 (c) C&I3-3

Figure 2.10.18. Impact response detected by FBG (h=50.0mm).

The influence of corrosion development on the dynamic motion process and the interaction between the free-fall weight and the test steel plate contributed to the varied patterns of wavelength variation. During the stable phase, the magnitude of Bragg wavelength changes increases with the number of impacts. Notably, a significant change in wavelength occurred between the 1st and 2nd impacts, followed by a gradual increase with subsequent impacts. This indicates that the impact response became more apparent as corrosion intensified, particularly during the initial stage of corrosion. For instance, the wavelength increases of C&I2-2 from 0 to the 2nd impact was 196.55pm, accounting for 71.78% of the total wavelength change from 0 to the 6th impact. In multiple impact tests at the same free-fall height, the residual wavelength after impact unloading initially increased significantly, then fluctuated from the 3rd to the 5th impact, and decreased at the 6th impact. This can be attributed to the generation and protrusion of corrosion products, which contributed to the residual wavelength. In the early stage of corrosion, rapid corrosion development led to the production of a substantial amount of rust. However, as rust accumulated and covered the corrosion pits, the corrosion process slowed down as it hindered the contact of steel with aggressive agents. In the combined test, impact loads not only densified the porous rust but also promoted its diffusion, explaining the decrease in residual wavelength observed at the 6th impact.

Figure 2.10.19 compares the impact-induced wavelength changes at three different heights for the same number of impacts. In the initial uncorroded stage, as shown in Figure 2.10.19(a) to Figure 2.10.19(c), the wavelength changes caused by impacts at 12.5mm and 25.0mm are similar, but slightly smaller than those induced by impact at 50.0 mm impact.

As the corrosion progressed, the differences in wavelength changes among the three impact heights became more pronounced. This can be attributed to the gradual reduction in stiffness of the corroded steel plates as corrosion intensified and corrosion products formed, leading to more significant dynamic responses. Higher impact heights resulted in more prominent dynamic responses during the stable phase, characterized by nonlinear increases in wavelength variation. For instance, C&I1-1, C&I1-2, and C&I1-3 had wavelength changes of 87.13pm, 136.93pm, and 251.58pm at the 4th impact, respectively. This indicates that the wavelength changes at adjacent height levels increased by 1.57 and 1.84 times, respectively. After impact unloading, the residual wavelength also demonstrated an increase with higher impact heights, suggesting that higher impact heights resulted in more severe impairment of coating properties, such as bonding performance, ultimately leading to intensified corrosion.

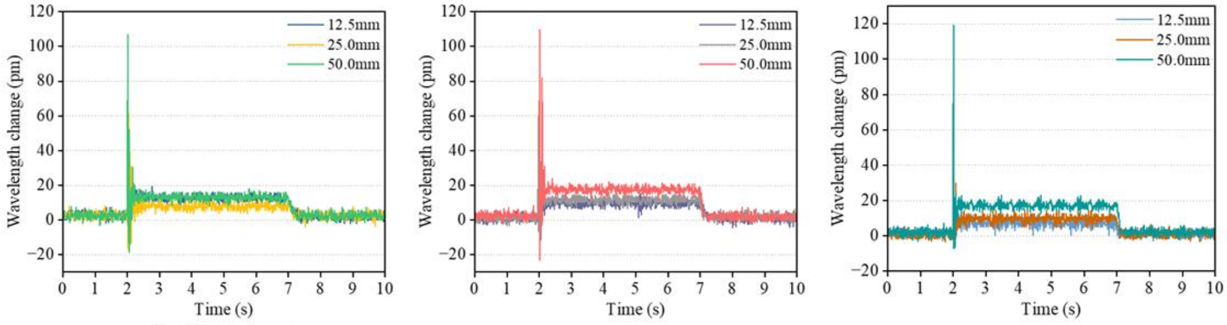

(a) C&I1, 0 impact

(b) C&I2, 0 impact

(c) C&I3, 0 impact

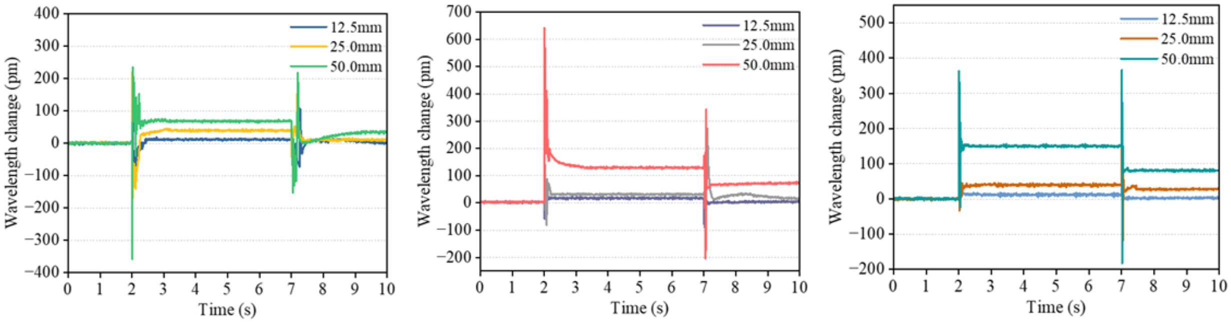

(d) C&I1, 1st impact

(e) C&I2, 1st impact

(f) C&I3, 1st impact

Figure 2.10.19. Comparison of impact responses under different free-fall heights.

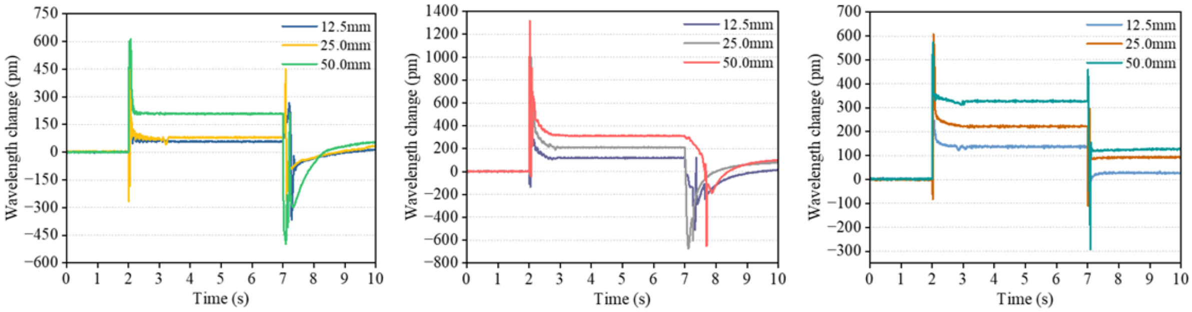

(g) C&I1, 2nd impact (h) C&I2, 2nd impact (i) C&I3, 2nd impact

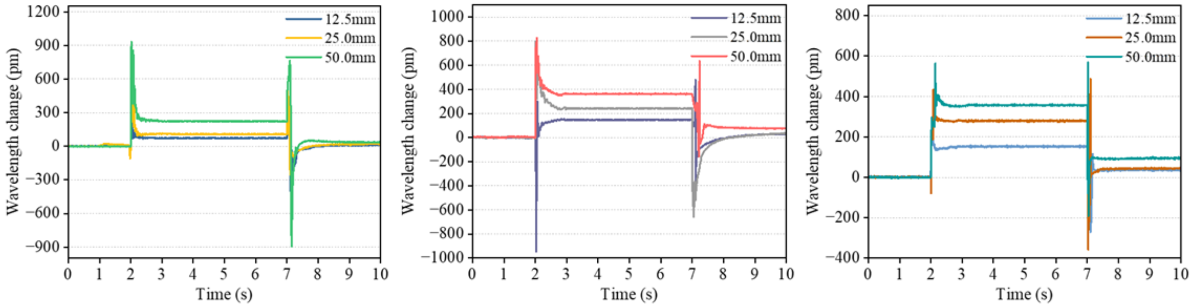

(j) C&I1, 3rd impact (k) C&I2, 3rd impact (l) C&I3, 3rd impact

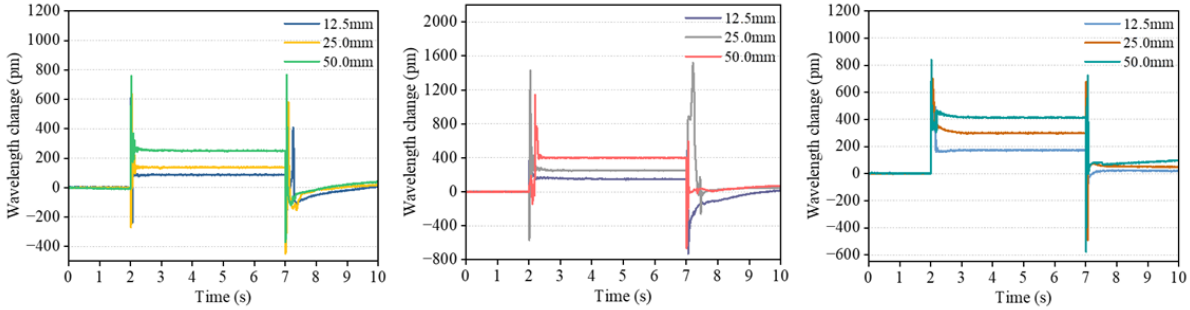

(m) C&I1, 4th impact (n) C&I2, 4th impact (o) C&I3, 4th impact

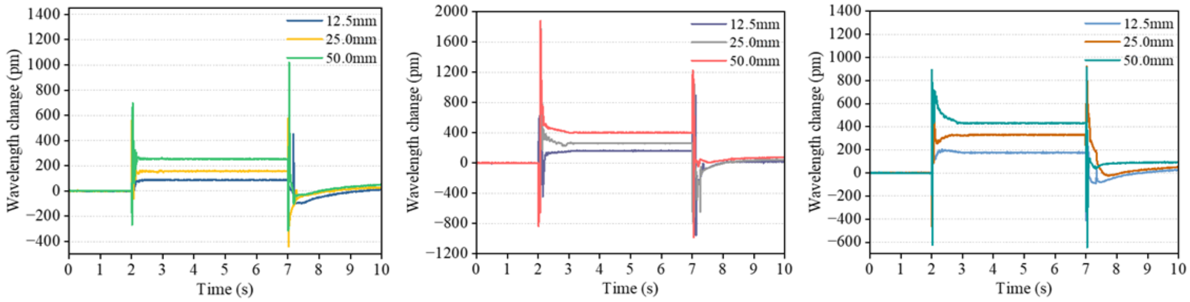

(p) C&I1, 5th impact (q) C&I2, 5th impact (r) C&I3, 5th impact

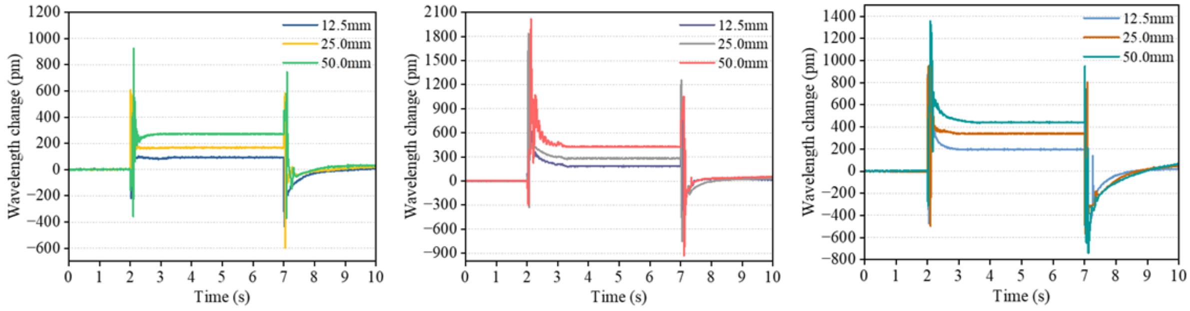

(s) C&I1, 6th impact (t) C&I2, 6th impact (u) C&I3, 6th impact

Figure 2.10.19. Comparison of impact responses under different free-fall heights.

2.10.4.2.2. Impact energy dissipation

To assess the impact load, an accelerometer was installed on the top surface of the specimen to measure the acceleration resulting from the applied impact load. To ensure the reliability and accuracy of the impact response assessment, only the peak acceleration data captured by the accelerometer were considered, mitigating any potential uncertainties or inconsistencies that could arise during the analysis. In addition, to intuitively evaluate the effect of corrosion on impact load, the impact energy dissipation index (μ) is defined as:

$$\mu = \frac{A_0 - A_n}{A_0} \times 100\% \tag{2.10.22}$$

where A_0 is the peak acceleration under the impact load without corrosion, and A_n is the peak acceleration under the n$^{\text{th}}$ impact load.

Figure 2.10.20 shows the relationship between peak acceleration and the number of impacts at different heights. In the 43-day corrosion progression, impact load tests were conducted every 6 days, resulting in a total of 6 impact tests. The peak acceleration under the 0$^{\text{th}}$ impact represents the acceleration generated by the impact load without corrosion. A correlation can be observed between the peak acceleration and corrosion severity. This can be attributed to the reduced stiffness of the specimens caused by the corrosion-induced reduction in cross-section. Consequently, the ability of the specimens to withstand the applied impact load was diminished due to the detrimental effects of corrosion. Furthermore, it can be observed that the acceleration decay rate for the first four impact loads of specimens C&I2 and C&I3 was higher compared to the subsequent curves. Conversely, C&I1 exhibited a relatively steady decline in acceleration at a lower rate than the other specimens. This discrepancy can be attributed to the less severe corrosion experienced by C&I1, resulting in a relatively higher ability to withstand the impact load. Moreover, in all specimens, the acceleration decay rate under the 50.0 mm impact was significantly higher than that under the 12.5mm and 25.0mm impacts, particularly during the first four impact loads. Subsequently, the decay rate decreased and approached a more consistent level. This indicates the general impact response of the specimens under the corrosion condition, with the rapid deterioration in the ability to withstand the impact load primarily occurring during the early stages of corrosion.

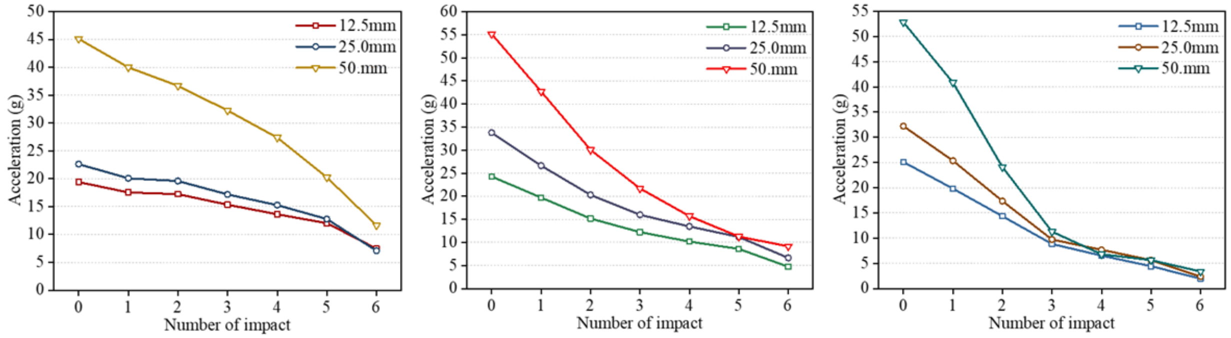

(a) C&I1 (b) C&I2 (c) C&I3

Figure 2.10.20. Acceleration history at different impact heights.

Figure 2.10.21 shows the impact energy dissipation of the specimens under different heights of impact loads. The energy dissipation curves of 12.5 mm and 25.0 mm exhibited similar trends and values. The energy dissipation curve of 50.0 mm was higher, indicating a greater energy dissipation rate. Notably, in the 6th impact test, the impact energy dissipation at the three different impact heights became closer, with specimens C&I2 and C&I3 even exhibiting almost identical values. This suggests that the influence of impact height on energy dissipation gradually diminished as corrosion progressed. In addition, based on visual inspection, it is apparent that specimens with more severe corrosion exhibited higher energy dissipation. Specifically, the highest values of the impact energy dissipation index (μ) for specimens C&I1, C&I2, and C&I3 were 74.17%, 83.39%, and 93.62%, respectively. This indicates that as corrosion became more pronounced, the specimens experienced greater energy dissipation during impact loading.

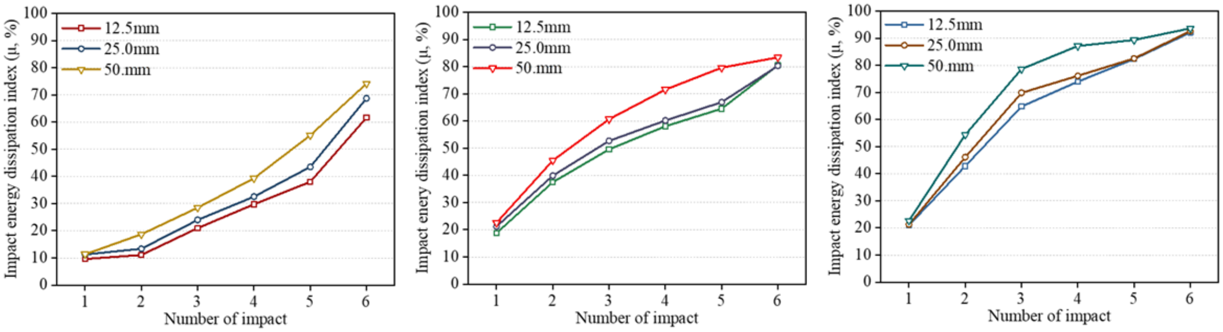

(a) C&I1 (b) C&I2 (c) C&I3

Figure 2.10.21. Impact energy dissipation at different impact heights.

2.10.5. Summary

This research investigated the behavior of steel plates under the combination effects of impact loads and corrosion using discrete and DFOS via experiments. A systematic assessment strategy was developed to estimate the corrosion severity and structural response of steel plates under impact loads and corrosion. The interaction between impact loads and corrosion of steel plates was investigated. Based on the above investigations, the following conclusions can be drawn:

- The experimental results demonstrate the feasibility and effectiveness of FBG sensors and OFDR-based DFOS in detecting impact load and corrosion, enabling real-time monitoring of their interaction. The measured Bragg wavelength change curves provided insights into the accelerated effect of impact load on corrosion, which was also observed in the corrosion distribution monitored by DFOS. This study revealed the correlation between the impact effect on corrosion and the performance of the coating. Specimens with more severe coating damage exhibited a more pronounced promotion of corrosion growth.

- The developed FBG-based generalized model was utilized to estimate the pit depth, which was validated against the scanned depth of pits. The results revealed a rapid development of pit depth during the initial stage of corrosion. For instance, specimen C&I3 exhibited a pit depth of 546 μm after approximately 450 hours of corrosion, gradually increasing to 599 μm by the end of the test. This behavior aligns with the typical pit depth development mechanism, characterized by a kinetic phase with a high corrosion rate followed by a concentration-controlled phase with slower growth. Furthermore, the impact load was found to significantly amplify the pit depth of the specimens, as indicated by the pit depth magnification index η_d, which exceeded 2 for all specimens and reached a maximum of 4.35. The trend of η_d stabilized after the rapid increase induced by the first two cycles of impact loading.

- The mass loss and average corrosion rate were estimated based on the measured Bragg wavelength change. The specimens subject to combined impact load-corrosion exhibited a greater mass loss compared to those subject to the individual corrosion test, indicating an intensified influence of the impact load on corrosion. Among them, specimens C&I1 and C1 showed the smallest difference in mass loss, with a value of 1.41g. This can be attributed to the relatively lower severity of coating damage caused by the impact load than the other specimens. In addition, the impact loading significantly exaggerated the average corrosion rate of the specimens, particularly in the early stage of corrosion. Specimens C&I3 and C3 showed the largest difference, with a value of 96 μm/year. Furthermore, according to the NACE specification, the average corrosion rate of specimens C&I2 and C&I3 was greater than 127 μm/year, indicating a moderate corrosion severity.
- The impact response of the specimens showed a distinct three-phase Bragg waveform. It was observed that during the stable stage, the impact response became increasingly prominent with the intensification of corrosion, particularly in the initial stage of impact loading. For example, specimen C&I2-2 displayed a Bragg wavelength increase of 196.55pm after the 2nd impact, which further rose to 273.83pm after the 6th impact. Besides, higher impact heights also resulted in more noticeable changes in Bragg wavelength. Similarly, the residual Bragg wavelength after impact unloading, influenced by different impact numbers and heights, followed the same pattern as the Bragg wavelength changes during the stable stage. This indicates that greater impact numbers and higher impact heights had a more pronounced effect on accelerated corrosion.
- The acceleration resulting from the impact load decreased as corrosion advanced, indicating a reduction in specimen stiffness and a diminished ability to withstand the impact load. This can be attributed to the corrosion-induced reduction in the cross-section of specimens. Additionally, higher impact heights were associated with a higher acceleration decay rate. On the other hand, as corrosion progressed, the impact energy dissipation index μ increased. It was observed that specimens with more severe corrosion exhibited higher energy dissipation. For instance, specimen C&I3, which experienced the most severe corrosion under the 50.0mm impact, displayed a maximum μ value of 93.62%.

2.11. Measurement of interactive bending, dent, notch, and corrosion

2.11.1. Overview

This section elaborates the research on the measurement of combined bending, dent, notch, and corrosion. Both discrete and distributed fiber optic sensors were utilized, and their results were compared. The combined use of the discrete and distributed fiber optic sensors represents the implementation of a distributed fiber optic sensor network, which integrates the capabilities of the discrete and distributed fiber optic sensors. Laboratory experiments were conducted using full-scale steel pipes, which were instrumented with FBG sensors, DFOS, and conventional sensors such as LVDT displacement sensors.

2.11.2. Materials and specimen preparation

Experimental testing was carried out to evaluate and differentiate the iterative effects of bending, dent, notch, and corrosion that occurred at the same position of each pipe specimen. The pipe specimen was made of carbon steel, which is commonly used for transmission natural gas and hydraulic fluid according to the standard ASTM A500 Grade B [74]. The outer diameter, wall thickness, and length of the pipe specimen were 114.3 mm (4.50 inch) and 6.02 mm (0.237 inch), 2,550 mm, respectively. The chemical composition and mechanical properties of the investigated pipe specimens is given in Table 2.11.1.

Table 2.11.1. Chemical composition and mechanical properties of investigated pipelines

Elements (wt. %)	C	Mn	P	S	Cu
	≤ 0.3	≤ 1.4	≤ 0.045	≤ 0.045	≥ 0.18
Mechanical properties	Elastic modulus E (GPa)	Yielding strength σ_{yd} (MPa)	Tensile strength σ_t (MPa)	Elongation (%)	σ_{yd}/σ_t
	≥ 30	≥ 290	≥ 400	≥ 23	≤ 0.9

Distributed fiber optic strain sensors were attached to the exterior surface of pipe specimens in a designed layout (yellow lines on the pipes). Before any installation of the optical fibers, the specimen was immersed in an acetic acid solution (concentration: 5%) to remove rust on the surfaces and then cleaned using alcohol wipes. Then, the optical fibers were attached to the specimens using tape at discrete spots following the designed layout which attempts to cover a large area of the specimens. The tape was used to hold the optical fiber in place during the installation process. Next, a fast-setting glue was used to attach the optical fibers to the specimens at discrete points between the tape spots. Once the glue was set, the tape was removed. The removal of tape must be careful to prevent damage to the optical fibers or the glue. Finally, a two-part epoxy was applied to the optical fiber for a strong attachment with reliable strain transfer between the test specimen and the optical fiber. Any epoxy that flowed away from the fiber optic cable was cleaned to avoid potential effect on pipe corrosion. In this study, the thickness of epoxy was about 250 µm (0.25 mm), which was around one tenth of the thickness of the specimens. The width of epoxy path was about 4-6 mm. The epoxy was cured in air at room temperature (22 ºC ± 2 ºC) and under normal humidity (50% ± 5%) for 24 hours. The installation of sensor for monitoring a continuous length of 1 m took less than 10 min by one person.

2.11.3. Experimental set-up

The specimens were loaded under four-point bending to generate dent deformation at the middle span using a universal load frame. The length between two loading points is 750 mm. The dent test was conducted under displacement control at a rate of 1 mm/min. The applied load was recorded by the load cell of the reaction frame, and an LVDTs were instrumented to record the support and mid-span deflections of pipe specimens. High resolution camera and depth camera are utilized to capture the deformation of pipelines. Eight fiber Brag grating (FBG) sensors were installed on Path-1 to Path-4 along the same direction to validate the strain distribution results obtained from the DFOS. Specifically, the optical fiber was passed through the dent region to measure the iterative effects of bending and dent. Optical fiber Path-1 to Path-3 were installed along the longitudinal direction of pipes, and Optical fiber Path-4 was installed along the helix loop, which is shown in Figure 2.11.1.

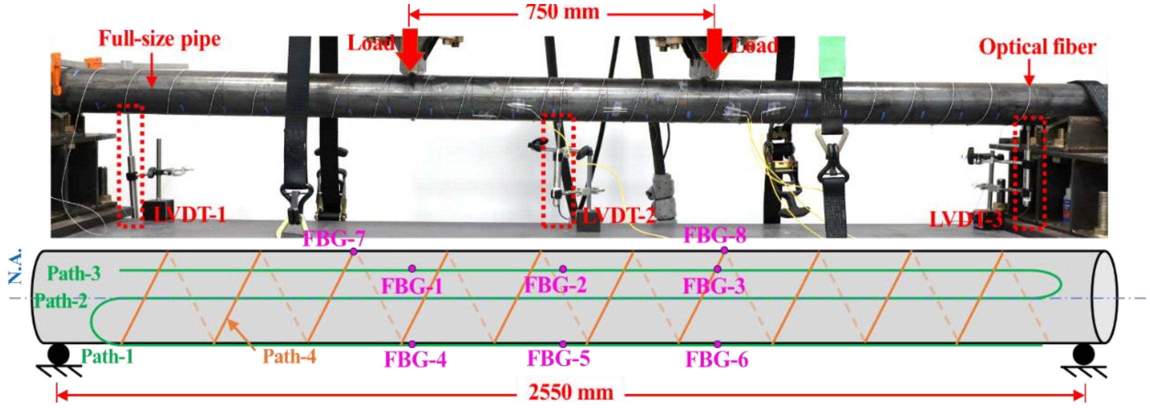

Figure 2.11.1. Specimen preparation, sensor instrumentation, and test setup for the bending-dent tests.

One end of optical fiber was connected to the data acquisition system for the DFOS, and the other end of the optical fiber was free. In this study, a data acquisition system (model: Luna ODiSi 6) was employed to perform OFDR measurements. The measurement accuracy specified by the manufacturer is ±5 με for strain and ±2.2 °C for temperature.

2.11.4. Results and discussions

2.11.4.1. Load-displacement curves and visual inspection

Figure 2.11.2 shows two representative load-displacement curves and a photo of a pipe specimen subject to four-point bending loads. The tests were conducted under displacement control with a constant displacement rate. Different pipe specimens showed similar curves which have two main stages: (1) Stage 1: elastic stage, where the load approximately linearly increases with the applied displacement. (2) Stage 2: plastic stage, where the load increases with the applied displacement with a decreasing slope. The loading tests were terminated after the slope was lower than 5% of the slope at the beginning of the tests. During the bending tests, obvious bending deformations of the pipe specimens were observed. After the pipe specimens were unloaded, dents were observed from the pipes at the spots where the specimens were in direct contact with the loading apparatus.

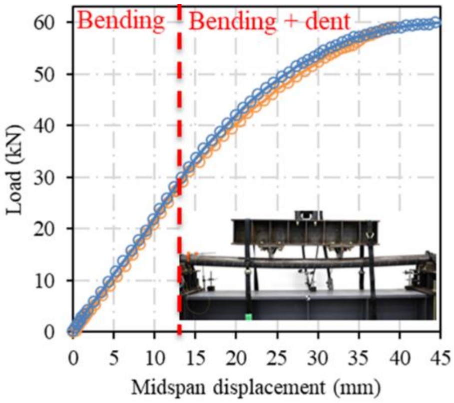

Figure 2.11.2. Load-displacement curves of specimens under four-point bending.

2.11.4.2. Strains

The strains measured from DFOS and FBG sensors were compared, as shown in Figure 2.11.3. FBG sensors FBG-1 to FBG-6 measured the strains along the longitudinal direction of the pipe following Path-1 to Path-3; and FBG sensors FBG-7 and FBG-8 measured the strains along the helix direction of the pipe following Path-4. Linear regression analysis was performed, and the coefficient of determination (R^2) was calculated. The results indicate a strong correlation between the results obtained from the DFOS and FBG sensors, overall.

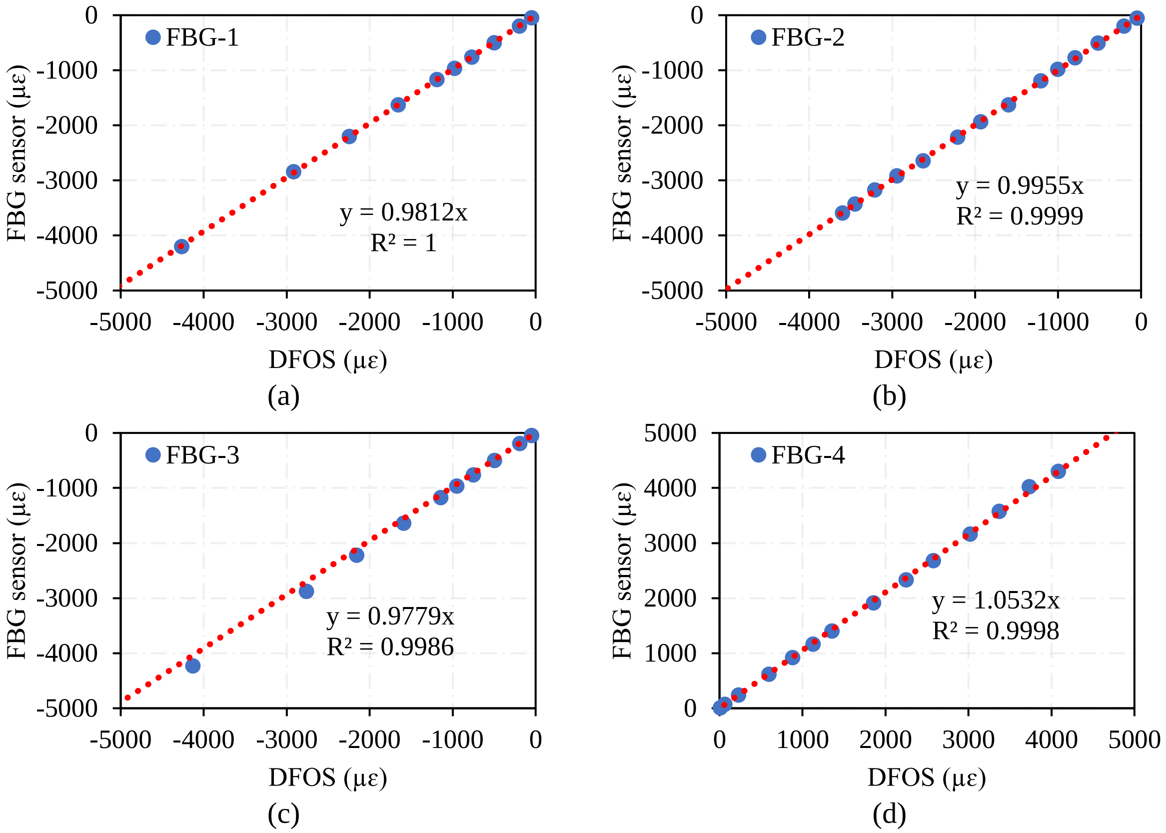

(a)

(b)

(c)

(d)

Figure 2.11.3. Comparison of the strains obtained using DFOS and the FBG sensors: (a) FBG-1; (b) FBG-2; (c) FBG-3; (d) FBG-4; (e) FBG-5; (f) FBG-6; (g) FBG-7; and (h) FBG-8.

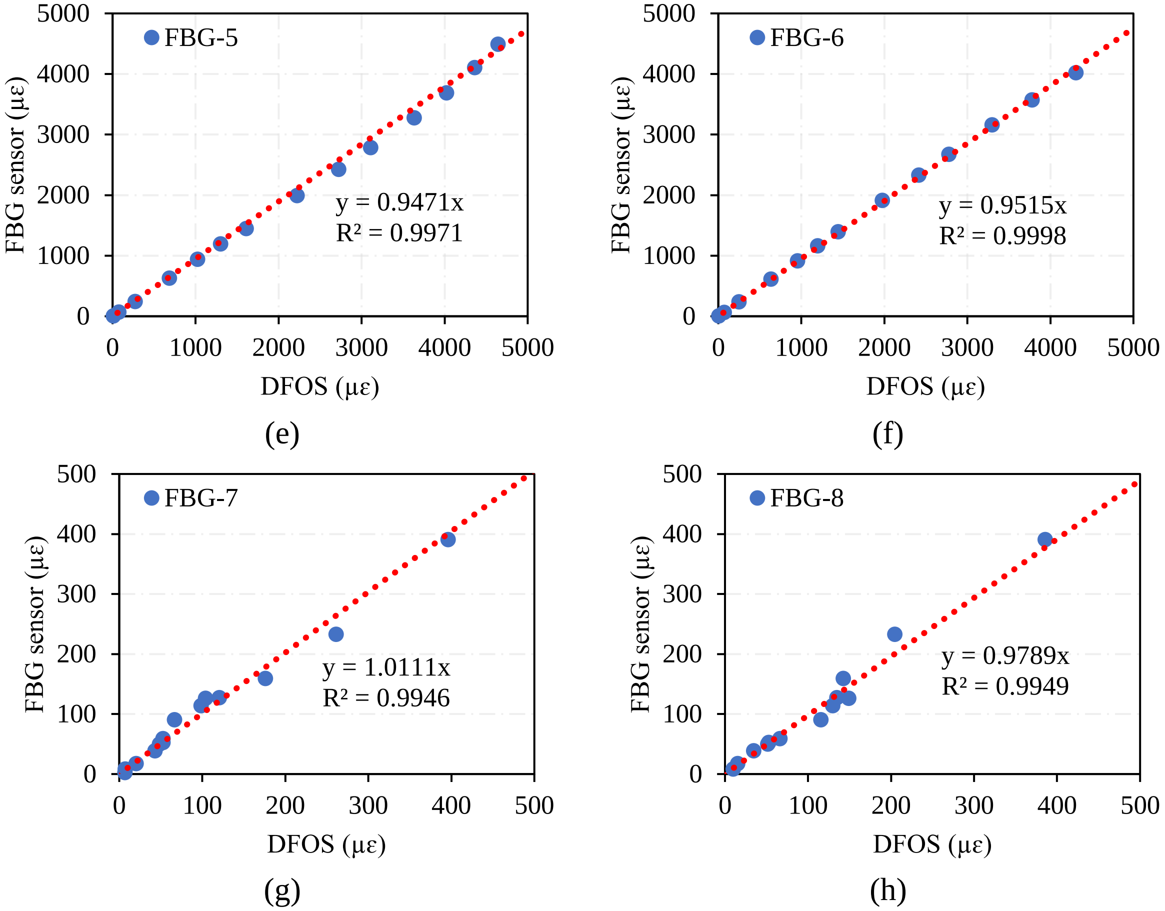

(e) (f)

(g) (h)

Figure 2.11.3. Comparison of the strains obtained using DFOS and the FBG sensors: (a) FBG-1; (b) FBG-2; (c) FBG-3; (d) FBG-4; (e) FBG-5; (f) FBG-6; (g) FBG-7; and (h) FBG-8.

2.11.4.3. Quantification of pipe deflection

The strain at each point of a pipe has longitudinal and circumferential components. Each of them includes bending and membrane strains. The membrane strain is constant in each cross section of the pipe, while the bending strain changes linearly regarding the neutral axis of the pipe under bending. When the pipe is only subject to the bending effect, the bending strain dominates, and the membrane strain can be neglected.

After dents were generated in the pipe, the direction of dent deformation was downward. The maximum bending strain occurred at the surface of the pipe. The governing equation describing the relationship between the dent deformation and bending strain is shown in Eq. (2.11.1):

$$\varepsilon_x^b = \left(R + \frac{t}{2}\right)\frac{\partial^2 w}{\partial x^2} \tag{2.11.1}$$

where ε_x^b is bending strain along the length (i.e., the longitudinal strain component) of the pipe; R is the mean radius of the pipe; t is the wall thickness of the pipe; w is the dent deformation along the vertical direction; and x is the coordinate along the length of the pipe.

If the strain profile along the pipe is known, then the dent deformation can be calculated Eq. (2.11.2), which is an integration of Eq. (2.11.1):

$$w(x) = \int_0^x \int_0^x \frac{2\varepsilon_x^b}{2R + t} dx\, dx + ax + b \tag{2.11.2}$$

where a and b are constants that can be determined by the boundary condition of the pipe.

According to the trapezoidal integration method, Eq. (2.11.2) is re-written as Eq. (2.11.3):

$$w_n = \frac{s_d}{4(R + \frac{t}{2})} \left[(2n - 3)\varepsilon_{x1}^b + \varepsilon_{xn}^b + 4 \sum_{i=2}^{n-1} (n - i)\, \varepsilon_{xi}^b \right] \tag{2.11.3}$$

where w_n is the dent deformation at the n-th point; and s_d is the distance between the measuring points of strains.

The bending deformation of the pipe specimen was reconstructed and compared with the data from the computer vision system and three LDVTs, as shown in Figure 2.11.4. The solid lines represent the shape of the deformed pipe obtained from the computer system method, the black dash lines represent shape of the deformed pipe derived from the strain distribution results, and the "*" markers represent the deflection of the pipe obtained from three LVDTs at different positions. The considered load increased from 0 to 60 kN.

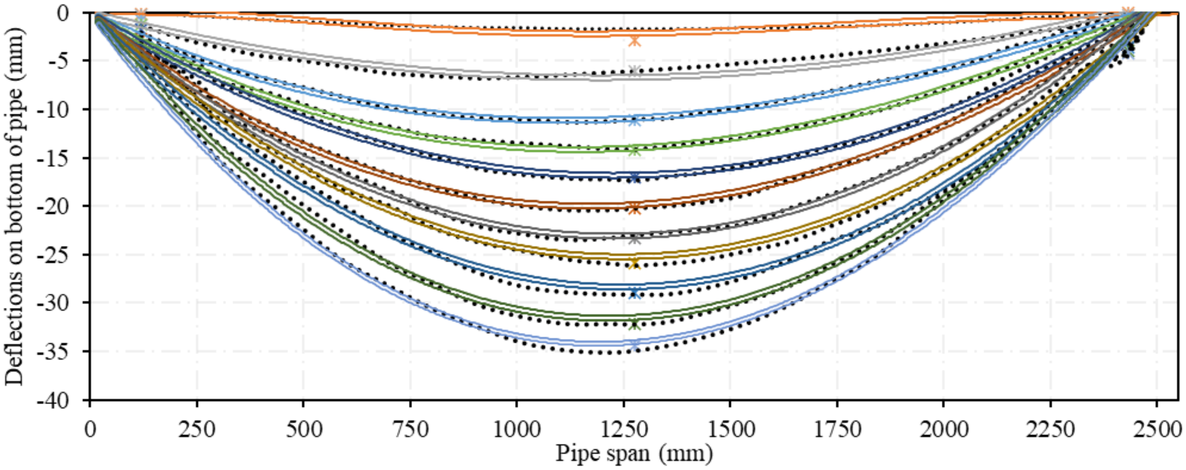

Figure 2.11.4. Deformation of the bottom of the pipe specimen obtained from shape reconstruction, LVDTs, and computer vision.

The deformed shapes obtained from the three methods agree well with each other, validating the pipeline deflection can be reconstructed by proposed method. The discrepancy among the deflections obtained from three methods was attributed to inherent inaccuracy of the sensors such as the DFOS, LVDTs, and high-resolution camara, data acquisition systems, and positions of the DFOS, as well as boundary conditions.

2.11.5. Corrosion-dent-crack interactive effect

2.11.5.1. Specimen preparation and experimental set-up

After dent was caused in steel pipes under bending loads, each pipe was cut into short segments, which are used to investigate the corrosion-dent-notch interactive effects. DFOS were attached to the exterior surfaces of the segments, as shown in Figure 2.11.5.

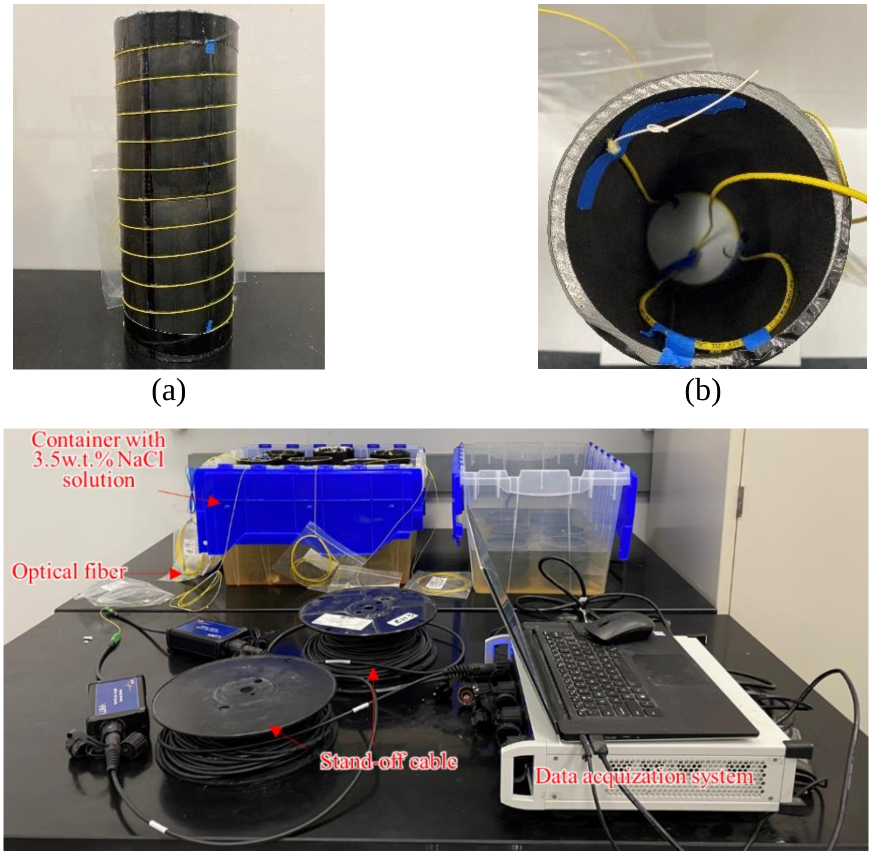

(a) (b)

(c)

Figure 2.11.5. Corrosion test of steel pipes experienced bending tests: (a) exterior surface of a pipe; (b) top view of a pipe instrumented with DFOS; and (c) corrosion test set-up.

The specimens were immersed in a sodium chloride solution (concentration: 3.5% by mass) in plastic containers for accelerated corrosion tests. The temperature was kept at room temperature (25 °C ± 2 °C). The fiber optic cable was connected to the DFOS system for data acquisition based on OFDR. Strain and temperature distributions along DFOS were measured. The measurement frequency was set at 2 Hz.

2.11.5.2. Investigated cases

Two representative pipe specimens, designated as C1 and C2, are listed in Table 2.11.2. Both of the two specimens had dent, and were subject to corrosion. Their main difference is that specimen C2 had a notch, which was manipulated to mimic the effect of a crack on the corrosion kinetics of the pipe. The dent depths of C1 and C2 were 11 mm and 10 mm, respectively.

Table 2.11.2. Investigated cases for combined corrosion, dent, and crack

Group	Cases	Sensor deployment pattern	Adjacent helix spacing (mm)	Dent depth (mm)
C1	Corrosion + Dent	Helix	25	11 mm
C2	Corrosion + Dent + Notch	Helix	25	10 mm

2.11.5.3. Results and discussions

The increase in pipe diameter caused by corrosion was monitored, as shown in Figure 2.11.6. The change of strain distributions was measured from DFOS at different immersion time (from 24 h to 549 h). The vertical axis represents the tensile strains induced by corrosion, and the horizontal axis represents the distance along the DFOS, with distance zero at the connector of the data acquisition system. In each figure, the length range of the DFOS is selected to show the strain distributions within the length of fiber optic cable wrapped on the pipes.

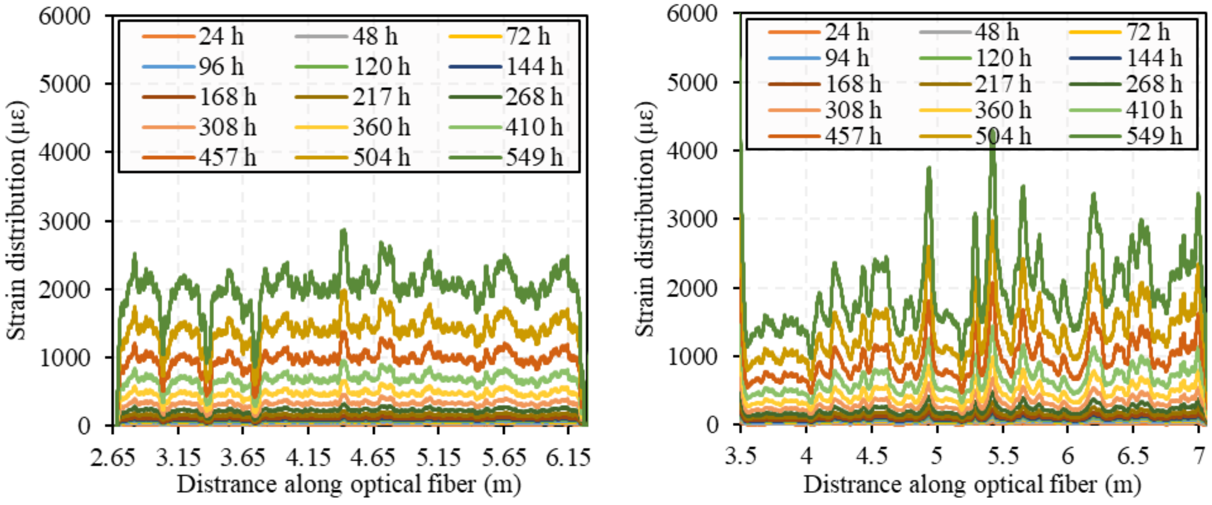

(a) (b)

Figure 2.11.6. Strain distributions measured from the DFOS along the pipes: (a) C1, and (b) C2.

The corrosion test results show that tensile strains were generated in the DFOS with the increase of corrosion of both specimens. The tensile strains can be attributed to the expansion of the radius of the pipes with the growth of rusts, as elaborated in references. Compared with the strain distributions obtained from previous research, the strain distributions measured from the pipes with dent show high spikes and deep valleys, which can be attributed to dent because dent caused residual strains in the steel pipes and modified the microstructures of the pipes. Compared with specimen C1, specimen C2 showed higher spikes, which can be attributed to the presence of the notch where corrosion was accelerated.

2.12. Investigations of different types of fiber optic cables and installation methods

2.12.1. Overview

This section elaborates the investigation into the measurement performance of different fiber optic cables, as shown in Figure 2.1.1, and three different fiber installation methods, as shown in

Figure 2.12.1. The three methods are designated as M1, M2, and M3. For the installation method M1, the fiber optic cable is continuously attached to the pipeline surface using adhesives (e.g., epoxy). For the installation method M2, the fiber optic cable is continuously attached to the surface of the pipeline using a metallic tape that covers the fiber optic cable for strain transfer and mechanical protection. For the installation method M3, the fiber optic cable is attached on the pipeline surface at discrete points with a certain spacing. The influences on different types of fiber optic cable and installation methods on strain measurements were compared.

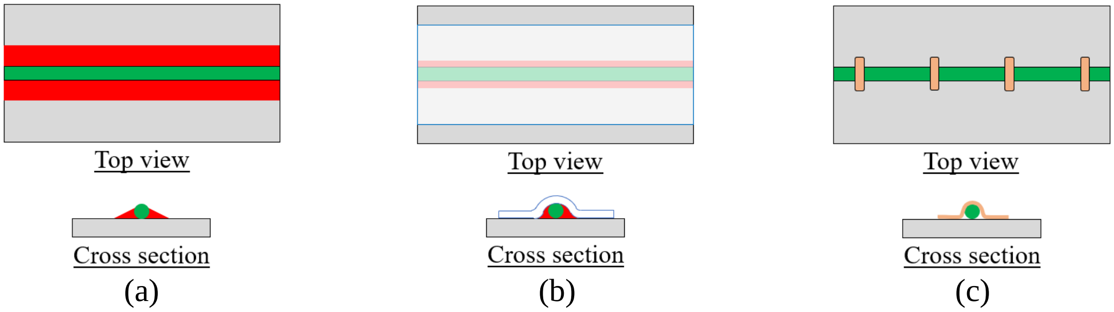

Figure 2.12.1. Schematic of three installation methods of distributed sensors: (a) M1, (b) M2, and (c) M3.

2.12.2. Experiments

The test setup and deployment of fiber optic cables in the pipe are shown in Figure 2.12.2. Pipe specimens were tested under four point bending. Strain distributions were measured from the fiber optic cables. The positions of fiber optic cables are shown in Figure 2.12.2(c).

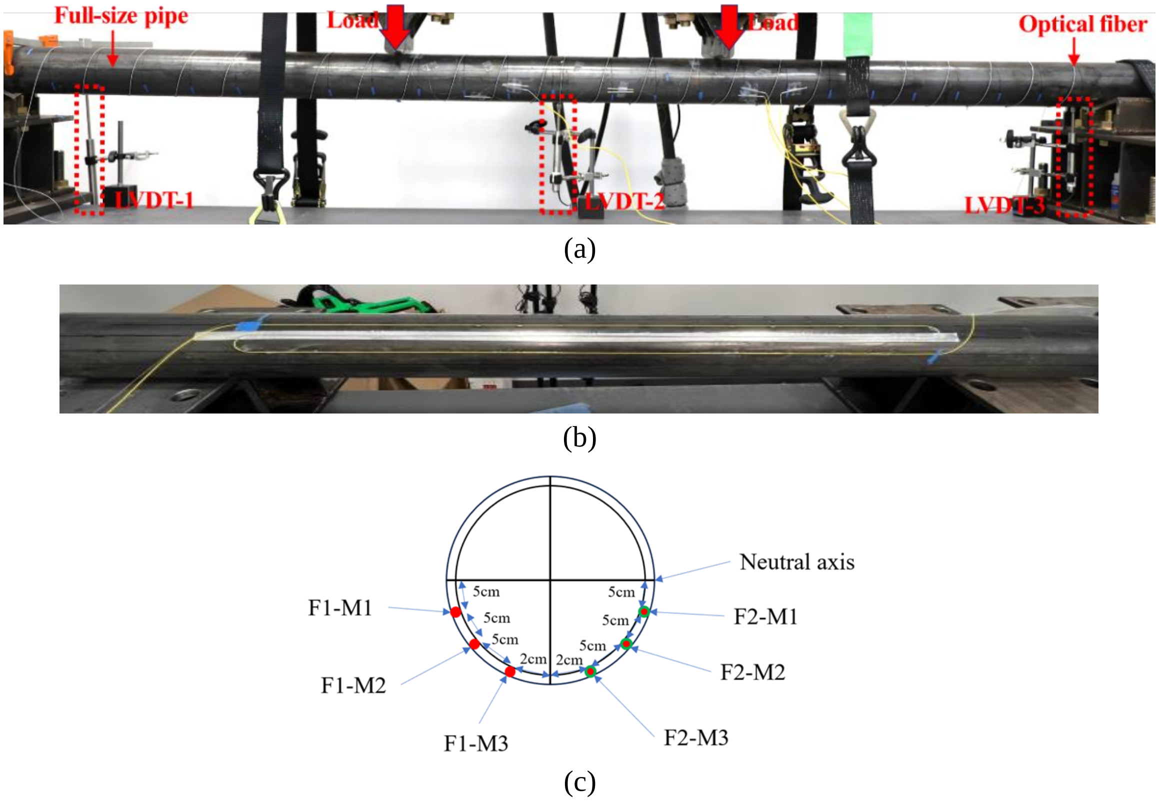

Figure 2.12.2. Test setup and sensor deployment: (a) setup, (b) sensor deployment, (c) cross section.

2.12.3. Experimental results and discussion

Representative results are plotted in Figure 2.12.3. F1-M1 represents the first type of fiber optic cable deployed using method M1. Very high frequency noises have been filtered out.

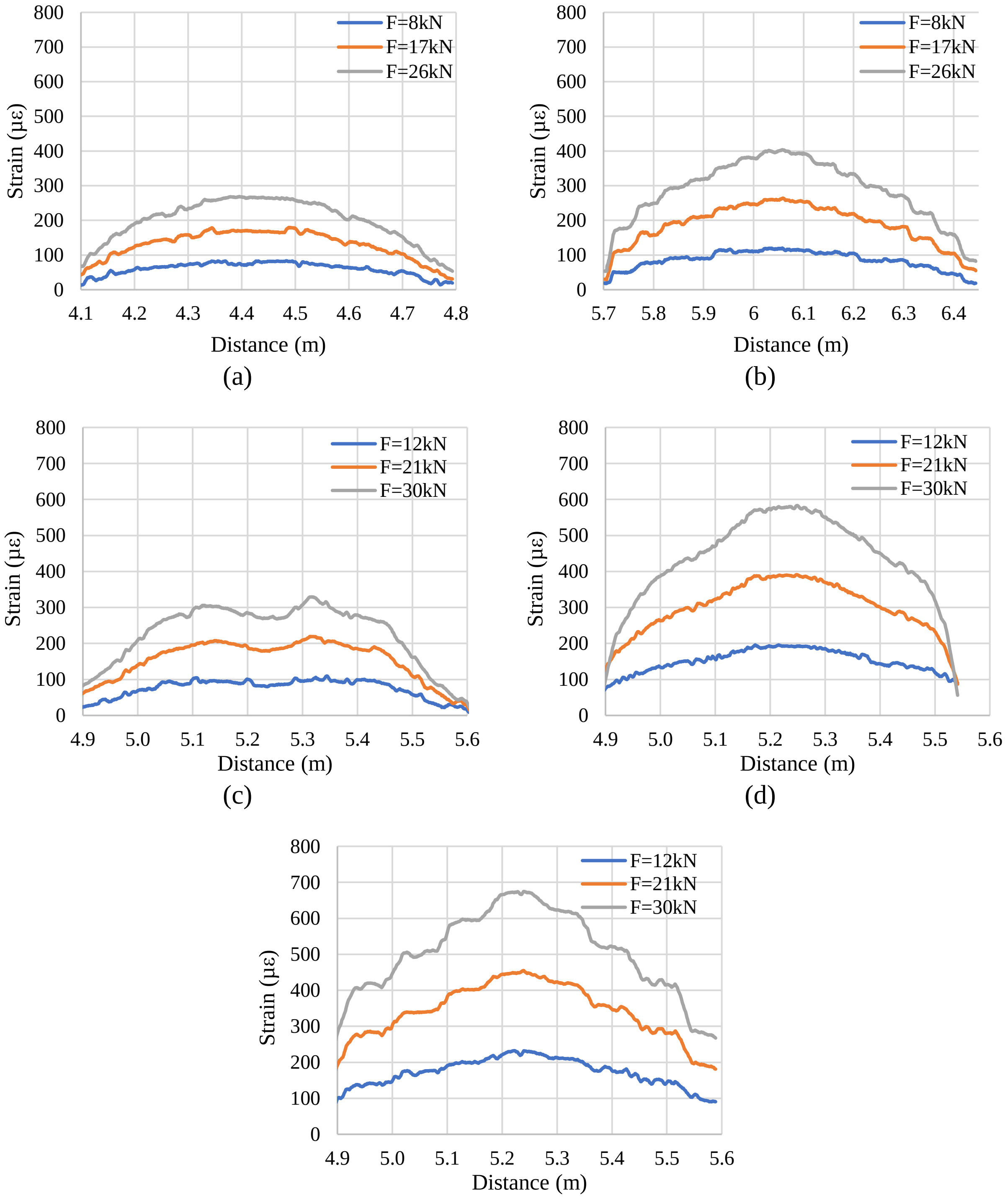

(a) (b) (c) (d) (e)

Figure 2.12.3. Representative measurement results of strain distributions: (a) F1-M1, (b) F1-M3, (c) F2-M1, (d) F2-M2, and (e) F2-M3.

More data have been measured from the different sensors during the experiments, and the other data are consistent with these representative data overall, so those data are not duplicated. All measurement results have been processed with temperature compensation, meaning that the effects of temperature change have been excluded, because the sensing methods developed in this research on various pipeline anomalies primarily focus on strain-based methods.

The results from F1-M1 and F2-M1 show typical strain distributions for four-point bending tests, as illustrated in Figure 2.12.4(a), when the strain transfer effect (see section 2.2) and the local dent effect (section 2.9) are considered. The absolute magnitudes of strains measured from F1-M1 and F2-M1 are not equal because of the different loads and the different positions in the pipe specimen. Although their distances away from the neutral axis are shown the same in Figure 2.12.1, there were errors in the experiments because the pipe specimen was not perfected placed without any rotation. Once the pipe was rotated, the distances of the sensors away from the neutral axis were changed. Besides, the pipe was slightly rotated during the loading tests due to the friction between the pipe and the test setup. Considering the above effects, it is believed that F1-M1 and F2-M1 provided consistent measurements, and the main differences are their strain transfer lengths due to different coating thicknesses which affect the strain transfer coefficients.

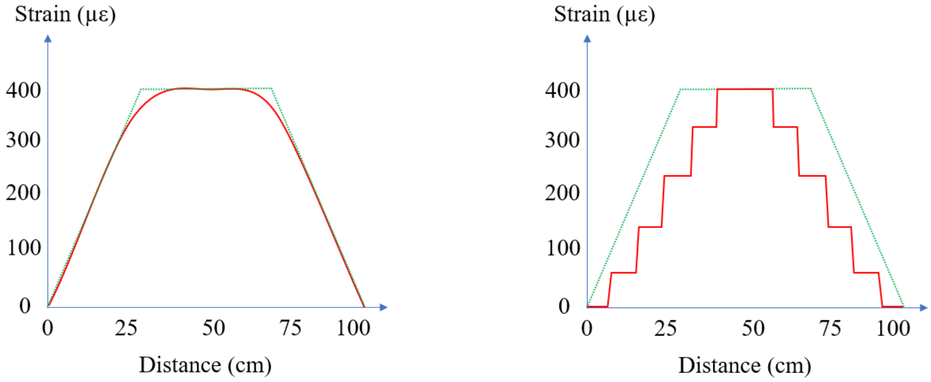

(a) (b)

Figure 2.12.4. Illustration of strain transfer behaviors: (a) continuous transfer, and (b) stepped transfer.

The results from F1-M3 and F2-M3 show typical stepped strain distributions, as illustrated in Figure 2.12.4(b). The step patterns are associated with the sensor deployment method. The strains between the adjacent attachment points are even because the sensor segment in between is free of external forces, and the strains are only transferred by the attachment points (i.e., epoxy). Therefore, a longer strain transfer length is demonstrated due to a lower strain transfer efficiency. Further in-depth research is needed to establish a holistic understanding of the strain transfer behavior of method M3.

The results from F2-M1 and F2-M2 show that the deployment method M2 also provides a continuous strain transfer behavior, which is similar to the strain transfer behavior of method M1. If the results measured from method M1 are used as the reference, then the results measured from method M2 show a longer strain transfer length, meaning that method M2 has a lower strain transfer efficiency. However, it should be careful to extend this conclusion for other types of tape because it is believed that the strain transfer efficiency is closely related to the material and the dimension (e.g., thickness) of the tape. Further in-depth research is needed to establish a holistic understanding of the strain transfer behavior of method M2.

2.12.4. Summary

The new findings from the above investigations can be summarized as follows:

(1) The proposed fiber optic cables can be utilized as distributed strain sensors for sensing nonuniform strain distributions in pipes. Different fiber optic cables have different strain transfer lengths due to the strain transfer efficiency. The strain transfer length can be estimated using the methods elaborated in section 2.2.

(2) The proposed sensor installation methods have different performance regarding the strain measurements. Attaching fiber optic cables to pipes using continuous adhesives such as epoxy (method M1) provides reliable strain measurements and efficient strain transfer; however, the installation method is time-consuming and labor-intensive, motivating the development of robots for enabling automatic sensor installation while maintaining consistent sensor installation quality. Attaching fiber optic cables to pipes using tapes (method M2) offers higher time efficiency; however, the strain transfer efficiency can be reduced, depending on the type of tape adopted. Attaching fiber optic cables to pipes using adhesives at discrete points (method M3) also achieves high time efficiency, but the strain transfer efficiency is reduced. Further in-depth research is needed to establish a holistic understanding of the strain transfer behavior of methods M2 and M3.

2.13. Detection of excavation near pipelines

2.13.1. Overview

This section elaborates the research on measurement of impact for excavation-related issues. The detection of impact is a challenging problem for underground pipelines which are unseen to excavation crews while the consequences of impacting pipelines during excavation can be serious. This project developed a strain-based method to detect impact effects using distributed fiber optic sensors based on the OFDR technique. Experiments of pipelines subjected to various boundary and loading conditions have been conducted, and signal analysis has been performed to develop and assess the performance of the method.

2.13.2. Experiments

The test setup of the pipe which was instrumented with distributed fiber optic sensors are shown in Figure 2.13.1. This test setup was adopted to simulate underground pipelines subjected to excavation-induced impact loads. Soil bags were placed on the top of the pipe specimen, which was also surrounded by soil, aiming to simulate the underground conditions of embedded pipes. Various types of fiber optic cables were installed on the external surface of the pipe specimen, including distributed strain sensors and distributed temperature sensors which were utilized for temperature compensation. Two hammers (steel and rubber) were used to apply the impact loads.

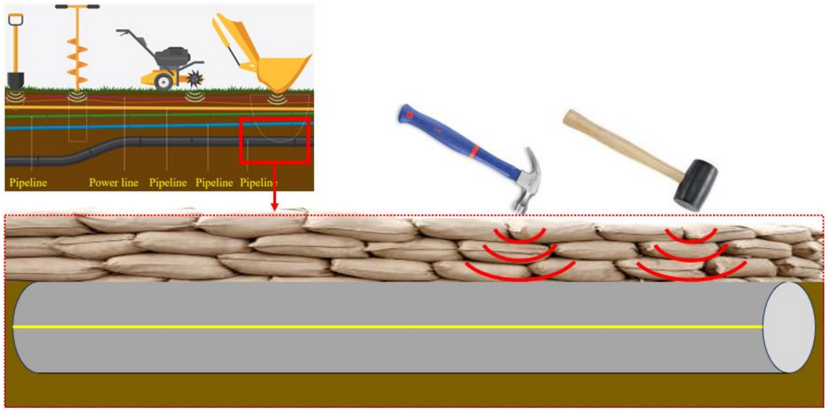

Figure 2.13.1. Illustration of the test setup for underground pipe subjected to excavation-induced impact.

Two types of pipe materials were investigated, which are steel and polyvinyl chloride (PVC), both being widely used in underground pipelines. The dimensions of the steel pipes are stated in section 2.11. The PVC pipe specimens measured 2 m in length and 102 mm in outer diameter, and the wall thickness was 5.8 mm.

2.13.3. Experimental results and discussion

Three experiments were conducted using different types of pipes to investigate the feasibility of detecting impacts applied to pipes. A set of representative results are shown in Figure 2.13.2. The data were measured from a distributed fiber optic sensor attached to the surface of a steel pipe, and the steel hammer was used to impact the pipe measuring 3 m in length.

The measurement results show that the distributed fiber optic sensor is sensitive to impacts applied to the pipe. When an impact was applied to the pipe, the energy density is largely reduced, as evidenced by the sparse sensing points. Such a response of the distributed fiber optic sensor can be attributed to the high-frequency vibration of the pipe after the impact was applied.

There was a short time period, which is a couple of milli seconds, when the energy density of the output signal was zero. Then, after a few milli seconds, the distributed fiber optic sensor repicked the signals, and the energy density returned to normal condition, the same as the signals before the impact was applied.

The above observations from the measurement results imply that it is possible to utilize the distributed fiber optic sensor to detect impact loads applied to pipelines. To further investigate the impact detection performance, the strain measurement data at two selected cross sections of the pipe specimen have been plotted in time domain, as shown in Figure 2.13.3. The measurement results from two different cross sections of the steel pipe specimen are displayed. These two sections include an impacted section (x = 2 m) and a section (x = 3 m) away from the impacted section of the pipe specimen.

These time domain strain measurement results also show that the strain response is zero at the impacted time instant, as marked by the red circles. Such a sensing response indicates that is possible to pinpoint the time instant when the impact load was applied to the pipe specimen.

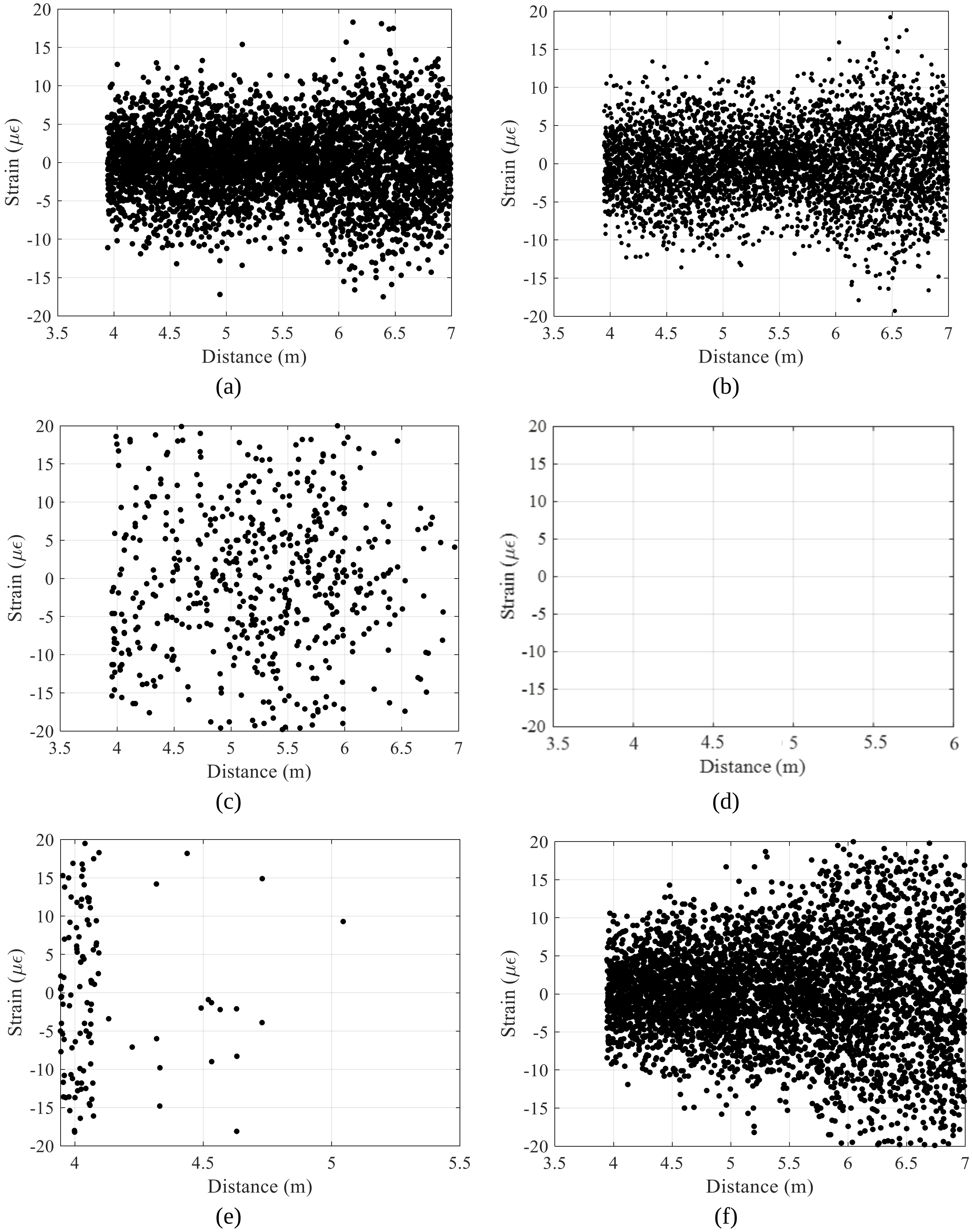

(a) (b)

(c) (d)

(e) (f)

Figure 2.13.2. Strain distribution along the pipe at different time instants: (a) at t=46.6 s, (b) t=47.0 s, (c) t=47.003 s, (d) t=47.004 s, (e) t=47.008 s, and (f) t=47.012 s.

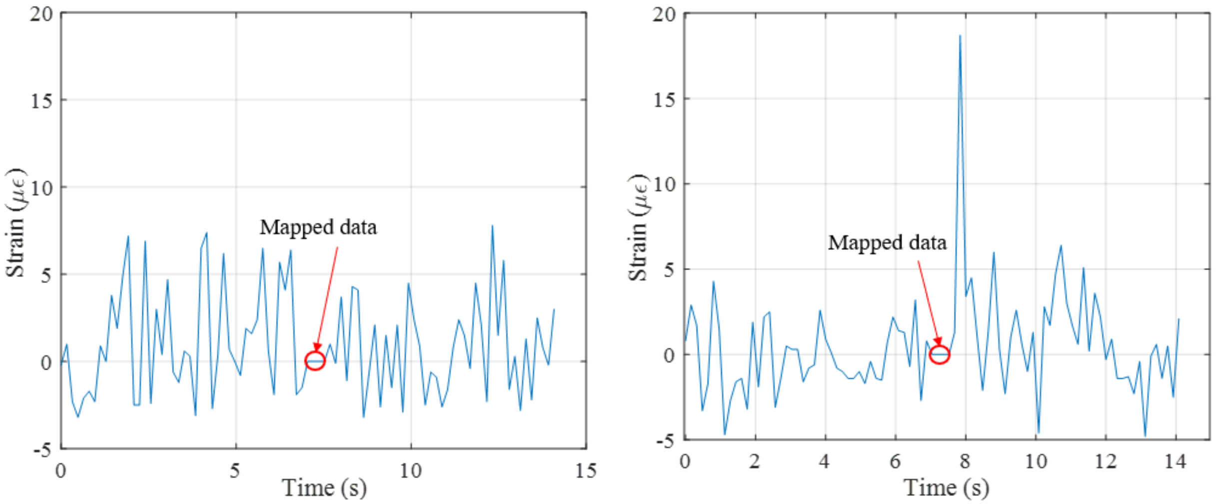

(a) (b)

Figure 2.13.3. Strain measurements at: (a) x = 2 m, and (b) x = 3m. The red circles mark the time when the impact was applied.

To achieve higher accuracy and robustness of determining the impact time instant, short time Fourier transform (STFT) has been used to conduct time-frequency analysis of the distributed sensor data, as shown in Figure 2.13.4. The time-frequency diagrams show the energy distribution as a function of frequency and time.

The procedure of performing STFT starts with dividing a long duration signal into numerous short duration segments of signals with equal time duration. Then, Fourier transform is performed for each short duration segment, generating the Fourier spectrum for each segment. Finally, the energy is plotted as a function of frequency and time, known as a spectrogram.

The time-frequency diagrams or spectrograms show that the energy distribution varies with time. In particular, at the time instant when impact loads are applied, the energy dropped to low value (-70 dB), which is consistent with the observations from Figure 2.13.3, therefore facilitating the determination of the impact time.

Another interesting observation from the time-frequency diagrams is that the time duration of the low energy band, or called the bandwidth of low energy, is associated with the distance away from the impacted cross section. In this experiment, the impacted section was at x = 2 m. The bandwidth if the widest at the impacted section, and the bandwidth showed a decreasing trend as the distance from the impacted section increased, as evidenced by Figures 2.13.4(a) to 2.13.4(c). Such observations make it possible to locate the impact loads. Consistent results have been obtained from other experimental cases, such as the tests of PVC pipes, different lengths of pipes, different types of hammer, different thicknesses of soil, and so on. The results are not duplicated in this section.

The limitation of this research is that the determination of the impact time and location relies on visual inspection of the sensing signals. When the pipeline is long, it will be impractical to use the proposed method. It is important to develop machine learning methods for automations.

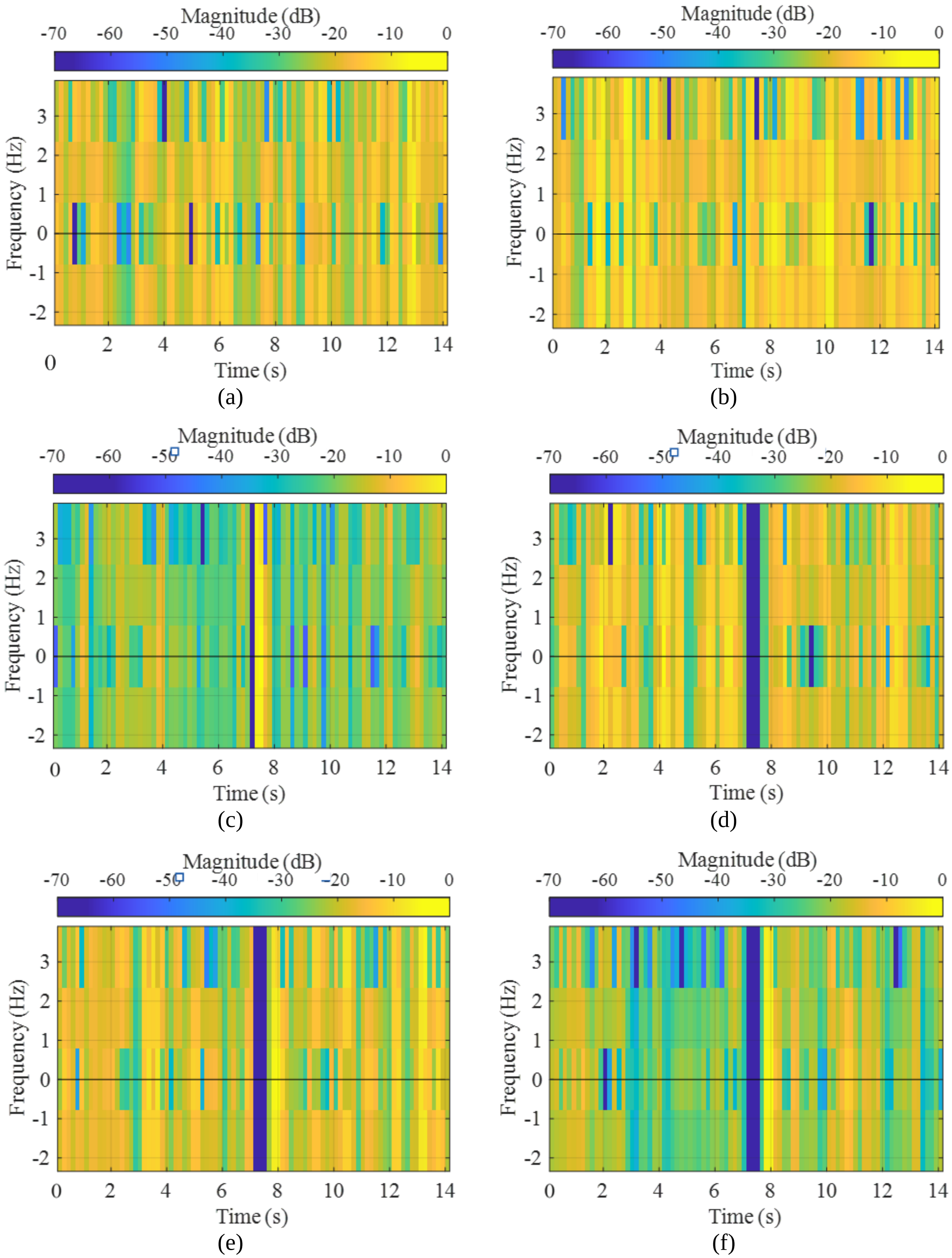

Figure 2.13.4. STFT of strain measurements versus time at different cross sections along the pipe specimen: (a) x = 0.5 m, (b) x = 1 m, (c) x = 1.5 m, (d) x = 2 m, (e) x = 2.5 m, and (f) x = 3 m.

2.13.4. Summary

The new findings from the above investigations can be summarized as follows:

(1) The proposed method is promising for detecting the time and location of impact loads applied to underground pipelines. The time-frequency diagrams created via STFT are useful for accurately determining the impact time and location based on visual inspection. The impact time can be determined by the time instant of the low energy band, and the bandwidth can be used to locate the impact event. This method can be applied to various types and dimensions of pipes subjected to different types of impact loads.

(2) It is promising to develop machine learning methods to automate the interpretation of distributed fiber optic sensor data for monitoring impact events for underground pipelines which have long lengths. Further research is necessary to develop machine learning methods for automating impact monitoring in the pipeline industry.

3. Conclusions

In this project, the university research team has developed and evaluated a distributed fiber optic sensor network for monitoring interactive anomalies of pipelines, aiming to improve the safety, facilitate pipeline management, reduce inspection and maintenance expenses, extend the service life of pipelines, and promote transport efficiency of pipelines by minimizing downtime. The distributed fiber optic sensor network has been deployed on various sizes of pipelines and utilized to measure strain fields of pipelines, as well as cracks, corrosion, and impacts applied to pipelines. The performance of distributed fiber optic sensor networks has been evaluated through comprehensive laboratory experiments using pipes under various testing conditions. Specifically, the distributed fiber optic sensor network has achieved the following capabilities:

- Measurement of 3D arbitrary strain fields of pipelines. Detailed strain fields of pipelines can be provided by the distributed fiber optic sensor network in real time. The strain fields can be subsequently utilized to assess the mechanical condition of pipelines and guide the operation and maintenance of pipelines.
- Detection, localization, quantification, and visualization of cracks in pipelines. Detailed crack conditions of pipelines can be measured by the distributed fiber optic sensor network based on the measurement of strain distributions. A theoretical model of cracked pipelines has been developed and validated to support the measurements.
- Detection, localization, quantification, and visualization of buckling/dents in pipelines. Detailed global and local deformations of pipelines can be measured by the distributed fiber optic sensor network based on the measurement of strain distributions. A theoretical model of globally and locally deformed pipelines has been developed and validated to support the measurements.

- Detection, localization, quantification, visualization, and warning of pipeline corrosion. Detailed corrosion conditions of pipelines can be measured by the distributed fiber optic sensor network based on the measurement of strain distributions. A theoretical model of corroded pipelines has been developed and validated to support the measurements.
- Detection and discrimination of interactive anomalies of pipelines. The investigated cases of interactive anomalies included: (1) global and local deformations (bending and dents); (2) deformations and cracks; (3) deformations and corrosion; (4) deformations, impacts, and corrosion; and (5) deformations, cracks, and corrosion.
- Detection and monitoring of impacts applied to pipelines. The impacts can be applied by third-party excavation or digging, which can possibly cause severe damages to pipelines. The capability of detecting impacts applied to pipelines has the potential to determine the time and location of impacts. This information is important for pipeline operators to decide when to mitigate or repair the damaged pipes in order to improve the safety of pipelines.

Based on these capabilities, further investigations reveal that the different types of anomalies promote each other and accelerate the degradation of pipelines when the anomalies occur at the same positions of a pipeline. For example, the occurrence of dent promoted the corrosion of pipes at the dent spots because the dents caused residual stresses and modified the microstructures of pipe materials in a negative way. The promotional effects make interactive anomalies more dangerous than individual anomalies for pipeline safety. It is essential to monitor the initiation and development of interactive anomalies for pipelines.

The investigations on various types of fiber optic cables and their installation methods reveal that the types of fiber optic cables and their installation methods have significant effects on the measurement results and the sensing performance of distributed fiber optic sensors. It is important to select appropriate types of fiber optic cables and installation methods in specific applications. In general, it is recommended to use packaged fiber optic cables for practical applications since the packaging provides mechanical protection for the survival of fiber optic cables in construction.

When distributed fiber optic sensors are utilized for monitoring pipelines, the measurement performance such as the accuracy and spatial resolution is associated with numerous parameters such as the type of fiber optic cable, the sensor installation method, and the spatial resolution. These parameters should be carefully selected depending on the specific application.

When appropriate parameters are selected, the measurement accuracy of crack opening width can achieve the scale of 10-20 micrometers in the laboratory experiments. Distributed fiber optic sensors can detect and monitor the development of microcracks and major cracks. The opening widths of microcracks monitored can be as narrow as tens of micrometers. However, it must be noted that the performance of distributed fiber optic sensors in field applications can be different from the laboratory test results. Further evaluation in relevant environments is yet to be performed.

4. Future Work

The capabilities developed in this preliminary research have created new opportunities for advancing the monitoring and management of pipelines. The following work has been identified, aiming to further the research and development toward commercialization and field applications of the developed distributed fiber optic sensor network.

(1) Evaluation of the performance of the developed approaches for other types and sizes of pipes. In this research, some experimental tests were conducted using small pipes or other specimens such as bars and plates. It is important to test the sensor installation methods and the sensor data analysis methods in further experiments using large pipe specimens and in field testing.

(2) Development, evaluation, and implementation of machine learning methods for automatic interpretation of data provided by distributed fiber optic sensor network deployed on pipes subject to interactive anomalies. Preliminary research has been conducted and shown that it is promising and feasible to interpret the data measured by distributed fiber optic sensor networks with advanced machine learning methods. The preliminary research is briefly reported in this section.

(3) Development, evaluation, and implementation of methods for efficient installation of fiber optic cables on the surfaces of pipelines. Considering the long distance of pipelines, it is time-consuming to install fiber optic cables along pipelines in practice. It is important and urgent to develop effective and efficient methods for installing fiber optic cables. Robots are promising solutions for the installation of fiber optic cables as distributed sensors for pipeline applications.

(4) Development, evaluation, and implementation of an Internet of Things (IoT) platform for automatic generation and utilization of digital twins of smart pipelines instrumented with distributed fiber optic sensor networks for improved asset management. This research has shown that it is feasible to generate and update digital twins with the data measured by distributed fiber optic sensor networks, accompanied by the machine learning methods for automatic data interpretation. Further research is necessary to integrate the developed methods into cloud and mobile devices for remote access of digital twins and remove control of distributed fiber optic sensor networks and pipelines for safety and efficiency.

(5) Education and training of students and pipeline professionals for developing the next-generation workforce for the pipeline industry. It is important to develop courses and certificate programs to support the vision for smart pipelines.

4.1. Challenges and objectives of AI assisted data analysis and interpretation

The research in Section 2 demonstrates the superior capabilities of DFOS networks for real-time in-situ monitoring of pipelines. The various anomalies were detected, located, quantified, and visualized based on the measurements of strains from DFOS and the developed sensor data analysis methods. For example, spikes can be identified from the strain distributions in DFOS deployed on pipes with cracks, and the identified spikes can be utilized to locate and quantify cracks of pipes without having to precisely predict the positions of cracks in advance.

However, in real practice, it is challenging for human experts to analyze and interpret the measurements from long-haul DFOS deployed on pipelines because of the large amount of data and the complexity of data analysis. While it is feasible for engineers to manually perform data processing, analysis, and interpretation for laboratory experiments with a short sensor length and limited number of cracks, manual operation is time-consuming in real applications. In addition to the low efficiency, the reliability of data analysis and data interpretation is also limited by the existence of human errors. It is challenging for engineers to identify, locate, and quantify the severity of various anomalies in host structures and monitor the development in real time. It is essential to automate the data analysis and interpretation to promote the application of DFOS for real-time monitoring of large structures.

Recently, with the advancement in data science, machine learning has shown great promise in facilitating data analysis and interpretation. However, to date, there are limited studies on the analysis of DFOS data. Karypidis et al. [75] proposed an autoencoder to help judge whether a concrete beam was damaged or not. The autoencoder was not used to assess the damage type and damage locations. Song et al. [76] proposed a convolutional neural network model to detect the presence of cracks based on strain distributions measured from DFOS measuring 50 m in length. Two spatial resolutions, which are 100 mm and 200 mm, were investigated. Cracks were located using windows with a fixed width which was determined through a trial-and-error process. Dai et al. [77] proposed a support vector machine to identify the extension of a crack in a steel frame based on the strain time history diagrams from a finite element model.

Previous research showed that it is promising to develop machine learning approaches to automatically interpret sensor data. To advance the capabilities toward engineering applications, further research is necessary to address various challenges:

- First, the existing research on using machine learning approaches to interpret DFOS data employed supervised learning methods that require manually labelling a large amount of sensor data.
- Second, the existing research focused on strain distributions measured at relatively coarse spatial resolutions.
- Third, it is still unknown whether the machine learning approaches are robust to different types of fiber optic cables with various protective packages.

Under such circumstances, this research project developed supervised and unsupervised machine learning approaches to automatically interpret DFOS data at different spatial resolutions to identify, locate, quantify, and visualize cracks, aiming to eliminate human interventions and human errors, enable real-time monitoring and interpretation of cracks, and maximize efficiency.

This research has three primary novelties:

(1) A framework is presented to integrate the capabilities of the machine learning approaches to automatically identify, locate, and quantify cracks from the strain distributions measured from DFOS.

(2) Both unsupervised and supervised machine learning approaches are developed to minimize human interventions in the inference of DFOS data for crack monitoring. A trend analysis method is developed to detect and locate cracks. Mathematical features are proposed to represent the DFOS data. The robustness of the proposed approaches to the spatial resolution and the sensor package is evaluated.

(3) A 3D building information modeling (BIM) approach is developed based on the ability to intelligently interpret sensor data to visualize cracks. The BIM serves as a live digital twin of the monitored structure. The model is updated in real time by using the DFOS measurements interpreted by the machine learning approaches.

4.2. Strain distribution-based method

4.2.1 Overview

The main components of the framework for the automatic interpretation of cracks are shown in Figure 4.2.1. There are five components:

(1) Data collection. Strain distributions are measured from DFOS.

(2) Crack identification. Both unsupervised and supervised machine learning approaches are developed to identify cracks from the measured strain distributions.

(3) Crack localization. An algorithm is developed to locate cracks from the strain distributions measured from DFOS.

(4) Crack quantification. An algorithm is developed to quantify the crack width based on the DFOS data.

(5) Crack visualization. A crack visualization approach based on BIM is developed to visualize the initiation and the evolution of cracks in the monitored structure.

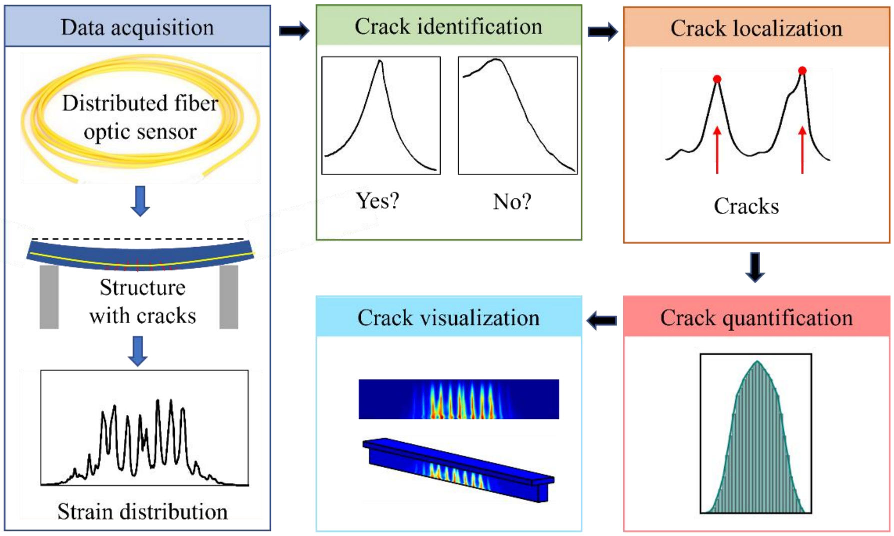

Figure 4.2.1. Proposed framework of automatic interpretation of cracks from DFOS measurements.

4.2.2 Crack identification

4.2.2.1 Collection of strain distribution

A spool of single-mode optical fiber (Corning® SMF-28e+® fiber) adopted in this research [78], as shown in Figure 4.2.2(a). The optical fiber consisted of a fused silica fiber core, a fused silica fiber cladding, and protective coatings made using multiple layers of polymer. The optical fiber served as a DFOS, which provides continuous measurement of temperature and strain along its entire length, and the transmission line. This study adopted a commercial sensing system (Luna ODiSi 6200 [79]) to perform measurements based on the OFDR [80]. The spatial resolution, measurement distance, sampling frequency, and measurement accuracy were 0.65 mm, 100 m, 1 Hz, and ±5 με, respectively.

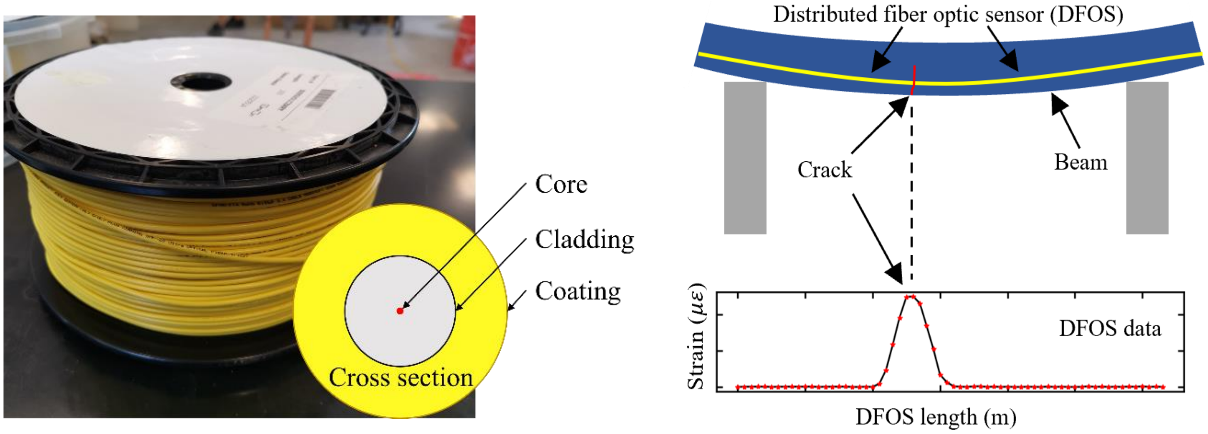

(a) (b)

Figure 4.2.2. Distributed fiber optic sensors: (a) the structure of the fiber; and (b) crack measurement.

The identification of cracks from a simple beam instrumented with a DFOS is shown in Figure 4.2.2(b). As a crack is generated, the DFOS passing the crack is stretched to a high strain level. The DFOS is not ruptured due to the protective coatings through the strain transfer effect, which causes a transfer length less than 100 mm at each side of the crack for the adopted optical fiber. The peak in the strain curve indicates the position of the crack in the beam.

4.2.2.2 Feature extraction

Both cracks and other factors such as strain gradients and noises are able to cause peaks in the measured strain distributions, as depicted in Figure 4.2.3. This represents a technical challenge in automatic interpretation of sensor data.

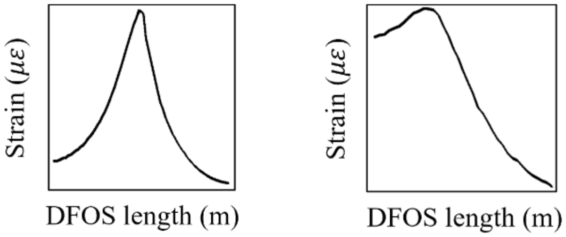

(a) (b)

Figure 4.2.3. Two representative segments of strain distributions: (a) a crack; and (b) not a crack.

This study proposes to use 20 mathematical statistical features of the strain distribution to represent cracks, as listed in Table 4.2.1. The results of the mathematic statistical features form a dataset denoted as D_{calc}. Some mathematical statistical features are illustrated in Figure 4.2.4.

Table 4.2.1. Extracted mathematical statistical features from the segments of strain distributions

Order	Symbol	Description
1	F1	The maximum strain (**Figure 4.2.4(a)**)
2	F2	The standard deviation
3	F3	The first quartile (**Figure 4.2.4(a)**)
4	F4	The third quartile (**Figure 4.2.4(a)**)
5	F5	The strain at the beginning (**Figure 4.2.4(a)**)
6	F6	The strain at the end (**Figure 4.2.4(a)**)
7	F7	The relative position of the maximum strain (**Figure 4.2.4(a)**)
8	F8	The slope before the maximum strain (**Figure 4.2.4(a)**)
9	F9	The slope after the maximum strain (**Figure 4.2.4(a)**)
10	F10	The difference between the maximum and the minimum strains (**Figure 4.2.4(a)**)
11	F11	The difference between the cumulative relative strains before and after the maximum strain (**Figure 4.2.4(a)**)
12	F12	The difference between the strains at the beginning and end (**Figure 4.2.4(a)**)
13	F13	The difference between the real distribution and the fitted normal distribution (**Figure 4.2.4(c)**)
14	F14	The number of peaks, obtained by SciPy signal library
15	F15	The direction of the strain distribution, calculated by Eq. (4.2.1)
16	F16	The tail of the strain distribution, calculated by Eq. (4.2.2)
17	F17	The sum (**Figure 4.2.4(b)**)
18	F18	The test result of the null hypothesis
19	F19	The p-value of the Shapiro-Wilk normality test
20	F20	The full width at half maximum (**Figure 4.2.4(a)**)

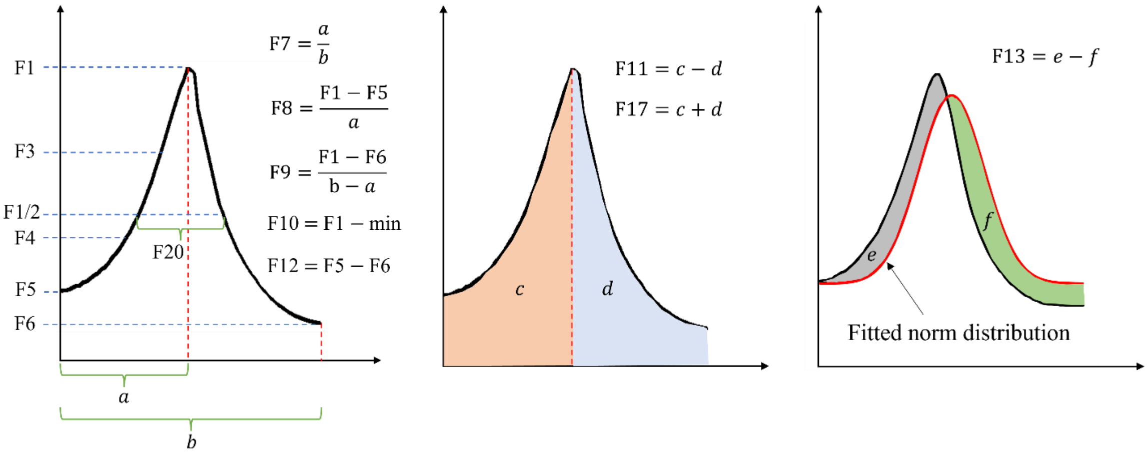

(a) (b) (c)

Figure 4.2.4. Mathematical statistical features: (a) F1, F3, F4, F5, F6, F7, F8, F9, F10, and F12; (b) F11 and F17; and (c) F13.

The direction or orientation of strain distribution (i.e., feature F15) is assessed by the Fisher-Pearson coefficient of skewness, which is a metric evaluating the symmetry of data [81]:

$$direction = \frac{\frac{1}{L}\sum_{j=1}^{L}\left(x_j - \bar{x}\right)^3}{\sqrt{\left[\frac{1}{L}\sum_{j=1}^{L}\left(x_j - \bar{x}\right)^2\right]^3}} \tag{4.2.1}$$

where L is the numbers of the strain values in the segment, x_j is the j-th strain, and $\bar{x}$ is the average strain of the segment of strain distribution.

The tail of each segment of strain distribution (i.e., the feature F16) is assessed by kurtosis, which is a smoothness metric. The tail of each segment of strain distribution is calculated as [81]:

$$tail = \frac{1}{L}\sum_{j=1}^{L}\left(\frac{x_j - \bar{x}}{\sigma}\right)^4 \tag{4.2.2}$$

where σ is the standard deviation of the segment of strain distribution.

The test result of the null hypothesis (i.e., the feature F18) and the p-value (i.e., the feature F19) are calculated from the Shapiro-Wilk hypothesis test, which examines whether a set of data follow a normal distribution. The similarity between each segment of strain distribution and random variables sampled from the standard normal distribution is calculated [82]. The values of the test result of the null hypothesis and the p-value range between 0 and 1, and number 1 means that the segment of strain distribution follows a normal distribution.

4.2.2.3 Unsupervised learning methods

The architecture of the unsupervised learning model is shown in Figure 4.2.5. The model has an autoencoder representation learning module and a clustering learning module. The input data are the features extracted from strain distributions. The autoencoder representation learning module includes an encoder and a decoder, as shown in Eq. (4.2.3) and Eq. (4.2.4). The autoencoder reconstructs the input data and compares the difference between the input data and the hidden representation of the input data in an unsupervised way, as shown in Eq. (4.2.5) [83].

$$\boldsymbol{h} = f(W_h\boldsymbol{x} + b_h) \tag{4.2.3}$$

$$\boldsymbol{z} = f(W_z\boldsymbol{h} + b_z) \tag{4.2.4}$$

$$\boldsymbol{e} = \|\boldsymbol{h} - \boldsymbol{x}\| \tag{4.2.5}$$

where f is the nonlinear transformation function; b and W are the bias and weight of the neural network, respectively; $\boldsymbol{x}$ is the input vector; $\boldsymbol{h}$ is the hidden representation of the input vector; $\|\cdot\|$ denotes the Euclidean distance between two vectors; and $\boldsymbol{e}$ is the reconstruction error, which is the difference between the reconstructed vector $\boldsymbol{z}$ and the original input vector $\boldsymbol{x}$.

The structure of the autoencoder is shown in Table 4.2.2. The encoder and the decoder consist of four fully-connected (FC) layers [84], respectively. Activation functions are used after the FC layers, including the hyperbolic tangent (Tanh) function [85] and the sigmoid function [86]:

$$tanh(x_a) = \frac{e^{x_a} - e^{-x_a}}{e^{x_a} + e^{-x_a}} \tag{4.2.6}$$

$$sigmoid(x_a) = \frac{1}{1 + e^{-x_a}} \tag{4.2.7}$$

where x_a is an input value. The output dimension of the hidden layer is three, meaning all the DFOS data are compressed into a 3D space with low errors.

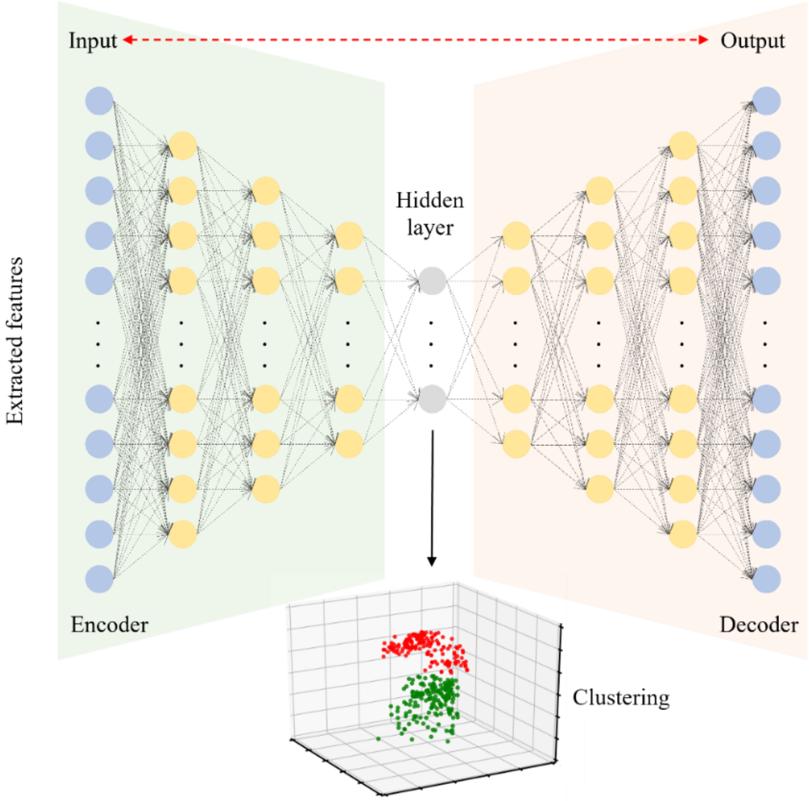

Figure 4.2.5. Architecture of the proposed autoencoder-based unsupervised learning model.

Table 4.2.2. Structure of the autoencoder neural network

Layer	Component	Input size	Output size	Layer	Note
1	Encoder	(20, 1)	(16, 1)	FC + Tanh	
2		(16, 1)	(8, 1)	FC + Tanh	
3		(8, 1)	(5, 1)	FC + Tanh	
4		(5, 1)	(3, 1)	FC	Hidden layer
5	Decoder	(3, 1)	(5, 1)	FC + Tanh	
6		(5, 1)	(8, 1)	FC + Tanh	
7		(8, 1)	(16, 1)	FC + Tanh	
8		(16, 1)	(20, 1)	FC + sigmoid	

The clustering learning module was realized using the K-means clustering algorithm due to its simplicity and effectiveness [87]. The input of the K-means clustering algorithm was the output of the hidden layer in the autoencoder module. The K-means clustering algorithm categorized all the compressed DFOS data into two disjointed clusters. Because the DFOS data representing no cracks are typically irregular, the cluster represented no cracks when its test results of the null hypothesis and the p-value were close to 0. In this case, the other cluster indicated that the DFOS data represent cracks.

The unsupervised learning model was implemented in Python 3.7 using PyTorch [88]. The training epoch was set at 300; the batch size was set at 32; the learning rate was set at 0.0001; and the loss function was the mean squared error (MSE). The Adam algorithm was used for stochastic gradient descent. In addition to the autoencoder-based unsupervised learning method, three representative unsupervised learning algorithms, which are the K-means clustering [89], Birch [90], and Gaussian mixture [91], were compared with the autoencoder-based method.

4.2.2.4 Supervised learning methods

Eight supervised learning methods were investigated for crack identification, which are (1) the random forest [92], (2) the ridge classifier [93], (3) the linear support vector machine with a linear kernel (SVM-linear) [42], (4) the support vector machine with a radial basis function kernel (SVM-RBF) [94], (5) the decision tree [95], (6) the k-nearest neighbors [96], (7) the multi-layer perceptron [97], and (8) the extreme gradient boosting (XGBoost) algorithm [98]. Hyperparameter tuning was performed for each of the machine learning models.

4.2.3 Crack localization

The flowchart of the proposed crack localization approach is shown in Figure 4.2.6. When a DFOS passes through cracks, each crack is identified by a peak in the strain distribution. The strain distribution is split into segments along the length of the DFOS. Each segment was analyzed by the machine learning models to identify cracks. When a segment is judged as a crack signal, the position of the segment is registered as the position of the crack.

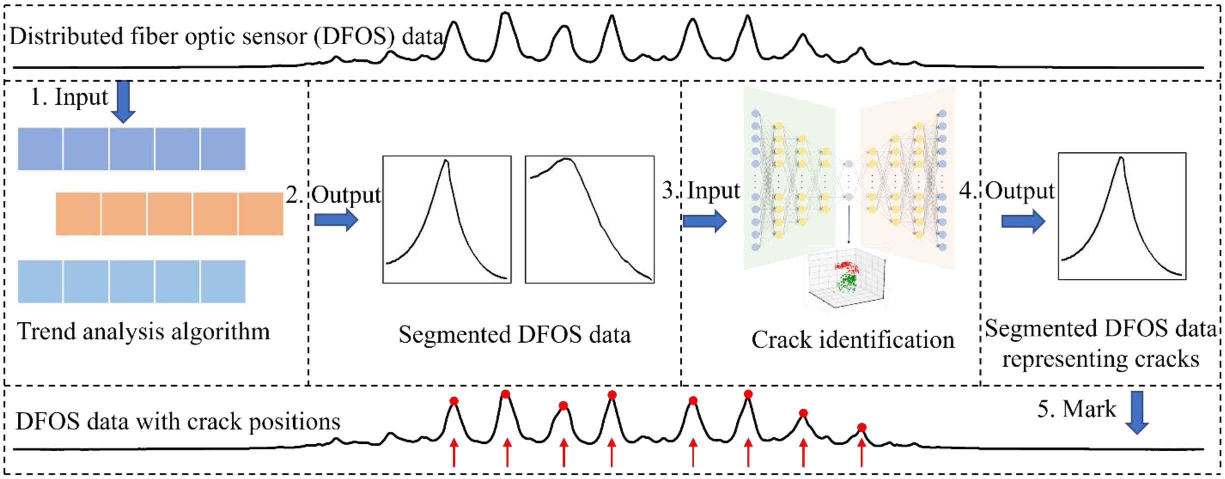

Figure 4.2.6. Flowchart of the crack localization approach proposed to analyze the strain distributions.

A trend analysis algorithm is presented to locate cracks, as shown in Figure 4.2.7. First, the strain distribution is stored in row A. Then, the data in row A is shifted to the left with one interval to form row B. Next, the difference between the data in row A and row B is calculated and stored in row C. The data in row C is input into the unit step function, as shown in Eq. (4.2.8) [99], to obtain row D. The data in row D is shifted to the right with one interval to form row E. Finally, an exclusive operation is performed for the data in row D and row E to obtain row F, where the position of number "1" indicates the position of the crack.

$$x_D = H(x_C) = \begin{cases} 1, & x_C > 0 \\ 0, & x_C \leq 0 \end{cases} \tag{4.2.8}$$

where x_C and x_D are the data in row C and row D, respectively; $H(\cdot)$ is the unit step function.

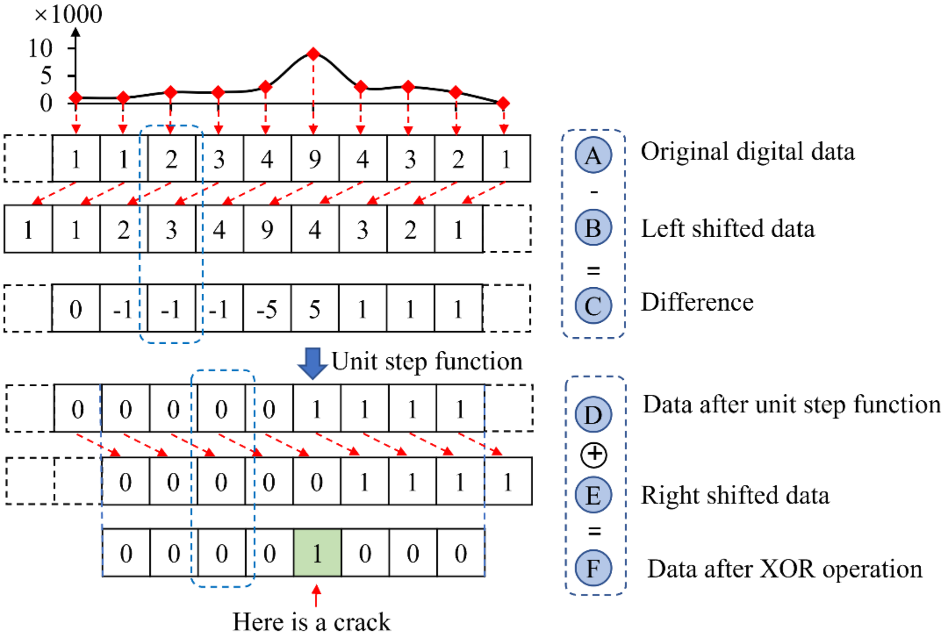

Figure 4.2.7. Main procedure of the localization algorithm. "XOR" represents exclusive operation.

4.2.4 Crack quantification

In recent research, the crack width was calculated using the strain distribution in the vicinity of the crack, as shown in Figure 4.2.8(a). The area of the strain distribution curve is the theoretical crack width. A method presented in section 2 for calculating the crack width using the strain distribution measured from DFOS is shown in Figure 4.2.8(b). The crack length can be determined by the positions of the intersection points of the cracks and DFOS, as shown in Figure 2.3.9. The intersection points can be connected to infer the crack length.

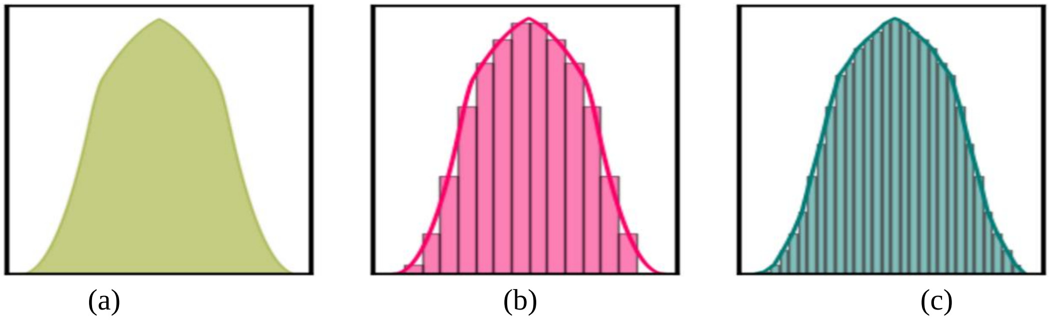

(a) (b) (c)

Figure 4.2.8. Determination of crack width using the measured strain distribution: (a) the theoretical method; (b) the method proposed in reference [11]; and (c) the method proposed in this study.

The strain distribution is represented by a series of columns. The width of each column is equal to the spatial resolution of the DFOS. The sum of the areas of the columns is used to obtain the crack width. To improve the accuracy of crack quantification, the column width is reduced using the nearest interpolation algorithm [100], as shown in Figure 4.2.8(c). The measured strain distribution was expanded five times. The sum of the areas of the columns in Figure 4.2.8(c) is closer to the shaded area in Figure 4.2.8(a) than the sum of the areas of the columns in Figure 4.2.8(b), meaning that the proposed method outperforms the previous method.

4.2.5 Crack visualization

This study proposes to develop a live 3D digital twin based on BIM and compare the 3D digital twin with a 2D contour of cracks. The live 3D digital twin is established in three steps: (1) The real-time information about cracks, such as the widths and positions of cracks, is stored in a cloud database (e.g., MongoDB 6.0). (2) A BIM model is constructed using a BIM program (e.g., Autodesk Revit). (3) The crack database and the BIM model are connected using linking tools (e.g., Revit DB link) to make the BIM model updatable by the crack database. When the information about cracks is updated by the measurements from DFOS, the BIM model is updated.

4.2.6 Performance metrics

The performance of crack identification is evaluated using accuracy, precision, recall, and F1-score [101]:

$$Precision = \frac{TP}{TP + FP} \tag{4.2.9}$$

$$Recall = \frac{TP}{TP + FN} \tag{4.2.10}$$

$$Accuracy = \frac{TP + TN}{TP + TN + FP + FN} \tag{4.2.11}$$

$$F1\ score = \frac{2 \times Precision \times Recall}{Precision + Recall} \tag{4.2.12}$$

where *TP*, *FP*, *FN*, and *TN* are the number of successfully detected cracks; *FP* is the number of wrongly detected cracks; *FN* is the number of missed cracks; and *TN* is the number of successfully detected non-cracks, respectively.

The performance of the crack localization method is assessed in terms of the localization error, which is the difference between the location determined by the proposed method and the manually marked location regarding the distance.

The performance of the crack quantification method is evaluated using the coefficient of determination (R^2) [101]:

$$R^2 = 1 - \frac{\sum_{k=1}^{N}(w_k - \widehat{w_k})^2}{\sum_{k=1}^{N}(w_k - \bar{W})^2} \tag{4.2.13}$$

where *N* is the number of cracks; w_k and $\widehat{w_k}$ are the true crack width and estimated crack width of the *k*-th sample, respectively; and $\bar{W}$ is the average of all the true crack widths.

4.2.7. Experiments and collected dataset

4.2.7.1 Experiments

The experiments are introduced in section 2.2.3.6.3. The contents are not duplicated here.

4.2.7.2. Collection and evaluation of dataset

Two methods were used to generate a DFOS dataset. The first method was experiment, and a total of 64,450 data were collected. Each strain distribution was divided into 1,000 segments along the sensor length, including 445 segments for “crack” and 555 data segments for “no crack”. The simulated strain distributions included random Gaussian noises with a mean value of zero. The simulated strain distributions were added to the dataset. A total of 1,500 data segments were generated. The experimental and simulated data were pre-processed to extract 20 mathematic features. The total data number were 2,500 (Table 4.2.3), including 20% experimental data that were randomly selected as a test dataset and the remaining data were used as a training dataset.

Table 4.2.3. Statistics of the segments of strain distributions

	Crack	No crack	All
Experimental data	445	555	1,000
Simulation data	750	750	1,500
Experimental + Simulation data	1,195	1,305	2,500

The Pearson correlation coefficients for the 20 features in the calculated dataset D_{calc} is shown in Figure 4.2.9. Most of the Pearson correlation coefficients off the diagonal were less than 0.7. The maximum correlation coefficient off the diagonal was 0.77, indicating that multicollinearity did not occur, and the 20 features in the dataset were appropriate.

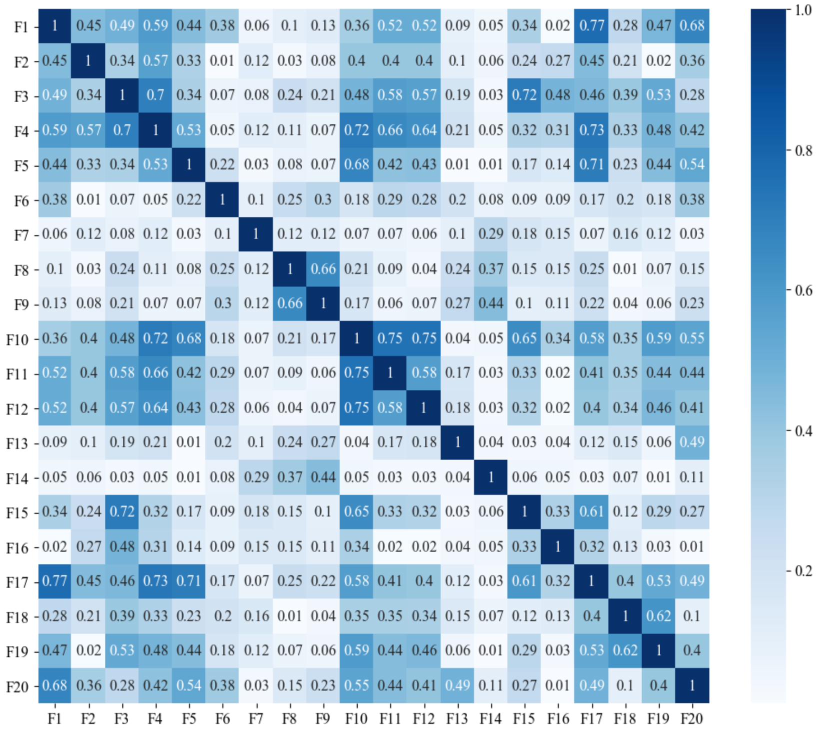

	F1	F2	F3	F4	F5	F6	F7	F8	F9	F10	F11	F12	F13	F14	F15	F16	F17	F18	F19	F20
F1	1	0.45	0.49	0.59	0.44	0.38	0.06	0.1	0.13	0.36	0.52	0.52	0.09	0.05	0.34	0.02	0.77	0.28	0.47	0.68
F2	0.45	1	0.34	0.57	0.33	0.01	0.12	0.03	0.08	0.4	0.4	0.4	0.1	0.06	0.24	0.27	0.45	0.21	0.02	0.36
F3	0.49	0.34	1	0.7	0.34	0.07	0.08	0.24	0.21	0.48	0.58	0.57	0.19	0.03	0.72	0.48	0.46	0.39	0.53	0.28
F4	0.59	0.57	0.7	1	0.53	0.05	0.12	0.11	0.07	0.72	0.66	0.64	0.21	0.05	0.32	0.31	0.73	0.33	0.48	0.42
F5	0.44	0.33	0.34	0.53	1	0.22	0.03	0.08	0.07	0.68	0.42	0.43	0.01	0.01	0.17	0.14	0.71	0.23	0.44	0.54
F6	0.38	0.01	0.07	0.05	0.22	1	0.1	0.25	0.3	0.18	0.29	0.28	0.2	0.08	0.09	0.09	0.17	0.2	0.18	0.38
F7	0.06	0.12	0.08	0.12	0.03	0.1	1	0.12	0.12	0.07	0.07	0.06	0.1	0.29	0.18	0.15	0.07	0.16	0.12	0.03
F8	0.1	0.03	0.24	0.11	0.08	0.25	0.12	1	0.66	0.21	0.09	0.04	0.24	0.37	0.15	0.15	0.25	0.01	0.07	0.15
F9	0.13	0.08	0.21	0.07	0.07	0.3	0.12	0.66	1	0.17	0.06	0.07	0.27	0.44	0.1	0.11	0.22	0.04	0.06	0.23
F10	0.36	0.4	0.48	0.72	0.68	0.18	0.07	0.21	0.17	1	0.75	0.75	0.04	0.05	0.65	0.34	0.58	0.35	0.59	0.55
F11	0.52	0.4	0.58	0.66	0.42	0.29	0.07	0.09	0.06	0.75	1	0.58	0.17	0.03	0.33	0.02	0.41	0.35	0.44	0.44
F12	0.52	0.4	0.57	0.64	0.43	0.28	0.06	0.04	0.07	0.75	0.58	1	0.18	0.03	0.32	0.02	0.4	0.34	0.46	0.41
F13	0.09	0.1	0.19	0.21	0.01	0.2	0.1	0.24	0.27	0.04	0.17	0.18	1	0.04	0.03	0.04	0.12	0.15	0.06	0.49
F14	0.05	0.06	0.03	0.05	0.01	0.08	0.29	0.37	0.44	0.05	0.03	0.03	0.04	1	0.06	0.05	0.03	0.07	0.01	0.11
F15	0.34	0.24	0.72	0.32	0.17	0.09	0.18	0.15	0.1	0.65	0.33	0.32	0.03	0.06	1	0.33	0.61	0.12	0.29	0.27
F16	0.02	0.27	0.48	0.31	0.14	0.09	0.15	0.15	0.11	0.34	0.02	0.02	0.04	0.05	0.33	1	0.32	0.13	0.03	0.01
F17	0.77	0.45	0.46	0.73	0.71	0.17	0.07	0.25	0.22	0.58	0.41	0.4	0.12	0.03	0.61	0.32	1	0.4	0.53	0.49
F18	0.28	0.21	0.39	0.33	0.23	0.2	0.16	0.01	0.04	0.35	0.35	0.34	0.15	0.07	0.12	0.13	0.4	1	0.62	0.1
F19	0.47	0.02	0.53	0.48	0.44	0.18	0.12	0.07	0.06	0.59	0.44	0.46	0.06	0.01	0.29	0.03	0.53	0.62	1	0.4
F20	0.68	0.36	0.28	0.42	0.54	0.38	0.03	0.15	0.23	0.55	0.44	0.41	0.49	0.11	0.27	0.01	0.49	0.1	0.4	1

Figure 4.2.9. Results of the correlation matrix of the mathematical features in the calculated dataset.

The 20 statistical results of the features in the calculated dataset D_{calc} are listed in Table 4.2.4. For each feature, the results include the range, average, skewness, and kurtosis. The skewness and kurtosis of a dataset are utilized to evaluate whether the dataset follows a normal distribution. The skewness ranged from -0.62 to 7.54, and the kurtosis ranged from -1.74 to 60.75. Most of the skewness and kurtosis were between -2 and 2, revealing that most of these features followed a normal distribution.

Table 4.2.4. Statistics of the variables in the calculated dataset

Variable	Unit	Range	Average	Skewness	Kurtosis
F1	$\mu\varepsilon$	400 to 18,593	5,693	0.90	-0.90
F2	$\mu\varepsilon$	0 to 5,702	2,980	-0.29	-1.68
F3	$\mu\varepsilon$	13 to 6,291	2,118	0.71	-0.79
F4	$\mu\varepsilon$	107 to 14,375	7,376	-0.16	-1.74
F5	$\mu\varepsilon$	1 to 2,475	842	0.31	-0.60
F6	$\mu\varepsilon$	0 to 2,702	850	0.42	-0.36
F7	1	0 to 0.99	0.48	-0.02	-0.42
F8	1	0 to 361.19	91.86	1.13	-0.34
F9	1	0 to 365.41	92.10	1.09	-0.42
F10	$\mu\varepsilon$	1 to 16,991	9,545	-0.28	-1.66
F11	1	0.01 to 166.07	7.01	7.54	60.75
F12	$\mu\varepsilon$	-1,514 to 1,504	-8	-0.05	2.34
F13	1	7.05 to 40.64	27.89	-0.53	-1.24
F14	1	0 to 23	4.84	1.16	0.03
F15	1	-1.51 to 1.37	0.23	-0.62	0.36
F16	1	-1.88 to 0.58	-1.08	0.76	0.52
F17	$\mu\varepsilon$	1,213 to 680,041	481,176	-0.18	-1.61
F18	1	0.76 to 0.99	0.90	-0.28	0.98
F19	1	0 to 0.99	0.15	1.78	2.14
F20	mm	0 to 130.65	13.83	3.23	13.83

4.2.8. Results and discussion

4.2.8.1 Identification

The results of crack identification are shown in Figure 4.2.10. The accuracy, precision, recall, and F1-score of the autoencoder-based unsupervised learning model are 0.94, 0.93, 0.94, and 0.94, respectively. The accuracy, precision, recall, and F1-score of the XGBoost supervised learning model are 0.98, 1.00, 0.96, and 0.98, respectively.

The crack identification results of the unsupervised learning model are plotted in Figure 4.2.11. In Figure 4.2.11(a), "no crack" data are mixed with crack data, meaning that the distributions of cracks were complex in the 3D space, making it more difficult to distinguish "crack" and "no crack" data. In Figure 4.2.11(b), the unsupervised learning model effectively identified some cracks.

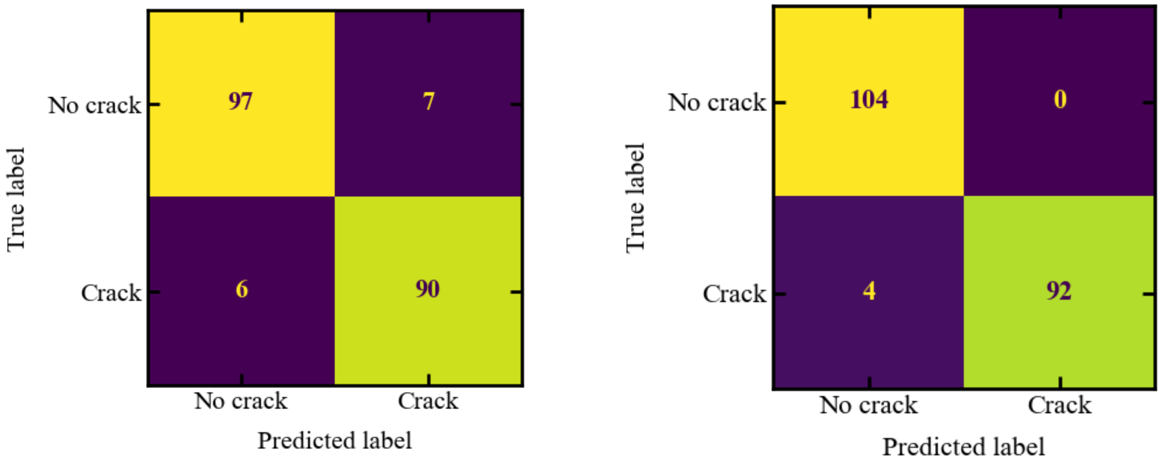

(a) (b)

Figure 4.2.10. Results of the confusion matrices of the crack identification model: (a) autoencoder-based unsupervised learning model, and (b) XGBoost supervised learning model.

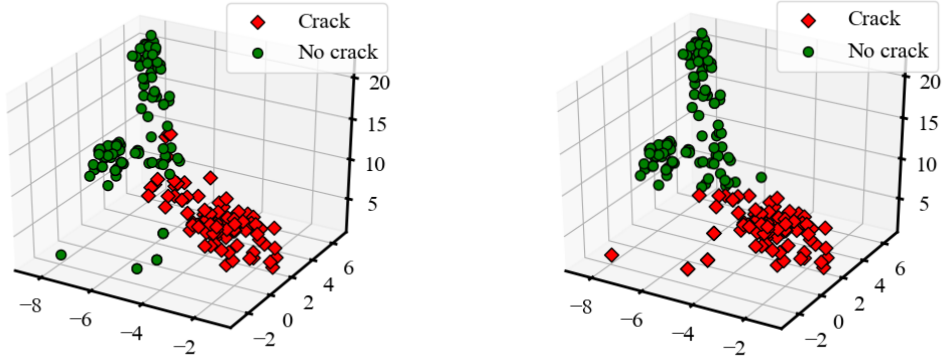

(a) (b)

Figure 4.2.11. Visualization of crack identification results: (a) ground truth; and (b) clustered results. The 3D coordinates are from the hidden representation layer in the autoencoder-based model.

This study compared 12 machine learning methods in terms of the efficiency and accuracy of crack identification. The hyperparameters of each machine learning model were optimized. The hyperparameters of the SVM-Linear and the SVM-RBF were optimized using the random search method [102]. The hyperparameters of the other machine learning methods were optimized using a grid search method [103]. K-fold cross-validation [104] was used to evaluate the generalizability of machine learning models, and k was equal to 5. The performance of the 12 machine learning methods is compared in Table 4.2.5.

The comparison shows that the XGBoost model outperforms the other machine learning models. The autoencoder-based model outperformed the other unsupervised learning models. The autoencoder-based method without feature extraction did not perform as well as the autoencoder-based method with feature extraction, revealing the feature extraction is effective in this study. Regarding the computation efficiency, the autoencoder-based model took 0.07 s, and the XGBoost model took 0.03 s to analyze 200 segments of strain distribution. The computation efficiency is adequate for real-time crack measurements.

Table 4.2.5. Performance comparison using different machine learning methods

Type	Methods	Time (s)	Accuracy	Precision	Recall	F1-score
Unsupervised learning	Gaussian mixture	0.22	0.34	0.94	0.46	0.62
	Birch	0.31	0.53	0.55	0.94	0.68
	K-means	0.11	0.56	0.56	0.92	0.69
	Autoencoder-based without feature extraction	0.10	0.57	0.54	0.98	0.70
	Autoencoder-based	0.07	0.94	0.93	0.94	0.94
Supervised learning	Ridge classifier	0.01	0.69	0.97	0.36	0.53
	SVM-RBF	0.07	0.76	0.66	1.00	0.80
	K-nearest neighbors	0.16	0.85	0.99	0.71	0.82
	Decision tree	0.02	0.85	0.85	0.85	0.85
	Random forest	0.26	0.93	0.96	0.90	0.92
	SVM-Linear	0.05	0.97	1.00	0.94	0.97
	Multi-layer perceptron	0.06	0.97	0.99	0.96	0.97
	XGBoost	0.03	0.98	1.00	0.96	0.98

The simulation data have been used to assist the training of the supervised learning models. The ratio of the number of simulation data to the number of experimental data was employed to control the mix of the simulation and experimental data. Four ratios were investigated, which are 0:1, 0.5:1, 1:1, and 1.5:1. All the data in the testing set were experimental data. The use of the simulation data enhanced the accuracy of the supervised learning models, as shown in Table 4.2.6. The F1-scores of the XGBoost model and autoencoder-based model increased with the ratio.

Table 4.2.6. Effect of the simulation data on the F1-score of machine learning methods

Number of data		Ratio	XGBoost	Autoencoder-based
Simulation	Experiment			
0	1,000	0:1	0.97	0.88
500	1,000	0.5:1	0.98	0.91
1,000	1,000	1:1	0.98	0.93
1,500	1,000	1.5:1	0.98	0.94

Regarding the labeling, the supervised learning methods relied on a large amount of labeled data. In this research, a total of 1,500 DFOS data measured from the tested beam were manually labelled. In practices, more DFOS data must be labeled to apply the supervised learning methods to large-scale structures. In comparison, the unsupervised learning methods eliminate the time-consuming labeling effort. Manual labeling operation also may involve mislabeling and reduce the accuracy and reliability.

In summary, the autoencoder-based unsupervised learning method performs slightly lower than the supervised learning method in terms of the accuracy of crack identification. However, the unsupervised learning method has higher efficiency than the supervised learning method because the unsupervised learning method does not require manual labeling of DFOS data. Thus, there is a trade-off between the labeling and accuracy. When the dataset size is small, supervised learning methods with manual labeling is a good choice to achieve high accuracy. When the dataset size is large, unsupervised learning method is an alternative to achieve high efficiency.

4.2.8.2 Localization

The crack localization results using the proposed methods are shown in Figure 4.2.12. The DFOS data under different loads are plotted along the beam in Figure 4.2.12(a). With the proposed crack localization algorithm, the peaks of all cracks were located, as shown in Figure 4.1.12(b). The supervised identification model was used to distinguish the cracks. The locations of cracks under different loads are shown in Figure 4.2.12(c).

Compared with manually annotating the cracks in Figure 4.2.12(d), cracks C2 to C21 were identified and located by the proposed approach. Crack C1 was not identified by human experts, and it did not generate a visible peak in the strain distributions. The positions of the identified cracks were the same as those identified manually.

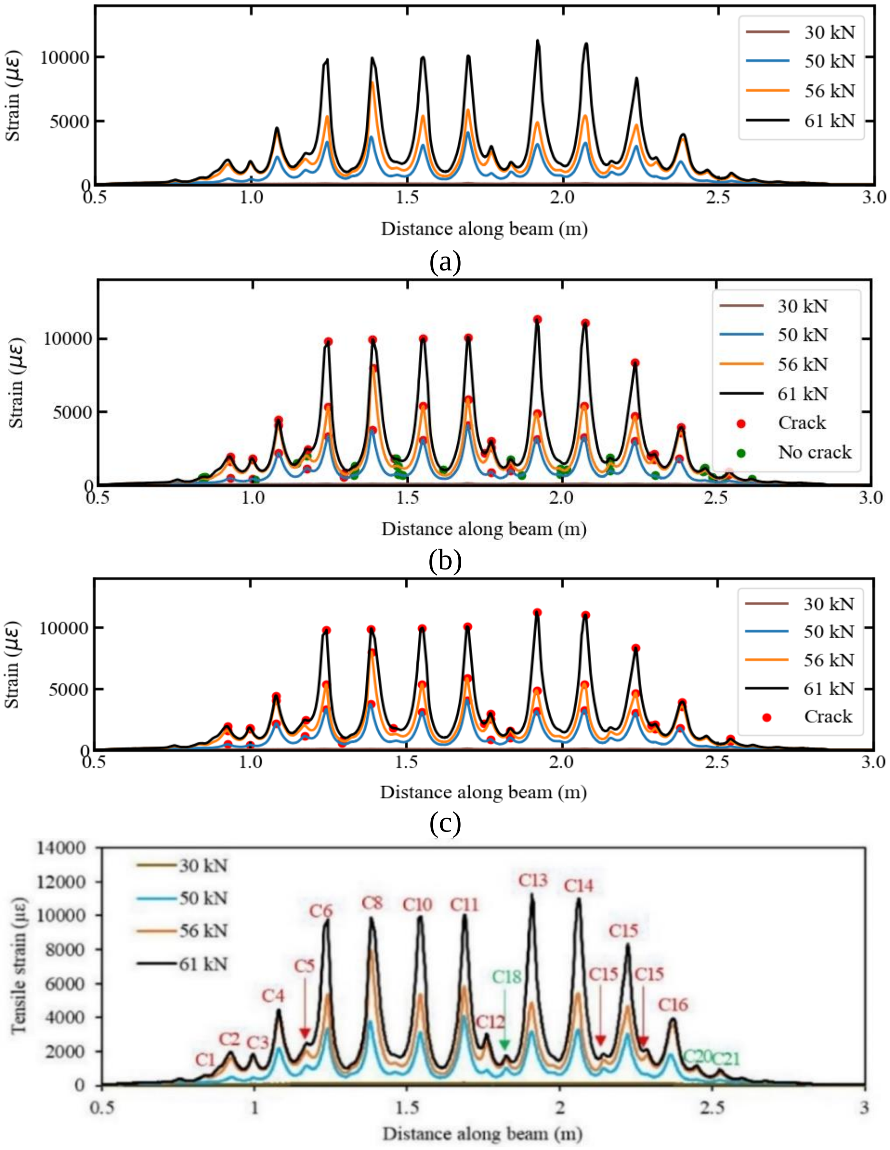

(a)

(b)

(c)

(d)

Figure 4.2.12. Crack localization results: (a) strain distributions; (b) possible cracks; (c) located and identified cracks; and (d) manually located cracks in previous research (permitted reprint).

4.2.8.3 Quantification

The results of crack width measured by the crack scope, calculated by the proposed method, and calculated by an existing method are shown in Figure 4.2.13. The calculation results of the proposed method were close to the measured crack widths. Regarding accuracy, R^2 of the proposed method was 0.950, which is higher than the result (0.938) of the existing method. The improvement of accuracy can be attributed to the finer resolution because accuracy is associated with the spatial resolution of the DFOS.

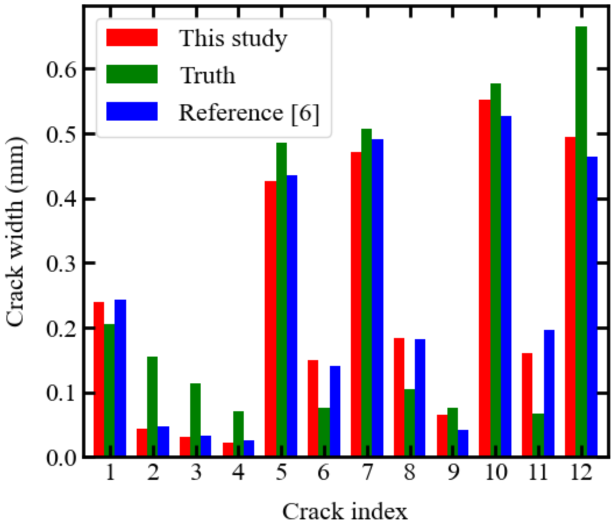

Figure 4.2.13. Results of crack quantification from the proposed approach and manual calculation.

4.2.8.4 Visualization

The cracks can be visualized in a 2D crack contour, as shown in Figure 4.2.14. The dark red areas indicate significant cracks. The center lines of these cracks and the corresponding crack widths are marked on the map. Only visible cracks with a crack width greater than 1 mm are automatically marked in the crack map. The cracks were mapped, showing the positions and widths of cracks. The model is updated in real time automatically. The model can be used to support sophisticated management of structures with cracks. The model can be utilized to visualize multi-scale cracks. The crack information is standardized and stored for subsequent analysis of crack evolution. The cracks obtained by the proposed method are visualized in a 2D projection.

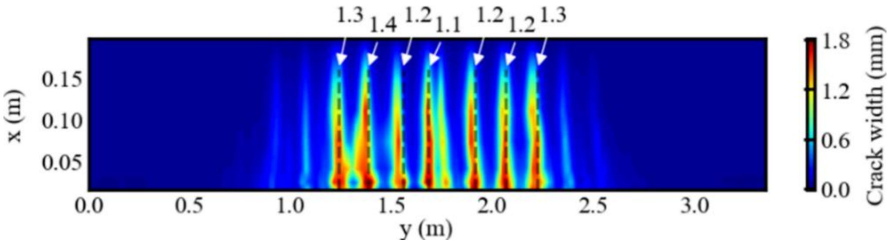

Figure 4.2.14. Crack visualization results presented in a 2D contour for the tested specimen.

4.2.9. Comparison with existing studies

The approaches proposed in this study and existing approaches are compared in Table 4.2.7. The features used for the comparison include: (1) whether human intervention is necessary; (2) whether crack identification is achieved; (3) whether crack localization is achieved; (4) whether crack quantification is achieved; and (5) the format of the crack visualization presentation.

Most existing studies required manually labelling the DFOS data or manually selecting strain segments that represent cracks [49]. The supervised and unsupervised machine learning methods proposed in this research are utilized to detect cracks automatically. Regarding crack localization, a strain distribution was divided into different segments using a fixed-width window and located cracks by identifying cracks for each segment of the DFOS sensor [76]. Domaneschi et al. integrated DFOS with camera [106] and acoustic emission [107] to achieve local and global crack detection and localization. However, this method relies on the acoustic emission technique [107]. This study implemented a strain trend analysis algorithm to find peaks for strain distribution to achieve accurate crack localization. Regarding crack visualization, this study develops a 3D digital twin to display cracks, while the existing methods used 2D strain contours to present cracks.

Table 4.2.7. Comparison between this research and the state-of-the-art studies

Source	Year	Sensor	Algorithm	Human intervention	A[1]	B[1]	C[1]	D[1]
This study	2023	DFOS	XGBoost and Autoencoder	Low	Yes	Yes	Yes	3D
[77]	2022	DFOS	SVM	High	Yes	No	No	/
[76]	2020	DFOS	CNN	High	Yes	Yes	No	/
[75]	2019	DFOS	Autoencoder	High	Yes	No	No	/
[106]	2021	DFOS and camera	DIC[2]	Low	Yes	Yes	Yes	/
[107]	2020	DFOS, acoustic emission, and camera	DIC[2]	Low	Yes	Yes	Yes	2D
[49]	2021	DFOS	/	High	Yes	Yes	Yes	2D
[105]	2022	DFOS	/	High	Yes	Yes	Yes	/

[1] "A", "B", "C", and "D" denote detection, localization, quantification, and visualization, respectively.

[2] "DIC" indicates the digital image correlation technique.

4.2.10. Discussion on DFOS parameters

This section discusses the spatial resolution, the strain transfer effect, and the measurement of microcracks near widely opened cracks. The spatial resolution of DFOS showed large effects on the measurement accuracy of crack width when cracks were monitored using DFOS under three different spatial resolutions, which are 0.65 mm, 1.3 mm, and 2.6 mm, respectively [27]. Based on the DFOS data obtained from experiments, the proposed machine learning approaches were applied to detect and quantify cracks automatically. The representative F1 scores of the crack detection and the R^2 values of the crack quantification are shown in Table 4.2.8. When the spatial resolution is changed, the high performance of the proposed methods is retained, revealing that the proposed approaches are robust to the spatial resolution.

Table 4.2.8. Effect of the different spatial resolution on the performance of the proposed methods

Spatial resolution (mm)	XGBoost method		Autoencoder-based method	
	Detection	Quantification	Detection	Quantification
0.65	0.98	0.95	0.94	0.95
1.3	0.95	0.95	0.95	0.95
2.6	0.95	0.95	0.94	0.95

The presence of the protective coatings of DFOS has significant effects on the strain results via the strain transfer effect, which enables the use of DFOS to monitor cracks because the abrupt strain change in the DFOS passing through a crack opening is distributed over a long length, also known as the development length, thus protecting the DFOS from being ruptured. When DFOS is utilized to monitor cracks, the strain transfer effect on the strain results is naturally imposed because the strain distributions measured from the DFOS are already the strain results under strain transfer effect. Based on the previous study [27], cracks were respectively evaluated using DFOS with three different coating thicknesses, which are 242 mm, 650 mm, and 900 mm, because the coating thickness directly affects the strain transfer effect. In this research, the proposed approaches are applied to detect and quantify cracks using the experimental data. The representative results are listed in Table 4.2.9. When the coating thickness is changed, the high performance of the proposed methods is retained, revealing that the proposed approaches are robust to the strain transfer effect of DFOS.

Table 4.2.9. Effect of the strain transfer on the performance of the proposed methods

Coating thickness (μm)	XGBoost method		Autoencoder-based method	
	Detection	Quantification	Detection	Quantification
242	0.98	0.95	0.94	0.95
650	0.97	0.95	0.95	0.95
900	0.95	0.95	0.94	0.95

It is still a challenge to use DFOS to precisely detect and quantify microcracks near widely opened cracks because the strain spikes caused by the microcracks near major cracks are usually concealed by the spikes caused by major cracks. Both the strain spikes that are caused by microcracks and major cracks are subject to the strain transfer effect. When microcracks are too close to major cracks, their strain transfer lengths will be overlapped, and microcracks do not provide visible and distinct local peaks along the length of measured strain distribution, making it difficult to distinguish the spikes of microcracks.

4.3. Strain contour-based method

4.3.1. Research objectives

The method in section 4.2 shows the feasibility of automatic interpretation of DFOS data in the context of crack monitoring. However, the method identifies cracks via segmenting DFOS data into short segments. Four limitations have been identified:

- First, it is difficult to ensure that the segmentation operation will not split one crack into multiple segments.

- Second, the existing approaches treat a crack detection task as a binary classification task, inconsistent with the fact that a single segment may contain multiple cracks, which compromises the detection accuracy.
- Third, it is difficult to determine the appropriate width of segments. The width was selected via trial and error. It is unknow whether the adopted segment width is applicable to other cases.
- Fourth, the performance of the existing approaches relies on a large amount of training data. However, it is difficult to establish a large database. Besides the lack of data, the database is often unbalanced because the majority of DFOS data is for crack-free conditions.

To address these challenges, a deep learning approach was developed to interpret spatially-distributed cracks from DFOS data automatically. The approach innovates in three aspects:

- First, a modified You Only Look Once (YOLO) method is developed to identify and locate cracks.
- Second, a transfer learning strategy is implemented to address the problem of the lack of DFOS data for the training of the deep learning model.
- Third, a new split-and-merge method is developed to improve the multi-crack detection accuracy.

The generalizability of the proposed approach is evaluated using test results from two types of experiments. This research will promote the applications of DFOS for structural health monitoring through improving the capability of intelligent analysis of the DFOS data while achieving high accuracy and high efficiency.

4.3.2. Overview of methods

Figure 4.3.1 shows the framework of the proposed approach, which includes seven main modules: (1) Collection of DFOS data. Strain distributions are collected with appropriate spatial resolution and sampling frequency, aiming at supporting the monitoring of cracks without overburdening data storage demands. (2) Generation of strain contour images. Strain distributions are converted into strain contour images. (3) Image augmentation. Seven methods are used to enlarge the dataset size. (4) Improved YOLOv5 network. An improved YOLOv5 network is developed to detect and locate cracks from strain contour images. (5) Transfer learning. Transfer learning is incorporated to enhance the performance of the deep learning model. (6) Data splitting and recovery. A split-and-merge method is proposed to handle DFOS data with many data points. (7) Quantification of crack width. A method is proposed to calculate the crack width. The above methods are elaborated in the following subsections.

When a DFOS passes through a crack, the DFOS will be stretched by the crack to achieve a high tensile strain, which is seen as a sharp spike in the strain distribution measured from the DFOS. The presence of the protective coating of the fiber optic cable protects the DFOS from rupturing at the crack [28]. When the crack opening width is narrow, as shown in Figure 4.3.2(b), the bond between fused silica and polymer coating is retained. When the crack is widened, the polymeric coating will rupture, and debonding will occur between the fused silica fiber and the polymeric coating, as shown in Figure 4.3.2(c). The occurrence of interfacial debonding helps transfer the abrupt deformation at the crack over a long length of the fused silica fiber via the strain transfer effect, thus reducing the magnitude of tensile strains and postponing the rupture of the fused silica fiber. While it is promising to use DFOS to monitor cracks, the challenge is that there are too many cracks to monitor by human experts in real practices, as shown in Figure 4.3.2(d).

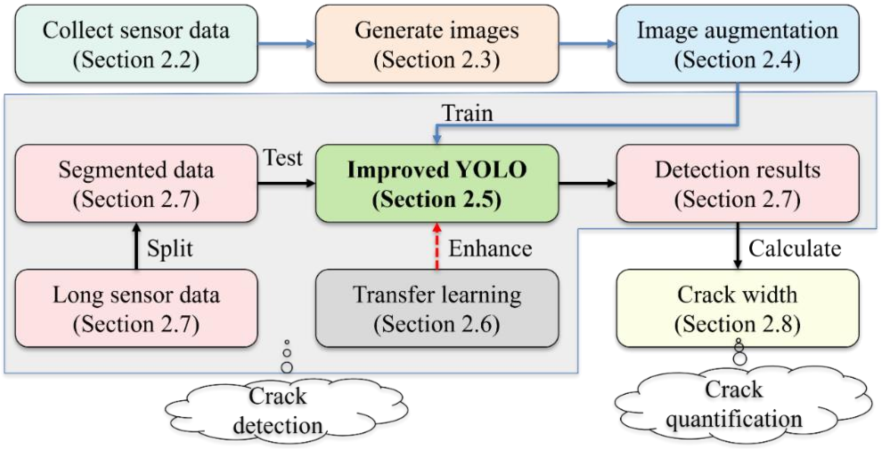

Figure 4.3.1. Framework of the proposed approach to intelligently monitor cracks based on DFOS data.

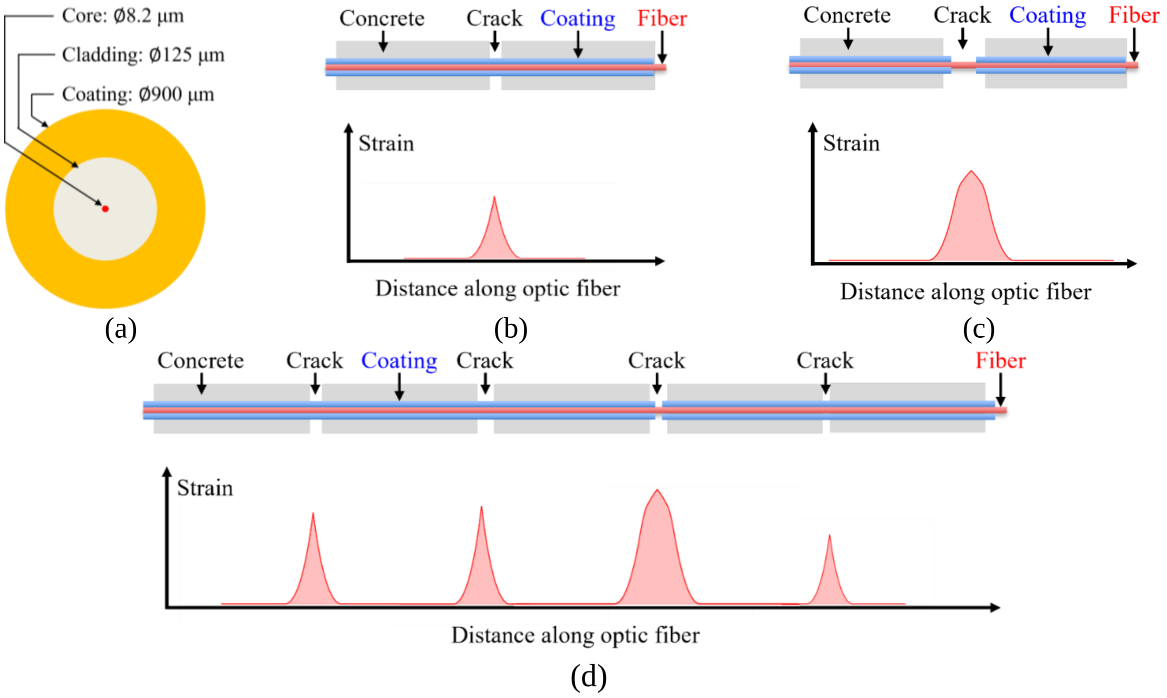

Figure 4.3.2. Monitoring cracks using DFOS: (a) cross section of a DFOS; (b) a narrow crack and strain distribution; (c) a wide crack and strain distribution; (d) distributed cracks and strain distribution.

4.3.3. Converting strain distributions into contour images

Because the amount of data measured by DFOS is too large to interpret by engineers, this subsection presents a method to convert the strain distribution measured from DFOS into a strain contour image to facilitate the interpretation of the strain distribution based on deep learning. The main procedure of generating a strain contour image is shown in Figure 4.3.3.

First, an arbitrary strain distribution can be expressed as a one-dimensional matrix:

$$\boldsymbol{\varepsilon_a} = \begin{bmatrix} \varepsilon_1 & \varepsilon_2 & \cdots & \varepsilon_N \end{bmatrix} \tag{4.3.2}$$

where N is the total number of data points of the arbitrary strain distribution, and N is an integer greater than 1. Each element of the matrix represents a strain value.

Second, the strain distribution is replicated in a new dimension to form a 2D matrix, which has 640 rows and N columns, because the default YOLOv5 script sets the input image size to 640 × 640 pixels, as shown in Eq. (4.3.3). The image size can be different, as long as the images are clear. The effect of the image size on the data interpretation results is investigated in Section 4.2.

$$\boldsymbol{\varepsilon_b} = \begin{bmatrix} \varepsilon_1 & \varepsilon_2 & \cdots & \varepsilon_N \\ \cdots & \cdots & \cdots & \cdots \\ \varepsilon_1 & \varepsilon_2 & \cdots & \varepsilon_N \end{bmatrix} \tag{4.3.3}$$

Third, in each row of the matrix, a total of M strain values are inserted between each pair of adjacent data points through linear interpolation [108], as shown in Eq. (4.3.4). This step is used to generate more strain data points between adjacent sensing points through interpolation, aiming to provide a smooth representation of the strain distribution using strain contour images.

$$\boldsymbol{\varepsilon_c} = \begin{bmatrix} \varepsilon_1 & \varepsilon_{1,1} & \cdots & \varepsilon_{1,M} & \varepsilon_2 & \cdots & \varepsilon_N \\ \cdots & \cdots & \cdots & \cdots & \cdots & \cdots & \cdots \\ \varepsilon_1 & \varepsilon_{1,1} & \cdots & \varepsilon_{1,M} & \varepsilon_2 & \cdots & \varepsilon_N \end{bmatrix} \tag{4.3.4}$$

where $M = \left\lfloor \frac{640SR}{100} \right\rfloor$. $\lfloor\cdot\rfloor$ denotes the round down function, and SR is the spatial resolution of the DFOS (unit: mm). The number of columns of $\boldsymbol{\varepsilon_c}$ is $(MN + N - M)$. In this study, SR is equal to 0.65 mm, which was deemed appropriate for measuring cracks.

Fourth, the elements in $\boldsymbol{\varepsilon_c}$ are used to calculate the red (R), green (G), and blue (B) values of each pixel of a strain contour image according to Eq. (4.3.5) to Eq. (4.3.7). The equations for generating strain contour images are elaborated in reference [109].

$$R(\varepsilon) = 255 \begin{cases} 0, & \varepsilon < \varepsilon_{min} + 0.5\Delta\varepsilon \\ \dfrac{4(\varepsilon - \varepsilon_{min} - 0.5\Delta\varepsilon)}{\Delta\varepsilon}, & \varepsilon_{min} + 0.5\Delta\varepsilon \le \varepsilon < \varepsilon_{min} + 0.75\Delta\varepsilon \\ 1, & \varepsilon \ge \varepsilon_{min} + 0.75\Delta\varepsilon \end{cases} \tag{4.3.5}$$

$$G(\varepsilon) = 255 \begin{cases} \dfrac{4(\varepsilon - \varepsilon_{min})}{\Delta\varepsilon}, & \varepsilon < \varepsilon_{min} + 0.25\Delta\varepsilon \\ 1, & \varepsilon_{min} + 0.25\Delta\varepsilon \le \varepsilon < \varepsilon_{min} + 0.75\Delta\varepsilon \\ \dfrac{4(\varepsilon_{min} + \Delta\varepsilon - \varepsilon)}{\Delta\varepsilon}, & \varepsilon \ge \varepsilon_{min} + 0.75\Delta\varepsilon \end{cases} \tag{4.3.6}$$

$$B(\varepsilon) = 255 \begin{cases} 1, & \varepsilon < \varepsilon_{min} + 0.25\Delta\varepsilon \\ \dfrac{4(\varepsilon_{min} + 0.5\Delta\varepsilon - \varepsilon)}{\Delta\varepsilon}, & \varepsilon_{min} + 0.25\Delta\varepsilon \le \varepsilon < \varepsilon_{min} + 0.5\Delta\varepsilon \\ 0, & \varepsilon \ge \varepsilon_{min} + 0.5\Delta\varepsilon \end{cases} \tag{4.3.7}$$

where ε is an arbitrary strain, and $\Delta\varepsilon = \varepsilon_{max} - \varepsilon_{min}$, where ε_{max} and ε_{min} are the maximum and minimum values, respectively. The RGB values are put into three matrices, respectively, which have the same dimensions as $\boldsymbol{\varepsilon_c}$.

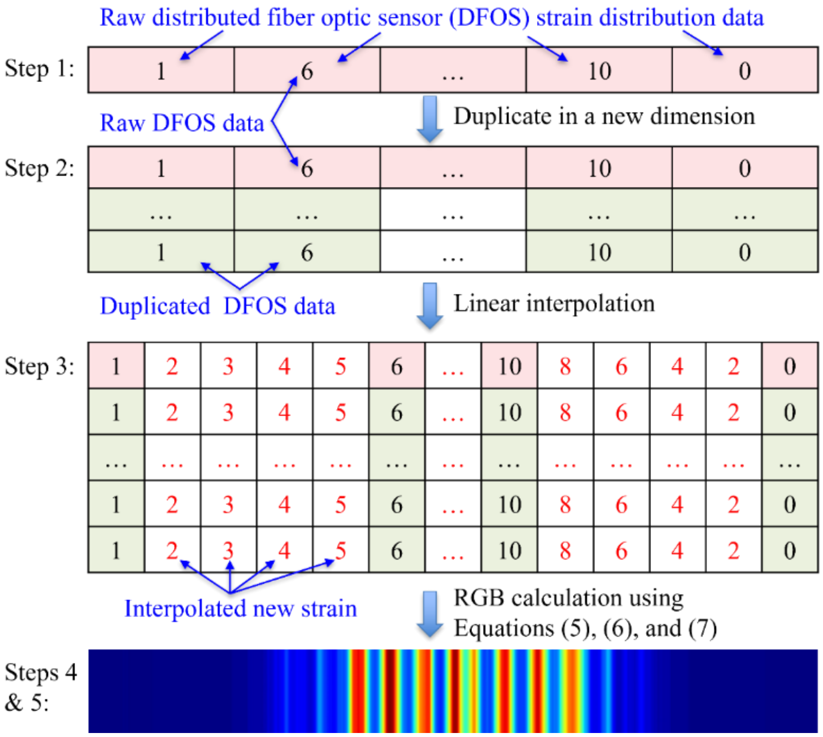

Figure 4.3.3. Flowchart of generating intuitive crack images using DFOS data.

Finally, the RGB matrices are converted into a colored strain contour image, as shown in Figure 4.3.3. A strain contour image is a graphic representation of the measured strain distribution.

3.3.4 Data augmentation

To enlarge the dataset size, seven augmentation methods are applied, including translation, scaling, flipping, hue, saturation, lightness, and mosaic [110]. Representative examples are shown in Figure 4.3.4. For each image from the training dataset, mosaic augmentation randomly merges four images, followed by performing random translation and scaling.

Then, the generated image is randomly flipped, and the hue, saturation, and lightness are randomly adjusted. The use of these data augmentation methods increases the variability of data and reduces the training time since the augmented dataset requires less graphics memory in the model training process.

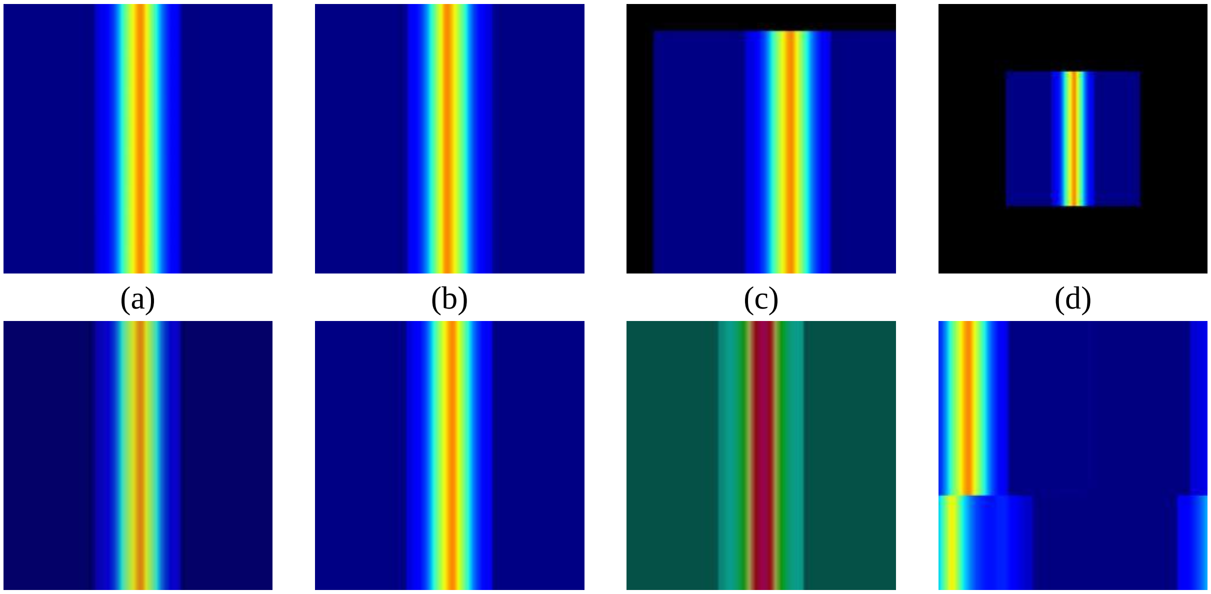

Figure 4.3.4. Representative examples of the seven data augmentation methods: (a) the original image; (b) flipping; (c) translation; (d) scaling; (e) hue; (f) saturation; (g) lightness; and (e) mosaic.

4.3.5 Improved YOLOv5 network

A deep learning network is developed to detect and locate cracks from strain contour images based on the YOLOv5 network, which is a cutting-edge artificial intelligence method [111]. The improved network is based on the original YOLOv5 network, consisting of three main parts: a backbone, a simplified neck, and a lightweight head, as shown in Figure 4.3.5.

The backbone is used to extract the feature information from input strain contour images. The simplified neck fuses the extracted feature information and generates three scales of feature maps. The output part detects the objects from the generated feature maps [112]. Each part is composed of different layers. “Conv” represents convolution, normalization, and activation operations. The two numbers after “Conv” are the kernel size and stride size of the convolutional operations, respectively. “C3” is the cross-stage partial (CSP) network with three convolutional layers. “Concat”, “SPPF”, and “UpSample” represent the concatenation layer, spatial pyramid pooling fast (SPPF) layer [111, 113], and up-sample layer, respectively. More details about these blocks are available in reference [111]. The improved YOLOv5 network has a total of 22 blocks and 5,235,014 trainable parameters.

Compared with the original YOLOv5, three modifications were made. First, transformer blocks were added to the backbone and neck. The original feature extraction network of YOLOv5 depends on the convolution layers, which extracts features from the input images but lacks the ability to handle long measurements from DFOS. A transformer block was added to the backbone to extract the features of images [114]. The architecture of the transformer block is shown in Figure 4.3.6. The input data of the transformer block is a sequence of fixed-size image patches with linearly embedded location information. The transformer block has multi-head self-attention [115] and multilayer perceptron layers. Following each layer, residual connections are performed with a summation operation. The normalization layers of the original YOLOv5 network are removed to reduce the number of parameters and improve the computational efficiency [116].

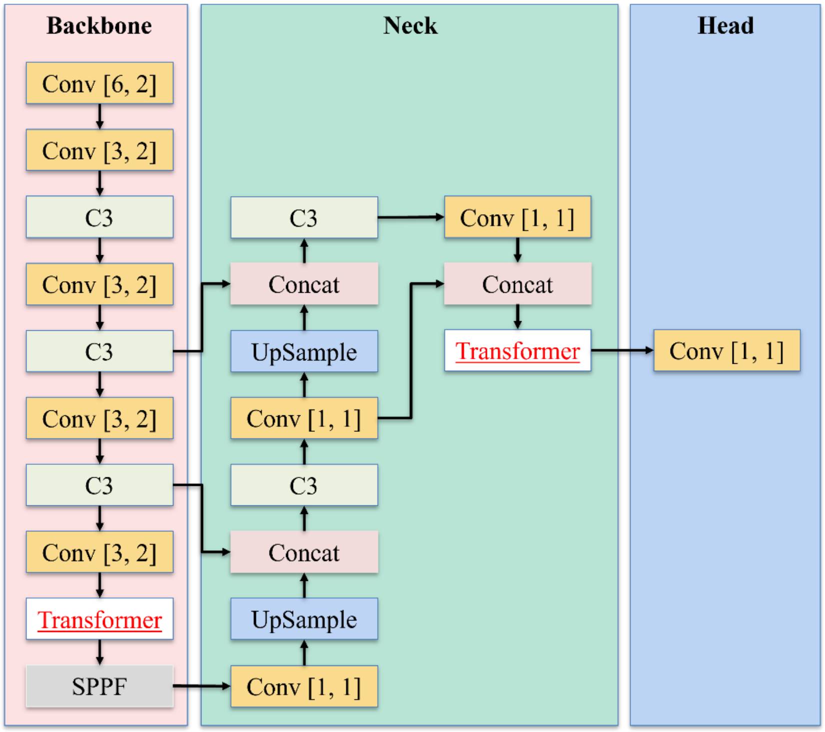

Figure 4.3.5. Architecture of the improved YOLOv5 network with a backbone, a neck, and a head.

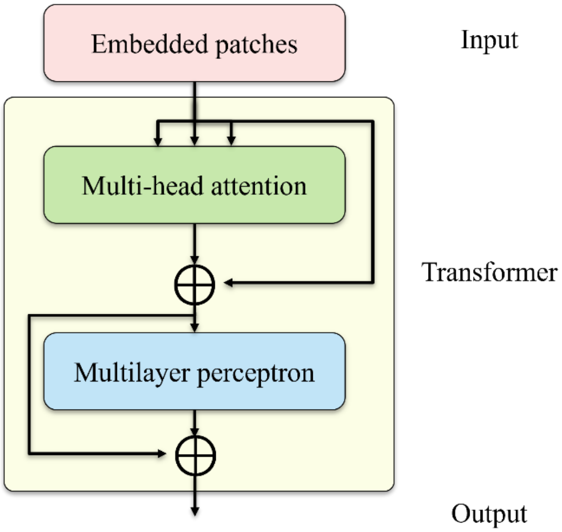

Figure 4.3.6. Architecture of the transformer block in this study. "⊕" indicates an adding operation.

Second, the number of detection heads is reduced to one. In the original YOLOv5 network, three heads are utilized for different sizes of detection targets. In this study, the dimensions of DFOS detection boundaries are countable. The height of the crack boundary was fixed at 640. The width of images is determined by the specific task and settings of DFOS. In this case, using three heads for multiple detection becomes insignificant and increases the complexity of the architecture. Thus, the extra heads are removed to simplify the network. There is only one head in the improved YOLOv5 network.

Third, unnecessary convolutional blocks in the neck are removed to further simplify the network. Compared with the original YOLOv5 network, the improved YOLOv5 network reduces the number of blocks from 25 to 22 (by 12%) and reduces the number of trainable parameters from 7,022,326 to 5,235,014 (by 25%).

4.3.6 Transfer learning

Transfer learning is applied to enhance the performance of the improved YOLOv5 model because of the lack of data. Figure 4.3.7 shows the workflow of transfer learning. First, DFOS data are generated using the strain transfer methods established in previous research [24, 25]. Second, based on the DFOS data, strain contour images are created. The data augmentation methods are applied to enlarge the dataset size. Third, the improved YOLOv5 model is trained using the strain contour images, and the trained parameters are stored. Fourth, DFOS data from various experiments are utilized to create strain contour images. Finally, the improved YOLOv5 model is retrained using the strain contour images obtained from tests.

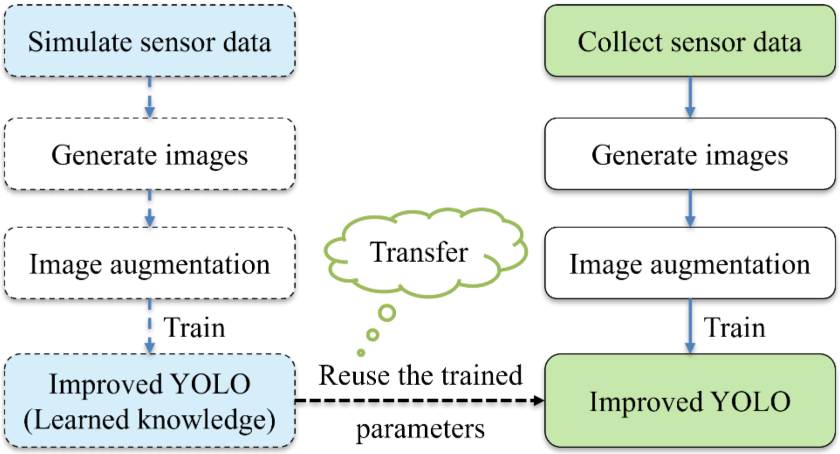

Figure 4.3.7. Flowchart of the transfer learning strategy adopted to improve the training of the model.

4.3.7 Data splitting and recovery

DFOS can continuously measure strains along its entire length. The length of a single DFOS can be up to hundreds of meters to kilometers. Although engineers can judge cracks based on strain distributions or strain contour images, it is difficult for engineers to monitor cracks in real time when a long DFOS is used to measure many cracks. When a YOLOv5 model is used, it is feasible to automate the data analysis process, but directly using the images created by the entire strain distributions from a long DFOS had limited effectiveness in crack detection tasks. To address this issue, a split-and-merge approach is proposed, as shown in Figure 4.3.8.

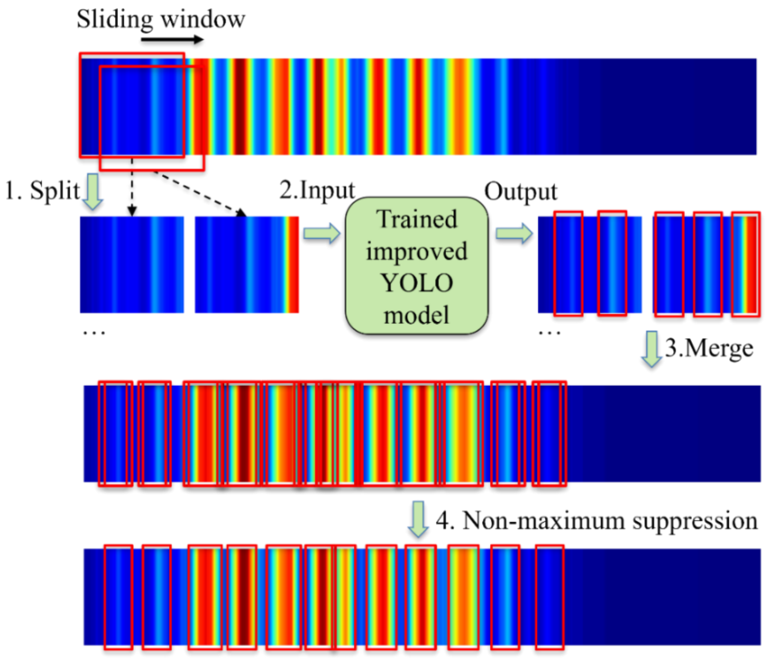

Figure 4.3.8. Workflow of the split-and-merge approach for crack detection with a long DFOS.

First, the strain contour image from a long DFOS is divided into many sub-images with equal width and height by employing a sliding window. For each pair of adjacent sub-images, half of the width is overlapped to avoid splitting the pixels of a crack into two sub-images. Half-width is adopted to minimize the overlap of images. Second, the sub-images are fed into the improved YOLOv5 model to detect cracks. Third, the crack detection results are merged to generate a large contour image according to their spatial positions, which are determined by the width and positions of the sliding windows. Finally, a non-maximum suppression (NMS) algorithm is implemented to eliminate the overlapped areas of the contour images and improve the overall accuracy [117].

4.3.8 Quantification of crack width

The crack width can be calculated using strain distributions measured from DFOS [118, 119]. One of the methods is to calculate the crack width by performing an integration operation of the strain distribution. The operation requires determining the boundaries of each crack, as shown in Figure 4.3.9. This study uses the improved YOLOv5 model to locate the boundaries of each crack. Linear interpolation is performed to increase the spatial resolution of the strain distribution. Finally, the crack width is calculated by performing an integration operation of the strain distribution, as marked by the green area under the strain peak.

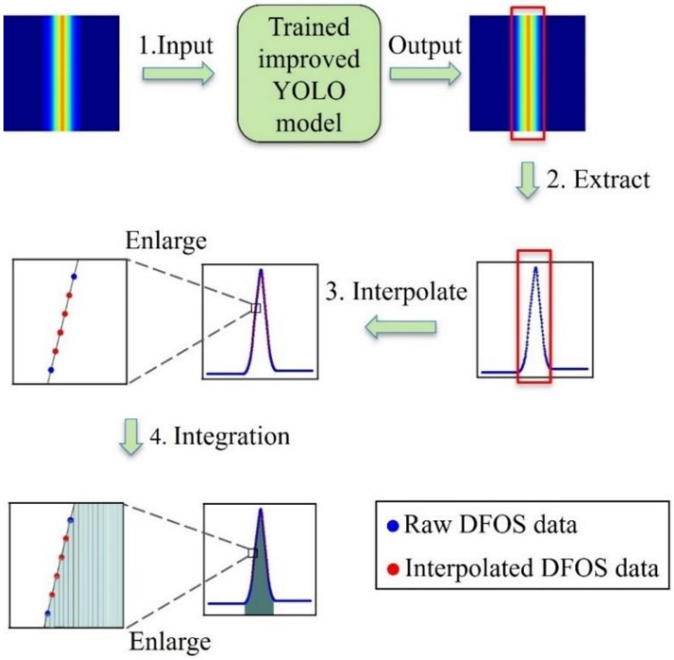

Figure 4.3.9. Quantification of crack width using an integration method based on the detection results.

4.3.9. Implementation and performance evaluation

4.3.9.1 Datasets

The proposed approach was implemented into the analysis of the DFOS data measured from a specimen tested under four-point bending. The length of the DFOS was 3.5 m. When the sampling resolution was 0.65 mm, the DFOS obtained 5,384 data points in one measurement. The test specimen was instrumented with two paths of DFOS. In the experiment, the DFOS measured 25 sets of strain distributions, which are referred to as the original strain distributions. The original strain distributions were divided into about 1000 segments of strain distributions with the same segment length. Among those segments of strain distributions, a total of 235 segments had cracks and were used as experimental data. In addition to the test data, 685 simulated strain distributions were obtained using a strain transfer model proposed in references [24, 25]. The strain distributions were randomly combined to augment the dataset size. The numbers of tested and simulated strain distributions were increased to 235×5 = 1175 and 685×5 = 3425, respectively. In each strain distribution, the number of cracks ranged from one to five.

The three datasets used in this study are shown in Table 4.3.1. The original strain distributions were utilized to test the performance of the trained model. The experimental data extracted from the original strain distributions were utilized to train, validate, and test the deep learning model. The simulated data were used for transfer learning.

Table 4.3.1. Summary of the dataset used in this study

Name	Number	Number after combination	Number of contour images		Used for
			Common	Augmented	
Original DFOS data	25	/	25	/	Testing
Experimental data	235	1,175	1,175	1,175	All
Simulated data	685	3,425	3,425	3,425	Transfer learning

Representative examples of the generated strain contour images are shown in Figure 4.3.10. The comparison of the simulated strain contour images with the experimental strain contour images reveals that the simulation method is reasonable. The generated strain contour images were manually labelled using *labelme* [120]. The strain contour images in the training dataset were augmented using the method elaborated in section 4.4, as shown in Figure 4.3.10(f).

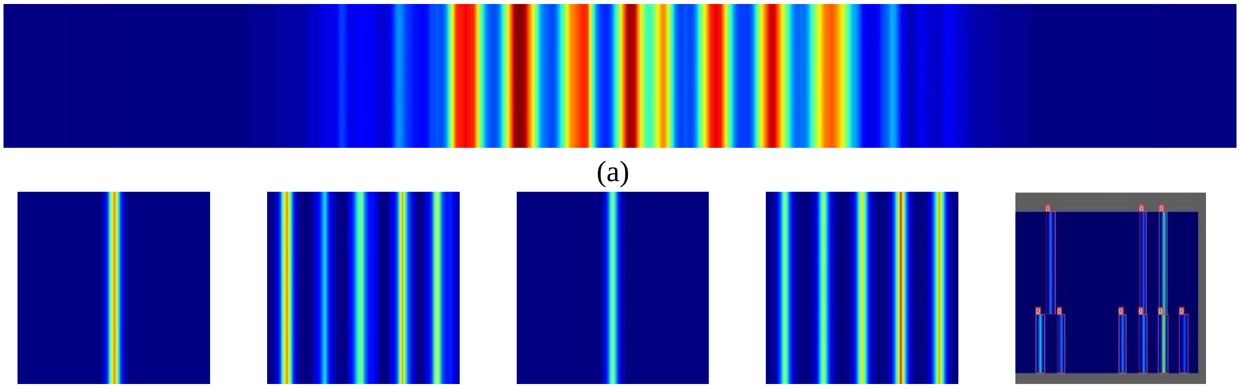

(a)

(b) (c) (d) (e) (f)

Figure 4.3.10. Examples of contour images generated with DFOS strain data: (a) long DFOS contour; (b) experimental contour with one crack; (c) experimental contour with five cracks; (d) simulated contour with one crack; (e) simulated contour with five cracks; and (f) augmented experimental contour.

4.3.9.2 Detection and quantification of cracks

The improved YOLOv5 network was coded with Python [121] and trained for 100 epochs. The learning rate and the batch size were set to 0.01 and 32, respectively. The weight decay was 0.0005 with the stochastic gradient descent (SGD) as the optimizer. The training, validation, and testing were conducted on Google Colaboratory using a 2.30-GHz Intel Xeon (R) CPU, 13-GB RAM, and a 15-GB Tesla K80 GPU.

The loss curves are shown in Figure 4.3.11, showing desired performance. The performance of the proposed deep learning model for crack detection is assessed using standard metrics commonly employed, including precision [122], recall [122], F1 score [122], and mean average precision (mAP) [123]. These metrics were calculated based on the ground truth values in the datasets and the estimated values from the proposed deep learning model. These metrics provide a comprehensive and reliable assessment of the accuracy and effectiveness in detecting cracks. Regarding mAP, mAP@0.5 and mAP@0.5:0.95 were considered. mAP@0.5 is the mAP value when the intersection over union (IOU) is higher than 0.5. mAP@0.5:0.95 is the average of mAP values when the IOU is from 0.5 to 0.95 with an interval of 0.05. More details about the metrics are available in references [122, 123].

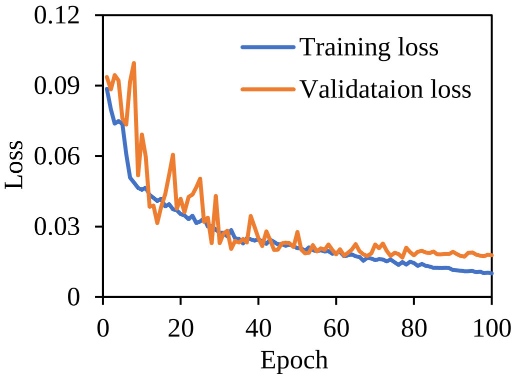

Figure 4.3.11. The loss curves of the training and validation process of the improved YOLOv5 model.

The performance improvement of the model in the training process is shown in Figure 4.3.12. In the first 20 epochs, the precision, recall, and F1 score rapidly increased from 0 to 0.9. After 100 epochs, the precision, recall, F1 score, mAP@0.5 and mAP@0.5:0.95 reached 0.923, 0.929, 0.926, 0.959, and 0.888, respectively.

The trained YOLOv5 model was then used to detect cracks from the strain contour images generated from 130 sets of DFOS data. The 130 contour images were not used in the training of the model, so they were unseen data for the trained model. All cracks were detected by the modified YOLOv5 model, regardless of the number of cracks. Three representative examples of crack detection results are shown in Figure 4.3.13. The efficiency of the modified YOLOv5 model was evaluated in terms of the processing time for the strain contour images. With a strain contour image including 10,000 strain data, the average processing time was shorter than 0.05 s.

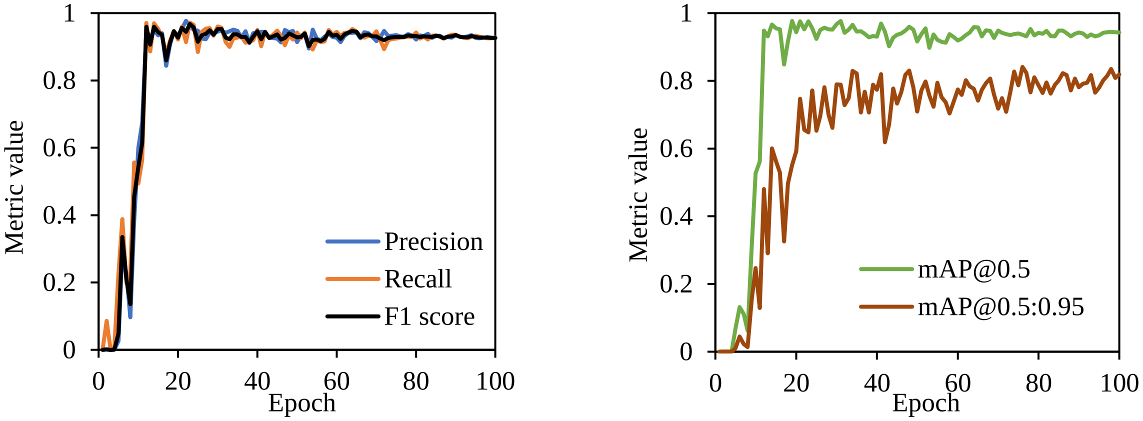

(a) (b)

Figure 4.3.12. Results of the performance metrics of the deep learning model for crack detection in the training process: (a) precision, recall, and F1 score and (b) mAP@0.5 and mAP@0.5:0.95.

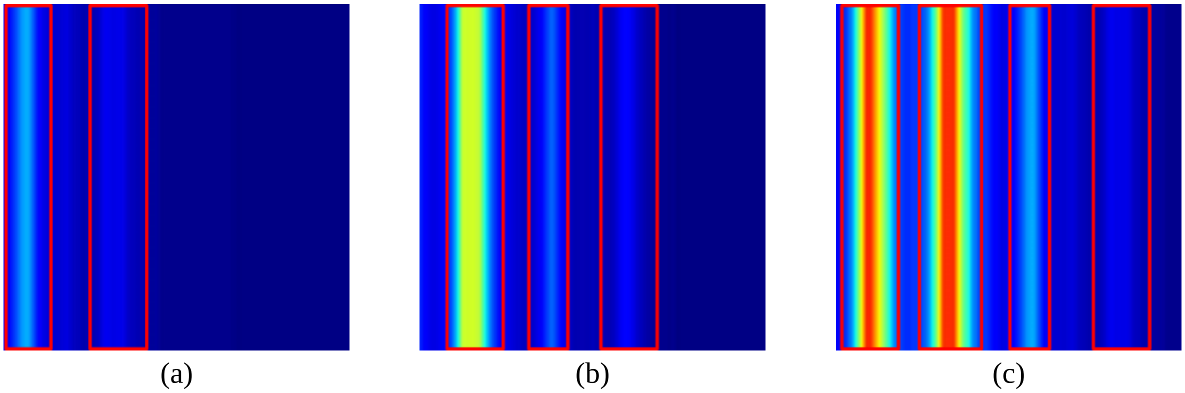

Figure 4.3.13. Representative examples of crack detection results of the proposed YOLOv5 model based on experimental data: (a) two cracks; (b) three cracks; and (c) four cracks.

The effect of the contour image size on the detection accuracy of the modified YOLOv5 model is investigated. Three different contour image sizes were used to generate strain contours, including 512 × 512, 640 × 640, and 1280 × 1280 pixels. Then, the generated strain contours were used to train and test the proposed modified YOLOv5 model. The mAP@0.5 of the modified YOLOv5 models using different image sizes remained the same, demonstrating that the accuracy of the model was not significantly affected by the image size. It is worth noting that the images must be large enough to be identifiable by human observers. A default image size of 640 × 640 pixels for the YOLOv5 model was utilized in this study.

The performance of the proposed approach with the modified YOLOv5 model and transfer learning is compared with the performance of the other approaches, as listed in Table 4.3.2. The comparison results reflect the benefits of the modifications of the YOLOv5 network and the incorporation of transfer learning. Compared with the original YOLOv5 model, the modified YOLOv5 model achieved higher accuracy and efficiency. For example, the mAP@0.5:0.95 was increased from 0.782 to 0.894 (by 14.3%), and the number of trainable parameters was reduced from 7,011,538 to 5,235,014 (by 25.3%). It should be noted that there is a trade-off between the performance and computational complexity of the deep learning model. By adding transformers, the mAP@0.5 increased from 0.885 to 0.948, and the number of trainable parameters increased to 7,011,922. The data augmentation methods increase the diversity of the training data and improve the mAP@0.5 from 0.930 to 0.959.

Table 4.3.2. Effect of each improvement point on the crack detection performance

Algorithm	F1 score	mAP@0.5	mAP@0.5:0.95	Number*
YOLOv5	0.922	0.885	0.782	7,011,538
YOLOv5 + Transformer	0.924	0.948	0.850	7,011,922
YOLOv5 + Transformer + reduced head	0.933	0.951	0.863	7,008,070
YOLOv5 + Transformer + reduced head + simplified neck (= Proposed network)	0.926	0.959	0.888	5,235,014
Modified YOLOv5 without data augmentation	0.920	0.930	0.826	5,235,014
Modified YOLOv5+ transfer learning	0.936	0.968	0.894	5,235,014

* The number of trainable parameters.

The performance of the improved YOLOv5 model for crack detection was compared with four other advanced deep learning models, which are YOLOv8, YOLOv5, YOLOv4, YOLOv3, Faster R-CNN [124], RetinaNet [125], fully convolutional one-stage (FCOS) [126], and single shot multibox detector (SSD) [127], which were trained and evaluated using the same dataset as the improved YOLOv5 model. The results of performance metrics are plotted in Figure 4.3.14. The highest accuracy and efficiency were achieved by the proposed modified YOLOv5 model, followed by the YOLOv8 model and faster RCNN model. The YOLOv8 model reached a good mAP@0.5 of 0.915, higher than that of the YOLOv5 model. However, the YOLOv8 model was not modified using the proposed methods. The faster RCNN model reached the third highest mAP@0.5, which is 0.870, but the processing time for each measurement was 0.147 s, much longer than that of the improved YOLOv5 model (0.008 s).

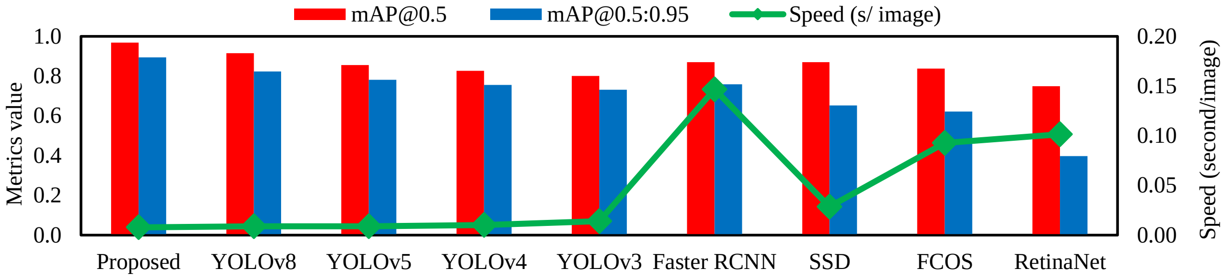

Figure 4.3.14. Performance comparison for the improved YOLOv5 model and eight other models.

To test the scalability of the proposed approach, DFOS data obtained from long DFOS were utilized. Representative results are shown in Figure 4.3.15(a). The image has 3,200×640 pixel and multiple cracks. When the modified YOLOv5 model was directly applied without incorporating the split-and-merge operation, multiple cracks were detected as a single crack by mistake. The cracks on the right side were not detected. After the proposed split-and-merge operation was incorporated with a fixed window measuring 640×640 pixel for data splitting and a threshold of IOU of 0.8, all cracks were successfully detected, and the different cracks were differentiated, as shown in Figure 4.3.15(b). These results reveal that it is essential to incorporate the split-and-merge operation in handling long DFOS data that involve complex crack distributions.

(a)

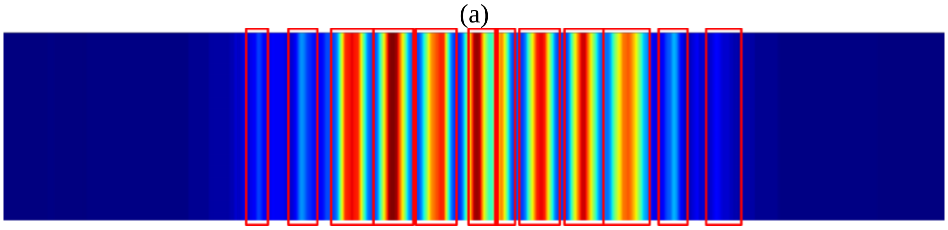

(b)

Figure 4.3.15. Detection results of the long fiber optic data: (a) directly using the trained deep learning model and (b) using the proposed split-and-merge approach in Section 2.7.

Based on the crack detection results, the opening widths of 103 cracks were quantified. The performance of crack quantification was evaluated using the coefficient of determination (R^2) in the range of 0 to 1, and 1 means no error. The evaluation results are shown in Figure 4.3.16. The value of R^2 was 0.998, indicating high accuracy.

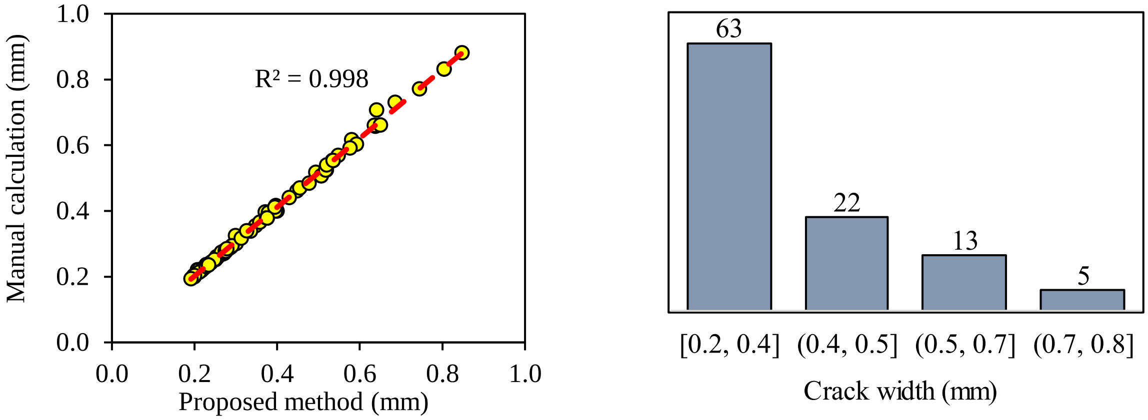

(a) (b)

Figure 4.3.16. Calculation results of crack width: (a) comparison between the calculated results by the proposed method and the manual calculated results, and (b) statistics of the calculated results.

In addition to the quantification of crack widths, the proposed method enabled the statistical analysis of crack patterns, as shown in Figure 4.3.16(b). The results showed that 61% cracks were finer than 0.4 mm, demonstrating the capability of the proposed approach to detect small cracks.

The capabilities of detecting, locating, and quantifying cracks facilitate the visualization of cracks, as shown in Figure 4.3.17. In the experiment, the minimal and maximum widths of the detected cracks were 0.19 mm and 0.85 mm, respectively. The detected cracks and their widths can be visualized.

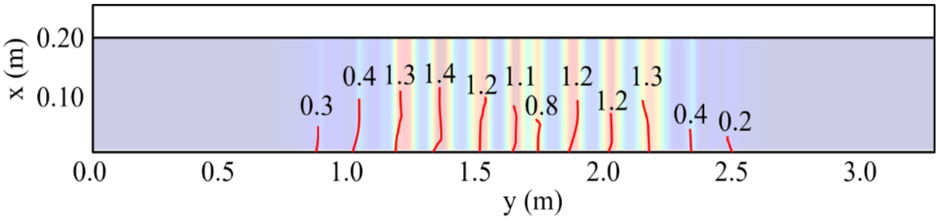

Figure 4.3.17. Mapping cracks and their widths. Red lines represent detected cracks. The numbers on the top represent the crack width and the unit is millimeter.

4.3.9.3. Discussion on generalization performance

The generalization performance of the proposed approach was tested using 10 new datasets. The first 5 datasets were obtained from a tensile test, as shown in Figure 2.3.1. A crack was manipulated by using two bars which could slide along two U-shaped channels. The crack widths ranged from 0.05 mm to 2.53 mm. The spatial resolution and coating thickness of DFOS have a significant effect on the monitoring of cracks. In the tensile tests, different spatial resolutions were considered, including 0.65 mm, 1.30 mm, and 2.60 mm. The use of different spatial resolutions generated three DFOS datasets. The use of different coating thicknesses of fiber optic cables (650 μm and 900 μm) generated two DFOS datasets. Five other datasets were generated by adding Gaussian white noises to the test data from the tests. Five noise-to-signal ratios of Gaussian white noise were considered, which are 1%, 2%, 3%, 4%, and 5%.

The performance of the proposed approach in crack detection and crack width quantification tasks is shown in Table 4.3.3. The performance of the proposed approach in the beam tests was used as the baseline. When the new datasets were analyzed using the trained model, the high values of the F1 score, mAP@0.5, mAP@0.5:0.95, and R^2 were retained, revealing that the proposed approach is robust to the use cases involving different spatial resolutions, fiber optic cables, and environmental noises. The minimal detected crack width was 0.05 mm.

Table 4.3.3. Generalizability of the proposed approach on crack detection and quantification

No.	Source of the dataset	Spatial resolution (mm)	Coating thickness (μm)	mAP@0.5	R^2
/	Baseline	0.65	1,332	0.968	0.998
1	Tensile experiment	0.65	242	0.965	0.994
2	Tensile experiment	1.30	242	0.978	0.997
3	Tensile experiment	2.60	242	0.965	0.995
4	Tensile experiment	0.65	650	0.975	0.996
5	Tensile experiment	0.65	900	0.981	0.998
6	Baseline + 1% noise	0.65	1,332	0.965	0.997
7	Baseline + 2% noise	0.65	1,332	0.962	0.990
8	Baseline + 3% noise	0.65	1,332	0.960	0.986
9	Baseline + 4% noise	0.65	1,332	0.957	0.981
10	Baseline + 5% noise	0.65	1,332	0.955	0.972

4.3.10. Summary

This project developed a deep learning approach to intelligently monitoring and interpreting spatially-distributed cracks based on strain distributions measured from DFOS in real time. Based on the above investigations, the following conclusions are drawn:

- The improved YOLOv5 model successfully detected spatially-distributed cracks based on the strain distributions measured from DFOS. The results of F1 score, mAP@0.5, and mAP@0.5:0.95 of the improved YOLOv5 model were respectively 0.936, 0.968, and 0.894. The average processing time of 10,000 strain data was shorter than 0.05 s. The modification of the YOLOv5 model improved the performance in terms of accuracy and efficiency. The improvement was attributed to the addition of transformer blocks and the simplification of the neck and head. The improved YOLOv5 model also outperformed eight other advanced deep learning methods.
- The incorporation of the transfer learning method improved the accuracy of the improved YOLOv5 model. The improvement was attributed to the addition of simulation data of strain distributions that increased the total number of data instances from 1175 to 4600. The mAP@0.5 was increased from 0.959 to 0.968. The improvement indicates that the

proposed transfer learning method can transfer useful features from the simulation data to the experimental data.

- The proposed approach was applied to quantify the opening widths of 103 cracks. The R^2 value was 0.998, indicating that the proposed approach accurately quantified the crack widths. In this research, the crack widths were in the range of 0.05 mm to 0.85 mm. Further research is necessary to test the performance of the proposed approach for the measurements of a wider range of crack widths.
- The robustness of the proposed approach was evaluated in different test scenarios with different types of test setup, specimens, crack patterns, and fiber optic cables. The crack detection performance was retained with an mAP@0.5 of 0.985. In addition, five types of Gaussian white noises were added into the beam testing data to evaluate the performance of the proposed approach under environmental variations. The mAP@0.5 was higher than 0.955, revealing that the proposed approach was robust to noises.

5. Papers Generated

5.1 Journal papers (published)

A total of 20 peer-reviewed journal papers have been published in highly-ranked journals in the fields of measurement, signal processing, automation, structural health monitoring, and machine intelligence. The published journal papers are listed below:

[1] Liu, Y. and Bao, Y.* (2024), "Intelligent monitoring of corrosion using distributed fiber optic sensors assisted by deep learning." *Measurement*. 226, 114190. https://doi.org/10.1016/j.measurement.2024.114190 (JCR: Q1, IF: 5.6)

[2] Xu, L., Shi, S., Huang, Y., Yan, F., Yang, X. and Bao, Y. (2024). “Corrosion monitoring and assessment of steel under impact loads using discrete and distributed fiber optic sensors.” *Optics & Laser Technology*, 174, p.110553. https://doi.org/10.1016/j.optlastec.2024.110553 (JCR: Q1, IF: 5)

[3] Liu, Y. and Bao, Y.*, (2023). “Intelligent monitoring of spatially-distributed cracks using distributed fiber optic sensors assisted by deep learning.” *Measurement*, 220, p.113418. https://doi.org/10.1016/j.measurement.2023.113418 (JCR: Q1, IF: 5.6)

[4] Liu, Y. and Bao, Y., (2023). “Automatic interpretation of strain distributions measured from distributed fiber optic sensors for crack monitoring.” *Measurement*, 211, p.112629. https://doi.org/10.1016/j.measurement.2023.112629 (JCR: Q1, IF: 5.6)

[5] Tan, X., Mahjoubi, S., Zou, X., Meng, W. and Bao, Y., (2023). “Metaheuristic inverse analysis on interfacial mechanics of distributed fiber optic sensors undergoing interfacial debonding.” *Mechanical Systems and Signal Processing*, 200, p.110532. https://doi.org/10.1016/j.ymssp.2023.110532 (JCR: Q1, IF: 8.4)

[6] Xu, L., Shi, S., Yan, F., Huang, Y. and Bao, Y., (2023). “Experimental study on combined effect of mechanical loads and corrosion using tube-packaged long-gauge fiber Bragg grating sensors.” *Structural Health Monitoring*, p.14759217231164961. https://doi.org/10.1177/14759217231164 (JCR: Q1, IF: 8.4)

[7] Liu, Y. and Bao, Y., (2023). “Real-time remote measurement of distance using ultra-wideband (UWB) sensors.” *Automation in Construction*, 150, p.104849. https://doi.org/10.1016/j.autcon.2023.104849 (JCR: Q1, IF: 10.3)

[8] Xu, L., Zhang, D., Huang, Y., Shi, S., Pan, H. and Bao, Y., (2022). “Monitoring epoxy coated steel under combined mechanical loads and corrosion using fiber Bragg grating sensors.” *Sensors*, 22(20), p.8034. https://doi.org/10.3390/s22208034 (JCR: Q2, IF: 3.9)

[9] Yan, M., Tan, X., Mahjoubi, S. and Bao, Y.* (2022), "Strain transfer effect on measurements with distributed fiber optic sensors." *Automation in Construction*, 139, p.104262. https://doi.org/10.1016/j.autcon.2022.104262 (JCR: Q1, IF: 10.3)

[10] Mahjoubi, S., Tan, X. and Bao, Y.* (2022), "Inverse analysis of strain distribution sensed by distributed fiber optic sensor subject to strain transfer." *Mechanical Systems and Signal Processing*, 166, p.108474. https://doi.org/10.1016/j.ymssp.2021.108474 (JCR: Q1, IF: 8.4)

[11] Tan, X., Guo, P., Zou, X., and Bao, Y.* (2022), "Buckling detection and shape reconstruction using strain distributions measured from a distributed fiber optic sensor." *Measurement*, 200, p.111625. https://doi.org/10.1016/j.measurement.2022.111625 (JCR: Q1, IF: 5.6)

[12] Liu, Y. and Bao, Y., (2022). “Review on automated condition assessment of pipelines with machine learning.” *Advanced Engineering Informatics*, 53, p.101687. https://doi.org/10.1016/j.aei.2022.101687 (JCR: Q1, IF: 8.8)

[13] Bai, H., Guo, D., Wang, W., Tan, X., Yan M., Chen, G., and Bao, Y.* (2022), " Experimental investigation on flexural behavior of steel-concrete composite floor slabs with distributed fiber optic sensors." *Journal of Building Engineering*, 54, p.104668. https://doi.org/10.1016/j.jobe.2022.104668 (JCR: Q1, IF: 6.4)

[14] Tan, X., Bao, Y.*, Zhang, Q., Nassif, H., and Chen, G., (2021), "Strain transfer effect in distributed fiber optic sensors under an arbitrary field." *Automation in Construction*, 124, p.103597. https://doi.org/10.1016/j.autcon.2021.103597 (JCR: Q1, IF: 10.3)

[15] Tan, X., Abu-Obeidah, A., Bao, Y.*; Nassif, N., and Nasreddine, W., (2021), "Measurement and visualization of strains and cracks in CFRP post-tensioned fiber reinforced concrete beams using distributed fiber optic sensors." *Automation in Construction*, 124, p.103604. https://doi.org/10.1016/j.autcon.2021.103604 (JCR: Q1, IF: 10.3)

[16] Tan, X., Bao, Y.* (2021), "Measuring crack width using a distributed fiber optic sensor based on optical frequency domain reflectometry." *Measurement*, 172, p.108945. https://doi.org/10.1016/j.measurement.2020.108945 (JCR: Q1, IF: 5.6)

[17] Tan, X., Fan, L., Huang, Y. and Bao, Y.* (2021), "Detection, visualization, quantification, and warning of pipeline corrosion using distributed fiber optic sensors." *Automation in Construction*, 132, p.103953. https://doi.org/10.1016/j.autcon.2021.103953. (JCR: Q1, IF: 10.3)

[18] Liu, Y. and Bao, Y., (2021). "Review of electromagnetic waves-based distance measurement technologies for remote monitoring of civil engineering structures." *Measurement*, 176, p.109193. https://doi.org/10.1016/j.measurement.2021.109193 (JCR: Q1, IF: 5.6)

[19] Mahjoubi, S., Barhemat, R., Guo, P., Meng, W. and Bao, Y., (2021). "Prediction and multi-objective optimization of mechanical, economical, and environmental properties for strain-hardening cementitious composites (SHCC) based on automated machine learning and metaheuristic algorithms." *Journal of Cleaner Production*, 329, p.129665. https://doi.org/10.1016/j.jclepro.2021.129665 (JCR: Q1, IF: 11.1)

[20] Fan, L., Tan, X., Zhang, Q., Meng, W., Chen, G. and Bao, Y.* (2020), "Monitoring corrosion of steel bars in reinforced concrete based on helix strains measured from a distributed fiber optic sensor." *Engineering Structures*, 204, p.110039. https://doi.org/10.1016/j.engstruct.2019.110039 (JCR: Q1, IF: 5.5)

5.2. Journal papers (under review)

In addition to the above 20 published journal papers, 2 peer-reviewed journal papers have been submitted for peer review. These journal papers are listed below:

[21] Tan, X., Poorghasem, S., Huang, Y., Feng, X., Bao, Y., "Monitoring of pipelines subjected to interactive bending and dent using distributed fiber optic sensors." Automation in Construction. Revised version under review.

[22] Tan, X., Du, J., Zhang, Q., Meng, W., and Bao, Y., (2023). "Monitoring restrained shrinkage and cracks of ultra-high-performance concrete (UHPC) using distributed fiber optic sensors." Construction and Building Materials. Revised version under review.

5.3. Conference proceedings and presentations

Besides the journal papers, 5 conference papers have been published, and all these papers have been presented in those conferences. The 5 conference papers are listed below:

[1] Tan, X., Xu, L., Huang, Y. and Bao, Y., (2020), "Distributed fiber optic sensor network (DFOS) for real-time monitoring of pipeline interactive anomalies", *2020 Pipeline Research & Development: Meetings - Forums*, PHMSA.

[2] Tan, X. and Bao, Y. (2021), "Achieving resilient and smart concrete bridges by mapping strains and cracks using distributed fiber optic sensors", *23rd Annual NJDOT Research Showcase*, New Jersey Department of Transportation, New Jersey.

[3] Tan, X. and Bao, Y. (2022), " Crack detection, location, quantification, and visualization using a distributed fiber optic sensor based on optical frequency domain reflectometry", *Engineering Mechanics Institute (EMI) Conference 2022*, ASCE, Georgia Tech, GA.

[4] Liu, Y. and Bao, Y. (2022). "Locating pipeline leakage using machine learning and network topology images." 2022 PRCI Research Exchange Meeting (REX2022), March 8-9, 2022, Orlando, Florida.

[5] Liu, Y. and Bao, Y. (2022). "Achieving sub-millimeter accuracy in displacement measurement from ultra-wideband (UWB) radio incorporating machine learning." The 13th International Workshop on Structural Health Monitoring (IWSHM), March 15-17, 2022, Stanford, CA.

Appendix: Literature review

A literature review was performed on existing pipeline detection methods and applications in the pipeline industry. The emphasis of the review was placed on understanding the strengths and limitations of existing methods, and identifying the challenges of monitoring interactive defects.

Pipelines are critical assets to the economy of the nation and security of modern communities [128]. Pipelines are considered the most preferred method of transportation of energy products and water from the economic, safety, and environmental points of view [129]. The total length of existing pipelines is phenomenal. Worldwide existing pipelines are more than 2 million miles (3.2 million km), and the fatalities due to accidents per ton-mile of petroleum products are respectively 87%, 4%, and 2.7% lower than those transported using truck, ship, and rail [130]. Thus, pipelines have been seen as the safest and most widely installed infrastructure [131].

However, pipeline incidents can cause serious ecological issues, casualties, and financial loss, particularly when the detection of pipeline leakage is delayed. According to PHMSA, there were more than 11,900 pipeline incidents in the U.S. in the past 20 years, which costed nearly $8.4 billion, killed over 300 people, and caused over 1300 injuries [132]. Unexpected pipeline failure can occur when the time dependent integrity threats are coupled with stable anomalies. ASME B31.8S identified nine primary threat conditions, which fall into three main categories: time-dependent threats (external, internal, and stress corrosion), stable threats (manufacturing, fabrication or construction, and equipment), and time-independent (third party or mechanical impacts, incorrect operations, environment-related/outside forces) [133].

Historical pipeline failures indicate that there are multiple factors that lead to pipeline failure [134]. Individual threats can be at “acceptable” levels, but there are circumstances when two or more anomalies occur coincidentally and interact with each other, causing serious consequences. Many pipeline incidents result from interactive anomalies which tend to cause more severe damages or pipeline failure greater than individual anomalies and the superposition of individual anomalies [135]. An example is earth movement exacerbating construction-related imperfections such as wrinkle-bends or certain vintages of girth welds. Either of these two conditions, absent the other, may not be a significant threat to pipeline safety. However, when they are both present at the same location, the resulting condition could be a concern [136]. Another example is the loss of corrosion protection, meaning a combination of aging coating, aggressive environment, and rapid corrosion growth that may lead to failure. This type of failure is not simply a corrosion failure, but a corrosion control system failure. Similar observations can be drawn for failures due to external interference and stress corrosion cracking [137]. Time-independent and time-dependent threats may also interact with resident threats on pipelines [138], such as:

- Corrosion can initiate from deficits due to manufacturing imperfections or damage
- Flooding in the area near pipeline right-of-way (ROW) can cause defects
- External corrosion and latent third-party damage
- Stress corrosion cracking at bottom side dents and/or at narrow axial external corrosion
- Fatigue at defects

Based on these analysis, it is difficult to eliminate pipeline incidents due to the diverse causes [139]. To mitigate the impacts of pipeline incidents, it is important to monitor pipelines for timely detection of breaches of integrity, as early detection of threats will allow quick responses, hence reducing the loss rate, injuries, and other social and environmental consequences due to pipeline failures [140]. In this project, a survey of pipeline integrity assessment methods was conducted based on IM regulations which allow four types of methods [141]:

- ILI: ILI is an internal pipeline inspection technique that uses magnetic flux leakage, ultrasound, eddy current, or other technologies to locate and characterize indications of defects, such as metal loss or deformation. The sensors are mounted on a device (known as a "smart pig"), which is inserted into a pipeline segment between a launching station and a receiving trap. The device moves through the pipe, scanning the pipe for specific types of defects. Pipeline segments that can accommodate ILI tools are considered "piggable". Different sensors have been used to detect different defects [142].
- Pressure testing: A pressure test can be used as a strength or leak test. A common type of pressure test is a hydrostatic test, which involves taking the pipeline out of service and pressurizing a section of pipe with water to a much higher percentage of the pipe material's maximum design strength than the pipe will ever operate at with natural gas. This verifies the capability of a pipeline to safely operate at the maximum allowable operating pressure and can reveal weaknesses that could lead to defects and leaks in the pipe. Pressure testing of pipelines is designed to find critical seam defects (as well as other defects caused by corrosion, stress corrosion cracking, and fatigue) by causing the pipe to fail at these critical defect locations [143].
- Direct assessment: Direct assessment relies on the examination of the pipeline at pre-selected locations to evaluate a pipeline for external corrosion, internal corrosion, or stress corrosion cracking threats. Most of the pipeline segment being inspected is usually not directly examined. Direct assessment uses multiple steps (four steps for external and internal corrosion, and two steps for stress corrosion cracking). For example, for external corrosion direct assessment, the steps are (NACE 2008): pre-assessment (the operator determines the feasibility of external corrosion direct assessment, determines external corrosion direct assessment regions, and selects tools for indirect inspection), indirect inspection (the operator conducts above-ground inspections, such as a close interval survey, to identify and classify indicators of corrosion and pipe coating defects), direct examination (the operator excavates the pipe at selected locations to measure actual corrosion damage), and post-assessment (the operator determines reassessment intervals and evaluates the effectiveness of the direct assessment process). This method requires the identification of regions within the pipeline segments for excavation and direct examination. Therefore, although a pipeline segment is inspected with direct assessment, typically only several small sub-segments, which are selected based on the corrosion severity prioritized by the indications from indirect inspection, are examined [144].
- Other technologies: These technologies include methodologies that follow performance requirements with documentation or methods that are industry-recognized, approved, and published by an industry consensus standards organization. A staggering number of different technologies are available and are being developed for inspection and monitoring

of pipelines, such as sensor technologies, which cover a wide range of physical principles, including electrical, optical, radiographic, chemical, and acoustic domains [145].

The above methods have been used successfully to prevent, detect, and mitigate the pipeline threats individually, but the same level of guidance is not as readily available for real-time monitoring of interactive anomalies [146]. Most methods focused on threats independent of each other, and only examines a small part of pipeline segment, which may result in overlooking the potentially more damaging effect of interactive anomalies, the result of which is more damaging than either of the individual threats themselves [147, 148]. For example, ILI tools can only consider “piggable” pipeline segments, which means not all pipelines contain a suitable ILI tool launcher and/or receiver [149]. Another problem is that the typical pipeline segment is roughly 50-100 miles long. Some pipelines are longer. Therefore, ILI is a tool for pipeline inspection, and it cannot be used for real-time monitoring of pipelines [150]. Moreover, intelligent pigs require a clean pipeline to function correctly, which means debris or obstruction in the line could lead to a stuck pig [151]. At the same time, there are weaknesses of pressure testing and direct assessment: pressure testing is a kind of destructive method; direct assessment involves multiple steps and only examines a small sub-segment of pipeline [152, 153].

In this project, an important task is to review promising inspection and real-time monitoring technologies for interactive anomalies of pipeline, such as fiber optic sensors [154, 155], acoustic emission [156, 157], ultrasonic [158, 159], ground penetration radar [160, 161], and infrared thermography [162, 163]. Research gaps and future research issues that required attention in the field of real-time monitoring for pipeline interactive anomalies are discussed.

Reviewed methods

Various inspection methods for real-time monitoring for pipeline anomalies were reviewed. These methods have been classified into hardware- and software-based methods [164, 165], or classified into direct methods, indirect methods, and other methods [166]. The methods have been classified based on different working principles: electromagnetic, acoustics, vibrations, robots, and fiber optic sensors [167]. A detailed classification of these methods is shown in Figure A1.

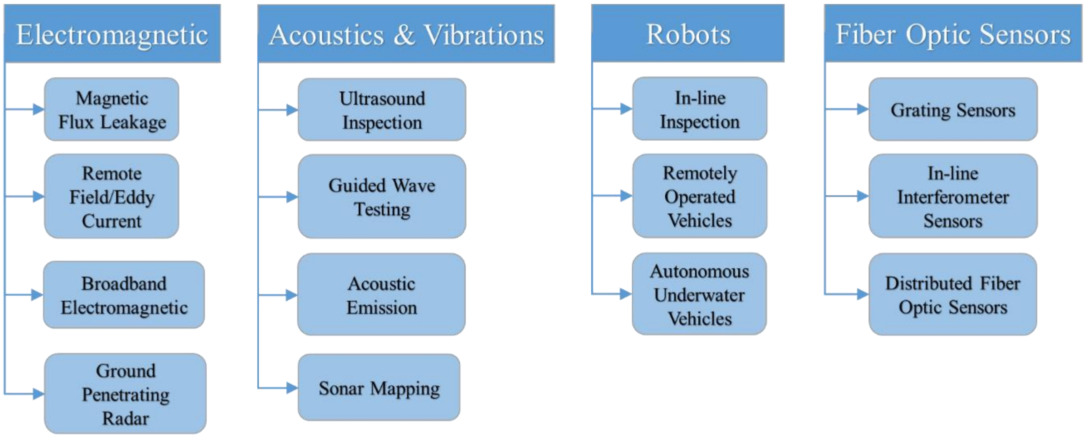

Figure A1. Flow chart of real-time monitoring methods for interactive anomalies.

The following sections attempt to cover the most commonly used sensor technologies while also including recent research into sensor advancements. The review begins with sensors that rely on electromagnetic phenomena. Thus, this section focuses on magnetic flux leakage (MFL), eddy current sensing, broadband electromagnetic, and ground penetrating radar (GPR). Then, the review focuses on the inspection technologies that rely on acoustics and vibrations, including ultrasonic inspection, guided wave testing (GWT), acoustic emission (AE) and sonar mapping, respectively. Finally, ILI is reviewed as robot technologies. The operational principle, strengths and weaknesses of these methods are discussed in the subsequent sections.

Electromagnetic methods

Magnetic flux leakage (MFL)

MFL method uses strong, powerful magnets to induce a saturated magnetic field around the wall of a ferrous pipe. If the pipe is in good condition, a homogeneous distribution of magnetic flux is obtained; however, anomalies will alter the distribution of the magnetic flux. The damaged areas cannot support as much magnetic flux as undamaged areas, resulting in an increase of the flux field at the damaged areas [168]. In other words, a damaged pipe causes a flux leakage. This aberration is referred to as the leakage, hence the name magnetic flux leakage. The properties of the leaked magnetic field can provide information about the cause of leakage. By scanning the surface systematically, defects in a pipeline can be detected and mapped out. Depending on the application, three different methods for magnetizing the pipe wall are available: direct current (DC) magnetization, alternating current (AC) magnetization, and permanent magnets [169].

AC magnetization in an external circuit is used to generate an oscillating magnetic field across the pipe surface. Due to its oscillating nature, eddy currents, which produce an opposing magnetic field, will be generated (i.e., the “skin effect”). The skin effect limits the magnetic field to a smaller area and also prevents the field from penetrating deeper into the pipe wall [170]. However, devices based on AC current are readily available, low cost, and easy to control. Due to low surface penetration, AC magnetization is mainly used for surface and near-surface inspection.

In DC magnetization, a unidirectional magnetic field is generated and can penetrate more than 10 mm into a pipe surface. As the residual magnetic field may interfere with other electronic components (e.g., using other electronic sensors in the future) or with any welding process (e.g., before the pipe segment is welded to the pipeline during the pipe-laying process), demagnetization of the pipe wall may be needed after using DC magnetization.

Permanent magnets are the most commonly used method for pipe wall magnetization. The penetration of magnetic fields generated by permanent magnets is similar to those of DC magnetic fields. The high energy density of rare earth magnets allows for small-sized magnets and coupled with the fact that no power is needed, make permanent magnets popular for MFL.

Although primarily used to detect corrosion, MFL tools can also be used to detect features that were not originally designed to identify [171]. The modern High Resolution MFL tool is proving to be able to accurately assess the severity of corrosion features, define dents, wrinkles, buckles, and, in some cases, even cracks. There are cases, where large non-axial oriented cracks have been found in a pipeline that was inspected by a magnetic flux leakage tool [172-174].

Advantages of MFL sensors in real-time monitoring of pipeline interactive anomalies is that the testing mode is non-invasive and accurately detects any kind of metal loss in a pipeline including cracks, corrosion, and the thinning of pipe walls [175]. Owing to their robust magnetic and sensor designs, MFL inspection devices ensure an excellent anomaly detection performance, even under harsh operating conditions [176].

Despite the advantages that make MFL a popular tool for pipeline inspection, there remain some drawbacks that are still subjects of research:

a) MFL is usable only on ferrous pipes and requires access to the surface of the pipe [177].

b) MFL measurements are influenced by the dimensions of the MFL tool, including the distance between magnet poles, speed of the pig, and quality of the brushes [178, 179].

c) External factors such as the strength of magnetic field in the pipe wall, reading experience, and debris in pipeline affect the MFL readings [180]. The strength of the applied magnetic field should be adjusted based on the pipe wall, with thick walls requiring stronger fields in order to reach full saturation. Reading MFL signals requires skill and experience. The distance of MFL tool to surface can also be affected by debris, further complicating interpretation of measurements.

d) The orientation of the defect along the pipe also affects the sensitivity of the MFL tool in detecting defects [181]. If the magnetic field direction is parallel to the defect shape, the magnetic field may not be deflected adequately to detect the anomaly.

Eddy current sensing

Eddy currents are another common non-destructive testing tool and are useful for crack detection and material thickness measurements. Eddy currents are circular patterned electrical currents due to changes of a magnetic field passing perpendicularly to the conductor. A varying magnetic field can be created by passing an alternating current into a coil. When the varying magnetic field penetrates the target inspection surface, induction occurs, and eddy currents are generated in the surface material. Due to their circular path, the eddy currents in the pipe wall produce a secondary magnetic field which is opposed to the primary field inducing it. Anomalies in the pipeline, such as cracking or corrosion, leads to a change of flow direction of eddy current, and then causes disruptions in the eddy current. Based on this effect, anomalies can be detected, and their properties determined by evaluating the amplitude and the phase shift between the input and output signals [182]. Several different methods are available: conventional eddy current, remote field eddy current (RFEC) [183], pulsed eddy current (PEC) [184], Lorentz force eddy current (LEC), and magnetic eddy current (MEC) [185].

RFEC is a method using low-frequency alternating current whose main application is finding defects in steel pipes and tubes. The main differences between RFEC and conventional eddy current is in the coil-to-coil spacing. The RFEC probe has widely spaced coils to pick up the through-transmission field. The conventional eddy current probe has coils or coil sets that create a field and measure the response within a small area, close to the object being tested. In PEC, the coil is electrified using a current following a pulse or step function, thus effectively exciting multiple frequencies simultaneously.

With the introduction of strong permanent magnets, eddy currents can be generated by relative motion between a constant magnetic field (e.g., a permanent magnet) and the pipeline surface. Lorentz forces are generated against the conductive metal of the pipe wall as the conductor moves relative to a magnetic field. By measuring the push back force on the magnet, defects can be detected in a pipeline. This process is generally called LEC testing.

MEC method introduces a magnetic field (in a similar manner as MFL) that can increase the effective measurement depth of eddy current inspection. Magnetization of the ferromagnetic pipeline material decreases the permeability of the pipe wall and thus increases the penetration depth of the eddy current.

In-line inspection tools equipped with an eddy currents detection system are considered in the industry as reliable inspection devices with high sensitivity and accuracy for the detection of internal corrosion, especially when combined with a geometry sensor for scanning the pipe surface for geometric anomalies such as dents [186]. RFEC seems to be the prevailing technology in the drinking water industry for inspection of ferromagnetic pipes and ferromagnetic components in composite pipes [187]. For example, the commercial RFEC systems are widely used for detecting broken wires in prestressed concrete pipes [188]; the See Snake tool is applied to small-diameter ferromagnetic pipes [189]; what’s more, the PipeDiver RFEC tool can be used to inspect large-diameter ferromagnetic pipes [190]. The Commercial PEC system has been used for inspection of insulated pipe/vessels in chemical plants and the oil and gas industry [191].

The advantages of the technology in real-time monitoring of interactive anomalies include:

a) The technology does not require the sensors to be in contact with a pipe wall [192].
b) RFEC can work in nonferromagnetic materials such as copper and brass [193].
c) PEC allows the interrogation of multiple depth layers at the same time [194].
d) The inspection tool is compact and can be easily deployed by remotely operated vehicles [195].
e) Compared with MFL, less power is needed for MEC (about 10 kA/m for MFL versus 3 kA/m for MEC). The synergy with the eddy current system means that greater distances can be inspected for a lower energy cost [196, 197].

A drawback of the eddy current is that the penetration depth is dependent on the AC frequency of the coil. The penetration depth decreases with frequency. Thus, with operations normally at higher frequencies, the eddy current method is limited to skin-level defects. While low-frequency excitation can provide additional depth, the energy required to maintain the excitation may be prohibitive [198].

Broadband Electromagnetic (BEM)

Unlike the conventional eddy current technique, which uses a single frequency for testing, the broadband electromagnetic technique transmits a signal that covers a broad frequency spectrum ranging from 50 Hz to 50 kHz [199]. A transmitter coil passes an alternating current to the pipe surface, which generates an alternating magnetic field. The alternating magnetic field induces a time varying voltage on the metallic pipe wall. This voltage produces eddy currents in the pipe wall, which induce a secondary magnetic field. Wall thickness is indirectly estimated by measuring signal attenuation and phase delay of the secondary magnetic field [200].

BEM technology has been used for condition assessment of water mains [201]. Commercial BEM system now is available to measure corrosion pits [202]. The BEM system is being further modified to facilitate the inspection of pipes exposed in keyhole excavations. This will help acquire information about pipe condition without disrupting service or full access excavations [203].

Compared with other electromagnetic inspection methods, advantage of application of BEM in real-time monitoring of pipeline is that BEM is immune to electromagnetic interference and differs from other electromagnetic inspection methods due to its frequency independence [204].

A primary drawback is that it can only be used on ferrous materials to measure wall thickness, quantify graphitization, and locate broken wires in prestressed concrete cylinder pipes [205].

Ground Penetrating Radar (GPR)

GPR is a non-invasive high-resolution instrument which utilizes electromagnetic wave propagation and scattering techniques to detect alterations in the magnetic and electrical properties of soil in the pipeline surrounding [206]. GPR antennae transmit electromagnetic wave pulses into the ground. The propagation of electromagnetic waves in soils is governed by parameters such as permittivity, magnetic permeability and conductivity. The occurrences of leaks increase the moisture content of the soil nearby and cause dielectric variation. Reflections occur at the interfaces between media with different electrical properties. The time lag between the transmitted and reflected waves determines the depth of the objects. The reflections are detected by a receiving antenna and subsequently interpreted [207]. A three-dimensional GPR image is obtained using the raw field data after significant work of software processing.

From the perspective of system design, GPR falls into three main categories [208]: (1) Time domain: impulse GPR. (2) Frequency domain: frequency modulated continuous waveform, stepped frequency continuous waveform, and noise-modulated continuous waveform GPR. (3) Spatial domain: single frequency GPR.

The GPR has proved impressive potential as an effective non-destructive tool for detecting underground objects [209]. Conventional GPR systems are operated from the ground surface. In-pipe GPR systems were also reported [210]. Such systems use two or three antennae with different frequencies to investigate the structure of the surrounding soil, the interface between the soil and pipe, and the structure of the pipe. A prototype ground penetrating imaging radar (GPIR) was recently developed within a European Commission supported project “WATERPIPE” [211]. The capabilities of this high resolution GPIR reportedly include: (1) detecting leaks and damages in water pipelines of all types of materials; (2) penetrating the ground to a depth of up to 200 cm; (3) image resolution of less than 50 mm.

GPR can potentially identify leaks in buried liquid pipes either by detecting underground voids created by the leakage or by detecting anomalies in the depth of the pipe as the radar propagation velocity changes due to soil saturation with leakage [212].

However, GPR signals can be corrupted by environmental noise [213]. The effectiveness of GPR may be significantly reduced for buried pipelines, depending on the depth of the pipe and the use of covering media such as concrete. Similarly, the operation is limited to a clay soil environment as iron pipe corrosion materials can hide cast iron pipelines from the GPR. In addition, they are not applicable for long pipeline networks [214].

Acoustics and Vibrations

Ultrasonic inspection

Ultrasonic testing is a non-destructive test method that utilizes sound waves to detect anomalies such as cracks, inclusions and laminations in parts and materials. It can also be used to determine a material’s thickness, such as measuring the wall thickness of a pipe to monitor pipeline corrosion [215].

The ultrasonic module to monitor pipeline corrosion is based on the measurement of the time-of-flight of ultrasonic signals reflected from internal/external surfaces of the pipe wall and flaws [216]. With a knowledge of the speed of sound in the liquid and in the pipe wall, it is relatively straightforward to determine the distances between the transducer and the inner and outer pipe walls and thereby determine the thickness of the pipe wall.

A typical ultrasonic crack detection inspection system consists of several transducers operated in an impulse-echo mode acting as both emitter and receiver. Slanted probes are used to ensure that the incident ultrasound signals are refracted in a manner such that they will propagate under 45° inside the pipe [217]. After emitting an ultrasonic testing pulse, each transducer listens for echoes originating from discontinuities in the pipe wall. Partial reflection of the ultrasound occurs at interfaces, such as the interface between two different materials, or cracks, inclusions and laminations in a homogeneous medium. External and internal crack echoes and their amplitudes can be assigned to associated time-of-flights. Reflected signals will be transformed into an electrical signal. Information about location, size and orientation received from the signals can be determined. Ultrasonic crack detection tools are designed for the detection of either circumferential or axial cracks [218].

Ultrasonic sensors are typically used in several configurations. As a single crystal, the sensor can be used to emit an unfocused, divergent beam of ultrasound along a straight trajectory. With multiple crystals, the sensors can form a sensing array that can reconstruct a cross-sectional image of the monitored structure. Furthermore, by adjusting the time delay of when each crystal emits the ultrasound wave, the overall wave front can be steered in order to cover a larger area and detect a wider range of defect orientations [219]. For example, efforts with an array of ultrasonic transducers have recently aimed to achieve online monitoring of pipeline wall thickness, and thus corrosion and erosion using ultrasound transducers can be permanently installed, and a map of a section of pipeline wall can be monitored [220].

Another widely used technique for ultrasound-based sensing is time-of-flight-diffraction [221]. In time-of-flight-diffraction, two ultrasound arrays are used as a transmitter and receiver, respectively. Instead of measuring only the reflection of the ultrasound waves, the time-of-flight diffraction technique also measures the effects of wave diffraction due to the edges/tips of defects in the pipe material. The expected signals come from lateral waves, which travel along the surface, and from the reflection of the wave from the opposing surface of the pipe wall. If a defect is present between the transmitter and receiver, then additional waves will arrive between the lateral and backwall reflection arrival times. Because this method has higher power potential than other non-destructive test types, ultrasonic testing can produce images that are more clearly defined than other methods and indicate characteristics deeper than surface level. Ultrasonic testing services for a variety of industries, including oil, gas, power generation and water supply [222].

Although ultrasonic inspection techniques offer excellent resolution in spot checking pipelines for anomalies, the use of these techniques for inspecting an entire pipeline is time consuming and expensive [223]. In addition, removal of pipeline coating is required for inspection, which makes point by point ultrasonic inspection become a more formidable problem [224]. It is promising to incorporate ultrasonic tools into ILI for inline inspection of pipelines.

Guided wave testing (GWT)

The guided wave technique (GWT) is based on the capability of propagating a wave over a long distance [225]. Guided waves are elastic waves that travel within a finite body. Elastic waves can be a combination of the fundamental longitudinal and shear waves, which can combine to form more complex types of waves (e.g., Rayleigh waves, Lamb waves, and Love waves) [226]. The propagation of the waves is guided by the geometry and boundary conditions of the body, hence the name “guided wave”. When these guided waves encounter an anomaly or pipe feature, laminar waves reflect back to the transducer’s original location (the transducers are used for both excitation and detection of the signals). The time-of-flight for each signature is calculated to determine its distance from the transducer. The amplitude of the signature determines the size significance of the defect.

Guided waves for pipeline inspection are usually generated in two ways. One way is using an array of angled piezoelectric transducers wrapped around the circumference of the pipeline. Another way is to use electromagnetic acoustic transducers (EMAT), which can excite guided waves through either the Lorentz or magneto strictive principles [227]. One of the key advantages of piezo-based transducers is the capability of generating stronger signals compared with EMATs. For EMATs, they do not require much surface preparation because they are non-contact and are not affected by non-metallic debris on the surface. What’s more, EMATs can be affected by any residual magnetic field in the pipeline and require more power than piezo-based transducers.

GWT can provide a much longer range (up to 100 m) inspection albeit at a lower resolution. Access to only a few points along the pipeline is required without the need to remove coatings for most of the pipeline [228]. The trade off in range and resolution is mainly due to the use of lower frequency waves (10–100 kHz) for GWT compared to the range of ultrasonic inspection [229]. Furthermore, the direction of the waves in GWT is also perpendicular to those used in ultrasonic inspection and will thus travel along the length of the pipeline [230]. Defects such as pipe wall thinning (e.g., due to corrosion), weld imperfections, cracks, and notches cause anomalous reflections with an amplitude that is proportional to the change in the cross-sectional area of the pipe at the defect [231].

For long-term monitoring, where the transducer array is permanently installed onto the pipeline, the use of a baseline (i.e., benchmark) is beneficial for detecting changes in the pipeline over time. The baseline signal can be effectively subtracted from the current signal to quantify changes. In this regard, index-based techniques have been developed to further provide insight into the pipeline status [232].

The guided wave system was originally designed for use on above-ground exposed or insulated pipes. It has been applied to buried and subsea pipes, but the range of inspection will be shorter due to the rapid attenuation of the signals [233]. To overcome this kind of weakness, recently, guided waves can be modulated using schemes such as pulse position modulation to encode information, which means a transducer can transmit a modulated guided wave through the pipeline to be received by another transducer further along the pipeline. Through a series of transmissions, information could theoretically be carried through the pipeline. Changes to the baseline of the transmission signal could also serve as a warning sign for damage in the pipeline. Such a communication method can allow a network of sensors to be permanently installed along a pipeline if there is power and a way to send and receive guided waves. Recent work in guided wave communications in different media is promising [234-236], and practical application to subsea pipelines is foreseeable in the near future.

Despite the advantages of GWT, there remain some drawbacks that inform further research:

a) Lower frequency waves can travel further than high frequency waves but are unable to effectively interact with small defects [237].
b) Guided wave signal is typically in the form of a pulse, and multiple excitation frequencies are inevitably involved, which may make signals from the desired mode drowned out by the coherent noise [238].
c) Viscous coatings such as bitumen and concrete will dampen the wave energy and limit the range of GWT [239].
d) The geometry of the pipe can also limit the range of GWT. Sharp bends in the pipeline can severely distort signals, and the selected mode can be converted to other propagation modes due to the change in geometry [240].
e) Welds, clamps and flanges will cause reflections that attenuate the energy of guided waves and thus limit the inspection range [241].
f) The presence of dispersion, scattering, and multiple modes can make data interpretation a difficult task [242].

Acoustic emission (AE)

According to American Society of Mechanical Engineering standard [243], acoustic emission (AE) is defined as "the class of phenomena whereby transient elastic waves are generated by the rapid release of energy from localized sources within a material, or the transient waves so generated". AE employs the release of localized stress energy within a pipeline structure (noise or vibration) due to several mechanical events, such as material failure, friction, cavitation, and impact, to detect the occurrence of pipeline leakage. By listening to these AE wave patterns with an array of dispersed sensors and by characterizing the wave pattern, the occurrence and severity of these events can be identified [244].

Acoustic methods for leak detection can be divided into two classes [245]: active and passive. Active methods detect pipeline defects by listening to the reflected echoes of sound pulses emitted due to leakage. On the contrary, passive methods detect defects by listening to changes in sound generated by pressure waves in the pipelines.

There are three major categories of acoustic sensors namely hydrophones, geophone and acoustic correlation techniques. Hydrophones require direct contact with hydrants and/or valves, while geophones listen to leaks on the surface directly above the pipeline. At the same time, steel rods can also be inserted into the buried pipe to transmit signals to mounted sensors on the rods. In acoustic correlation method, two sensors are required to be positioned on either side of the pipe to detect leakage. The time lag between the acoustic signals when the sensors sense a leak is used to detect and identify the point of leakage [246, 247].

The use of acoustic emission methods for pipeline leaks detection have been reported in several studies [248-250]. In addition, severe obstruction of the pipe lumen can be detected within several kilometers [251].

Experimental investigation of pipeline leakage subjected to socket joint failure using acoustic emission and pattern recognition was proposed in [252]. This indicates that acoustic emission-based methods can exhibit high sensitivity over long distances. Jia et al. conducted a gas leakage detection experiment on a gas pipeline length of 3.13 km using measured acoustic waves with the sensors positioned at different locations along the gas pipeline [253]. they concluded that applying acoustic emission for detecting leakage on pipeline networks can achieve early leaks detection, estimation of leak sizes and leak point localization [254]. Chen et al. demonstrated that small pipe leaks signal can be efficiently differentiated from noise and effectively localized. For prestressed concrete pipes, steel wires break release energy and cause a series of discrete events, which can be monitored by acoustic technics. As suggested by Shehadeh et al. [255], monitoring the AE, and thus the pipe stress, can be a method for real-time monitoring of the subsea pipeline. While such leakage detection research has not yet been deployed in subsea conditions, it is foreseeable that additional marinization redesigning of sensor and instrumentation components will be able to bridge the gap from lab testing to field implementation.

In general, the benefit of using acoustic emission for monitoring of pipeline network are easy utilization of interrogation and the convenience of installation as it does not require system shutdown for installation or calibration.

An important drawback is their high susceptibility to noise sources, such as system noises, environmental noises, radio chatter, wind, Doppler effects, etc. To eliminate system noises, various techniques, such as band pass filtering [256], Fast Fourier Transform (FFT) and time-averaging Wigner-Ville distribution [253], can be used. Acoustic sensors can be used along with other sensors to overcome these limitations.

Sonar mapping

Sonar refers to the use of sound waves underwater to detect objects, typically for navigation and mapping. In the pipe inspection field, it has been adapted to provide information about elements in the pipe that are submerged below the water line. These may include submerged debris in the pipe (sewers), grease level (sewers), differential settling and other submerged deformations and defects. A sonar system may consist of an underwater scanner unit, collapsible sonar siphon float, sonar processor/monitor, skid set, and all necessary interconnect cables [257]. Each pulse provides an outline of the cross-section of the submerged part of the pipe [258]. Accurate measurements can be performed based on these outlines.

The sonar profiling system can be used with different frequencies to achieve different goals [259]. High frequency sonar can provide a higher resolution scan, but a high-resolution pulse attenuates quickly and therefore has a relatively low penetration capability. In contrast, low frequency sonar has a high penetration capability but is limited in its scanning resolution. High frequency sonar can be suitable for clear water conditions, turbid water with high concentrations of suspended solids may require a lower frequency signal. Small defects are more likely to be observed by a high frequency signal.

A system that integrates multiple sonars for use in submerged and large semi-submerged pipelines is also available. The use of multiple sonars overcomes the disadvantages of using one sonar and one ping at a time to map. However, depending on the size of the sonar array, computational costs can become increasingly significant. Thus, although costing more than the use of a single sonar, the use of multiple sonars may save the costs for long-term monitoring [260].

Wideband sonars are capable of a multi-frequency (each frequency component backscatters differently depending on the material reflecting the pulse) scan to obtain maximum information. Advantages of wideband sonars include higher resolution and wide range for customization and optimization according to the situation [261]. Wideband sonar has been recently used to not only inspect the positioning of subsea pipelines, but also inspect whether flow is being obstructed in pipeline [263].

Regarding the drawbacks of sonar devices, they cannot be operated above and below the water line simultaneously and they cannot be used for gas pipes. In addition, the cost of sonar inspections varies depending on the diameter of the pipe to be inspected.

Robots

In-Line Inspection (ILI)

In the last few decades, pipeline inspection gauges (PIGs) have become more prevalent for ILI and non-destructive evaluation of the pipelines [263, 264]. The advanced versions of these autonomous systems, also called “smart pigs”, can move inside pipelines and measure irregularities that may represent corrosion, cracks, joints, deformation (e.g., dents, pipe ovality), laminations or other defects (e.g., weld defects) in the pipeline.

The most common ILI methods that have been installed on smart PIGs and confirmed to be successful for pipeline inspection are MFL [265], ultrasonic transducers [266], electromagnetic acoustic transducers (EMAT) [140] and eddy currents [267].

However, certain constraints seriously limit the applications of the aforementioned methods.

- In the MFL method, it is difficult to effectively saturate the entire cross section of the pipeline with magnetic flux, and the servicing process involves frequent calibration. Moreover, the method is not suitable to inspect non-ferrous pipelines [268, 269].
- The ultrasonic transducers method works well in liquid pipelines; however, the application in gas pipelines is not common since it requires liquid coupling between the transducer and the surface of the pipeline [270]. Ultrasonic transducer is more suitable for thick-wall pipelines rather than thin-wall pipelines (less than 7 mm) [271]. Echo loss is another major challenge reported in the literature [272].
- The EMAT method cannot be used in non-conductive materials such as plastics or ceramics, and it is not suitable for long pipeline inspection, which requires high power and complex signal processing in real-time [273]. This method faces challenges for high-speed scanning in pipelines, and it can be applicable up to 2.5 m/s [274].
- The eddy current method requires deep magnetic penetration in ferrous pipelines, and the major drawback is the spacing problem, which occurs while mounting the sensor array on the circumference of the smart pig [275, 276].
- Recently, a few ILI methods have been developed for the inspection of pipelines such as closed-circuit television (CCTV) [161] and mechanical contact probe (MCP) [277]. For CCTV methods, the high-power supply and lack of visibility inside the long pipelines are the drawbacks [278]. The MCP method can inspect only convex defects such as deposit corrosion. It is not suitable for cavity corrosion or metal loss corrosion, and the friction involved in the inspection process is a major risk [268].

References

[1] United States Department of Transportation, PHMSA. https://www.phmsa.dot.gov/safety-awareness/pipeline/historical-pipeline-incidents. Accessed on December 24, 2023.

[2] United States Department of Transportation, PHMSA. Data and Statistics Overview: https://www.phmsa.dot.gov/data-and-statistics/pipeline/data-and-statistics-overview. Accessed on December 24, 2023.

[3] United States Department of Transportation, PHMSA. https://www.phmsa.dot.gov/incident-reporting/accident-investigation-division/pipeline-failure-causes. Accessed on December 24, 2023.

[4] Pipeline Operation Forum. Specifications and requirements for in-line inspection of pipelines. 2016.

[5] Kishawy, H.A. and Gabbar, H.A., 2010. Review of pipeline integrity management practices. International Journal of Pressure Vessels and Piping, 87(7), pp.373-380.

[6] Liu, Z. and Kleiner, Y., 2013. State of the art review of inspection technologies for condition assessment of water pipes. Measurement, 46(1), pp.1-15.

[7] Vanaei, H.R., Eslami, A. and Egbewande, A., 2017. A review on pipeline corrosion, in-line inspection (ILI), and corrosion growth rate models. International Journal of Pressure Vessels and Piping, 149, pp.43-54.

[8] National Transportation Safety Board. 2015. Integrity Management of Gas Transmission Pipelines in High Consequence Areas. Safety Study NTSB/SS-15/01. Washington, DC.

[9] American Society of Mechanical Engineers. 2004. Managing System Integrity of Gas Pipelines (ASME B31.8S-2004). ASME: New York.

[10] Vanaei, H.R., Eslami, A. and Egbewande, A., 2017. A review on pipeline corrosion, in-line inspection (ILI), and corrosion growth rate models. International Journal of Pressure Vessels and Piping, 149, pp.43-54.

[11] Rempel, R.G., 2005. Anomaly detection using magnetic flux leakage technology. In Rio Pipeline Conference & Exposition.

[12] Bickerstaff, R., Vaughn, M., Stoker, G., Hassard, M. and Garrett, M., 2002. Review of sensor technologies for in-line inspection of natural gas pipelines. Sandia National Laboratories, Albuquerque, NM.

[13] Noronha Jr, D.B., Martins, R.R., Jacob, B.P. and de Souza, E., 2010. Procedures for the strain based assessment of pipeline dents. International Journal of Pressure Vessels and Piping, 87(5), pp.254-265.

[14] https://www.thestar.com/news/gta/2013/11/29/hightech_pipeline_inspection_tools_have_limitations.html, Accessed on April 15, 2019.

[15] Wang, S., Huang, S., Zhao, W. and Wei, Z., 2015. 3D modeling of circumferential SH guided waves in pipeline for axial cracking detection in ILI tools. Ultrasonics, 56, pp.325-331.

[16] Inaudi, D. and Glisic, B., 2010. Long-range pipeline monitoring by distributed fiber optic

sensing. Journal of Pressure Vessel Technology, 132(1), 011701.

[17] Huang, S.C., Lin, W.W., Tsai, M.T. and Chen, M.H., 2007. Fiber optic in-line distributed sensor for detection and localization of the pipeline leaks. Sensors and Actuators A: Physical, 135(2), pp.570-579.

[18] Nikles, M., 2009, April. Long-distance fiber optic sensing solutions for pipeline leakage, intrusion, and ground movement detection. In Fiber optic sensors and applications VI (Vol. 7316, pp. 13-25). SPIE.

[19] López-Higuera, J.M., Cobo, L.R., Incera, A.Q. and Cobo, A., 2011. Fiber optic sensors in structural health monitoring. Journal of Lightwave Technology, 29(4), pp.587-608.

[20] Chen, Y., Tang, F., Bao, Y., Chen, G. and Tang, Y., 2016. Fe-C coated long period fiber grating sensors for steel corrosion monitoring. Optics Letters, 41(13), pp.344-346.

[21] Huang, Y., Gao, Z., Chen, G. and Xiao, H., 2013. Long period fiber grating sensors coated with nano iron/silica particles for corrosion monitoring. Smart Materials and Structures, 22(7), p.075018.

[22] Huang, Y., Tang, F., Liang, X., Chen, G., Xiao, H. and Azarmi, F., 2015. Steel bar corrosion monitoring with long-period fiber grating sensors coated with nano iron/silica particles and polyurethane. Structural Health Monitoring, 14(2), pp.178-189.

[23] Chen, Y., Tang, F., Bao, Y., Chen, G. and Tang, Y., 2016. Fe-C coated long period fiber grating sensors for steel corrosion monitoring. Optics Letters, 41(13), pp.344-346.

[24] Tan, X., Bao, Y., Zhang, Q., Nassif, H. and Chen, G., 2021. Strain transfer effect in distributed fiber optic sensors under an arbitrary field. Automation in Construction, 124, p.103597.

[25] Mahjoubi, S., Tan, X. and Bao, Y., 2022. Inverse analysis of strain distributions sensed by distributed fiber optic sensors subject to strain transfer. Mechanical Systems and Signal Processing, 166, p.108474.

[26] Yan, M., Tan, X., Mahjoubi, S. and Bao, Y., 2022. Strain transfer effect on measurements with distributed fiber optic sensors. Automation in Construction, 139, p.104262.

[27] Tan, X. and Bao, Y., 2021. Measuring crack width using a distributed fiber optic sensor based on optical frequency domain reflectometry. Measurement, 172, p.108945.

[28] Tan, X., Mahjoubi, S., Zou, X., Meng, W. and Bao, Y., 2023. Metaheuristic inverse analysis on interfacial mechanics of distributed fiber optic sensors undergoing interfacial debonding. Mechanical Systems and Signal Processing, 200, p.110532.

[29] Tan, X., Guo, P., Zou, X. and Bao, Y., 2022. Buckling detection and shape reconstruction using strain distributions measured from a distributed fiber optic sensor. Measurement, 200, p.111625.

[30] Tan, X., Fan, L., Huang, Y. and Bao, Y., 2021. Detection, visualization, quantification, and warning of pipe corrosion using distributed fiber optic sensors. Automation in Construction, 132, p.103953.

[31] Von Der Weid, J.P., Passy, R., Mussi, G. and Gisin, N., 1997. On the characterization of

optical fiber network components with optical frequency domain reflectometry. Journal of Lightwave Technology, 15(7), pp.1131-1141.

[32] Bao, Y., Meng, W., Chen, Y., Chen, G. and Khayat, K.H., 2015. Measuring mortar shrinkage and cracking by pulse pre-pump Brillouin optical time domain analysis with a single optical fiber. Materials Letters, 145, pp.344-346.

[33] Pak, Y.E., 1992. Longitudinal shear transfer in fiber optic sensors. Smart Materials and Structures, 1(1), pp.57-62.

[34] Sirkis, J.S. and Haslach Jr, H.W., 1991. Complete phase-strain model for structurally embedded interferometric optical fiber sensors. Journal of Intelligent Material Systems and Structures, 2(1), pp.3-24.

[35] Cox, H.L., 1952. The elasticity and strength of paper and other fibrous materials. British Journal of Applied Physics, 3(3), pp.72-79.

[36] Ansari, F. and Libo, Y., 1998. Mechanics of bond and interface shear transfer in optical fiber sensors. Journal of Engineering Mechanics, 124(4), pp.385-394.

[37] Duck, G. and LeBlanc, M., 2000. Arbitrary strain transfer from a host to an embedded fiber-optic sensor. Smart Materials and Structures, 9(4), pp.492-497.

[38] Li, Q., Li, G., Wang, G., Ansari, F. and Liu, Q., 2002. Elasto-plastic bonding of embedded optical fiber sensors in concrete. Journal of Engineering Mechanics, 128(4), pp.471-478.

[39] Li, D., Li, H., Ren, L. and Song, G., 2006. Strain transferring analysis of fiber Bragg grating sensors. Optical Engineering, 45(2), pp.024402.

[40] Huang, Y., Bao, Y., Chen, G. and Zhou, Z., 2019. A constrained cylinder model of strain transfer for packaged fiber Bragg grating sensors embedded in inelastic medium. Structural Control and Health Monitoring, 26(5), p.e2335.

[41] Li, H.N., Zhou, G.D., Ren, L. and Li, D.S., 2007. Strain transfer analysis of embedded fiber Bragg grating sensor under nonaxial stress. Optical Engineering, 46(5), pp.054402-054402.

[42] Ling, H.Y., Lau, K.T., Cheng, L. and Chow, K.W., 2005. Embedded fibre Bragg grating sensors for non-uniform strain sensing in composite structures. Measurement Science and Technology, 16(12), pp.2415-2424.

[43] Li, H.N., Zhou, G.D., Ren, L. and Li, D.S., 2009. Strain transfer coefficient analyses for embedded fiber Bragg grating sensors in different host materials. Journal of Engineering Mechanics, 135(12), pp.1343-1353.

[44] Jiang, Z., Lian, J., Yang, D. and Dong, S., 1998. An analytical study of the influence of thermal residual stresses on the elastic and yield behaviors of short fiber-reinforced metal matrix composites. Materials Science and Engineering: A, 248(1-2), pp.256-275.

[45] Zhang, Q., Sun, Y., Zhang, Z., Zeng, P., Duan, J., Zhu, N., Bai, J. and Rong, F., 2019. Strain transfer in distributed fiber optic sensor with optical frequency domain reflectometry technology. Optical Engineering, 58(2), pp.027109-027109.

[46] Falcetelli, F., Rossi, L., Di Sante, R. and Bolognini, G., 2020. Strain transfer in surface-

bonded optical fiber sensors. Sensors, 20(11), p.3100.

[47] Wang, H. and Zhou, Z., 2014. Advances of strain transfer analysis of optical fibre sensors. Pacific Science Review, 16(1), pp.8-18.

[48] Feng, X., Zhou, J., Sun, C., Zhang, X. and Ansari, F., 2013. Theoretical and experimental investigations into crack detection with BOTDR-distributed fiber optic sensors. Journal of Engineering Mechanics, 139(12), pp.1797-1807.

[49] Tan, X., Abu-Obeidah, A., Bao, Y., Nassif, H. and Nasreddine, W., 2021. Measurement and visualization of strains and cracks in CFRP post-tensioned fiber reinforced concrete beams using distributed fiber optic sensors. Automation in Construction, 124, p.103604.

[50] Gentry, T.W., Wiliamowski, B.M. and Weatherford, L.R., 1995. A comparison of traditional forecasting techniques and neural networks. Intelligent Engineering Systems Through Artificial Neural Networks, 5, pp.765-770.

[51] Bao, Y., Tang, F., Chen, Y., Meng, W., Huang, Y. and Chen, G., 2016. Concrete pavement monitoring with PPP-BOTDA distributed strain and crack sensors. Smart Structures and Systems, 18(3), pp.405-423.

[52] Tan, X. and Bao, Y., 2021. Measuring crack width using a distributed fiber optic sensor based on optical frequency domain reflectometry. Measurement, 172, p.108945.

[53] Bassil, A., Wang, X., Chapeleau, X., Niederleithinger, E., Abraham, O. and Leduc, D., 2019. Distributed fiber optics sensing and coda wave interferometry techniques for damage monitoring in concrete structures. Sensors, 19(2), p.356.

[54] Yan, M., Tan, X., Mahjoubi, S. and Bao, Y., 2022. Strain transfer effect on measurements with distributed fiber optic sensors. Automation in Construction, 139, p.104262.

[55] Zhang, S., Liu, H., Cheng, J. and DeJong, M.J., 2020. A mechanical model to interpret distributed fiber optic strain measurement at displacement discontinuities. Structural Health Monitoring, p.1475921720964183.

[56] Tan, X., Abu-Obeidah, A., Bao, Y., Nassif, H. and Nasreddine, W., 2021. Measurement and visualization of strains and cracks in CFRP post-tensioned fiber reinforced concrete beams using distributed fiber optic sensors. Automation in Construction, 124, p.103604.

[57] Bao, Y., Valipour, M., Meng, W., Khayat, K.H. and Chen, G., 2017. Distributed fiber optic sensor-enhanced detection and prediction of shrinkage-induced delamination of ultra-high-performance concrete overlay. Smart Materials and Structures, 26(8), p.085009.

[58] Calabrese, A.S., Colombi, P. and D'Antino, T., 2019. Analytical solution of the bond behavior of FRCM composites using a rigid-softening cohesive material law. Composites Part B: Engineering, 174, p.107051.

[59] Zou, X., Sneed, L.H. and D'Antino, T., 2020. Full-range behavior of fiber reinforced cementitious matrix (FRCM)-concrete joints using a trilinear bond-slip relationship. Composite Structures, 239, p.112024.

[60] Simpson, T.R.E. and Keddie, J.L., 2003. Evidence from infrared ellipsometry for covalent

bonding at a polymer/polymer interface with relevance to" lock-up" in pressure-sensitive adhesive laminates. Journal of Adhesion, 79(12), pp.1207-1218.

[61] Intel RealSense. ID Solution F450/F455 Datasheet. https://dev.intelrealsense.com/docs/intel-realsense-id-solution-data-sheet. Accessed on December 5, 2021.

[62] Intel® RealSense™ Depth Camera D455. https://www.intelrealsense.com/depth-camera-d455/. Accessed on December 5, 2021.

[63] Gentry, T.W., Wiliamowski, B.M. and Weatherford, L.R., 1995. A comparison of traditional forecasting techniques and neural networks. Intelligent Engineering Systems Through Artificial Neural Networks, 5, pp.765-770.

[64] NACE SP0775, 2013. Preparation, installation, analysis, and interpretation of corrosion coupons in oilfield operations. NACE International Institute, Houston, Texas, USA. https://store.nace.org/sp0775-2013-formerly-rp0775-18854

[65] Sun, Y., Shi, B., Chen, S.E., Zhu, H.H., Zhang, D. and Lu, Y., 2014. Feasibility study on corrosion monitoring of a concrete column with central rebar using BOTDR. Smart Structures and Systems, 13(1), pp.41-53.

[66] Xu, L., Zhang, D., Huang, Y., Shi, S., Pan, H. and Bao, Y., 2022. Monitoring epoxy coated steel under combined mechanical loads and corrosion using fiber Bragg grating sensors. Sensors, 22(20), p.8034.

[67] Gao, J., Wu, J., Li, J. and Zhao, X., 2011. Monitoring of corrosion in reinforced concrete structure using Bragg grating sensing. NDT & E International, 44(2), pp.202-205.

[68] Li, W., Chen, L. and Bao, X., 2013. Compensation of temperature and strain coefficients due to local birefringence using optical frequency domain reflectometry. Optics Communications, 311, pp.26-32.

[69] Shojai, S., Schaumann, P. and Brömer, T., 2022. Probabilistic modelling of pitting corrosion and its impact on stress concentrations in steel structures in the offshore wind energy. Marine Structures, 84, p.103232.

[70] Bertolini, L., Elsener, B., Pedeferri, P., Redaelli, E., and Polder, R. B., 2013. Corrosion of steel in concrete: prevention, diagnosis, repair. John Wiley & Sons.

[71] Deng, F., Huang, Y., and Azarmi, F. J. C., 2019. Corrosion behavior evaluation of coated steel using fiber Bragg grating sensors. 9, 55.

[72] Deng, F., Huang, Y., Azarmi, F., and Wang, Y. J. C., 2017. Pitted corrosion detection of thermal sprayed metallic coatings using fiber Bragg grating sensors. 7, 35.

[73] Melchers, R., 1997. Modeling of marine corrosion of steel specimens. 1300, 20-33.

[74] R.R. Fessler, Pipeline corrosion: Final report, Pipeline and Hazardous Materials Safety Administration (PHMSA), U.S. Department of Transportation, Evanston, IL, 2008.

[75] Karypidis, D.F., Berrocal, C., Rempling, R., Granath, G. and Simonsson, P.J.I., 2019. Structural health monitoring of RC structures using optic fiber strain measurements: A deep learning approach. In 2019 IABSE Congress. New York City.

[76] Song, Q., Zhang, C., Tang, G. and Ansari, F., 2020. Deep learning method for detection of structural microcracks by brillouin scattering based distributed optical fiber sensors. Smart Materials and Structures, 29(7), p.075008.

[77] Dai, T.T., Ren, L., Jia, Z.G., Li, Y.T. and Li, Y., 2022. Crack extension identification based on distributed fiber sensing measurement and optimized support vector regression. Ocean Engineering, 245, p.110515.

[78] The Corning, Inc., Corning® SMF-28e+® optical fiber production information. https://www.corning.com/media/worldwide/coc/documents/Fiber/PI-1463-AEN.pdf (accessed on December 1, 2022)

[79] LUNA. ODiSI 6000 Series: Optical distributed sensor interrogator 2022. https://lunainc.com/product/odisi-6000-series (accessed on December 1, 2022)

[80] LUNA. ODiSI 6000 series: Optical distributed sensor interrogators data sheet 2022:1–6. https://lunainc.com/sites/default/files/assets/files/data-sheet/Luna%20ODiSI%206000%20Data%20Sheet.pdf (accessed on December 1, 2022)

[81] Kokoska, S. and Zwillinger, D., 2000. CRC standard probability and statistics tables and formulae. CRC Press. https://doi.org/10.1201/b16923

[82] Razali, N.M. and Wah, Y.B., 2011. Power comparisons of Shapiro-Wilk, Kolmogorov-Smirnov, Lilliefors and Anderson-Darling tests. Journal of Statistical Modeling and Analytics, 2(1), pp.21-33.

[83] Baduge, S.K., Thilakarathna, S., Perera, J.S., Arashpour, M., Sharafi, P., Teodosio, B., Shringi, A. and Mendis, P., 2022. Artificial intelligence and smart vision for building and construction 4.0: Machine and deep learning methods and applications. Automation in Construction, 141, p.104440.

[84] Lin, Y.Z., Nie, Z.H. and Ma, H.W., 2022. Dynamics-based cross-domain structural damage detection through deep transfer learning. Computer-Aided Civil and Infrastructure Engineering, 37(1), pp.24-54.

[85] Dong, Y., Patil, S., van Arem, B. and Farah, H., 2022. A hybrid spatial–temporal deep learning architecture for lane detection. Computer-Aided Civil and Infrastructure Engineering, 31, pp.1-29.

[86] Kiranyaz, S., Avci, O., Abdeljaber, O., Ince, T., Gabbouj, M. and Inman, D.J., 2021. 1D convolutional neural networks and applications: A survey. Mechanical systems and signal processing, 151, p.107398.

[87] Ryu, J., McFarland, T., Haas, C.T. and Abdel-Rahman, E., 2022. Automatic clustering of proper working postures for phases of movement. Automation in Construction, 138, p.104223.

[88] Paszke, A., Gross, S., Massa, F., Lerer, A., Bradbury, J., Chanan, G., Killeen, T., Lin, Z., Gimelshein, N., Antiga, L. and Desmaison, A., 2019. Pytorch: An imperative style, high-performance deep learning library. Advances in Neural Information Processing Systems, 32.

[89] Hartigan, J.A. and Wong, M.A., 1979. Algorithm AS 136: A k-means clustering algorithm. Journal of the Royal Statistical Society. Series C (Applied Statistics), 28(1), pp.100-108.

[90] Zhang, T., Ramakrishnan, R. and Livny, M., 1996. BIRCH: An efficient data clustering method for very large databases. ACM SIGMOD Record, 25(2), pp.103-114.

[91] Bilmes, J.A., 1998. A gentle tutorial of the EM algorithm and its application to parameter estimation for Gaussian mixture and hidden Markov models. International Computer Science Institute, 4(510), p.126.

[92] Breiman, L., 2001. Random forests. Machine Learning, 45(1), pp.5-32.

[93] Marquardt, D.W. and Snee, R.D., 1975. Ridge regression in practice. The American Statistician, 29(1), pp.3-20.

[94] Burges, C.J., 1998. A tutorial on support vector machines for pattern recognition. Data Mining and Knowledge Discovery, 2(2), pp.121-167.

[95] Quinlan, J.R., 1986. Induction of decision trees. Machine Learning, 1, pp.81-106.

[96] Keller, J.M., Gray, M.R. and Givens, J.A., 1985. A fuzzy k-nearest neighbor algorithm. IEEE Transactions on Systems, Man, and Cybernetics, (4), pp.580-585.

[97] Pal, S.K. and Mitra, S., 1992. Multilayer perceptron, fuzzy sets, and classification. IEEE Transactions on Neural Networks, 3(5), pp.683-697.

[98] Chen, T., and Guestrin, C., 2016. XGBoost: A scalable tree boosting system. Proceedings of the 22nd ACM SIGKDD International Conference on Knowledge Discovery and Data Mining, pp.785-794.

[99] Towers, J.D., 2009. Finite difference methods for approximating Heaviside functions. Journal of Computational Physics, 228(9), pp.3478-3489.

[100] Diana Earshia, V. and Sumathi, M., 2018, January. A Comprehensive Study of 1D and 2D Image Interpolation Techniques. International Conference on Communications and Cyber Physical Engineering, pp.383-391.

[101] Wang, W., Hu, W., Wang, W., Xu, X., Wang, M., Shi, Y., Qiu, S. and Tutumluer, E., 2021. Automated crack severity level detection and classification for ballastless track slab using deep convolutional neural network. Automation in Construction, 124, p.103484.

[102] Bangaru, S.S., Wang, C., Busam, S.A. and Aghazadeh, F., 2021. ANN-based automated scaffold builder activity recognition through wearable EMG and IMU sensors. Automation in Construction, 126, p.103653.

[103] Ghimire, S., Deo, R.C., Casillas-Perez, D., Salcedo-Sanz, S., Sharma, E. and Ali, M., 2022. Deep learning CNN-LSTM-MLP hybrid fusion model for feature optimizations and daily solar radiation prediction. Measurement, 202, p.111759.

[104] Gorges, C., Öztürk, K. and Liebich, R., 2019. Impact detection using a machine learning approach and experimental road roughness classification. Mechanical Systems and Signal Processing, 117, pp.738-756.

[105] Zhao, L., Tang, F., Li, H.N. and Ansari, F., 2023. Characterization of OFDR distributed optical fiber for crack monitoring considering fiber-coating interfacial slip. Structural Health Monitoring, 22(1), pp.180-200.

[106] Morgese, M., Domaneschi, M., Ansari, F., Cimellaro, G.P. and Inaudi, D., 2021. Improving distributed fiber-optic sensor measures by digital image correlation: Two-stage structural health monitoring. ACI Structural Journal, 118(6).

[107] Domaneschi, M., Niccolini, G., Lacidogna, G. and Cimellaro, G.P., 2020. Nondestructive monitoring techniques for crack detection and localization in RC elements. Applied Sciences, 10(9), p.3248.

[108] Luo, Y., and Lu, K., 2022. An online state of health estimation technique for lithium-ion battery using artificial neural network and linear interpolation. Journal of Energy Storage, 52, p.105062.

[109] Bourke, P., 1995. RGB colour space. http://paulbourke.net/miscellaneous/colourspace/ (accessed on May 1, 2023).

[110] Hao, W., and Zhili, S., Improved mosaic: Algorithms for more complex images, in: Journal of Physics: Conference Series, 2020: pp.0–8.

[111] Jocher, G., Chaurasia, A., Stoken, A., and Borovec, J., 2022. Ultralytics/yolov5: v7.0 - YOLOv5 SOTA realtime instance segmentation (v7.0). Zenodo. https://doi.org/10.5281/zenodo.7347926.

[112] Marín-garcía, D., Bienvenido-huertas, D., Carretero-ayuso, M.J., and Della, S., 2023. Deep learning model for automated detection of efflorescence and its possible treatment in images of brick facades. Automation in Construction, 145, p.104658.

[113] He, K., Zhang, X., Ren, S., and Sun, J., 2015. Spatial pyramid pooling in deep convolutional networks for visual recognition. IEEE Transactions on Pattern Analysis and Machine Intelligence, 37, pp.1904–1916. https://doi.org/10.1109/TPAMI.2015.2389824.

[114] Dosovitskiy, A., Beyer, L., Kolesnikov, A., Weissenborn, D., Zhai, X., Unterthiner, T., Dehghani, M., Minderer, M., Heigold, G., Gelly, S., Uszkoreit, J., and Houlsby, N., 2020. An image is worth 16x16 words: transformers for image recognition at scale. http://arxiv.org/abs/2010.11929.

[115] Vaswani, A., Shazeer, N., Parmar, N., Uszkoreit, J., Jones, L., Gomez, A.N., Kaiser, Ł., and Polosukhin, I., 2017. Attention is all you need. Advances in Neural Information Processing Systems, 2017-Decem, pp.5999–6009.

[116] Zhu, X., Lyu, S., Wang, X., and Zhao, Q., 2021. TPH-YOLOv5: Improved YOLOv5 based on transformer prediction head for object detection on drone-captured scenarios. Proceedings of the IEEE International Conference on Computer Vision, pp.2778–2788.

[117] Guo, F., Qian, Y., Wu, Y., Leng, Z., and Yu, H., 2021. Automatic railroad track components inspection using real-time instance segmentation. Computer-Aided Civil and Infrastructure Engineering, 36, pp.362–377.

[118] Berrocal, C.G., Fernandez, I., Bado, M.F., Casas, J.R., and Rempling, R., 2021. Assessment and visualization of performance indicators of reinforced concrete beams by distributed optical fibre sensing. Structural Health Monitoring, 20, pp.3309–3326.

[119] Berrocal, C.G., Fernandez, I., and Rempling, R., 2021. Crack monitoring in reinforced

concrete beams by distributed optical fiber sensors. Structure and Infrastructure Engineering, 17, pp.124–139.

[120] Torralba, A., Russell, B.C., and Yuen, J., 2010. LabelMe: Online image annotation and applications. Proceedings of the IEEE, 98, pp.1467–1484.

[121] Paszke, A., Gross, S., Massa, F., Lerer, A., Bradbury, J., Chanan, G., Killeen, T., Lin, Z., Gimelshein, N., Antiga, L., Desmaison, A., Köpf, A., Yang, E., DeVito, Z., Raison, M., Tejani, A., Chilamkurthy, S., Steiner, B., Fang, L., Bai, J., and Chintala, S., 2019. PyTorch: An imperative style, high-performance deep learning library. Advances in Neural Information Processing Systems, 32.

[122] Wang, W., Hu, W., Wang, W., Xu, X., Wang, M., Shi, Y., Qiu, S., and Tutumluer, E., 2021. Automated crack severity level detection and classification for ballastless track slab using deep convolutional neural network. Automation in Construction, 124, p.103484.

[123] Yin, X., Chen, Y., Bouferguene, A., Zaman, H., Al-Hussein, M., and Kurach, L., 2020. A deep learning-based framework for an automated defect detection system for sewer pipes. Automation in Construction, 109, p.102967.

[124] Ren, S., He, K., Girshick, R., and Sun, J., 2017. Faster R-CNN: Towards real-time object detection with region proposal networks. IEEE Transactions on Pattern Analysis and Machine Intelligence, 39, pp.1137–1149.

[125] Lin, T.Y., Goyal, P., Girshick, R., He, K., and Dollar, P., 2020. Focal loss for dense object detection. IEEE Transactions on Pattern Analysis and Machine Intelligence, 42, pp.318–327.

[126] Tian, Z., Shen, C., Chen, H., and He, T., 2019. FCOS: Fully convolutional one-stage object detection. Proceedings of the IEEE International Conference on Computer Vision, pp.9626–9635.

[127] Liu, W., Anguelov, D., Erhan, D., Szegedy, C., Reed, S., Fu, C.Y., and Berg, A.C., 2016. SSD: Single shot multibox detector. Lecture Notes in Computer Science, pp.21–37.

[128] Bakir, S.A., Elms, D.G. and Lamb, J., 1994. Risk management and lifeline engineering. In 12th World Conference on Earthquake Engineering (pp. 1-8).

[129] Liu, H., 2003. Pipeline Engineering. CRC Press.

[130] Adegboye, M.A., Fung, W.K. and Karnik, A., 2019. Recent advances in pipeline monitoring and oil leakage detection technologies: Principles and approaches. Sensors, 19(11), p.2548.

[131] Groeger, L., 2012. Pipelines Explained: How safe are America's 2.5 million miles of pipelines? ProPublica. November 15, 2012.

[132] https://portal.phmsa.dot.gov/analytics/saw.dll?Portalpages

[133] Kishawy, H.A. and Gabbar, H.A., 2010. Review of pipeline integrity management practices. International Journal of Pressure Vessels and Piping, 87(7), pp.373-380.

[134] Fact Sheet: Pipe Defects and Anomalies. https://primis.phmsa.dot.gov/comm/FactSheets/FSPipeDefects.htm?nocache=7250

[135] Ersoy, D., 2016. Underground Natural Gas Storage System Risk Assessment, Mitigation,

and Research Needs. PHMSA Pipeline Safety Research and Development Forum. November 16-17, 2016. https://primis.phmsa.dot.gov/rd/mtgs/111616/Daniel%20Ersoy.pdf

[136] Quickel, G.T. and Beavers, J.A., 2016, September. Pipeline failures resulting from interacting integrity threats. In International Pipeline Conference (Vol. 50251, p. V001T03A049). American Society of Mechanical Engineers.

[137] Cosham, A. and Hopkins, P., 2002, January. The pipeline defect assessment manual. In International Pipeline Conference (Vol. 36207, pp. 1565-1581).

[138] Integrity Management of Gas Transmission Pipelines in High Consequence Areas. https://www.ntsb.gov/safety/safety-studies/Documents/SS1501.pdf

[139] Adegboye, M.A., Fung, W.K. and Karnik, A., 2019. Recent advances in pipeline monitoring and oil leakage detection technologies: Principles and approaches. Sensors, 19(11), p.2548.

[140] Belvederesi, C., Thompson, M.S. and Komers, P.E., 2018. Statistical analysis of environmental consequences of hazardous liquid pipeline accidents. Heliyon, 4(11).

[141] ASME B31.8S-2016, Managing System Integrity of Gas Pipelines. American Society of Mechanical Engineers, 2016.

[142] Tiratsoo, John. Pipeline Pigging & Integrity Technology. Clarion Technical Publishers, 2013.

[143] Pipeline Hydrostatic Testing Explained. https://hanginghco.com/pipeline-hydrostatic-testing/.

[144] Kuprewicz, R.B., 2004. Pipeline integrity and direct assessment a layman’s perspective. Pipeline Saf. Trust, 33(7).

[145] McGrath, M.J., Scanaill, C.N., McGrath, M.J. and Scanaill, C.N., 2013. Sensing and sensor fundamentals. Sensor technologies: Healthcare, wellness, and environmental applications, pp.15-50.

[146] https://www.phmsa.dot.gov/sites/phmsa.dot.gov/files/docs/technical-resources/pipeline/risk-modeling-work-group/65681/interactive-threats-discussionrmwg0816.pdf. Accessed on May 9, 2023.

[147] Incorporating Interactive Threats in Kiefner/NYGAS and other Risk Models. https://www.nysearch.org/tech_briefs/T-768_InteractiveThreats_TBv2011_012412.pdf.

[148] Interacting Threats to Pipeline Integrity – Defined and Explained. https://www.ingaa.org/File.aspx?id=20210.

[149] https://www.northeastgas.org/pdf/d_dzurko_transmission.pdf.

[150] An introduction to unpiggable pipelines. https://ww2.energy.ca.gov/2019publications/CEC-500-2019-053/CEC-500-2019-053-APA-F.pdf.

[151] https://www.pipeliner.com.au/2016/03/16/an-introduction-to-unpiggable-pipelines/.

[152] Parfomak, P.W., 2015. DOT's federal pipeline safety program: Background and key issues for congress. Congressional Research Service.

[153] https://www.govinfo.gov/content/pkg/FR-2019-10-01/pdf/2019-20306.pdf.

[154] Eisler, B. and Lanan, G.A., 2012, April. Fiber optic leak detection systems for subsea pipelines. In Offshore Technology Conference (pp. OTC-23070). OTC.

[155] Li, L.J., Pan, R., Zhang, W.H. and Li, H., 2013. Overview of fiber optic pipeline monitoring sensors. Applied mechanics and materials, 246, pp.872-876.

[156] Henrie, M., Carpenter, P. and Nicholas, R.E., 2016. Pipeline leak detection handbook. Gulf Professional Publishing.

[157] Datta, S. and Sarkar, S., 2016. A review on different pipeline fault detection methods. Journal of Loss Prevention in the Process Industries, 41, pp.97-106.

[158] Maltby, P.M., Edwards, J.S. and Hamilton, J.C., TDW Delaware Inc, 1995. Method and apparatus for ultrasonic pipeline inspection. U.S. Patent 5,460,046.

[159] Jiao, J., He, C., Wu, B., Wu, B. and Wang, X., 2002. Application of ultrasonic guided waves in pipe’s NDT. Journal of Experimental Mechanics, 1, p.000.

[160] Moorman, B.J., Robinson, S.D. and Burgess, M.M., 2003. Imaging periglacial conditions with ground-penetrating radar. Permafrost and Periglacial Processes, 14(4), pp.319-329.

[161] Jol, H.M. and Smith, D.G., 1995. Ground penetrating radar surveys of peatlands for oilfield pipelines in Canada. Journal of Applied Geophysics, 34(2), pp.109-123.

[162] Weil, G.J., 1993, May. Non contact, remote sensing of buried water pipeline leaks using infrared thermography. In Water Management in the'90s: a Time for Innovation (pp. 404-407). ASCE.

[163] Fan, C., Sun, F. and Yang, L., 2005, September. Investigation on nondestructive evaluation of pipelines using infrared thermography. In 2005 joint 30th international conference on infrared and millimeter waves and 13th international conference on terahertz electronics (Vol. 2, pp. 339-340). IEEE.

[164] Datta, S. and Sarkar, S., 2016. A review on different pipeline fault detection methods. Journal of Loss Prevention in the Process Industries, 41, pp.97-106.

[165] Bai, Y. and Bai, Q., 2014. Subsea pipeline integrity and risk management. Gulf Professional Publishing.

[166] Boaz, L., Kaijage, S. and Sinde, R., 2014, July. An overview of pipeline leak detection and location systems. In Proceedings of the 2nd Pan African International Conference on Science, Computing and Telecommunications (PACT 2014) (pp. 133-137). IEEE.

[167] Baroudi, U., Al-Roubaiey, A.A. and Devendiran, A., 2019. Pipeline leak detection systems and data fusion: A survey. IEEE Access, 7, pp.97426-97439.

[168] Liu, Z. and Kleiner, Y., 2013. State of the art review of inspection technologies for condition assessment of water pipes. Measurement, 46(1), pp.1-15.

[169] http://www.engineering.com/ask@/qactid/7/qaqid/5576.aspx

[170] Henrie, M., Carpenter, P. and Nicholas, R.E., 2016. Pipeline leak detection handbook. Gulf Professional Publishing.

[171] Rempel, R. Anomaly detection using magnetic flux leakage technology. Rio Pipeline Conference & Exposition. 2005.

[172] https://en.wikipedia.org/wiki/Magnetic_flux_leakage.

[173] L. Clapham. Detection of Mechanical Damage Using the Magnetic Flux Leakage Technique. Queen's University, Canada.

[174] http://www.mfeenterprises.com/what-is-mfl.

[175] https://eddyfi.com/en/technology/magnetic-flux-leakage-mfl.

[176] Orazem, M. ed., 2014. Underground pipeline corrosion (No. 63). Elsevier.

[177] Baroudi, U., Al-Roubaiey, A.A. and Devendiran, A., 2019. Pipeline leak detection systems and data fusion: A survey. IEEE Access, 7, pp.97426-97439.

[178] Shi, Y., Zhang, C., Li, R., Cai, M. and Jia, G., 2015. Theory and application of magnetic flux leakage pipeline detection. Sensors, 15(12), pp.31036-31055.

[179] Zhang, L., Belblidia, F., Cameron, I., Sienz, J., Boat, M. and Pearson, N., 2015. Influence of specimen velocity on the leakage signal in magnetic flux leakage type nondestructive testing. Journal of Nondestructive Evaluation, 34(2), p.6.

[180] Valentine, F., 2001. The effect of debris on MFL inspection results. Corrosion Prevention and Control 47.1 (2000): 25-32.

[181] Mandache, C., Shiari, B. and Clapham, L., 2005. Defect separation considerations in magnetic flux leakage inspection. Insight-Non-Destructive Testing and Condition Monitoring, 47(5), pp.269-273.

[182] Atherton, D.L., 1995. Remote field eddy current inspection. IEEE Transactions on Magnetics, 31(6), pp.4142-4147.

[183] Schmidt, T.R., 1989. History of the remotes field eddy current inspection technique. Materials Evaluation, 47(1), pp.14-22.

[184] Sophian, A., Tian, G.Y., Taylor, D. and Rudlin, J., 2003. A feature extraction technique based on principal component analysis for pulsed Eddy current NDT. NDT & e International, 36(1), pp.37-41.

[185] Nestleroth, J.B. and Davis, R.J., 2007. Application of eddy currents induced by permanent magnets for pipeline inspection. NDT & E International, 40(1), pp.77-84.

[186] Brockhaus, S., Ginten, M., Klein, S., Teckert, M., Stawicki, O., Oevermann, D., Meyer, S. and Storey, D., 2014. In-line inspection (ILI) methods for detecting corrosion in underground pipelines. In Underground pipeline corrosion (pp. 255-285). Woodhead Publishing.

[187] Liu, Z. and Kleiner, Y., 2013. State of the art review of inspection technologies for condition assessment of water pipes. Measurement, 46(1), pp.1-15.

[188] http://osp.mans.edu.eg/elbeltagi/Infra%203-4%20Water%20mains%20condition.pdf.

[189] https://www.ridgid.com/us/en/seesnake-microdrain-camera.

[190] Lee, A., Kleiner, Y., Rajani, B., Wang, L. and Condit, W., 2017. Condition Assessment Technologies for water transmission and sewage conveyance systems. UBC Sustainability scholar program 2017 & Metro Vancouver.

[191] https://www.tuv.com/tunesia/en/pulsed-eddy-current-(pec).html.

[192] Haniffa, M.A.M. and Hashim, F.M., 2011, September. Recent developments in in-line inspection tools (ILI) for deepwater pipeline applications. In 2011 National Postgraduate Conference (pp. 1-6). IEEE.

[193] https://en.wikipedia.org/wiki/Remote_field_testing.

[194] DiMambro, Joseph, Ciji L. Nelson, and David Glenn Moore. Pulsed Eddy Current Crack Detection Capability Assessment Using Aircraft Repair Standards. No. SAND2007-2225C. Sandia National Lab.(SNL-NM), Albuquerque, NM (United States), 2007.

[195] Shepherd, K. Remotely operated vehicles (ROVs). (2001): 2408-2413.

[196] Drury, J.C. and Marino, A., 2000, October. A comparison of the magnetic flux leakage and ultrasonic methods in the detection and measurement of corrosion pitting in ferrous plate and pipe. In 15th world conference on nondestructive testing.

[197].http://www.innospection.com/images/PDF/Technology_-_Magnetic_Eddy_Current_MEC_Inspection_Technique-min.pdf.

[198] https://hemantmore.org.in/science/physics/eddy-currents/4617/.

[199] Schwarze, S., Schneider, N.L., Reichl, T., Dreyer, D., Lefeldt, N., Engels, S., Baker, N., Hore, P.J. and Mouritsen, H., 2016. Weak broadband electromagnetic fields are more disruptive to magnetic compass orientation in a night-migratory songbird (Erithacus rubecula) than strong narrow-band fields. Frontiers in behavioral neuroscience, 10, p.55.

[200] Liu, Z. and Kleiner, Y., 2013. State of the art review of inspection technologies for condition assessment of water pipes. Measurement, 46(1), pp.1-15.

[201] https://www.wef.org/globalassets/assets-wef/3---resources/topics/a-n/collection-systems/te

chnical-resources/epato592010reportonconditionassesmentofwwcs-1.pdf.

[202] Yin, L., 2018. FEM Modelling of Micro-galvanic Corrosion in Al Alloys Induced by Intermetallic Particles: Exploration of Chemical and Geometrical Effects (Doctoral dissertation, KTH Royal Institute of Technology).

[203] http://www.electroscan.com/wp-content/uploads/2015/05/2012-03-01-USEPA-Report.pdf.

[204] Baroudi, U., Al-Roubaiey, A.A. and Devendiran, A., 2019. Pipeline leak detection systems and data fusion: A survey. IEEE Access, 7, pp.97426-97439.

[205] Condition Assessment of Wastewater Collection Systems. https://brownfields-toolbox.org/download/office_of_water/Condition%20Assessment%20of%20WW%20Collection%20Systems.pdf.

[206] https://clu-in.org/characterization/technologies/gpr.cfm.

[207] https://archive.epa.gov/esd/archive-geophysics/web/html/ground-penetrating_radar.html.

[208] Baroudi, U., Al-Roubaiey, A.A. and Devendiran, A., 2019. Pipeline leak detection systems and data fusion: A survey. IEEE Access, 7, pp.97426-97439.

[209] Ni, S.H., Huang, Y.H., Lo, K.F. and Lin, D.C., 2010. Buried pipe detection by ground penetrating radar using the discrete wavelet transform. Computers and Geotechnics, 37(4), pp.440-448.

[210] https://en.wikipedia.org/wiki/Ground-penetrating_radar.

[211] Bimpas, M., Amditis, A., Uzunoglu, N., Lorenzo, A. and Vega, A. eds., 2010. Integrated High resolution imaging radar and decision support system for the rehabilitation of water pipelines. IWA publishing.

[212] Amran, T.S.T., Ismail, M.P., Ahmad, M.R., Amin, M.S.M., Sani, S., Masenwat, N.A., Ismail, M.A. and Hamid, S.H.A., 2017, January. Detection of underground water distribution piping system and leakages using ground penetrating radar (GPR). In AIP Conference Proceedings (Vol. 1799, No. 1). AIP Publishing.

[213] Xue, W., Luo, Y., Yang, Y. and Huang, Y., 2019. Noise suppression for gpr data based on svd of window-length-optimized hankel matrix. Sensors, 19(17), p.3807.

[214] Adegboye, M.A., Fung, W.K. and Karnik, A., 2019. Recent advances in pipeline monitoring and oil leakage detection technologies: Principles and approaches. Sensors, 19(11), p.2548.

[215] https://www.element.com/materials-testing-services/ultrasonic-testing-and-inspection-services.

[216] Bai, Y. and Bai, Q., 2018. Subsea engineering handbook. Gulf Professional Publishing.

[217] Orazem, M. ed., 2014. Underground pipeline corrosion (No. 63). Elsevier.

[218] Brockhaus, S., Ginten, M., Klein, S., Teckert, M., Stawicki, O., Oevermann, D., Meyer, S.

and Storey, D., 2014. In-line inspection (ILI) methods for detecting corrosion in underground pipelines. In Underground pipeline corrosion (pp. 255-285). Woodhead Publishing.

[219] Safari, A., Zhang, J., Velichko, A. and Drinkwater, B.W., 2018. Assessment methodology for defect characterisation using ultrasonic arrays. NDT & E International, 94, pp.126-136.

[220] Ho, M., El-Borgi, S., Patil, D. and Song, G., 2020. Inspection and monitoring systems subsea pipelines: A review paper. Structural Health Monitoring, 19(2), pp.606-645.

[221] Manjula, K., Vijayarekha, K., Venkatraman, B. and Karthik, D., 2012. Ultrasonic time of flight diffraction technique for weld defects: A review. Research Journal of Applied Sciences, Engineering and Technology, 4(24), pp.5525-5533.

[222] https://www.intertek.com/themes/ndt/.

[223] Ultrasonic Inspection Technology. https://www.sgs.com/-/media/global/documents/third-party-documents/ultrasonic-inspection-technology-world-pipelines-november14.pdf.

[224] Non-destructive testing methods for geothermal piping. https://www.osti.gov/servlets/purl/777718.

[225] Ledesma, V.M., Baruch, E.P., Demma, A. and Lowe, M.J.S., 2009. Guided wave testing of an immersed gas pipeline. Materials Evaluation, 67(2), pp.102-115.

[226] http://www.gwultrasonics.com/knowledge/gw-intro/.

[227] Kogia, M., 2017. High temperature electromagnetic acoustic transducer for guided wave testing. Diss. Brunel University London.

[228] Cawley, P., Lowe, M.J.S., Alleyne, D.N., Pavlakovic, B. and Wilcox, P., 2003. Practical long range guided wave inspection-applications to pipes and rail. Mater. Eval, 61(1), pp.66-74.

[229] Pedram, S.K., Mudge, P. and Gan, T.H., 2018. Enhancement of ultrasonic guided wave signals using a split-spectrum processing method. Applied sciences, 8(10), p.1815.

[230] Ho, M., El-Borgi, S., Patil, D. and Song, G., 2020. Inspection and monitoring systems subsea pipelines: A review paper. Structural Health Monitoring, 19(2), pp.606-645.

[231] Ghavamian, A., Mustapha, F., Baharudin, B.H.T. and Yidris, N., 2018. Detection, localisation and assessment of defects in pipes using guided wave techniques: A review. Sensors, 18(12), p.4470.

[232] Liu, C., Harley, J.B., Bergés, M., Greve, D.W. and Oppenheim, I.J., 2015. Robust ultrasonic damage detection under complex environmental conditions using singular value decomposition. Ultrasonics, 58, pp.75-86.

[233] Liu, Z. and Kleiner, Y., 2013. State of the art review of inspection technologies for condition assessment of water pipes. Measurement, 46(1), pp.1-15.

[234] Wu, A., He, S., Ren, Y., Wang, N., Ho, S.C.M. and Song, G., 2019. Design of a new stress

wave-based pulse position modulation (PPM) communication system with piezoceramic transducers. Sensors, 19(3), p.558.

[235] Jin, Y., Ying, Y. and Zhao, D., 2013. Data communications using guided elastic waves by time reversal pulse position modulation: Experimental study. Sensors, 13(7), pp.8352-8376.

[236] Jin, Y., Zhao, D. and Ying, Y., 2011, March. Time reversal data communications on pipes using guided elastic waves: Part i. basic principles. In Health Monitoring of Structural and Biological Systems 2011 (Vol. 7984, pp. 92-103). SPIE.

[237] https://en.wikipedia.org/wiki/Guided_wave_testing.

[238] Nakhli Mahal, H., Yang, K. and Nandi, A.K., 2019. Defect detection using power spectrum of torsional waves in guided-wave inspection of pipelines. Applied Sciences, 9(7), p.1449.

[239] https://membership.corrosion.com.au/wp-content/uploads/2018/01/CM-November-2017-LR.pdf.

[240] Bo, Z., Jiangong, Y., Lefebvre, J.E., Weijiang, X., Xiaoming, Z. and Pingmei, M., 2019. Guided wave propagation in functionally graded cylindrical structures with sector cross-sections. Mathematics and Mechanics of Solids, 24(2), pp.434-447.

[241] Lowe, M. J. S., and P. Cawley. Long range guided wave inspection usage–current commercial capabilities and research directions. Department of Mechanical Engineering, Imperial College London: London, UK (2006).116

[242] Dhutti, A., Lowe, S. and Gan, T.H., 2019. Monitoring of critical metallic assets in oil and gas industry using ultrasonic guided waves. Advances in Structural Health Monitoring, 1, p.13.

[243] ASTM, ASTM E976-99: Standard guide for determining the reproducibility of acoustic emission sensor response, Annual Book of ASTM Standards, Vol. 3.03, (1999), pp. 395-403.

[244] AE Source Location Techniques. https://www.nde-ed.org/EducationResources/CommunityCollege/Other%20Methods/AE/AE_Source%20Location.php.

[245] Grosse, C.U., Ohtsu, M., Aggelis, D.G. and Shiotani, T. eds., 2021. Acoustic emission testing: Basics for research–applications in engineering. Springer Nature.

[246] Pensieri, S. and Bozzano, R., 2017. Chapter Active and Passive Acoustic Methods for In-situ Monitoring of the Ocean Status. Advances in Underwater Acoustics. IntechOpen, 2017.

[247] Adegboye, M.A., Fung, W.K. and Karnik, A., 2019. Recent advances in pipeline monitoring and oil leakage detection technologies: Principles and approaches. Sensors, 19(11), p.2548.

[248] Quy, T.B., Muhammad, S. and Kim, J.M., 2019. A reliable acoustic EMISSION based technique for the detection of a small leak in a pipeline system. Energies, 12(8), p.1472.

[249] Juliano, T.M., Meegoda, J.N. and Watts, D.J., 2013. Acoustic emission leak detection on a metal pipeline buried in sandy soil. Journal of Pipeline Systems Engineering and Practice, 4(3), pp.149-155.

[250] Nicola, C., Nicola, M., Hurezeanu, I., Vintila, A., Aciu, A., Sacerdotanu, D., 2017. Pipeline leakage detection by means of acoustic emission technique. Proc., International Conference on Hydraulics and Pneumatics HERVEX–23rd edition, Băile Govora.

[251] Ho, M., El-Borgi, S., Patil, D. and Song, G., 2020. Inspection and monitoring systems subsea pipelines: A review paper. Structural Health Monitoring, 19(2), pp.606-645.

[252] Li, S., Song, Y. and Zhou, G., 2018. Leak detection of water distribution pipeline subject to failure of socket joint based on acoustic emission and pattern recognition. Measurement, 115, pp.39-44.

[253] Jia, Z., Ren, L., Li, H. and Sun, W., 2018. Pipeline leak localization based on FBG hoop strain sensors combined with BP neural network. Applied Sciences, 8(2), p.146.

[254] Scott, S.L. and Barrufet, M.A., 2003. Worldwide assessment of industry leak detection capabilities for single & multiphase pipelines (pp. 1-8). College Station, TX, USA: Offshore Technology Research Center.

[255] Wang, F., Ho, S.C.M., Huo, L. and Song, G., 2018. A novel fractal contact-electromechanical impedance model for quantitative monitoring of bolted joint looseness. Ieee Access, 6, pp.40212-40220.

[256] https://electronicsforu.com/resources/learn-electronics/band-stop-high-low-pass-filter.

[257] https://cuesinc.com/media/W1siZiIsIjIwMTgvMDgvMjcvNDNvZjE4MmM2cF9Tb25hcl9Qcm9maWxlcl9Mb1Jlcy5wZGYiXV0/Sonar_Profiler_LoRes.pdf.

[258] Liu, Z., Ukida, H., Ramuhalli, P. and Niel, K., 2015. Integrated Imaging and Vision Techniques for Industrial Inspection. Advances in Computer Vision and Pattern Recognition.

[259] Christ, Robert D., and Robert L. Wernli Sr. The ROV manual: a user guide for remotely operated vehicles. Butterworth-Heinemann, 2013.

[260] U.S. Navy Employment Options for Unmanned Surface Vehicles (USVs). https://www.rand.org/content/dam/rand/pubs/research_reports/RR300/RR384/RAND_RR384.pdf.

[261] https://www.rfwireless-world.com/Terminology/Advantages-and-Disadvantages-of-SONAR.html.

[262] Hines, P.C., Risley, W.C. and O'Connor, M.P., 1998, September. A wide-band sonar for underwater acoustics measurements in shallow water. In IEEE Oceanic Engineering Society. OCEANS'98. Conference Proceedings (Cat. No. 98CH36259) (Vol. 3, pp. 1558-1562). IEEE.

[263] Vanaei, H.R., Eslami, A. and Egbewande, A., 2017. A review on pipeline corrosion, in-line inspection (ILI), and corrosion growth rate models. International Journal of Pressure Vessels and Piping, 149, pp.43-54.

[264] Bickerstaff, R., Vaughn, M., Stoker, G., Hassard, M. and Garrett, M., 2002. Review of sensor technologies for in-line inspection of natural gas pipelines. Sandia National Laboratories,

Albuquerque, NM.

[265] Sun, Y. and Kang, Y., 2010. A new MFL principle and method based on near-zero background magnetic field. Ndt & E International, 43(4), pp.348-353.

[266] Murayama, R., Makiyama, S., Kodama, M. and Taniguchi, Y., 2004. Development of an ultrasonic inspection robot using an electromagnetic acoustic transducer for a Lamb wave and an SH-plate wave. Ultrasonics, 42(1-9), pp.825-829.

[267] Nestleroth, J.B. and Davis, R.J., 2007. Application of eddy currents induced by permanent magnets for pipeline inspection. NDT & E International, 40(1), pp.77-84.

[268] Sampath, S., Bhattacharya, B., Aryan, P. and Sohn, H., 2019. A real-time, non-contact method for in-line inspection of oil and gas pipelines using optical sensor array. Sensors, 19(16), p.3615.

[269] Stalenhoef, J.H.J., 1998. MFL and PEC tools for plant inspection. In Proceedings of the 7th ECNDT (pp. 1831-1837).

[270] Chapter 18: Pipeline inspection, maintenance and repair. Ocean Engineering Series, 3, 2001, pp.325-352

[271] Bai, Y. and Bai, Q., 2005. Subsea pipelines and risers (Vol. 3). Elsevier.

[272] https://en.wikipedia.org/wiki/Ultrasonic_testing.

[273] Li, Y., Cai, R., Yan, B., Zainal Abidin, I.M., Jing, H. and Wang, Y., 2018. A capsule-type electromagnetic acoustic transducer for fast screening of external corrosion in nonmagnetic pipes. Sensors, 18(6), p.1733.

[274] Mohebbi, H. and Li, C.Q., 2011. Experimental investigation on corrosion of cast iron pipes. International Journal of Corrosion, 2011.

[275] Ulapane, N., Alempijevic, A., Vidal Calleja, T. and Valls Miro, J., 2017. Pulsed eddy current sensing for critical pipe condition assessment. Sensors, 17(10), p.2208.

[276] https://en.wikipedia.org/wiki/Eddy-current_testing.

[277] Duran, O., Althoefer, K. and Seneviratne, L.D., 2003, September. A sensor for pipe inspection: model, analysis and image extraction. In Proceedings 2003 International Conference on Image Processing (Cat. No. 03CH37429) (Vol. 3, pp. III-597). IEEE.

[278] Li, X., Zhang, S., Liu, S., Jiao, Q. and Dai, L., 2015. An experimental evaluation of the probe dynamics as a probe pig inspects internal convex defects in oil and gas pipelines. Measurement, 63, pp.49-60.